THE CAVENDISH LABORATORY
UNIVERSITY OF CAMBRIDGE

THIS DISSERTATION IS SUBMITTED FOR THE DEGREE OF
DOCTOR OF PHILOSOPHY

ENHANCING FLUORESCENCE AND CHARGE TRANSPORT IN DISORDERED ORGANIC SEMICONDUCTORS

TUDOR H. THOMAS

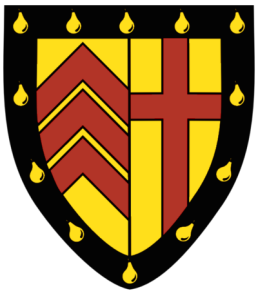

CLARE COLLEGE

April, 2018
Cambridge, United Kingdom

To my parents.

I bind unto myself today
The virtues of the starlit heaven,
The glorious sun's life-giving ray,
The whiteness of the moon at even,
The flashing of the lightning free,
The whirling wind's tempestuous shocks,
The stable earth, the deep salt sea,
Around the old eternal rocks.

I bind unto myself the Name,
The strong Name of the Trinity;
By invocation of the same.
The Three in One, and One in Three,
Of Whom all nature hath creation,
Eternal Father, Spirit, Word:
Praise to the Lord of my salvation,
Salvation is of Christ the Lord.

St. Patrick's Breastplate (vv. 4 & 9)

Declaration

I hereby declare that except where specific reference is made to the work of others, the contents of this dissertation are original and have not been submitted in whole or in part for consideration for any other degree or qualification in this, or any other university. This dissertation is my own work and contains nothing which is the outcome of work done in collaboration with others, except as specified in the text. This dissertation of not more than 60,000 words in length, inclusive of abstract, tables, footnotes, and appendices, but excluding the table of contents, figure captions, bibliography and acknowledgements, in accordance with the Statutes and Ordinances of the University of Cambridge and as approved by the Degree Committee for the Faculty of Physics and Chemistry.

Tudor H. Thomas
April, 2018

Acknowledgements

I would like to thank Professor Henning Sirringhaus, FRS for supervision of this project. For many helpful ideas and discussions, I also thank the optoelectronics group in the Cavendish Laboratory. In particular, I thank Drs David Harkin, Emrys Evans, Dan Credgington, S. Matthew Menke, Mark Nikolka, Jasmine Rivett, and Felix Deschler, and Messrs Alex Gillett, John Armitage, Sam Schott and Edward Booker, with whom I worked closely.

I would like to acknowledge the EPSRC and Merck Chemicals Ltd. for funding via the 'Industrial CASE Studentship' scheme, and Drs Aurélie Morley and Mark James for their help and guidance. I would also like to thank the Cambridge Commonwealth, European and International Trust for its scholarship and the Department of Physics at the University of Cambridge for its award.

Outside research, my time in Cambridge has been enriched immeasurably by singing, and I would like to thank Oscar Osicki, Imogen Russell, and Cameron Richardson-Eames, Matthew Smith and Krishnan Ram-Prasad, Sam Hewitt, Fiona Fraser, and Angie Wittmann, with whom a mutual passion for music has led to countless memories which I treasure. To this end, I would also like to thank Stephen Layton, and the Choir of Trinity College Cambridge with whom I sang for four years.

There are a few others which I would like to thank especially. To Jack Fowles and Elise Mercurio, Ted Tregear and Tessa Peres, and Annabel Green, thank you ever so much for your advice, encouragement, and friendship which I hold very dear. Finally, to my brother, and to my parents, I cannot thank you enough for your abiding support, for your many sacrifices, and for your love and kindness.

Abstract

High performance optoelectronic applications require simultaneously high mobility (μ) and high quantum efficiency of fluorescence (Φ). While this has been realised for organic small molecule semiconductors, applications such as high efficiency organic photovoltaics and bright organic light-emitting diodes towards electrically driven lasing are hampered by an apparent trade-off between μ and Φ in disordered systems. Recent reports of state-of-the-art device performance often optimise μ and Φ in disordered organic materials separately, and employ multi-layer architectures. In this work, we investigate materials in a class of donor-acceptor polymer materials; the indacenodithiophene-*alt*-benzothiadiazole family, which demonstrate high μ in spite of a low long-range structural order, to understand the interplay between these two important device figures-of-merit.

In the first section, we evaluate the effect of various tuneable parameters on μ and device performance in organic field-effect transistors. Using chemical modifications to the solubilising side chains, we observe that the substitution of bulky groups leads to a reduction of the hole mobility $\mu_{\mathrm{h}} > 2$ cm^2/Vs to ~ 0.5 cm^2/Vs in the benchmark polymer of this family, indacenodithiophene-*alt*-benzothiadiazole. Crystallographic and exciton-quenching based experiments confirm this observation is closely related to the degree of polymer backbone aggregation, and this leads to a different temperature evolution of the transport behaviour. In order to reliably improve μ in these systems, an elongation of the donor subunit is required. This increases the π-electron density on the donor, and can lead to an improvement in μ where the side chain density is decreasing. This chemical design, leading to a more highly aggregated structural motif is much more potent in determining μ, it seems, than design strategies to further improve the energetic disorder in the joint density of states and the potential barrier to torsion, which may be near optimised in these low-disorder systems.

In the second section, we unpick the precise relationship between the degree of aggregation apparently linking high μ to low Φ. With a prototype system, we compare the photophysics of two indacenodithiophene-*alt*-benzothiadiazole polymers differing by side chain bulkiness. Despite the aforementioned suppression of μ, we observe an improvement to Φ of < 0.02 to ~ 0.18 upon backbone separation. This derivative has the highest Φ reported for any polymer with μ exceeding that of amorphous-Si. However, the Φ in the more aggregated derivative is not limited by the formation of non-emissive excitons, but rather by an additional internal conversion pathway which is strongly temperature dependent, and mediated by Raman-active vibrations and close chain coupling. Extending this study, we analyse additional materials in this family with the highest $\Phi \cdot \mu$ values reported for conjugated polymers. We find that increasing the energy gap leads to an increase in Φ, and secondary emission pathways via weakly luminescent inter-chain charge transfer species. By solving the rate equations for exciton recombination, we use the radiative rate of inter-chain luminescence as a probe to show strong wavefunction mixing at close-contact points for some polymers, and suggest this as the origin for a superior μ in dithiopheneindenofluorene-*alt*-benzothiadiazole compared to indacenodithiophene-*alt*-benzothiadiazole. We demonstrate how low μ can be decoupled from the energy gap (E_g), and propose backbone elongation leading to increased inter-chain wavefunction overlap and a higher E_g as a design rule to increase Φ and μ together.

Finally, we assess the role of low-frequency vibrations in organic semiconductors displaying thermally activated delayed fluorescence (TADF). In the low-aggregation limit where Φ is maximised, we show that non-radiative triplet recombination is strongly related to low frequency torsional motion, and both are reduced in the presence of a rigid polymer host matrix for various TADF materials across different classes. However, we also explore the importance of rotational freedom in determining the oscillator strength, exchange energy, and spin-orbit coupling matrix elements which mediate luminescence in the absence of a rigid host. We demonstrate that suppressing dynamic motion is a powerful tool to modulate the photophysical properties of these emitters, and can lead to improved Φ particularly for low E_g emitters.

Contents

Chapter 1

Introduction

1.1 Organic semiconductors

The discovery by Heeger, MacDiarmid, and Shirakawa of high electrical conductivity in doped polyacetylene in 1977 galvanised a new way of thinking about organic materials.[1] The first explicit observation of electrical conductivity in organic molecules was reported by Eley in 1948,[2] but it was not for another thirty years that room-temperature conductivities comparable to single crystals of the organic metal TTF-TCNQ; combining tetrathiofulvalene and 7,7,8,8,-tetracyanoquinodimethane respectively, were measured. This opened up enormous possibilities for applications which no longer relied on semiconducting inorganic crystals of Si, Ge, or GaAs. Instead, a high degree of chemical tuneability in organic materials is afforded by the hybridisation of the carbon atom. This leads to different forms of covalent bonding and delocalisation of electron density in polyenes, which confers its high mobility.

This tuneability is key to the subsequent success of organic semiconductors. This has two facets, and improvements to organic semiconductor charge transport properties have been in tandem with improvements to suitability in electronic applications. Underpinning both is an understanding of the charge transport mechanism, particularly in disordered systems, as investigations move towards increasingly complex chemical structures.[3] The charge carrier mobility (μ) is the main figure of merit when comparing the charge transport properties between materials, and organic field-effect transistors (OFETs) - themselves a fundamental building-block of organic electronic circuits - are a robust way to probe the charge carrier properties. In the past thirty years, low $\mu \sim 10^{-4}$ $\mathrm{cm}^2/\mathrm{Vs}$ typical in OFETs[4, 5] have been improved to above 1 $\mathrm{cm}^2/\mathrm{Vs}$ simultaneously

for electrons and holes in ambipolar polymer devices,[6] and > 10 cm^2/Vs for p-type transport in small molecule devices.[7] State-of-the-art OFET devices using organic semiconductors now outcompete those using amorphous-Si. On the other hand, the tuneability of the organic chemical structure, particularly the length and stereochemistry of solubilising aliphatic sidechains,[8] and self-organising of the π-conjugated system[9] leads to solution-processible devices towards the inexpensive fabrication of large-area applications.

1.2 Organic chromophores

Thirty years after the first observations of electroluminescence in organic materials,[10, 11] the first high efficiency solution-processed organic light-emitting diodes (OLEDs) based on conjugated polymers were reported.[12, 13] In luminescent devices, the main figure of merit is the device quantum efficiency (QE), or the light emitted as a fraction of charges injected. The spin statistics of excitons formed of injected charges leads to a three-fold excess of triplets (with vanishing luminescence), and limits first-generation OLED device QEs to 25 %, since the 75 % yield of triplet excitons usually cannot recombine radiatively. The device efficiency is directly related to the luminescence QE (Φ), and early devices with the best performance used blue emitters with a high value of Φ.[14, 15] To overcome this efficiency limitation, second-generation OLEDs used organometallic complexes (typically employing heavy metals) to increase singlet-triplet mixing via effective spin-orbit coupling (SOC)[16] to increase the radative decay of the triplet state (phosphorescence) towards unitary QEs.[17] Despite the high phosphorescence QEs in Ir(ppy)$_3$ (Tris(2-phenylpyridine) iridium(III)),[18] or PtOEP, (2,3,7,8,12,13,17,18-octaethyl-porphine platinum(II))[19] the expense and toxicity of heavy metals, together with low device stability for deep-blue emitters,[20] are problematic for commercial applications. Recently, a new class of materials showing thermally activated delayed fluorescence (TADF) has shown very promising device QEs up to 19 %,[21] leading to the third-generation of OLED devices. Characterised by a small singlet-triplet energy gap and strong SOC to mediate triplet-to-singlet upconversion (or reverse intersystem crossing), triplet excitons can be harvested through the luminescent singlet pathway,[22] even in the absence of heavy metals, toward the goal of low-cost manufacturing of all-organic large-area display applications.[23]

1.3 Organic applications

Some organic applications have already come to market. Organic light-emitting diode (OLED) displays are now commercialised on a large scale.[24] These offer a number of advantages over the best liquid-crystal displays (LCDs). These can include very fast response times, true black colours leading to superior contrast, and thin designs, and improved viewing angles.[25] OLED displays are usually realised with an active matrix (AM) backplane. The AM in commercial displays most often employs metal-oxide semiconductor thin-film transistors whose $\mu \sim 20 - 50$ cm^2/Vs, and current-stress stability is presently unparalleled in organic materials.[26] However, organic materials with high μ in spite of a low degree of structural order present an opportunity to create high-performance backplane circuits on flexible substrates. It is uncommon for materials to have both desirable properties, particularly for inorganic materials, but recently the donor-*alt*-acceptor copolymer class has shown $\mu > 1$ cm^2/Vs in the absence of long-range crystallinity.[27] This is a key development towards realising pliable OLED displays (and organic photovoltaic (OPV) architectures), flexible displays and wearable next-generation electronics.

1.4 This work

Chapter 2 introduces the theoretical basis for this work, and is broken into three sections. Starting from the Hamiltonian for an atomic system, we begin with the principles of atomic orbitals and discuss how hybridisation and the formation of molecular orbitals can lead to bonding. We extend this to large molecular systems, and the formation of bands. Next, we discuss the formation, transfer, and decay of neutral excitations in organic semiconductors, and how electron-phonon coupling and thermal activation can be important factors in these processes. Finally, we discuss charge transport. Specifically for OFETs, we introduce various transport models which are helpful towards understanding the transport of polarons in disordered organic semiconductors.

In **Chapter 3**, we summarise our experimental methods. Here, we include important information concerning the materials, fabrication, measurement, and extraction of various parameters in this thesis. In the remaining chapters, we discuss our experimental results, and supplementary information pertaining to these experiments is included,

where referred to, in the relevant appendix.

Chapter 4 presents a broad study of charge transport in numerous polymer semiconductors belonging to the same donor-acceptor family. In this chapter, first we show a detailed device optimisation of a representative polymer semiconductor, and then we extend this study to other polymers in the family. We extract important charge transport parameters and compare them to various optical and structural parameters. In this way, we evaluate the relative importance of these parameters in determining μ, and propose design rules to increase μ.

In **Chapter 5** (and Appendix I), we focus this study to discuss in detail the role of chain coupling in determining the luminescent properties of these materials. Using a combination of transient photoluminescence and absorption measurements, we unpick the relationship between the low Φ in films and the degree of inter-chain interaction, and discuss possible causes for ultrafast quenching in these systems.

In **Chapter 6** (and Appendix II), we extend this study to other materials in the same class. Using optical spectroscopy as a probe, we analyse the photophysics of sub-energy gap signatures arising from luminescent inter-chain states, and use this as a tool to demonstrate that increased aggregation of the right kind can lead to high μ and Φ simultaneously.

In **Chapter 7** (and Appendix III), we turn our attention to TADF materials, and determine how the rates of radiative and non-radiative decay, and also the intersystem crossing, can depend on the rotational freedom of the organic chromophore. In the context of Φ and SOC, we discuss the importance of low-frequency vibrations in mediating efficient luminescence.

Chapter 2

Theory

2.1 Introduction

In this chapter, we present a selection of theoretical considerations which are fundamental to understanding the experimental results in this thesis. As such, it is not intended to represent a comprehensive review of the current physical understanding of the concepts presented herein, but rather to provide an overview of the broad concepts on which our experimental work is founded. Accordingly, we break this chapter into three sections. In the first, we begin with a description of electronic structure in atoms, simple organic molecules, and extended molecules with more complicated organic structures. Secondly, we consider the interaction of light and matter, particularly that which leads to the formation of neutral excitations in organic semiconductors. We discuss energy transfer to other states, but focus on processes leading to decay via luminescence or radiationless internal conversion. Finally, we discuss charge transport in organic semiconductors, particularly disordered ones, and how various mechanisms leading to the localisation of charges call for different models to explain the behaviour.

2.2 Electronic structure

The simplest Hamiltonian $\hat{H}$ for a particle of mass m in a potential energy surface V mapped by vector from an arbitrary point $\vec{r}$ has two parts: a kinetic energy term $\hat{T}$, and a potential energy term $\hat{V}$. The (time-independent) Schrödinger wave equation

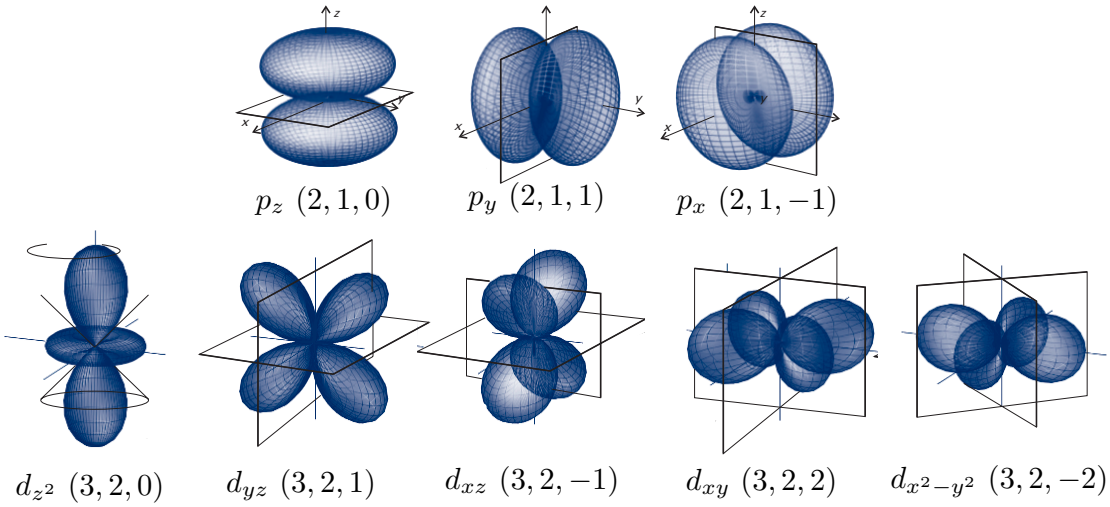

Figure 2.1 Cartesian representation of p (top) and d (bottom) atomic orbitals with (n, l, m) quantum numbers in parentheses. Figure adapted from reference [28].

leads to the solution for energy eigenvalues $E(n)$ and eigenstates $|n\rangle$,

$$\hat{H}\,|n\rangle = \left(\hat{T} + \hat{V}\right)|n\rangle = \left(-\frac{\hbar^2}{2m}\vec{\nabla}^2 + V(\vec{r})\right)|n\rangle = E(n)\,|n\rangle \tag{2.1}$$

where $\hbar = h/2\pi$ (and h is the Planck constant), and $\{|n\rangle\}$ forms a complete and orthonormal basis for the system, such that any eigenfunction of the system $|\psi\rangle$ can be expressed as $|\psi\rangle = \sum_n c_n\,|n\rangle$ with $\sum_n |c_n|^2 = 1$.

2.2.1 Atomic orbitals

For electrons in a static atomic system, the Hamiltonian is given by the sum of the electron momentum, electron-nucleus potential energy, and the electron-electron potential energy;

$$\hat{H} = -\frac{\hbar^2}{2m_e}\sum_i \vec{\nabla}_i^2 - \frac{e^2}{4\pi\varepsilon_0}\cdot\left(Z\sum_i \frac{1}{|\vec{r}_i|} - \sum_{i<j}\frac{1}{|\vec{r}_i - \vec{r}_j|}\right) \tag{2.2}$$

where Z is the atomic number, m_e is the mass of the electron, e is the elementary charge, ε_0 is the permittivity of free space, and $|\vec{r}_i|$ denotes the distance of electron i from the nucleus. In the case of a single electron, the eigenstates $|n\rangle = \phi_n(\vec{r}_n)$ can be found analytically by a separation of variables,[1] $\phi_n(\vec{r}_n) = \phi(r,\theta,\varphi) = R_{n,l}(r)Y_{l,m}(\theta,\varphi)$, where

[1] Here, using spherical angular coordinates is convenient due to the symmetry of the problem.

(n, l, m) are quantum numbers (ignoring electron spin here). Mathematical solution of these non-linear differential equations is shown elsewhere,[28] but the solutions for $n = 1, 2, 3$ are shown here. This leads to radial solutions

$$R_{1,0} \propto e^{-\rho} \tag{2.3}$$

$$R_{2,0} \propto (1-\rho)e^{-\rho} \qquad R_{2,1} \propto \rho e^{-\rho} \tag{2.4}$$

$$R_{3,0} \propto \left(1 - 2\rho - \frac{2}{3}\rho^2\right) e^{-\rho} \qquad R_{3,1} \propto \rho\left(1 - \frac{1}{2}\rho\right) e^{-\rho} \qquad R_{3,2} \propto \rho^2 e^{-\rho} \tag{2.5}$$

where $\rho = Zr/na_0$, and a_0 is the Bohr radius,[2] and the angular solutions

$$Y_{0,0} = \text{const.} \tag{2.6}$$

$$Y_{1,0} \propto \cos\theta \qquad Y_{1,\pm1} \propto \mp \sin\theta \; e^{\pm i\varphi} \tag{2.7}$$

$$Y_{2,0} \propto 3\cos^2\theta - 1 \qquad Y_{2,\pm1} \propto \mp \sin\theta\cos\theta \; e^{\pm i\varphi} \qquad Y_{2,\pm2} \propto \sin^2\theta \; e^{\pm 2i\varphi}. \tag{2.8}$$

This quantisation is fundamental to the physics of atomic systems, and can be extended to systems with multiple electrons. Since the probability density function of an electron in state $n \sim |\phi_n(r, \theta, \varphi)|^2$, these solutions have distinct probability density geometries which depend on (n, l, m) quantum numbers, and so they are called orbitals (by comparison to a classical picture). These are commonly categorised by their angular (orbital) quantum number l, and for each principal quantum number n (where n is sufficiently large), there is a single 's' orbital ($l = 0$) which has a spherical symmetry, three 'p' orbitals ($l = 1$) each polarised in a singular orthogonal cartesian direction with a node at $r = 0$, five 'd' orbitals ($l = 2$), seven 'f' orbitals ($l = 3$), and so on. The shape of these orbitals is sketched in Figure 2.1 for $n = 2$ and 3.

2.2.2 Hybridisation

The bonding of atoms is more complicated, since in the presence of other atoms, orbital wavefunctions of individual atoms can mix, and new geometric wavefunction configurations are realised in order to minimise the free energy. These are called hybrid atomic orbitals, and they can be represented in terms of a linear combination of the atomic orbitals. As an example, in its neutral (atomic) form, carbon ($Z = 6$) has an electronic structure $(1s)^2(2s)^2\,(2p)^1_{\hat{z}}\,(2p)^1_{\hat{x}}$, where $\hat{z}$ and $\hat{x}$ are orthogonal. Hybridisation of the s and p atomic orbitals leads to the formation of sp, sp^2, and sp^3 atomic orbitals.

[2] $a_0 = \frac{\hbar^2}{m_e}\frac{4\pi\varepsilon_0}{e^2}$.

Hybridised orbitals adopt a new geometry to minimise their spatial overlap, and molecules with bonding via the sp^3 orbitals have a tetragonal shape (approximately), whereas the sp^2 orbitals span a plane. Therefore, in the case that carbon has sp^2 hybridisation, the configuration $(1s)^2(2sp^2_{\hat{a}})^1(2sp^2_{\hat{b}})^1(2sp^2_{\hat{c}})^1\,(2p)^1_{\hat{z}}$ is adopted.[3] This is shown in Figure 2.2 (middle) and discussed further below.

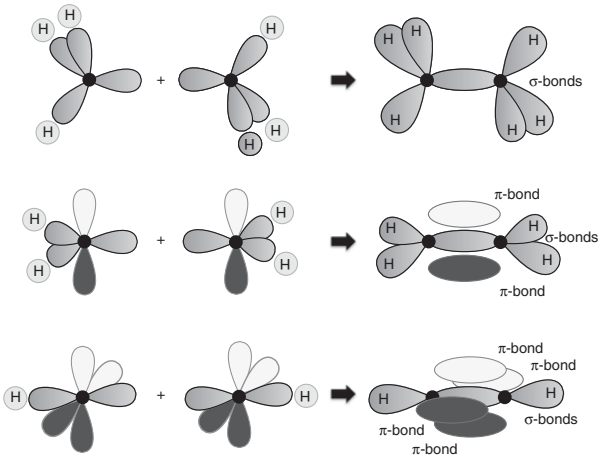

Figure 2.2 Carbon hybridisation and coupling in ethane (top), ethene (middle), and ethyne (bottom). Figure adapted from reference [29].

2.2.3 Molecular orbitals and bonding

When atoms come close, they can mix their atomic orbitals in order to share electrons. This can also involve altering the atomic electronic configuration, which proceeds when a lower energy configuration exists. The mixing of these atomic orbitals leads to the formation of molecular orbitals (MOs). MOs are the eigenstates of the multiple-atom system, but these can also usually be expressed to a good approximation as a linear combination of the atomic orbitals. In the case of diatomic helium (He_2), the two He atoms (each with $(1s)^2$ configuration) can form two MOs: σ_{1s} and σ^*_{1s}. The energy, $E(\sigma_{1s}) < (1s)$ is reduced by an amount, but $E(\sigma^*_{1s}) > E(1s)$ is raised by the same amount to conserve energy. Conservation of charge requires that electrons doubly occupy both MOs. Since this does not lead to a decrease in internal electron energy of two helium atoms, the weak bonding in He_2 is not covalent. On the other hand, diatomic hydrogen (H_2), (with each atom having $(1s)^1$ configuration), lowers its energy by doubly occupying the σ_{1s} MO, leading to stronger bonding.

[3]Here, $\hat{c}$ is contained in the span of $\hat{a}$ and $\hat{b}$, and $\hat{z}$ is orthogonal to this plane.

The physics is interesting when considering more complicated molecules. In particular, the versatility of carbon is exemplified by its different bonding motifs in the presence of other carbon atoms, and this is facilitated by hybridisation. In Figure 2.2, we show the motif for ethane (C_2H_6; top), ethene (C_2H_4; middle), and ethyne (C_2H_2; bottom). In the case of ethane (top), both carbon atoms (black dots) have sp^3 hybridisation and sp^3-orbitals are polarised to adopt a near-tetragonal structure which minimises the electrostatic interaction. Overlap of these orbitals and the $1s$ hydrogen atomic orbital leads to C-H σ-bonding throughout (shown left). Additionally, spatial overlap of the remaining two sp^3-orbitals (one on each carbon) leads to the covalent C-C σ-bonding (right).

In the case of ethene (middle), both carbon atoms have sp^2 hybridisation. Similar to ethane, analogous C-H and C-C coupling (instead involving sp^2 hybrid atomic orbitals) leads to five σ-bonds which are all contained in a plane. Additionally, each carbon also contributes an unpaired electron in p-orbitals polarised out of the plane of the molecule. These electrons also form bonding pairs, but decreased wavefunction mixing leads to weaker (π-) bonding. This is the difference between σ- and π-bonding. Finally, in ethyne (bottom), both carbon atoms have sp hybridisation, which has the electronic structure $(1s)^2\,(2sp_{\hat{z}})^1\,(2sp_{-\hat{z}})^1\,(2p)^1_{\hat{x}}\,(2p)^1_{\hat{y}}$, leading to a linear molecule with one C-C and two C-H σ-bonds, and two perpendicularly polarised π-bonds.

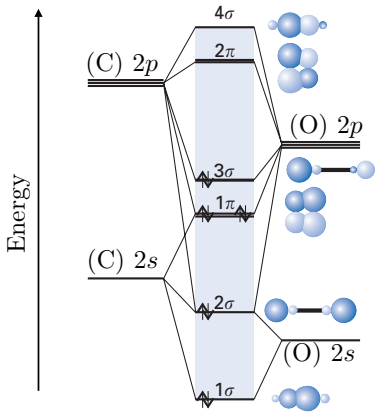

Figure 2.3 Energy and geometry of molecular orbitals in carbon monoxide. Figure adapted from reference [28].

The weaker wavefunction interaction in π-bonding leads to a smaller energy splitting between the (low energy) bonding character, and the (high energy) anti-bonding

character than for σ-bonds. It is for this reason that many organic semiconductors π MO is the highest occupied (HO) MO, and the π^* MO is the lowest unoccupied MO, as is the case in ethene. However, in molecules where the atoms are different, such as carbon monoxide (CO), a more complicated energetic ordering emerges. This is shown in Figure 2.3, where the HOMO is the third σ-MO and the LUMO second π-MO, each having an anti-bonding character (shown right). In general, electronic transitions exhibit mixed σ-/π-character in complex molecular systems.

2.2.4 Larger molecular systems

It is often the case that in organic materials with sp^2 carbon hybridisation, important electronic and optical properties arise from the π MOs. Therefore, a general method for understanding the energy and wavefunctions of MOs is desirable. However, explicit treatment of both electronic and nuclear motion (including electron-phonon coupling) leads to a highly complicated Hamiltonian without analytical solutions to the Schrödinger equation, and such calculations that identify eigenstates typically scale poorly with number of atoms and electrons. Instead, it is often sufficient to consider a static case at the equilibrium nuclear geometry, assuming a Hamiltonian which varies slowly in time. Its (eigen)wavefunctions, are then said to be adiabatic, and separable with respect to electronic and nuclear parts. This is the Born-Oppenheimer approximation. This leads to the Hamiltonian in Equation 2.2. By expressing this in terms of non-interacting and interacting electron terms, we write

$$\hat{H} = \sum_n \epsilon(n) \left|n\right\rangle \left\langle n\right| + \sum_{m \neq n} t(m,n) \left(\left|m\right\rangle \left\langle n\right| + \left|n\right\rangle \left\langle m\right|\right) + \sum_n u(n) \left|n\right\rangle \left\langle n\right| + \sum_{m<n} v(m,n) \left(\left|mn\right\rangle \left\langle mn\right|\right) \quad (2.9)$$

where $\epsilon(n)$ is the energy of occupying state n, $t(m,n)$ is the energy of electron transfer from m to n, $u(n)$ is the electron-electron interaction energy between electrons in a doubly occupied state n, and $v(m,n)$ is the electron-electron interaction energy between electrons in states m and n. It is this Hamiltonian for which density functional theory (DFT) seeks solutions to the Schrödinger equation.

However, by making several (severe) simplifications to this Hamiltonian, we can find analytical expressions for the wavefunctions of a one-dimensional chain of 'tightly bound' electronic sites. Perhaps surprisingly, using the Hückel method, we progress a

long way towards a quantum mechanical understanding of a low disorder polymer chain. For a chain of N σ-bonded sp^2-hybridised carbon atoms, each carbon contributes a single p-electron to a π-electron system of wavefunctions $|k\rangle$ with quantum number k. In the low disorder limit, we assume that (i) each position on the chain is degenerate ($\epsilon(n) \to \epsilon$), and (ii) that the energy of transfer between nearest neighbours is constant ($t(m,n) \to t$ if $|m-n|=1$) but (iii) hopping further is not possible ($t(m,n)=0$ if $|m-n|>1$). We (iv) ignore electron-electron interactions $u(n)=v(m,n)=0$, and (v) assume that $E(\sigma^*_{2s}) \gg E(\pi^*_{2p})$ and $E(\sigma_{2s}) \ll E(\pi_{2p})$ so that only p-orbitals participate in the MOs near the Fermi level. In this case, for a linear chain, the eigenenergies are

$$E(k) = \epsilon + 2t\cos\left(\frac{k\pi}{N+1}\right) \tag{2.10}$$

where k is a positive integer less than or equal to N. In this model, t is an integral of the form $\langle\phi_i|\hat{H}'|\phi_{i+1}\rangle$, where ϕ_i and ϕ_{i+1} represent nearest neighbour states, and $\hat{H}'$ is the perturbation to the potential energy of the crystal lattice. Where $k < N/2$, this leads to 'bonding' π MOs, and $k > N/2$ leads to 'anti-bonding' MOs. Furthermore, when this model is applied to cyclic sp^2-hybridised systems, it predicts an additional stabilisation for rings with $(4n+2)$ π-electrons (where $n = 0, 1, \dots$) through aromaticity. However, in the limit that N is large, this model also predicts a continuum of states with bandwidth approaching $4t$ with the Fermi level in the middle, which should lead to the behaviour of a conductor. This is not observed in polyenes (which instead behave as semiconductors). This discrepancy can be understood within the Peierls distortion: in a 1-dimensional periodic lattice, the equally-spaced microstate is unstable, and relaxes to elongate one bond by shortening another. This leads to a structure with twice the period, and these electron-phonon coupling leads to a band gap which is observed.

2.2.5 Bands

In some materials, charge transport is best described in terms of continuums of states called bands. This is often the case in materials which have a high degree of crystallinity. Here, we present two brief descriptions of the density of states (DOS) in one-dimensional solids. In the first, the 'tight-binding approximation' imagines a solid comprised of a chain of tightly bound identical states. In the simplest case, this is the same as the Hückel method for the π MOs of a sp^2-hybridised carbon chain. In this case, in the

limit that $N \to \infty$, $E(k)$ becomes a continuous function in k. The DOS $\rho(E) = dn/dE$ where $dn/dk = 1$, is therefore

$$\rho(E - \epsilon) = -\frac{(N+1)/2t\pi}{\sqrt{1 - [(E-\epsilon)/2t]^2}} \tag{2.11}$$

and ρ diverges towards the edges of the band, $E - \epsilon \to \pm 2t$. In higher dimensional solids, $\rho(E - \epsilon)$ tends to a Gaussian centered at ϵ.

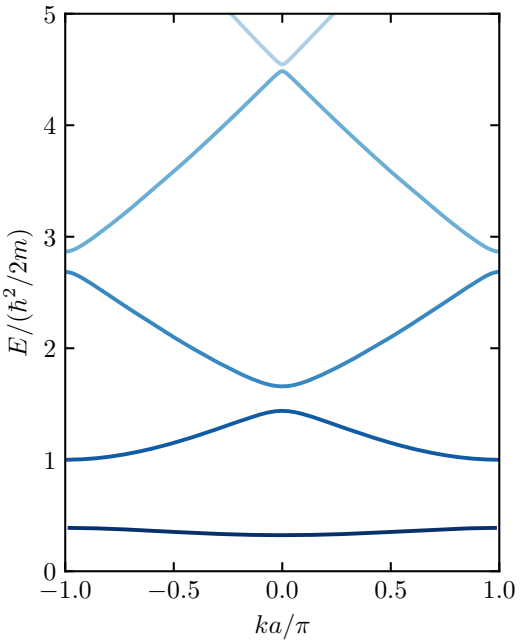

Figure 2.4 Energy dispersion diagram for the (1-dimensional) Kronig-Penney model.

A different (simple) approach is achieved by the Kronig-Penney model, which assumes periodicity of the potential energy explicitly, $\hat{V} = V(x) = V(x + (a + b))$. Here, $V(x)$ is a square wave potential with a constant potential V in domains of length b separated by a vanishing potential in domains of length a. This approach solves the Schrödinger equation for separable wavefunctions of the form $\psi_k(x) = u_k(x)e^{ikx}$, where $u_k(x)$, called Bloch functions, have the same periodicity as $V(x)$. This leads to a well-known dispersion relation, which, in the limit that the periodic potential wells become infinite ($V \to \infty$), allowed bands which are parabolic towards $k \to 0$ become separated by gaps. The energy dispersion of the numerical solution is shown in Figure 2.4, where allowed bands (blue) are separated by energy gaps.

2.2.6 Indistinguishable particles and exchange

While building up a picture of quantisation in solid systems, we have left out the quantum mechanical details of electron spin. However, in order to transition to a discussion about neutral excitations in molecular systems, we briefly summarise the notion of indistinguishable particles, the Pauli exclusion principle, and the exchange energy.

If a system has a set of eigenstates $|n\rangle$ which can also be written $\phi_n(\vec{r}_n)$, we naively suppose that the eigenstates of two such systems can be written $|m\rangle\,|n\rangle = |mn\rangle$ where the first particle occupies the state m, and the second n. If these particles are indistinguishable, observation of the first particle in state m and the second in n is indistinguishable from observation of the first particle in state n and the second in m. It follows that these two basis states must differ only by a phase, and the wavefunction of the system can be written $|mn\rangle \pm |nm\rangle$. In other words, if the exchange operator $\hat{P}$ permutes particles, the two-particle states must also be eigenvalues of this operator. Here, $\hat{P}$ has eigenvalues ± 1 for symmetric and antisymmetric wavefunctions respectively.

Extending this to N particles,

$$|n_1 n_2 \dots n_i\rangle = \sqrt{\frac{\prod_n m_n!}{N!}} \sum_p \left| n_{p(1)} n_{p(2)} \dots n_{p(N)} \right\rangle \tag{2.12}$$

in the symmetric case, where m_n is the number of times state n appears in the collection N, so $\prod_n m_n = N$, and $p(i)$ is the ith element of particle permutation p, and

$$|n_1 n_2 \dots n_i\rangle = \sqrt{\frac{1}{N!}} \sum_p \mathrm{sgn}(p) \left| n_{p(1)} n_{p(2)} \dots n_{p(N)} \right\rangle \tag{2.13}$$

where $\mathrm{sgn}(p) = \pm 1$ for even and odd numbers of transpositions respectively. Bosons, such as photons and excitons, have symmetric wavefunctions. Fermions, such as electrons, have antisymmetric wavefunctions. For fermions, only singular occupancy of each quantum state ($m_n = 1$) is allowed, and this is Pauli's exclusion principle. More generally for electrons, Pauli's exclusion principle states that no two electrons can have an identical set of quantum numbers describing its state.

We revisit the Hamiltonian in Equation 2.2. It is convenient to consider the electron-electron Coulomb interaction as a perturbation $\hat{H}'$ to the Hamiltonian in the absence of electron-electron interaction $\hat{H}_0$, for which there are analytical eigensolutions $E_0(n)$ and $|n_0\rangle$. Expanding the perturbed eigenstate in terms of $|n_0\rangle$, it can be shown that the energy $E(n) = E_0(n) + E'(n)$, where

$$E'(n) = \langle n_0|\hat{H}'|n_0\rangle + \sum_{n\neq m} \frac{\left|\langle m_0|\hat{H}'|n_0\rangle\right|^2}{E_0(n) - E_0(m)} + \dots. \tag{2.14}$$

For a two-electron system (such as the helium atom), assuming electron 1 in $|n\rangle$ and electron 2 in $|m\rangle$, the first-order perturbation matrix element term is the Coulomb integral, and can also be written

$$J_{mn} = \frac{e^2}{4\pi\varepsilon_0} \langle mn| \left(\frac{1}{|\vec{r}_m - \vec{r}_n|}\right) |mn\rangle \tag{2.15}$$

or in terms of the wavefunction density overlap,

$$J_{mn} = \frac{e^2}{4\pi\varepsilon_0} \int |\phi_m(\vec{r}_m)|^2 \left(\frac{1}{|\vec{r}_m - \vec{r}_n|}\right) |\phi_n(\vec{r}_n)|^2 \, d^3\vec{r}_m d^3\vec{r}_n \tag{2.16}$$

Even though the Hamiltonian has no explicit spin-dependency, substitution of the 'indistinguishable particle criterion', $|mn\rangle \to |mn\rangle \pm |nm\rangle$ leads to a difference in the expectation energy of the perturbation $\hat{H}'$ depending on which (spatial) combination is substituted. For $|\Phi^{\pm}\rangle = |mn\rangle \pm |nm\rangle$,

$$\left\langle \Phi^{\pm}\middle|\hat{H}'\middle|\Phi^{\pm}\right\rangle = J_{mn} \pm K_{mn} \tag{2.17}$$

$$= J_{mn} \pm \frac{e^2}{4\pi\varepsilon_0} \langle mn| \left(\frac{1}{|\vec{r}_m - \vec{r}_n|}\right) |nm\rangle \tag{2.18}$$

where the latter term, K_{mn}, is the exchange energy. This can also be written explicitly in terms of wavefunction overlap,

$$K_{mn} = \frac{e^2}{4\pi\varepsilon_0} \int \phi_m(\vec{r}_m)^* \phi_n(\vec{r}_n)^* \left(\frac{1}{|\vec{r}_m - \vec{r}_n|}\right) \phi_m(\vec{r}_n)\phi_n(\vec{r}_m) d^3\vec{r}_m d^3\vec{r}_n. \tag{2.19}$$

Pairs of indistinguishable electrons can couple in four distinct ways; three of these ways lead to a symmetric spatial wavefunction with $S = 1$ (triplets), and one leads to an

antisymmetric spatial wavefunction with $S = 0$ (singlet). In the case of a two-electron atomic system (neglecting nuclear repulsion), the energy is given by

$$E_n = E_n^{(0)} + J_{12} - (2S - 1)K_{12} \tag{2.20}$$

to first order. This leads to a lower energy of the triplet compared to the singlet configuration. More generally, the highest-spin configuration has the lowest energy, and this is Hund's rule.

2.3 Neutral excitations

To a good approximation, the interaction of light with semiconductors can be thought of as a perturbation due to an oscillating electric field $\vec{E}(t)$ on a collection of electric dipoles.[30] The perturbation Hamiltonian $\hat{H}'$ can be written

$$\hat{H}' = -\hat{p}_e \cdot \vec{E}(t) \tag{2.21}$$

in terms of the operator for the electronic dipole moment $\hat{p}_e$ of the system. If an incident photon is in energy resonance with transitions in the system, then this interaction may lead to the (i) absorption of the incident photon energy forming a neutral excitation or (ii) the stimulated emission of a photon with the same energy. Otherwise, it can also be scattered by the electron density of the system.

2.3.1 Fermi's golden rule, absorption, and emission

For a transition from an initial state $|i\rangle$ to a final state $|f\rangle$, the rate k_{if} is given by Fermi's golden rule:

$$k_{if} = \frac{2\pi}{\hbar} \left| \langle f|\hat{H}'|i\rangle \right|^2 \delta\left[E(f) - E(i)\right] \rho_f \tag{2.22}$$

where $E(n)$ and ρ_n are the energy and DOS of n respectively, and the δ-function ensures conservation of energy. To describe the absorption of a photon in a molecular semiconductor, if $|f\rangle$ is an excited electronic state of the system, the incident photon energy may be absorbed by an electron leading to its promotion to a higher energy MO. In the absence of spin-orbit coupling (SOC) or hyperfine interaction terms in $\hat{H}'$, spin angular momentum must be conserved, and the selection rules require that there is no change to the spin angular momentum of the neutral excitation. The excitation itself leaves a va-

cancy in state i which has a positive charge (called a hole) with a different wavefunction.

Depending on the photon energy, these charged particles can either correlate in space and form 'excitons', or dissociate to become 'free' charges. Central to this branching is the exciton binding energy (E_b), or the potential energy of the Coulomb interaction, which can be decreased to ~ 10 meV in highly polarisable media ($\varepsilon_r > 10$) where local electric dipoles screen the exciton dipole electric field.[31] This leads to Mott-Wannier excitons which have a large exciton radius.[32] In organic semiconductors, Frenkel excitons are more common. Here, the decreased screening from lower dielectric constants ($\varepsilon_r < 4$) in these materials leads to much a higher $E_b \sim 1$ eV, and a more localised exciton wavefunction.[33]

Absorption is closely related to stimulated emission, and treatment via Fermi's golden rule leads to the relation $B_{12}/B_{21} = \rho_2/\rho_1$ where B_{ij} is the rate of stimulated transition from state $|i\rangle$ to $|j\rangle$. This is also predicted by Einstein's famous treatment of a two state system where occupation is given by Boltzmann statistics.[34] Spontaneous emission is different, and its rate A_{21} is given by

$$A_{21} = \frac{2\omega^3 n^3}{3\hbar\varepsilon_0 \pi c^3} |\mu_{12}|^2 \tag{2.23}$$

where ω is the angular frequency of the photon, n is the refractive index, c is the speed of light, and $\mu_{12} = \langle 1|\hat{H}'|2\rangle$ is the transition dipole moment.

2.3.2 Franck-Condon approximation

The Born-Oppenheimer approximation assumes that nuclear motion is slow compared to electronic transitions. If this is applied, then $\hat{H}'$ can be re-written in terms of electronic and nuclear parts

$$\hat{H}' = -\hat{p} \cdot \vec{E}(t) = -\left(\hat{p}_e(\vec{r}) + \hat{p}_N(\vec{R})\right) \cdot \vec{E}(t) \tag{2.24}$$

where e and N subscripts denote electron and nuclear parts respectively, and $\vec{r}$ and $\vec{R}$ are the position of the electrons and nuclei respectively. This leads to the separable solution of electronic and nuclear wavefunctions, and we can write the vibronic state $|\epsilon;\nu\rangle$

$$|\epsilon;\nu\rangle = \left|\epsilon(\vec{r};\vec{R})\right\rangle \left|\nu(\vec{R})\right\rangle \tag{2.25}$$

where $|\epsilon\rangle$ is the electronic wavefunction and $|\nu\rangle$ is the vibrational wavefunction. This is the Franck-Condon approximation. Physically, this allows us to describe a transition between two states whose equilibrium geometries differ marginally. Applying Fermi's golden rule in Equation 2.22, the perturbation matrix element μ_{12} depends on the overlap of the two vibrational states in their respective electronic states.[28] Therefore, in absorption and emission spectra, electronic transitions usually become progressions of transitions with energy differing by the energy of the vibrations to which the transition couples strongly, and with relative intensity related to the displacement of the excited state equilibrium position with respect to that of the ground-state.

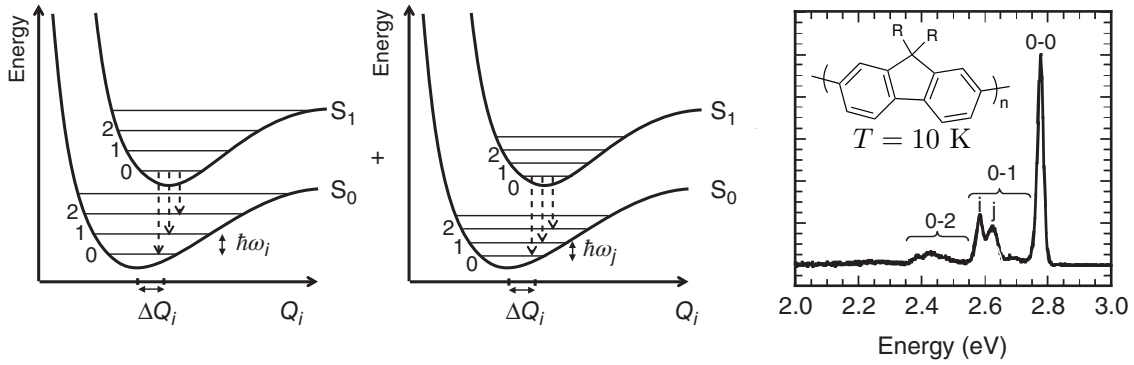

Figure 2.5 The Franck-Condon progression in the PFO emission spectrum. Figure adapted from reference [29].

This is exemplified in Figure 2.5 (right) in the low-temperature emission spectrum of poly(9,9-di-alkylfluorenyl-2,7-diyl) (PFO, sidechains (R) unspecified; structure inset). By uncoupling vibrational and electronic wavefunctions, we see that luminescence is dominated by excitons in the vibrational ground-state ($\nu = 0$) of first electronic excited-state (S_1) decaying to vibrational excited-states ($\nu = m > 0$) of the electronic ground-state (S_0) manifold; $S_1(\nu = 0) \rightarrow S_0(\nu = m)$, heredunder $|\epsilon > 0; \nu = 0\rangle \rightarrow |\epsilon = 0; \nu = m\rangle$ (or $0 - m$ for brevity). In a complex molecular system like a polymer, there are many vibrational degrees of freedom, and a projection along the coordinates ith normal mode Q_i leads to vibrational energy levels as lines on the potential energy surface (shown left). Here, decay is represented by vertical dashed arrows to the different vibrational quanta in the ground-state manifold (separated by $\hbar\omega_i$, to a good

approximation).[4] However, excitons can couple strongly to more than one phonon, represented here by the different vibration (j projected along Q_i; centre). Since $\omega_i \neq \omega_j$, we see a superposition of the two vibronic progressions (right). Discussed in more detail below, the relative intensity of the two progressions is intimately related to the degree of relaxation (or displacement) between equilibrium positions of electronic ground- and excited-states.

2.3.3 Radiative decay

In Figure 2.5 (right), we see that luminescence proceeds from the vibrational ground-state. Since energy transfer from some excited vibrational state $|\epsilon;\nu>0\rangle$ to the ground vibrational state $|\epsilon;\nu=0\rangle$ is much faster than exciton decay (via luminescence), we expect only to see luminescence from the latter. This is Kasha's rule. In this case of spontaneous emission, the vibronic progression of the luminescence is given by

$$I_{0-m} \propto (\hbar\omega)^3 n^3 \frac{S^m \exp(-S)}{m!} \tag{2.26}$$

where I_{0-m} is the strength of transition of $|\epsilon>0;\nu=0\rangle \rightarrow |\epsilon=0;\nu=m\rangle$ and S is the Huang-Rhys parameter which is a measure of the strength of coupling to the vibrational mode ν.[35, 36]

2.3.3.1 Chromophore aggregation

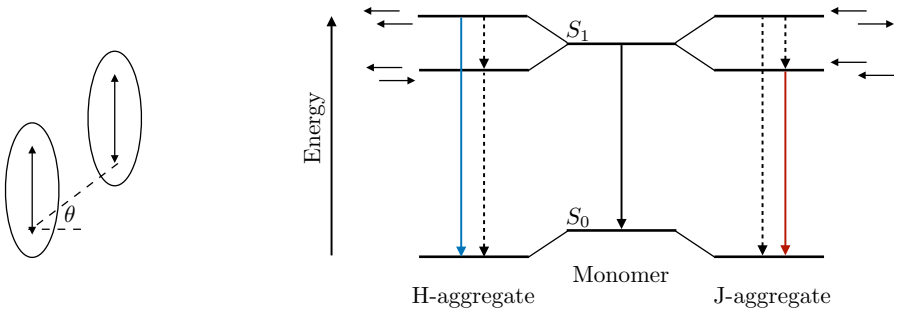

Figure 2.6 Schema of dimer aggregation lead to H- and J-type properties.

[4]The energy separation between vibrational quanta approaches $\hbar\omega$ in the limit that the potential energy surface becomes harmonic. This is a good approximation towards the minimum of the potential well.

In molecular systems, there are two additional complexities when describing the lineshape of luminescence, and both are related to the chromophore morphology. The first involves aggregation of the chromophore. In general, the transition electric dipole moment associated with absorption and luminescence has a polarisation. In organic semiconductors, this polarisation is often along an axis of the chromophore, as is shown in the cartoon of Figure 2.6 (left). However, in the presence of a second chromophore, the dipole moments couple, and the dimer has its own emergent dipole moment. In the dimer, the individual dipole moments can couple in a parallel or antiparallel fashion which lead to different transition energies conferred by the specific geometry of the dimer. In particular, the nature of this coupling depends strongly on the angle subtended between chromophore dipole moments (θ), which is is turn determined by the energetics of chromophore packing. Chromophores can adopt a packing which leads to transition dipole moments which couple in a (i) head-to-tail, or (ii) side-by-side fashion, and this the difference between J-aggregates and H-aggregates, respectively.

This difference in transition dipole moment coupling leads to different photophysical properties, as shown in Figure 2.6 (right) for the luminescence of a monomer and dimer; however this argument applies equally to absorption. The formation of the dimer leads to a splitting of the S_1 energy, in which the transition energy of the parallel configuration is redshifted (blueshifted) for J-aggregates (H-aggregates) relative to the monomer (shown as solid arrows). To conserve energy, the opposite is true for the antiparallel configuration. Importantly, because the rate of radiative transition increases with the strength of the dimer transition electric dipole moment, this leads to vanishing luminescence from the forbidden antiparallel configuration. Non-radiative relaxation from higher lying states can populate this state, but decay to the ground-state relies on non-radiative decay (shown as dashed arrows). This is the origin of weak fluorescence typical of H-aggregates.

In disordered semiconductors, the microstructure can lead to a mixed (H- and J-) aggregation.[38] In this vein, the antiparallel coupling can gain a non-zero oscillator strength. Furthermore, identifying H- or J-aggregation from spectral shifts between film and dilute solution measurements alone can be dubious, because changing phase may modulate the exciton delocalisation, which also leads to spectral shifting. Such is the case for poly(3-hexylthiophene) (P3HT), whose luminescence in dilute is strongly blueshifted compared to films, as shown in Figure 2.7. This is owing to an increased

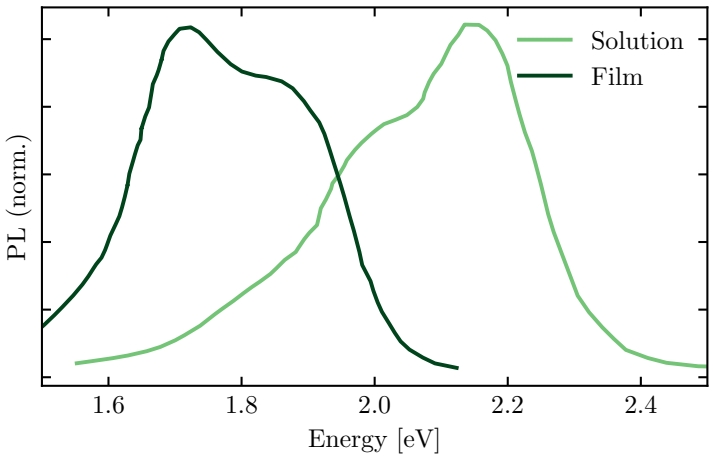

Figure 2.7 PL of P3HT (10 kDa) in toluene and film. Data from reference [37].

intra-chain planarisation in films,[39] despite their H-aggregate nature.[38]

Instead, the degree of H- or J-aggregation in disordered materials can be loosely assigned by the ratio $r = I_{0-0}/I_{0-1}$, and r is typically larger for J-aggregates than H-aggregates. As an example, donor-*alt*-acceptor polymers (which are the focus of this thesis) consist of alternating fused electron rich/poor units, leading to transition dipole moments aligned with the direction of the polymer chain. A single polymer chain can be thought of as a J-aggregate,[38] and r increases at low-temperature. H-aggregates, by contrast, have a decreasing r at low temperature and this aggregation is often mediated by a 'face-on' packing motif like in the case of P3HT.[40]

2.3.3.2 Exciton coherence

Another factor influencing r is the exciton coherence. Since the coherence length $L_{\text{coh.}}$ is directly proportional to r, it can be difficult to disentangle the effects of H-aggregation with exciton localisation. Even in the absence of polymer chain aggregation, the localisation of excitons can be mediated by static or dynamic disorder in the morphology, leading to lower energy chain microstructures which 'trap' excitons.

2.3.3.3 Broadening of electronic transitions

We also comment briefly on the mechanisms by which the emission spectrum can be broadened. There are two classes of mechanisms, those leading to (i) homogeneous

broadening which has a Lorentzian lineshape, or (ii) inhomogeneous broadening which is better fit by a Gaussian lineshape. Static disorder, or disorder which is slowly varying compared to electronic transitions, manifests via inhomogeneous broadening, and constitutes the largest part of broadening in disordered organic semiconductors.[41] This can arise from contributions due to chemical defects, a broadened DOS due to intermolecular aggregation or chain coupling, or even 'twists' perturbing the π-conjugation of the backbone. By contrast, dynamic disorder including ultrafast fluctuations in the equilibrium geometry; particularly torsion which transiently disrupts the π-system, has been shown to lead to homogeneous broadening in conjugated polymers.[41, 42] It is by the same mechanisms that the absorption lineshape can be broadened.

2.3.4 Non-radiative processes

Determining the efficiency of luminescence requires evaluation of radiative and non-radiative decay pathways. In this section, we discuss the factors which lead to (i) non-radiative vibrational decay $|\epsilon; \nu = m\rangle \rightarrow |\epsilon; \nu = 0\rangle$, (ii) decay of singlet excitons via radiationless processes $|\epsilon > 0; \nu \geq 0\rangle \rightarrow |\epsilon = 0; \nu > 0\rangle$, and (iii) energy transfer processes whereby the energy of a state is transferred to a second state which may be weakly luminescent. We turn our focus to the exciton dynamics after optical excitation, since this is the excitation method of the experiments presented herein, but we note that many of the processes are general and hold in the case of charge injection.

2.3.4.1 Vibrational cooling

This thesis is in part concerned with understanding the photophysics of disordered semiconductors. To probe the excited states of the materials presented herein, we use the optical absorption to prepare excitons in a single excited state. However, we note that even coherent light sources have a spectral bandwidth, so the preparation of the excited states likely involves a superposition of various vibrational various states. These cool quickly to the 'band-edge', or the lowest vibrational state of the excited manifold; a process which proceeds over timescales in the range of 50fs -1.3 ps.[44] In this section, we describe this vibrational cooling process.

For simplicity, here we assume that we excite into the first electronic excited state, $|\epsilon = 1; \nu = m\rangle$. What follows is an internal conversion process whereby $|\epsilon = 1; \nu = m\rangle \rightarrow |\epsilon = 1; \nu = 0\rangle$. This is shown in Figure 2.8 ($\mathrm{B}' \rightarrow \mathrm{C}$). The excess energy, namely, the dif-

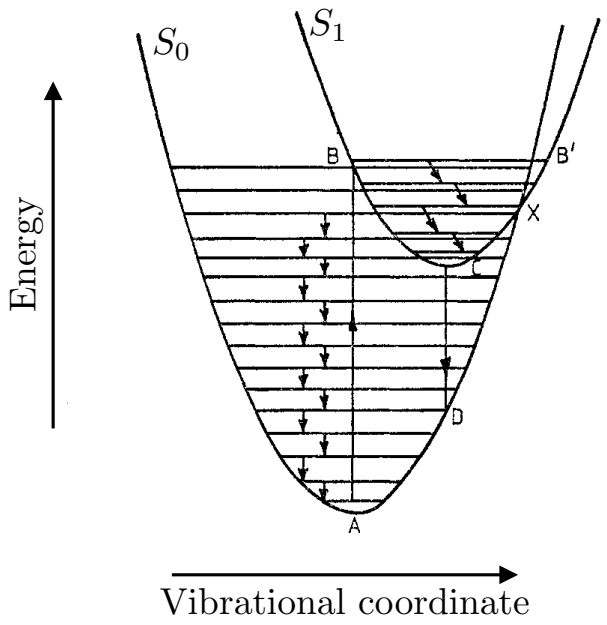

Figure 2.8 Radiative and non-radiative pathways in semiconductors: absorption (A $\rightarrow$ B′), vibrational cooling (B′ $\rightarrow$ C, D $\rightarrow$ A)), and luminescence (C $\rightarrow$ D) pathways. Figure adapted from reference [43].

ference in energy between $|\epsilon = 1; \nu = m\rangle$ and $|\epsilon = 1; \nu = 0\rangle$ is (i) partitioned in the vibrational degrees of freedom of the molecule, and (ii) transferred as heat to the surrounding environment. The high efficiency of this process can lead to internal conversion of this kind proceeding on ultrafast timescales.[44, 45] Fermi's golden rule applies here, so the rate of internal conversion depends heavily on wavefunction overlap between vibrational states, and can lead to a cascade through $(\nu = m) \rightarrow (\nu = m - 1) \rightarrow \cdots \rightarrow (\nu = 0)$ quantum states, often represented on Morse potential energy diagrams as vertical arrows between vibrational states, like in Figure 2.8 (X $\rightarrow$ A). Even at very low temperatures $T \rightarrow 0$, partitioning of energy through anharmonic interactions with other vibrational modes ν' can still occur, although the dissipation of this energy as heat to the environment is in general slower.[43]

2.3.4.2 Radiationless decay

For all semiconductors, high-lying vibrational states of the ground electronic state $|\epsilon = 0; \nu \gg 0\rangle$ are degenerate with vibrational states of the excited electronic state, $|\epsilon > 0; \nu \geq 0\rangle$. Transfer from the latter to the former can be followed by the same internal conversion as discussed in the previous section. This is shown diagrammatically

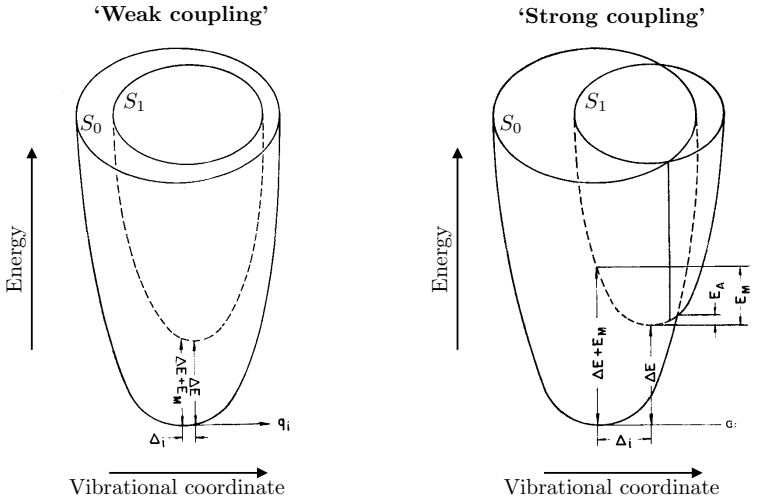

Figure 2.9 Exciton decay according to Marcus theory: weak and strong coupling. Figure adapted from reference [46].

in Figure 2.8 where the vibrational energy levels of the two electronic states are near resonance towards C. As before, Fermi's golden rule determines this rate of transfer. Here, we present two cases. In the first, the coupling between excited and ground-state electronic bands is 'weak', meaning any exciton-band intersection points are not thermally accessible. In this case, non-radiative decay is determined by the wavefunction overlap of vibrational states in excited and ground electronic states thermally accessible in the excited electronic state. Here, if the energy gap E_g separating the two electronic manifolds is large, then there is poor wavefunction overlap and a slow rate.[46] Empirical evidence shows that the rate of transfer increases exponentially with a decreasing E_g, and this is is called the energy gap law, discussed further with our experiments. Non-radiative decay of this kind can also be mediated via transfer to the environment, and decay lifetimes are often longer in solutions with only low frequency vibrations.[28] The second case has 'strong' wavefunction coupling: in harmonic potentials, the higher-order vibrational wavefunctions are concentrated near the edge of the potential well. In the case that the bands cross, Fermi's golden rule leads to strong overlap and a fast rate. However, to reach this crossing point depends on the reorganisation required to reach this state, and the observed rate may depend strongly on temperature. This situation is shown in Figure 2.8 (C,B$'$ $\rightarrow$ X $\rightarrow$ A) and also discussed further with our experiments. Englman and Jortner summarise the two extremes in Figure 2.9,[46] where ΔE and Δ_i are the energy and momentum separations between equilibrium positions, respectively, $\Delta E + E_{\mathrm{M}}$ is the reorganisation energy, E_{A} is the activation energy to

reach the band intersection, and q_i is the S_0 equilibrium position. The two mechanisms are also discussed within Marcus theory for electron transfer (in Section 2.3.4.4).

The purity of semiconductors is an important consideration in determining the rate of non-radiative decay. Recently, Di Pietro *et al.* highlighted the importance of controlled polymerisation reactions, and the removal of leftover catalyst in order to reduce the charge trapping of electrons and holes in a crystalline polymer.[47] In materials where the exciton diffusion is substantial, even a small density of impurities can lead to additional fast decay pathways. One such impurity - a ketone defect - has been shown to lead to an additional (redshifted) luminescence channel in polyfluorene which proceeds by a Shockley-Read-Hall (trap assisted) decay mechanism, and decreases the fluorescence quantum yield.[48, 49] These can be formed by photo-oxidation,[50] and are likely to be a cause of long term environmental instability shown by some similar polymer materials. Using exciton diffusion measurements, Mikhnenko *et al.* suggest that a density $\sim 10^17 - 10^18$ cm^{-3} of 'intrinsic' exciton quenching sites which is comparable between various polymer and small molecule semiconductors leads to a similar exciton diffusion length of $3 - 8$ nm.[51] By comparison with a reported universal electron trap due to water-oxygen complex,[52] this same species has been implicated in forming fast non-radiative decay channels.

In addition to first-order decay processes, two-exciton decay is also possible in the case of high excitation densities above $\sim 10^17$ cm^{-3}.[53] Singlet-singlet annihilation, in which one singlet recombines passing its energy to another, which is promoted to a higher lying singlet state, obeys bimolecular decay dynamics. Fast ($\sim 10 - 100$ fs) non-radiative deactivation often occurs thereafter, leading to a single exciton. Assuming two equilibrated singlets in the first-excited electronic state, the process $|\epsilon = 1; \nu = 0\rangle + |\epsilon = 1; \nu = 0\rangle \rightarrow |\epsilon = 0; \nu \geq 0\rangle + |\epsilon \geq 1; \nu > 0\rangle \rightarrow |\epsilon = 1; \nu = 0\rangle + |\epsilon = 0; \nu = 0\rangle$ is in general non-radiative. We note that triplet-triplet annihilation can also occur leading to an excited singlet (assuming spin is conserved), and also, higher-order processes (such as Auger recombination) can also occur at very high excitation densities above $\sim 10^{18}$.[54]

2.3.4.3 Energy transfer

As for all other processes, the rate of energy transfer is intimately related to Fermi's golden rule. Energy transfer is a radiationless process, and efficient transfer to weakly

luminescent states can ultimately increase non-radiative decay. In polymer systems, excitons may undergo energy transfer to states with poor wavefunction overlap of electron and hole, such as charge transfer (CT) states. This can be mediated by a larger exciton radius, or hole and electron partition, such as for neat polymer systems which form inter-chain CT excitons. This is discussed in more detail with the experimental results. Energy transfer from the singlet to triplet triplet manifold (or back) can occur, and this is called (reverse) intersystem crossing. The mechanism for this in organic semiconductors often requires strong SOC to conserve angular momentum. For this reason, or for systems with a large exchange energy (where $T_1 \rightarrow S_1$ up-conversion cannot occur) phosphorescent lifetimes can be orders of magnitude longer than singlet emission.[55]

In organic semiconductors, two general methods of (incoherent) energy transfer are available to Frenkel excitons; (i) Förster- and (ii) Dexter-type energy transfer. For Förster-type transfer, an exciton can be transfered 'through space' from a donor (D) to an acceptor (A) if there is good spectral agreement between the donor luminescence (L_D) and the acceptor absorption (ε_A). In this case,

$$k_\mathrm{DA} \propto \frac{\Phi_\mathrm{D}}{\tau_\mathrm{D}} \frac{1}{r^6} \int L_\mathrm{D}(\lambda)\varepsilon_\mathrm{A}(\lambda)\lambda^4 d\lambda \tag{2.27}$$

where Φ_D and τ_D are the luminescence quantum efficiency and lifetime in the absence of the acceptor, and r is the distance between point dipoles. By contrast, Dexter transfer is more short-range, since it requires wavefunction overlap 'through bond', but can lead to energy transfer of triplets on much faster timescales.[56]

2.3.4.4 Thermodynamic considerations

We finish our discussion of energy transfer mechanisms with Marcus theory for electron transfer. In its simplest form, this mechanism is semi-classical, and describes the thermodynamic properties of electron transfer. This treatment was originally devised to explain the temperature dependence of chemical oxidation and reduction reactions, shown in the following scheme, where reactants A and B form a complex X^* which undergoes some electron transfer process to form X, and ultimately products,

$$\mathrm{A} + \mathrm{B} \rightleftharpoons \mathrm{X}^* \rightleftharpoons \mathrm{X} \rightarrow \text{products} \tag{2.28}$$

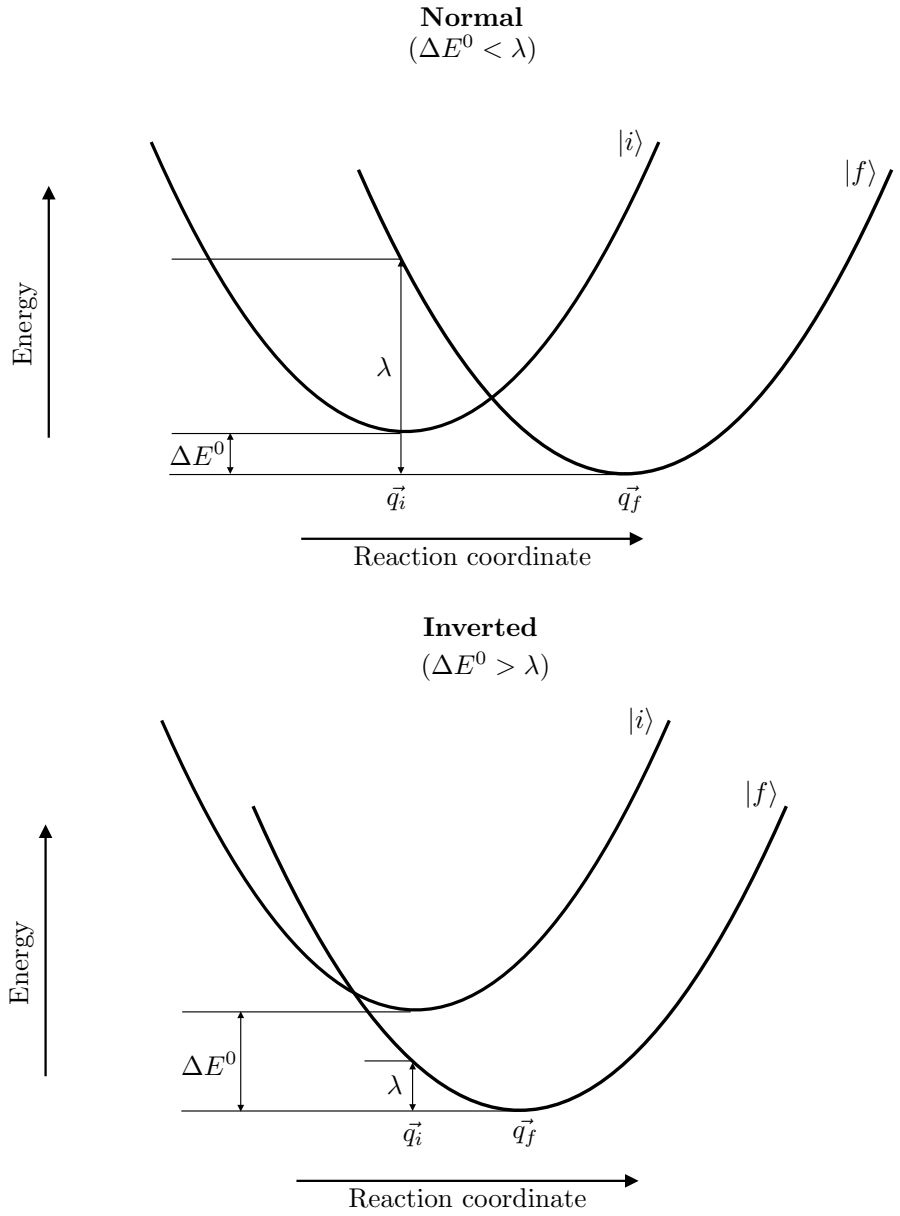

Figure 2.10 Electron transfer according to Marcus theory.

but focuses on the thermodynamics of the general case of electron transfer.[57]

$$X_1^* + X_2 \rightleftharpoons X_1 + X_2^* \tag{2.29}$$

It assumes that an initial electronic state $|i\rangle$ and a final state $|f\rangle$ each has a potential energy surface with equilibrium geometries $\vec{q_i}$ and $\vec{q_f}$ respectively, as shown diagrammatically in Figure 2.10. The energy E of the $|i\rangle$ at equilibrium $\vec{q_i}$ is writ-

ten $E\left(|i(\vec{q}_i)\rangle\right)$. The enthalpy of transfer from the intital to final state is therefore $\Delta E^0 = E\left(|f(\vec{q}_f)\rangle\right) - E\left(|i(\vec{q}_i)\rangle\right)$. The 'reorganisation energy' is defined as the difference in energy between $\vec{q}_i$ and $\vec{q}_f$ in the final electronic configuration, $\lambda = E\left(|f(\vec{q}_i)\rangle\right) - E\left(|f(\vec{q}_f)\rangle\right)$, and in the limit that the potential energy surfaces are harmonic (with the same curvature), the 'activation energy' energy where the bands intersect can be written $\Delta E^\dagger = (\Delta E^0 - \lambda)^2/4\lambda$. Combining this thermodynamic picture (using Maxwell-Boltzmann statistics) with a simplified quantum mechanical picture (Fermi's golden rule), we can write

$$k_{if} \propto \frac{|\mu_{if}|^2}{\sqrt{\lambda k_B T}} \exp\left[-\frac{(\Delta E^0 - \lambda)^2}{4\lambda k_B T}\right] \tag{2.30}$$

and the rate is maximised where $\Delta E^\dagger \to 0$. There are two thermally activated regimes which scale differently with λ: (i) $\Delta E^0 < \lambda$, called the Marcus (or 'normal') regime, and (ii) $\Delta E^0 > \lambda$, called the Marcus inverted regime, where the reorganisation energy is small. These two regimes are shown in Figure 2.10. Since energy transfer of neutral excitations involves charge transfer, we can use it to describe exciton dynamics;[58] particularly for charge transfer excitons which may have a significant reorganisation energy.[59] This is also discussed in Section 2.3.4.4.[5] Equally, this framework applies to charge transport processes,[60] which we discuss in the following section.

2.4 Charge transport

Ohm's law states that the current density observed ($\vec{J}$) between two points is proportional to the electric field applied (-$\vec{\nabla}V$). The constant of proportionality, called the conductivity (σ), can be written

$$\sigma = en\mu \tag{2.31}$$

where e is the elementary charge of the electron, n is number density of charges, and μ is the mobility. There is a one-to-one relation between σ, voltage applied (V) and current observed (I), so this equation connects observable quantities with μ. It is the basis of our electronic characterisation techniques.

In this work, we use field-effect transistors (FETs) to electrically characterise our materials, and measure various charge transport properties including μ values. FETs are convenient since optimised fabrication leads to good reproducibility, and it is possible to

[5] In Figure 2.9, the authors write ΔE^0 as ΔE, and λ as $\Delta E + E_{\mathrm{M}}$.

measure the conductivity with a variable (and high) charge carrier accumulation. The architecture and device physics of FETs are summarised in the following section, but we briefly comment on other methods for measuring μ. In addition to FET architectures, measurement of space-charge limited current ($I_{\mathrm{SCLC}} \propto \mu V^2$) is possible in diodes, and semiconductor alignment (or comparison of vertical/lateral device architectures) can lead to directional sensitivity of the μ in anisotropic semiconductors. Time-of-flight measurements are based on the principle of charge-carrier drift, and time-resolved conductivity measurements using a time-varying electric field can lead to determination of drift velocities and μ, although this method usually requires low 'deep trap' densities as well as high carrier densities. Another time-resolved technique uses microwaves to interact with 'free charges', which are either injected or photogenerated[61,62] to create an oscillating conductivity of magnitude proportional to μ. Finally, in materials with high mobilities > 5 cm^2/Vs, the Hall effect can be measured.[63] Mobile carriers in current density $\vec{J}$ experience a Lorentz force in an applied magnetic field ($\vec{B}$) parallel to $\vec{J} \times \vec{B}$, leading to a Hall voltage (V_{Hall}) perpendicular to $\vec{J}$. In this case, $\mu \propto \sigma V_{\mathrm{Hall}}/IB$. This has emerged as a popular technique to verify high values for μ measured using other techniques.[64,65]

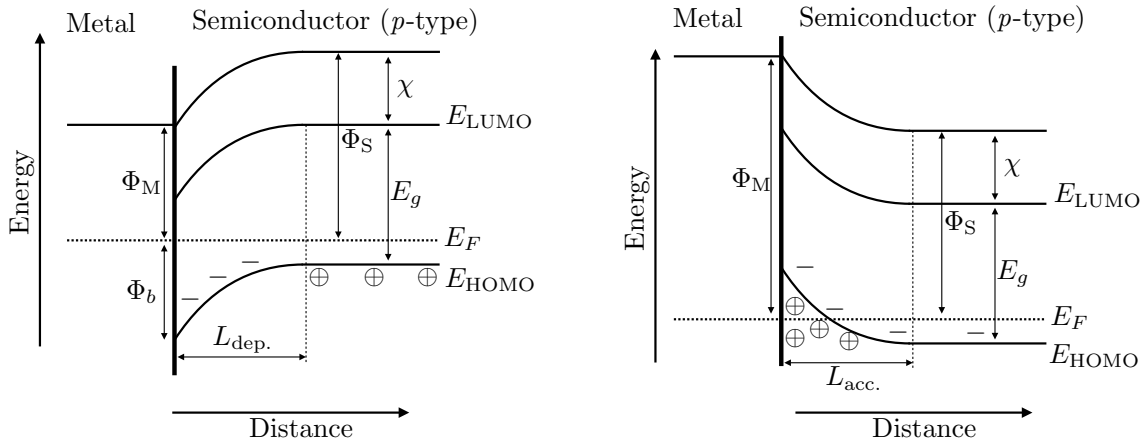

Figure 2.11 Energetics of metal-semiconductor interfaces: $\Phi_{\mathrm{M}} < \Phi_{\mathrm{S}}$ (left) and $\Phi_{\mathrm{M}} > \Phi_{\mathrm{S}}$ (right), with $\oplus$ and $-$ denoting holes in the HOMO band and acceptor ions, respectively.

2.4.1 Metal-semiconductor interfaces

In this thesis, a good understanding of why device performance correlates with energetic parameters is underpinned by the physics of metal-semiconductor interfaces. In particular, many of the electronic characterisation techniques described in following sections rely on the formation of Ohmic contacts between metal and semiconductor in the various device architectures. What follows is a brief discussion of this physics and how it relates to *p*-type semiconductors; using the nomenclature of organic semiconductors for succinctness. However, we note that this formulation applies equally to both *n*-type semiconductors and inorganic semiconductors.

The Fermi level (E_F) of a material is defined by the highest energy (unexcited) electron in a system as $T \to 0$. In a metal, this energy falls over a continuum of states in the density of states - leading to typically high ambipolar electrical conductivities of $\sim 10^6 - 10^7$ S/m. In a semiconductor, E_F falls inside the band gap (E_g) (where there are no states), and so the conductivities are usually orders of magnitude lower < 10 S/m.[66] This is the key difference between metals and semiconductors. E_F is determined by the work function (Φ) of the material; that is, the energy required to eject an electron from E_F. In a metal, Φ_{M} is the same as the ionisation energy, but for a *p*-type semiconductor, E_F lies above the energy of the HOMO (E_{HOMO}), E_F and Φ_{S} are not the same. The electron affinity (χ) is given by the energy of the LUMO (E_{LUMO}).

When a metal and *p*-type semiconductor come into contact, charges flow in either direction to equalise the chemical potential over the two materials. This leads to E_F becoming constant over the interface, shown diagrammatically in Figure 2.11. Concomitantly with this, in the semiconductor, E_{HOMO} and E_{LUMO} bend near the interface, where the curvature (or sign) of bending depends on the relative size of Φ_{M} and Φ_{S}. If $\Phi_{\mathrm{M}} < \Phi_{\mathrm{S}}$, the situation (left) arises that injection of holes from the metal to the semiconductor must overcome an additional barrier; a Schottky barrier with height Φ_b. Furthermore, the curvature of the bands leads to the migration of any holes in the vicinity of the interface region towards the bulk. This effect acts to deplete the charges in this region (that is thus called a 'depletion' region), which has a penetration length scale into the semiconductor bulk $L_{\mathrm{dep.}} \sim n_d^{-1/2}$ (where n_d is the number density of ionised donors).

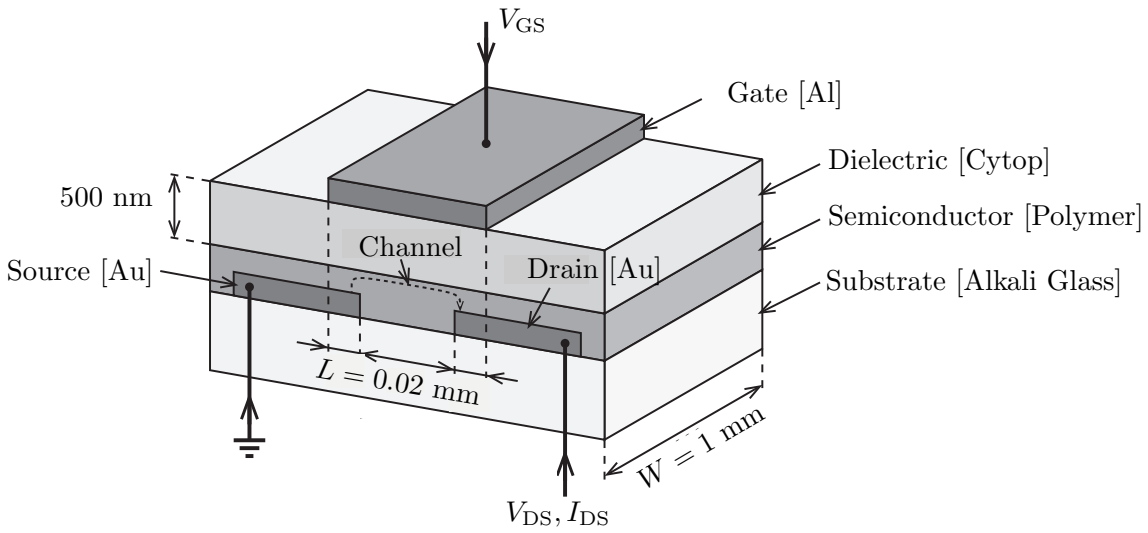

Figure 2.12 OFET architecture used in this work. Figure adapted from reference [67].

On the other hand, if $\Phi_M > \Phi_S$, the situation (right) arises that holes from the ionised bulk semiconductor are naturally accumulated in the semiconductor without a Schottky barrier locally to the interface (in the 'accumulation' region), whose penetration length scale ($L_{acc.}$) is determined by the same physics. Upon application of an external potential over this interface, E_F (at equilibrium) becomes discontinuous. Specifically, applying a negative bias decreases E_F in the semiconductor, and this leads to diode-like behaviour if $\Phi_M < \Phi_S$ (left). However, if $\Phi_M > \Phi_S$ (right), the semiconductor conductivity increases linearly with applied electric field; which is Ohmic behaviour. This is the origin of Ohmic contacts, discussed further in the following section.

2.4.2 Field effect transistors

2.4.2.1 General principles

Fabrication and reproducibility of FETs benefit from a simple architecture. Two electrodes, the source (S) and drain (D), contact a semiconductor thin film, and the distance between them defines the length of the channel (L).[6] The current between source and drain (I_{DS}) is measured as a function of applied voltage (V_{DS}). Parallel to the semiconductor, an insulating film (the gate dielectric) separates the channel from a third electrode, the gate (G). Since no current can pass between the channel and

[6]The length of the contact defines the channel width (W).

the gate, the voltage applied between gate and source (V_{GS}) acts only to increase the chemical potential in the semiconductor channel. An intrinsic semiconductor has a low conductivity, but application of $|V_{GS}| > 0$ draws a number of positive charges (related to the gate capacitance C and V_{GS}) from the source electrode, and electrostatic interactions distribute these accumulated charges at the semiconductor-dielectric interface. Not all states in the DOS lead to charge transport, and some accumulated charges become immobilised in localised states, and are said to be 'trapped', leading to an effective accumulation ($V_{eff.}$) which differs from the applied: $V_{eff.} = V_{GS} - V_{Th}$.

The application of V_{GS} changes the conductivity of the channel (which we measure), and allows for extraction of μ, specifically the field-effect mobility, as a function of charge carrier accumulation. Throughout this thesis, any FETs reported use the top-gate, bottom-contact device architecture shown in Figure 2.12, where (i) source and drain electrodes are patterned on an alkali glass substrate, (ii) semiconductor and dielectric materials are solution-processed on top, and (iii) a gate electrode is patterned on top of the stack, as discussed further in Section 3.2.1. Other device architectures, including bottom-gate/bottom-contact, are discussed elsewhere.[68–70]

2.4.2.2 MOSFET formulation

Here, we describe the analytical formulas for a metal-oxide semiconductor (MOS) FET. In MOSFET devices, there are two regimes which differ by the lateral voltage applied, $|V_{DS}|$, compared to the degree of effective charge carrier accumulation, $|V_{GS} - V_{Th}|$ (where V_{Th} is the threshold voltage). These are summarised diagramatically in Figure 2.13. In the regime where $|V_{DS}| \ll |V_{GS} - V_{Th}|$, the charge carrier distribution (grey) is approximately uniform across the channel. This case is shown in Figure 2.13 (top). Here, I_{DS} depends (approximately) linearly on $|V_{DS}|$, and also $|V_{GS} - V_{Th}|$:

$$I_{DS} = \mu_{lin.} C \frac{W}{L} \left((V_{GS} - V_{Th}) V_{DS} - \frac{(V_{DS})^2}{2} \right). \tag{2.32}$$

For this reason, this regime is called the 'linear regime'. As $|V_{DS}|$ becomes comparable to $|V_{GS} - V_{Th}|$, the carrier distribution over the channel becomes non-uniform. At the point where there is no voltage difference between the gate and drain electrodes, there is no accumulated charge above this electrode, and the channel is said to 'pinch off'. At this point, the carrier distribution is approximately linear across the channel. This

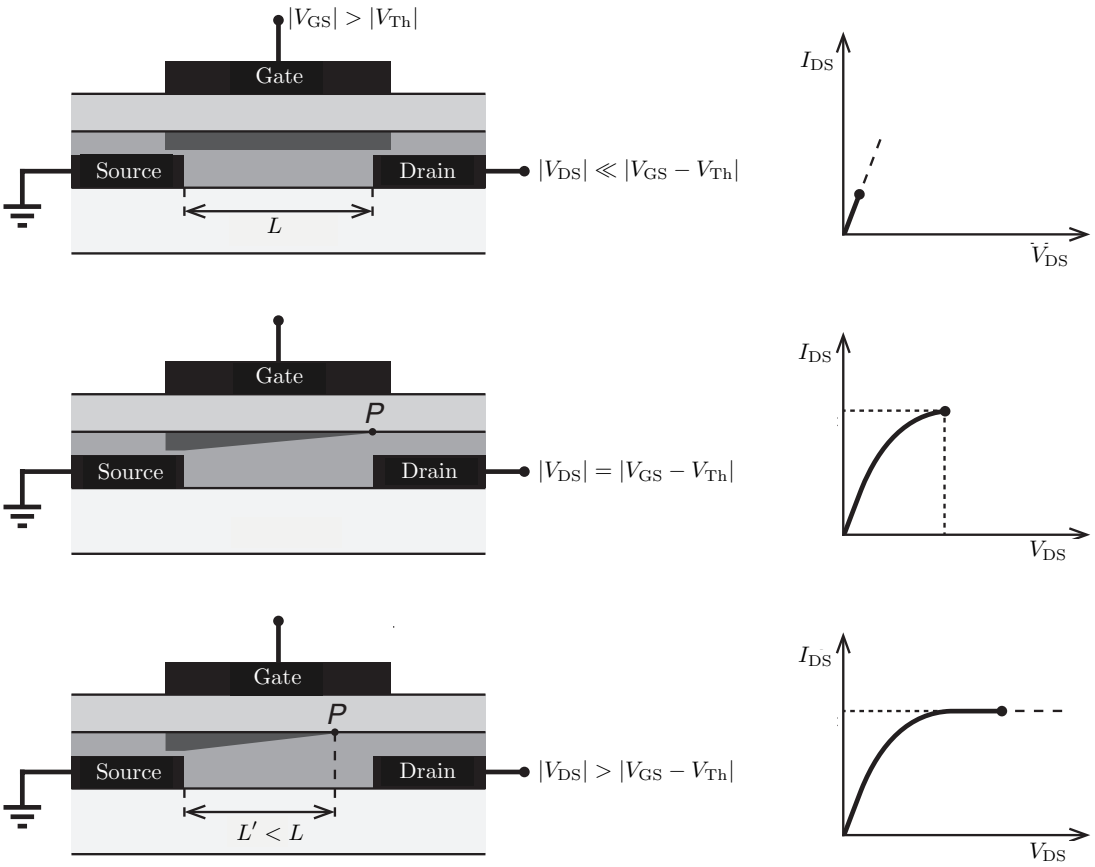

Figure 2.13 Operational principles of a FET in linear (top) and saturation (bottom) regimes, with the intermediate regime near 'pinch off' (middle). Figure adapted from reference [67].

case is shown in Figure 2.13 (middle), and the point at which the channel pinches off is labelled P. Under these conditions, the the output current begins to saturate, and no longer increases with increased $|V_{DS}|$. Finally, in the regime where $|V_{DS}| > |V_{GS} - V_{Th}|$, P moves deeper into the channel, but I_{DS} does not increase further. This is when the device is in saturation, shown in Figure 2.13 (bottom). In saturation,

$$I_{DS} = \mu_{sat.} C \frac{W}{2L} (V_{GS} - V_{Th})^2 . \tag{2.33}$$

2.4.2.3 Contact resistance

In this treatment, we have assumed Ohmic contacts of source and drain electrodes. In organic semiconductors, in general this is not the case. Non-Ohmic contacts lead to contact resistance in devices. In the case of p-type transport in organic materials,

energetic mismatch between the Fermi level of the source contact and the HOMO of the organic semiconductor can be a source for contact resistance. Where the HOMO energy is deeper than the work function of the electrode material, a Schottky barrier is formed at the source-semiconductor interface. However, even when electrode materials are chosen to minimise the Schottky effect, contact resistance at source and drain electrodes can arise from bulk-transport processes in the semiconductor near the electrode interface.[71] This can lead to a temperature (T) dependence of the contact resistance which is similar to the behaviour of $\mu(T)$.[72]

2.4.3 Polaron transport

A charge induces a polarisation in a dielectric environment. By interacting with local dipole moments, a rearrangement of the environment can lead to a significant reduction in the energy of the charge as it is screened. Therefore, a proper treatment of the charge - particularly towards describing its motion - needs also to deal with the dynamics of the polarisation cloud which follows it. Together, this quasiparticle is called a polaron, and can have strikingly different properties to a charge in a vacuum. An early model by Holstein considered a one-dimensional molecular crystal,[73] and explicitly considered electron-lattice interactions in the Hamiltonian, describing the quantum states as 'self-trapped'.

In conjugated polymers, the preferential direction for charge transport is parallel to the chain axis,[74] since polaron wavefunctions are localised in the π-system.[75] This leads to transport in one-dimension, in general. However, structural disorder - static or dynamic - can lead to a broken π-conjugation, and therefore an additional DOS which has suppressed charge transport. This is often detected instead as a broadening of the DOS in transport measurements (discussed below) or the joint DOS as an absorption tail due to these localised states decreasing into the energy gap.[76] This can lead to thermal activation and accumulation dependency in the charge transport, as 'shallow traps' are filled by high charge carrier densities, and de-filled by thermal effects. However, it is not enough that organic semiconductors have good one-dimensional transport, and high μ in poly(3-hexylthiophene-2,5-diyl) (P3HT) is observed when polarons which are diffuse in two orthogonal directions over multiple chains.[77] This is conferred by strong π-π MO overlap.[78] The same observation is thought to be the origin of high μ in some small molecular systems, such as rubrene.[79] For disordered polymers, on-chain polaron localisation presents a potential problem for between-chains

transport. This has recently been addressed by Noriega *et al.* who suggest that disordered polymers behave similarly to semicrystalline polymers, and high μ relies on the formation of such semicrystalline domains which maximise inter-chain coupling.[80] The role of inter-chain coupling in determining μ and various optical parameters is discussed at length later.

In most cases, the transport of polarons between molecules or along polymer chains is thermally activated. As such, it is often treated as an electron-transfer process using Marcus theory, developed in Section 2.3.4.4, which leads to the famous expression for the electron transfer rate:

$$k_{\mathrm{ET}} \propto \frac{t^2}{\sqrt{\lambda k_B T}} \exp\left[-\frac{\lambda/4 - t}{k_B T}\right] \tag{2.34}$$

where t is the transfer integral between the initial and final states. Importantly, and as before, this has (i) an 'activationless' regime where the reorganisation is small compared to the energy transfer, and this leads to band-like transport when $\lambda < 2t$. The more common case is when the reorganisation energy is large and $\lambda > 2t$ leads to transport by 'hopping' of localised polarons. The mobility predicted by Marcus theory is $\mu \propto k_{\mathrm{ET}}/k_B T$.

2.4.4 Disordered organic semiconductors

In a non-crystalline material, localised states typically appear at lower energies.[81] In the density of states of a material $\rho(\epsilon)$, the 'mobility edge' model is based on the assumption that there is an energy edge ϵ_c which separates mobile from immobile states. It posits that states $\rho(\epsilon > \epsilon_c)$ participate in activationless ('band-like') transport and have a constant mobility, and states $\rho(\epsilon < \epsilon_c)$ have vanishing mobility. In the case of a large ϵ_c, this leads to a strong thermal activation of the transport, since the mobility directly relies on the ability of a polaron to 'hop' to higher energy states $> \epsilon_c$ to contribute to the bulk conductivity. This idea is powerful, since it predicts a temperature dependence of the transport, and unifies band-like and hopping characters in the transport.[82] However, the idea of a 'sharp' mobility edge was later disputed by Mott, and a treatment involving electron-phonon coupling, specifically inelastic scattering with phonons, leads to a broadening of this edge, even at $T = 0$ K.[83]

Nonetheless, this idea is extended by Horowitz and coworkers via the multiple trapping and release (MTR) mechanism. This had been used previously to explain (i) the V_{GS} dependence of the μ in amorphous silicon FETs,[84] and (ii) temperature dependence of μ in organic small molecules,[85] and is later restated with an explicitly unified thermal and gate-voltage picture.[86] Central to this approach is a robust determination of the DOS of the system, and such an approach which utilises FET architectures had been reported previously.[87]

The idea of variable-range hopping (VRH) transport is that a carrier can 'hop' between states with a variable energy barrier, and this barrier decreases with increasing 'hopping' distance. This idea is explored by Mott in the context of low-temperature behaviour of electrical conductivity, and leads to the famous temperature dependency $\ln(\sigma) \sim T^{1/4}$ in a three-dimensional system.[88] However, around the same time, this idea was invoked to explain the temperature dependence of impurity conduction in Ge and Si,[89] with a full formalism presented later by Miller and Abrahams.[90] An important development towards our current understanding of transport in disordered organic semiconductors was made by Vissenberg and Matters, who unified percolation theory with a VRH exponential DOS,

$$\rho(\epsilon) = \frac{n_t}{k_B T_0} \exp\left(\frac{\epsilon}{k_B T_0}\right) \qquad (-\infty < \epsilon \leq 0) \tag{2.35}$$

where n_t is the number of states per unit volume, and T_0 is a parameter which indicates the width of the exponential distribution.[91] In FETs, this leads to a temperature dependency of the behaviour of I_{DS} which differs depending on the charge carrier density profile at the semiconductor-dielectric interface. In the case that the charges assume a profile which decreases with the square of the distance from the interface, the profile is said to be three-dimensional (3D). However, if the charges are confined close to the interface (by the FET architecture or otherwise), the profile is said to be 2D. In this case

$$I_{\mathrm{DS}}^{(\mathrm{3D})} \propto (V_{\mathrm{GS}} - V_{\mathrm{Th}})^{2T_0/T} \tag{2.36}$$

$$I_{\mathrm{DS}}^{(\mathrm{2D})} \propto (V_{\mathrm{GS}} - V_{\mathrm{Th}})^{T_0/T} \tag{2.37}$$

in the limit that V_{GS} is large.[92, 93]

A good understanding of charge transport in disordered polymer semiconductors is a primary focus of this thesis. To achieve this, the temperature dependence of μ must be considered, and compared to these theoretical studies. In this work, considerable effort was made to optimise the performance of devices presented, and in many cases, treatment of organic polymer FETs as ideal MOSFETs at room temperature: obeying the theoretical description in Section 2.4.2, is appropriate. Regardless, as described in this section, a quantifiable (non-vanishing) disorder requires a more complicated treatment of the mobility at low temperature, and a more detailed discussion of the charge transport temperature dependence is included with our experimental results.

Chapter 3

Experimental Methods

3.1 Materials

3.1.1 Semiconductors

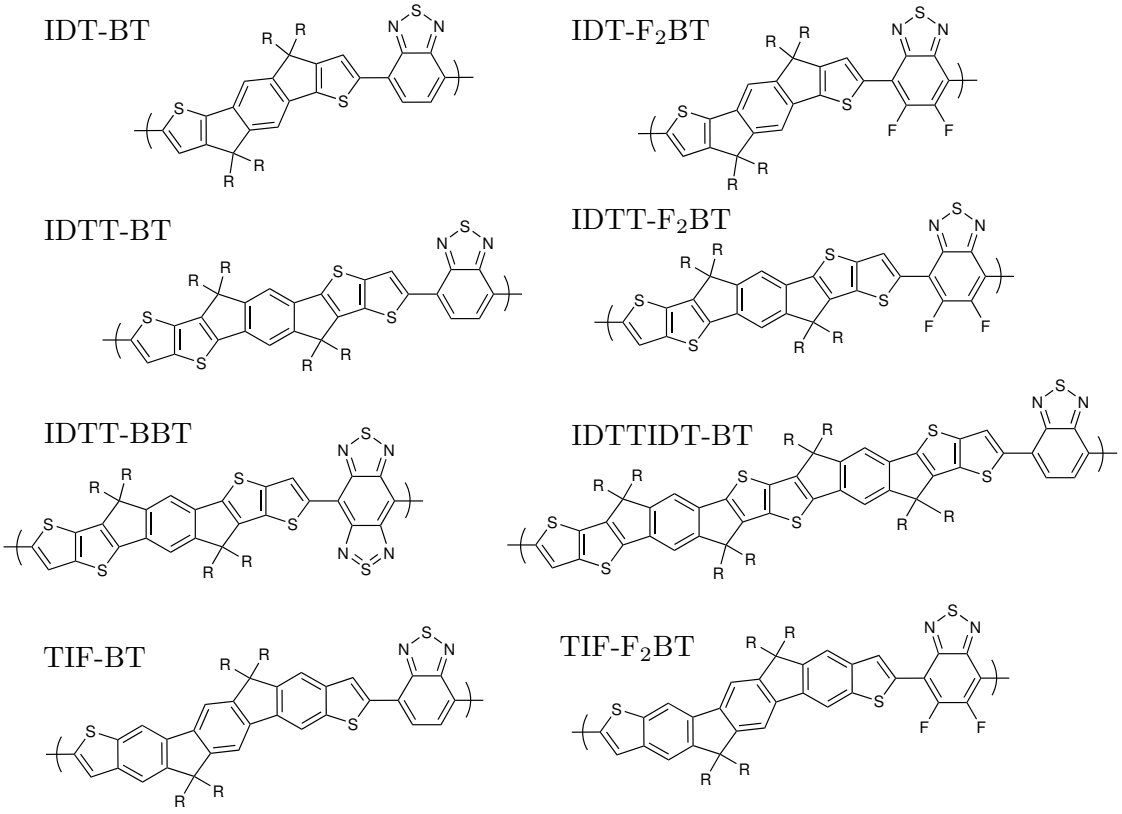

Figure 3.1 Structures of polymer materials used in this work.

3.1.1.1 Polymers

The semiconducting donor-acceptor polymers measured in this thesis are shown in Figure 3.1 with their number average molar mass (M_n), mass average molar mass (M_w), and polydispersity index (PDI). These were kindly provided by Prof. Iain McCulloch from *Imperial College London* (I), Dr. Hu Chen from *King Abdullah University of Science and Technology* (K), and Dr. Aurélie Morley from *Merck Chemicals Ltd.* (M) as indicated in Table 3.3.

Table 3.1 Donor-acceptor polymers used in this work. Sidechains (R): *n*-hexadecyl ($\star$), 2-ethylhexyl ($\circ$), 3,7,11-trimethyldodecyl ($\bullet$), and *p*-hexadecylbenzyl ($\diamond$).

Polymer (R)	Provider	M_n [kDa]	M_w [kDa]	PDI
IDT-BT ($\star$)	I	110	290	2.6
IDT-BT ($\circ$)	M	76	310	4.1
IDT-BT ($\bullet$)	M	60	188	3.1
IDT-BT ($\diamond$)	M	91	210	2.3
IDTT-BT ($\diamond$)	M	67	151	2.3
IDTIDTT-BT ($\diamond$)	M	91	567	6.2
TIF-BT ($\star$)	I/K	85	116	1.4
IDT-F_2BT ($\star$)	M	45	77	1.7
IDTT-F_2BT ($\diamond$)	M	63	200	2.7
TIF-F_2BT ($\star$)	I/K	67	98	1.5
IDTT-BBT ($\diamond$)	M	30	105	3.5

3.1.1.2 Small molecule emitters

All small molecule emitters were purchased from either *Lumtec Corp.* (Lumtec) or *Xi'an Polymer Light Technology Corp.* (PLT), or provided by Prof. Manfred Bochmann and Dr. Alex Romanov from *University of East Anglia* (UEA) as indicated in Table 3.2.

3.1.2 Insulators

In this work, we used the following (wide bandgap) insulators; Cytop, poly(methylmethacrylate) (PMMA), polystyrene (PS), and 1,4-bis(triphenylsilyl)benzene (UGH2). These were used for (i) dielectric layers in thin film electronic devices, (ii) to decrease inter-chain coupling in polymer blends, and (iii) as a rigid host for guest emitters to reduce low

Table 3.2 Source of small molecule emitters used in this work.

Emitter	Provided by
2CzPN	PLT
4CzIPN	PLT
4CzTPN-Ph	PLT
TXO-TPA	Lumtec
TXO-PhCz	Lumtec
DMAC-DPS	PLT
PXZ-DPS	Lumtec
CMA1	UEA

frequency motion. The source and specification of these materials is summarised in Table 3.3.

Table 3.3 Source of insulators used in this work.

Insulator	Specification	Provided by
Cytop	CTL-809M:CT-Solv180 (3:1)	*Asahi Glass Co.*
PMMA	$M_w = 221.5$ kDa, PDI = 1.04	*Polymer Source, Inc.*
PS	$M_w = 10$ kDa	*Sigma Aldrich*
PS	$M_w = 100$ kDa	*Sigma Aldrich*
PS	$M_w = 1$ MDa	*Sigma Aldrich*
UGH2	LT-N448	*Lumtec Corp.*

3.1.3 Dopants and additives

All small molecule dopants and additives were purchased from *Tokyo Chemical Industry Co., Ltd.* (TCI), *Novaled AG* (Novaled), or *Sigma Aldrich* (Sigma), as indicated in Table 3.4.

Table 3.4 Source of additives and dopants used in this work.

Additive/dopant	Provided by
TCNQ	Sigma
F_2-TCNQ	TCI
F_4-TCNQ	TCI
F_6-TCNNQ	Novaled

3.1.4 Solvents

For solution processing under a N_2-atmosphere, all solvents in this work were purchased from the Hi-Dry (anhydrous) range by *ROMIL Ltd.*. All other solvents were purchased from *Sigma Aldrich*.

3.2 Field-effect transistor measurements

3.2.1 Sample fabrication

Organic field-effect transistors (OFETs) were fabricated using a bottom contacted, top gated architecture.

3.2.1.1 Fabrication of interdigitated bottom contacts

Smoothed alkali glass (1317F, *Corning*) was cut to an appropriate size (1.5×1.5 cm^2) and sonicated sequentially in deionised water, acetone, and propan-2-ol. These were blown dry and cleaned with oxygen plasma at high power (300 W, 10 mins.; *TEGAL*). Patterning the substrates was achieved by a lift-off process using two orthogonal photoresists (LOR3B, *Micro Chemical Corp.*, then S1813, *Dow Rohm and Haas Shipley*), UV sensitisation using an aligned optical mask (MJB3, *Karl Suss*), and development (MF319, *Dow Rohm and Haas Shipley*). Thermal evaporation of Cr (2 nm) then Au (20 nm) at low base pressures ($\sim 10^{-6}$ mBar) followed, and the lift-off was completed using N-methyl-2-pyrrolidone (> 6 hrs.). This yielded interdigitated bottom-contacts (Au, $L = 20$ µm, $W = 1$ mm).

3.2.1.2 Fabrication of the device

OFET substrates were then sonicated sequentially in NMP, acetone, and propan-2-ol, blown dry and cleaned with oxygen plasma (300 W, 10 mins.; *TEGAL*). Hereafter, the samples were exposed only to a N_2-atmosphere. Under N_2, polymer semiconductors were dissolved (using chlorobenzene except as indicated) at 10 g/L, heated to 60 °C, and spin-coated to give a film ~ 25 nm thick.[1] At this stage, an optional step of annealing the semiconductor on a hot plate was included as indicated. The dielectric (Cytop, unless as indicated) was spin-coated on top of the polymer thin film in a

[1] This involved a three-step process: (i) 500 rpm, 5 secs., 1 secs. ramp; (ii) 1400 rpm, 60 secs., 3 secs. ramp, (iii) 5000 rpm, 10 secs., no ramp

N_2-atmosphere and annealed for the shortest time possible (70 °C, < 5 secs.) to dry the film.[2] The samples were gated by thermal evaporation of Al (30 nm) which was patterned by a shadow mask. The completed device architecture is summarised in Figure 2.12.

3.2.2 Electrical measurements

3.2.2.1 Room temperature

OFET devices were electrically characterised in a N_2-atmosphere by simultaneous current measurements on three 3 SMUs (4155B SPA, *Agilent*), recorded using a bespoke LabView (*National Instruments*) program. Transfer characteristics swept the gate-source voltage (V_{GS}) with fixed source-drain voltage (V_{DS}). Unless otherwise stated, we used $|V_{DS}| = 5$ V to measure the linear characteristics, and $|V_{DS}| = 50 - 60$ V for saturation.[3] Output characteristics swept V_{DS} at fixed values of V_{GS} to verify saturation and good agreement between on-currents $I_{DS}(|V_{DS}| = |V_{GS}| = 50 - 60$ V).

3.2.2.2 Cryogenic measurements

OFET measurements at low temperature used a probe station (TTP4 SPA, *Desert Cryogenics*). Measurements were recorded as above in high vacuum ($\sim 10^{-6}$ mBar) after thermal equilibration ($\sim$ 15 mins) of the substrate (mounted on a metal stage) between liquid-N_2 flow and a resistive heater (331S, *Lakeshore*).

3.2.3 Mobility extraction

In this thesis, a discussion of the *p*-type mobility is included, but we do not discuss the *n*-type mobility at length. This is for two main reasons; (i) in disordered organic materials (which are the focus here), we expect similar physics of energetic and dynamic disorder, and microstructure-facilitated charge transport to govern *p*-type and *n*-type transport, such that an increase in the former is likely to imply an increase to the latter, and (ii) we find the fabrication of *n*-type transistors to be particularly sensitive to atmospheric species, leading to unreliable devices with low batch-to-batch

[2]For each batch of OFETs, a blank substrate was also prepared in this way and the dielectric thickness was determined using atomic force microscopy (AFM Surface Profilometer; *DekTak3*).

[3]While fixing $V_{DS} = V_{GS}$ explicitly 'pinches off' the charge-carrier accumulation across the channel (ensuring saturation at all values of V_{GS}), we observe negligible change in the characteristics with this measurement technique.

reproducibility. This is discussed further in the following chapter.

In a similar vein, Bittle and coworkers describe a common problem in the literature with the robust extraction of the *p*-type mobility.[94] The true mobility in a material is, of course, independent of the contact effects. Applying the ideal MOSFET equations to devices with non-ideal behaviour can be problematic, and a gate-bias dependency of the contact resistance can lead to substantial overestimation of the true mobility in both polymers and small molecules.

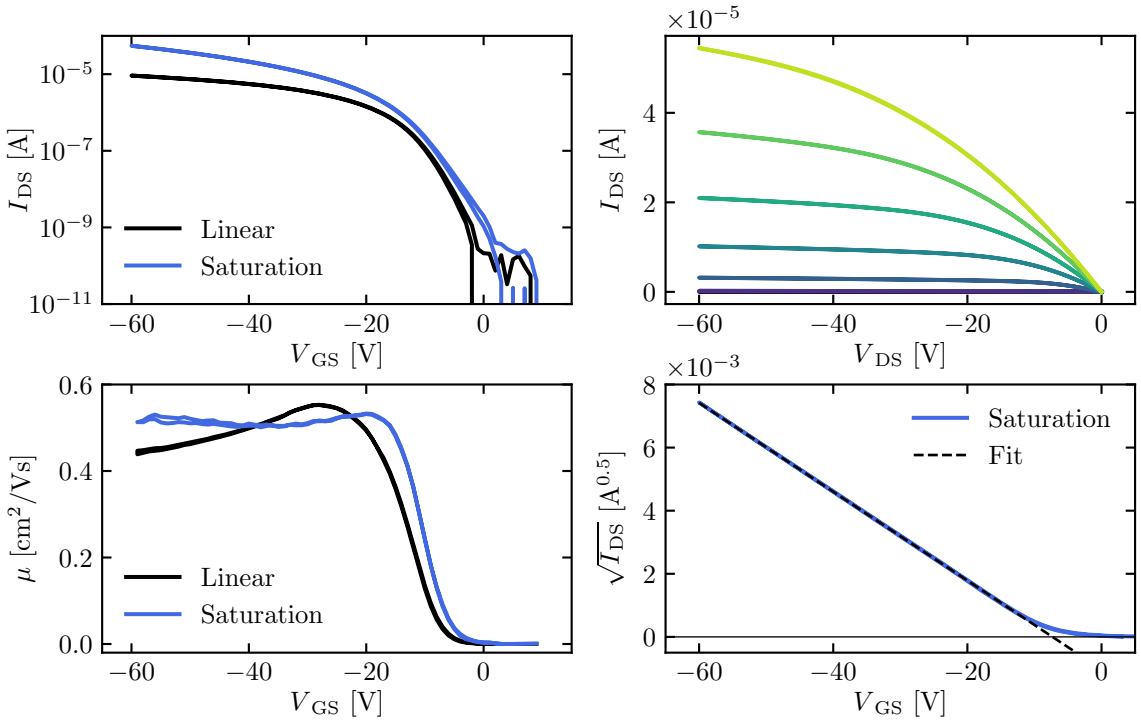

Figure 3.2 Mobility extraction in an OFET. Transfer (top left) and output (top right) characteristics, and extracted mobility as a function of accumulation (bottom left) compared with conventional mobility extraction (bottom right).

To ensure robust extraction and indicate deviation from ideality, we present the guidelines we followed in this work for meaningfully presenting real transistor data, and verifying the integrity of the extracted mobility. For M_{13}, a proprietary polymer (*Merck Chemicals Ltd.*), we show the measured transistor characteristics in Figure 3.2 (top). We start with the formulation for an ideal MOSFET in Section 2.4.2, and use the expressions for linear and saturation regimes given in Equations 2.32 and 2.33.

A typical extraction of the mobility and threshold voltage is shown in Figure 3.2 (bottom right). This utilises a linear fitting of the $\sqrt{I_{\mathrm{DS}}} - V_{\mathrm{GS}}$ curve in saturation, so the gradient is proportional to the mobility. Furthermore, extrapolation of the fit to $I_{\mathrm{DS}} = 0$ A gives $V_{\mathrm{GS}} = V_{\mathrm{Th}}$, and hence the threshold voltage. Using this methodology, we extract $\mu_{\mathrm{sat.}} = 0.5$ cm^2/Vs and $V_{\mathrm{Th}} = -8$ V. We include the output characteristics in Figure 3.2 (top right), where we have used $V_{\mathrm{GS}} = 0$ to -60 V (decreasing by 10 V increments; blue to green lines). By examining the output characteristics, we observe good saturation for low V_{GS}, and very little contact resistance, which can otherwise appear as a sigmoidal shape in I_{DS} near $V_{\mathrm{DS}} \approx 0$. Difficulties occur in this extraction when there are non-idealities arising from (i) hysteresis due to trapping, (ii) a large contact resistance or (iii) high threshold voltage leading to deviation from $I_{\mathrm{DS}} \sim (V_{\mathrm{GS}} - V_{\mathrm{Th}})^2$ for $V_{\mathrm{GS}} > V_{\mathrm{Th}}$. This can result in a substantial overestimation of the mobility. Furthermore, this method is blind to small deviations in ideality, and the degree of agreement between mobility linear and saturation regimes with charge accumulation.

While in the MOSFET formulation the mobility is a constant (and $\mu_{\mathrm{lin.}} = \mu_{\mathrm{sat.}}$), rearrangement of Equations 2.32 and 2.33 allows for the evaluation of the mobility, which, in general, has a dependency on $|V_{\mathrm{GS}}|$,

$$\mu_{\mathrm{lin.}}(V_{\mathrm{GS}}) = \frac{1}{V_{\mathrm{DS}}} \frac{1}{C_{\mathrm{ox.}}} \frac{L}{W} \left(\frac{\partial I_{\mathrm{DS}}}{\partial V_{\mathrm{GS}}} \right) \tag{3.1}$$

in the linear regime, and

$$\mu_{\mathrm{sat.}}(V_{\mathrm{GS}}) = \frac{1}{C_{\mathrm{ox.}}} \frac{2L}{W} \left(\frac{\partial \sqrt{I_{\mathrm{DS}}}}{\partial V_{\mathrm{GS}}} \right)^2 \tag{3.2}$$

in saturation.

By expressing $\mu_{\mathrm{lin.}}(V_{\mathrm{GS}})$ and $\mu_{\mathrm{sat.}}(V_{\mathrm{GS}})$ in Figure 3.2 (bottom left), we diagnose several deviations from ideal behaviour in a seemingly good transistor which we are otherwise unable to resolve. Firstly, in saturation, the peak in mobility at $|V_{\mathrm{GS}}| < 20$ V is not real, but instead is the artefact due to a gate voltage dependence of the contact resistance (which is small here) which Bittle *et al.* discuss.[94] The evidence for this is (i) a decreasing saturation mobility for $|V_{\mathrm{GS}}| = 20 - 30$ V and (ii) a linear mobility which is still increasing towards $|V_{\mathrm{GS}}| = 30$ V, indicating that the device is

slow to switch on fully. Furthermore, while the linear mobility seems to suffer less from the contact-induced mobility overestimation, we see a non-physical decrease in the mobility at high $|V_{GS}| > 30$. Nonetheless, there is good agreement between the mobility extracted in linear and saturation regimes. In this work, we express deviation from ideal MOSFET behaviour via a reliability factor r, defined as the average mobility predicted by an ideal MOSFET of the same architecture whose current output is measured, divided by the claimed mobility;[63]

$$r_{\text{lin.}} = \left(\frac{|I_{DS}^{\text{max.}}| - |I_{DS}^{\text{off}}|}{|V_{GS}^{\text{max.}}|} \right) \left(\frac{L}{WC|V_{DS}|} \right) \frac{1}{\mu_{\text{lin.}}} \tag{3.3}$$

and

$$r_{\text{sat.}} = \left(\frac{\sqrt{|I_{DS}^{\text{max.}}|} - \sqrt{|I_{DS}^{\text{off}}|}}{|V_{GS}^{\text{max.}}|} \right)^2 \left(\frac{2L}{WC} \right) \frac{1}{\mu_{\text{sat.}}} \tag{3.4}$$

where $I_{DS}^{\text{max.}}$ is the maximum (on-)current at $V_{GS}^{\text{max.}}$, I_{DS}^{off} is the off-current (where $V_{GS} = 0$ V), and the other parameters are as defined earlier. An effective mobility $\mu_{\text{eff.}}$ can therefore be thought of as

$$\mu_{\text{eff.}} = r\mu_{\text{claimed}} \tag{3.5}$$

and hence we hence claim $\mu_{\text{lin.}} = 0.50$ cm^2/Vs (with $r_{\text{lin.}} = 0.66$) and $\mu_{\text{sat.}} = 0.52$ cm^2/Vs (with $r_{\text{sat.}} = 0.63$). As a final comment, for most of the materials considered herein, near-ideal MOSFET like behaviour (i.e. $r > 0.5$) was achieved by appropriate optimisation of the solution processing. However, for materials which did not behave in this way, particular care was taken so as not to overestimate the mobility, and only devices with (i) high on-currents (and agreement) in both transfer and output characteristics, (ii) a reasonable V_{Th} and sweeping to the range where $V_{GS} \gg V_{Th}$, and (iii) good on:off current ratios were reported here, together with their mobility and reliability factor.

3.3 Spectroscopy

3.3.1 Sample fabrication

Thin polymer films were spin-coated as for OFETs on clean alkali glass. Polymer solutions (10 g/L, heated to 60 °C) were spin-coated under N_2, and encapsulation was achieved by sealing the polymer film against a glass cover slip with an epoxy.

3.3.2 Absorption spectroscopy

3.3.2.1 Steady state absorption

Steady state absorption at room temperature was measured on a calibrated spectrophotometer (HP8453, *Hewlett-Packard*) between $250 - 900$ nm. Spectra acquired in this way were 'zeroed' with a blank substrate, but an additional scattering background due to the film was fit with a polynomial and subtracted.

3.3.2.2 Photothermal deflection spectroscopy

For scattering-free measurements, photothermal deflection spectroscopy (PDS) was employed. Here, a monochromatic beam was directed on the sample - a film on a fused quartz (water-free Spectrosil) substrate. Absorption produces a thermal gradient near the sample surface due to heating from non-radiative relaxation. This results in a refractive index gradient in the area surrounding the sample surface. This refractive index gradient is further enhanced by immersing the sample in an inert liquid (FC-72 Fluorinert, *3M Company*) which has a high refractive index change per unit change in temperature. A (non-exciting) continuous wave laser beam is passed through this refractive index gradient, producing a deflection proportional to the absorbed light at that particular wavelength, which is detected by a photodiode and lock-in amplifier. Scanning through different pump wavelengths builds up the absorption spectra with a very high sensitivity.

By approximating the absorption tail near the band-edge (for $\hbar\omega \approx E_g$) to an exponential, we fit the relationship

$$\alpha(\hbar\omega) \sim \exp\left(\frac{\hbar\omega - E_g}{E_\mathrm{U}}\right) \tag{3.6}$$

where α is the absorption coefficient, $\hbar\omega$ is the photon energy, and E_g is the energy gap to determine the Urbach energy (E_U). The Urbach energy can be thought of as the width of the joint density of states (JDOS) of the transition, and a smaller value of E_U, or a sharper JDOS near the energy gap, indicates lower energetic disorder of the JDOS. Typically, high-mobility polymers have a low $E_\mathrm{U} < 100$, including poly(3-hexylthiophene) (P3HT; $E_\mathrm{U} = 50$ meV) and poly[2,5-bis(3-alkylthiophen-2-yl)thieno[3,2-b]thiophene] (pBTTT; $E_\mathrm{U} = 58$ meV).[93]

3.3.2.3 Transient absorption spectroscopy

Transient absorption spectroscopy (TA) measures the differential change in transmission of a sample with and without excitation by a pump. If the pump creates a population of excitons in the sample, TA allows us to measure the absorption of this exciton population. Therefore, TA data is typically expressed in terms of the differential transmission ($\Delta T/T$), which is defined in terms of the transmission with and without a pump pulse; T_p and T_0 respectively:

$$\frac{\Delta T}{T} = \frac{T_p - T_0}{T_0} \tag{3.7}$$

By delaying the probe pulse by a variable time after the pump, we measure the differential transmission at that time, and therefore gain information about the exciton population at that instant. Therefore, we build up a $\Delta T/T$ map in wavelength and time, typically averaging spectra over a number of pulses (or 'shots') before changing the time step. The length of the pulses (in time) determines the time resolution of the experiment, and we describe the specific procedure below.

For measurements with $\sim$ 100 *fs time resolution*: the output of a Ti:Sapphire amplifier system (800 nm, 90 fs, 1 kHz, Solstice Ace, *Spectra-Physics*) was split into pump and probe beam paths. For the probe, visible and near-IR broadband beams were generated in home-built non-collinear optical parametric amplifiers (NOPAs). For the pump, second harmonic generation (and another NOPA) generated the pump beam at 400 nm ($490 - 760$ nm). The transmitted pulses were collected with an InGaAs dual-line array detector (G11608-512, *Hamamatsu*) driven and read out by a custom-built board (Entwicklungsbüro, *Stresing*).

For measurements with ~ 2 *ns time resolution*: the probe pulses are generated and measured as before, but the pump uses the nth harmonic of an electrically triggered Nd:YVO_4 laser (1064 nm, ~ 2 ns, *Advanced Optical Technologies*).

For measurements with < 40 *fs time resolution*: the output of a Nd:YAG laser system (1025 nm, 38 kHz, PHAROS, *Light Conversion*) was split into pump and probe beam paths. The pump was selectively amplified by the third harmonic of the laser and compressed with chirped mirrors (530 nm, $20 - 30$ fs, HIRO, *Light Conversion*). The probe beam was generated as before. Following the sample, the probe was split

using a hot and cold mirror into visible and near-IR spectra and these beams are then detected simultaneously with a pair of spectrometers; an InGaAs photodiode array for the near-IR band (*Sensors Unlimited*) and a silicon detector array (*Stresing*) for the visible band.

3.3.2.4 Cryogenic absorption measurements

Absorbance at low temperatures ($< 20 - 300$ K) was measured on a spectrophotometer (6000i: double beam, *Cary*) with a cold-finger helium cryostat (CF-V, *Oxford Instruments*).

3.3.3 Photoluminescence spectroscopy

3.3.3.1 Steady state photoluminescence

Samples were exposed to continuous wave laser illumination with wavelength as specified ($\sim$ 1 mW, spot waist $\sim 2mm$, *ThorLabs*) leading to low excitation densities of $10^12 - 10^15$ cm^{-3} inside an integrating sphere (6 inch, *Labsphere*). The integrated signal was coupled with an optical fibre to a spectrometer which had a Si detector array (SR-303i-B, *Andor Technology*). The sphere-fibre-detector system was calibrated over $357 - 1051$ nm.

3.3.3.2 Photoluminescence quantum efficiency

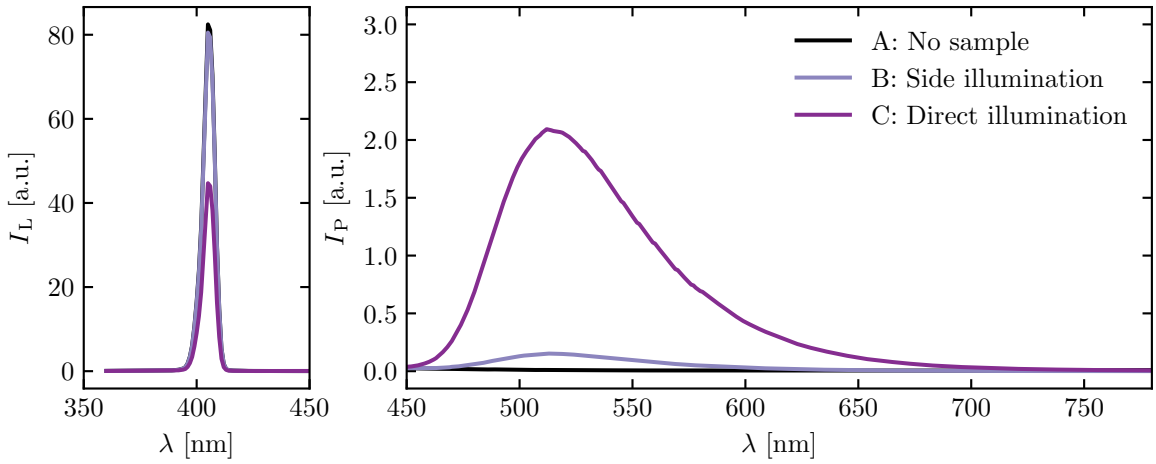

Figure 3.3 Example spectra for extraction of the PLQE

The photoluminescence quantum efficiency (PLQE) is defined as the fraction of photons re-emitted of those which are absorbed. To quantify this, we follow the approach of de Mello *et al.*, who propose a three measurement determination.[95] For each sample, we measure three spectra in the setup described above. In the first (A), the laser is directed into an empty sphere. In the second (B), the sample is loaded but not directly excited by the laser path. In the third (C), the sample is directly excited. Example spectra (of TXO-TPA in a PS film) were shown in Figure 3.3. Where the sample was not encapsulated, the sphere was purged with N_2 for > 5 mins.

The number of photons is proportional to the intensity recorded (I), and to determine the number of photons due to the laser (L) or the photoluminescence (P), we integrated under the curve. We can then calculate the PLQE with the equations,

$$A = 1 - \frac{L_{\mathrm{C}}}{L_{\mathrm{B}}} \tag{3.8}$$

$$\mathrm{PLQE} = \frac{P_{\mathrm{C}} - (1 - A)P_{\mathrm{B}}}{L_{\mathrm{A}}A} \tag{3.9}$$

and hence, we extract a PLQE of 0.40.

3.3.3.3 Pulsed photoluminescence

Samples were exposed to a pulsed-UV diode laser (407 nm, 20 MHz, PDL 800-B (trigger), LDH-P-C 400B (laser head), *PicoQuant*) and the photoluminescence spectra were recorded by integrating on-chip with a silicon diode array (SpectraPro 2500i, *Acton Research Co.*). Where the sample was not encapsulated, a high vacuum ($\sim 10^{-6}$ mBar) was used.

3.3.3.4 Time-correlated single photon counting

With the same setup, photoluminescence decays were determined using time-correlated single photon counting (LifeSpec - ps, *Edinburgh Instruments*). In this measurement, an external electronic trigger is simultaneously sent to a laser (which creates a pulse) and to the detector (which measures the time delay between the trigger arriving and the arrival of a photon). A histogram of detection frequency in various time bins gives the decay kinetic of the photoluminescence, although the instrument response of the setup leads to meaningful extraction of lifetimes > 300 ps. Detection at a specific

wavelength was achieved using a monochromator.

3.3.3.5 Determining the radiative and non-radiative rates

From independent measurement of the photoluminescence quantum efficiency and lifetime (in Sections 3.3.3.2 and 3.3.3.4), it is possible to determine the rates of radiative (k_{R}) and non-radiative (k_{NR}) decay. By first assuming monomolecular decay of the exciton population (n), first order ODE $\dot{n} \propto n$ describes the exciton decay dynamics, and we write

$$I(t) \propto \frac{dn(t)}{dt} \propto \exp\left(-t/\tau_{\mathrm{PL}}\right) \propto n(t) \tag{3.10}$$

where $I(t)$ is the intensity of photoluminescence at time t, and τ_{PL} is the photoluminescence lifetime. Fitting this equation to the transient photoluminescence decay, we determine τ_{PL}, or equivalently $k_{\mathrm{PL}} = \tau_{\mathrm{PL}}^{-1}$ where k_{PL} is the photoluminescence decay rate. Furthermore, in the case of a single emissive species, we can write

$$k_{\mathrm{PL}} = k_{\mathrm{R}} + \sum k_{\mathrm{NR}} \tag{3.11}$$

where there is in general more than one non-radiative decay channel. Then, the photoluminescence quantum efficiency (PLQE) of the decay pathway can be expressed in terms of the k_{R} and k_{NR},

$$\mathrm{PLQE} = \frac{k_{\mathrm{R}}}{k_{\mathrm{PL}}} = \frac{k_{\mathrm{R}}}{k_{\mathrm{R}} + \sum k_{\mathrm{NR}}}. \tag{3.12}$$

Using Equations 3.11 and 3.12, it is possible to determine k_{R} and $\sum k_{\mathrm{NR}}$, and we usually write the sum $\sum k_{\mathrm{NR}} \rightarrow k_{\mathrm{NR}}$.

3.3.3.6 Cryogenic photoluminescence measurements

Pulsed time-integrated and time-resolved photoluminescence measurements at low temperatures ($4 - 300$ K) were conducted using a helium cryostat (CF-V, *Oxford Instruments*) and the setup described above.

3.3.3.7 Ultrafast transient grating photoluminescence

For measurements with time resolution < 200 fs, an up-conversion setup that has already been described in detail elsewhere[96, 97] was used.

3.3.4 Raman spectroscopy

Thin film and powder samples were measured in air at room temperature. Raman measurements were conducted by back-scattering (T64000, *HORIBA*) a continuous wave diode line ($\sim$ 1 mW, spot waist $\sim$ 2 mm) with wavelength ($\lambda = 532, 633, 785$ nm) as indicated with experiments, with both a single and triple stage. Spectra were collected for low-frequency vibrations, < 10 cm^{-1} in some cases, where the CCD detector (Synapse Open-Electrode, *HORIBA*) has a monotonically increasing quantum efficiency. Acquisitions employed a 100$\times$ optical objective and used short acquisitions and low excitation densities below 10^15 cm^{-3} to avoid laser damage.

3.4 Structural characterisation

3.4.1 Sample fabrication

Thin film samples for structural characterisation used a bare Si wafer (with $\sim 2-3$ nm native SiO_2) as a substrate. This was cleaned in the same way, and the polymer was spin-coated as for OFET devices.

3.4.2 Ellipsometry

Measurements to determine the thickness of polymer thin films used a spectroscopic ellipsometer in the reflection mode (with a 70 $^\circ$ angle of incidence relative to the substrate normal). This had a rotating compensator (M-2000, *J.A. Woollam*). Data were collected between $400-900$ nm, and the polymer thickness was determined by fitting the non-absorbing spectral region using a Cauchy model.

3.4.3 X-ray diffraction

X-ray diffraction (XRD) measurements were conducted on thin films in air (D8 Advance X-ray Diffractometer, *Bruker AXS*) using a Cu-K_α source ($\lambda = 1.5418$ Å). The incident beam slit width was 0.1 mm. Data were collected in 2D mode from the total reflection

edge at room temperature. Contributions to the signal from $K_{\alpha 2}$ were uniformly small and close to the strong $K_{\alpha 1}$, so data were not pre-processed.

3.5 Density functional theory calculations

All (TD-)DFT calculations in this thesis used the 'ORCA' package[98] with the B3LYP hybrid functional[99, 100] and 6-31G(d,p) double-ζ Pople basis set with added polarisation[101] (unless otherwise stated). Benchmarking of the B3LYP/6-31G* functional/basis combination has been well-documented for organic materials, and it typically performs well optimising ground-state geometries,[102, 103] and calculating vibrational spectra.[104, 105] In order to calculate meaningful properties of materials in this thesis, we (i) estimated the three-dimensional geometry from the chemical structure which we expect to be reasonably close to the true equilibrium geometry, (ii) run a (non-redundant) optimisation calculation where all degrees of freedom (including bond lengths, angles, and dihedral angles) are able to move to find the free energy minimum, (iii) checked that the output geometry was as we expect and that the calculation is convergent, and (iv) used this geometric output to perform single point (energy determining) calculations, determine vibrational frequencies (which are devoid of non-equilibrium imaginary modes), and for TD-DFT calculations where relevant.

Chapter 4

Charge transport in amorphous donor-acceptor co-polymers

4.1 Amorphous donor-acceptor co-polymers

Since 1977, a preference for solution-processable materials with high mobilities[7, 9, 106, 107] has led to the development of materials with complicated molecular structures and packing geometries. Making sense of these requires insight of the polymer microstructure on both molecular and macroscopic length scales, and how different geometric conformations can change the electronic structure of the polymer.[108, 109] This remains the biggest challenge in the field, since a meaningful structural probe can be hard to identify; particularly for more disordered materials.[110]

4.1.1 Structural order and charge transport

Using poly(3-hexylthiophene-2,5-diyl) (P3HT) as an example of a semicrystalline film, its high hole mobility of up to 0.1 cm^2/Vs[111, 112] is achieved due to a microstructure which facilitates good transport in the π-π stacking direction in addition to along the π-conjugated system of a single polymer chain.[77] With only 'on-chain' transport, the mobility is reduced to $\sim 10^{-4}$ cm^2/Vs. More generally, to achieve high mobilities in disordered polymers, charges must be conducted both along and between polymer chains. In semicrystalline materials, this requires transport between high mobility crystalline domains, where increased delocalisation allows charges to cross between chains with a low energetic barrier. Therefore, improvements can be made by increasing

the molecular weight of the polymer,[113] which can increase the size of the crystalline domains with appropriate solution processing, and increase the number of crystallites bridged by a single polymer chain.

In the limit that these crystalline domains are smallest; and comprise interacting segments of only two chains, the polymer is described as amorphous. Poly(indacenodithiophene-*alt*-benzothiadiazole) (IDT-BT) is an example of such a material, and a very high hole mobility in the direction of the π-conjugated system affords delocalisation over long distances in one dimension.[27] Such good transport, even in a single direction, relies on a low degree of electronic localisation, or trapping, due to microstates with misaligned energy levels. Since each conformation maps to a specific energy level, a low degree of energetic disorder, or a narrow density of states (DOS) implies only a small distribution of structural microstates at any one time. While most amorphous polymers typically have a high degree of energetic disorder,[80] IDT-BT is shown to have a trap density (or broadening of the DOS) among the lowest for any polymer, as described by its low Urbach energy $E_{\mathrm{U}} = 25$ meV.[27] For the extreme case that these 'crystalline domains' involve only two adjacent chains, they are better described as 'close contact points' where the transfer integral for charge-carrier hopping becomes large at points where the respective π-wavefuctions mix.

The important work of Salleo and coworkers attempts to reconcile these two extremes via a paracrystallinity parameter, which is defined by the standard deviation in the local static crystal lattice spacings probability density function.[80] In the case of IDT-BT, it is unclear precisely how paracrystalline the material is, or perhaps to what extent this model accurately describes the physics of disordered polymers. Indeed, numerous other structurally disordered materials with high mobility have been reported[114–118] which rely heavily on backbone rigidity[110, 119] and low energetic disorder.[26]

4.1.2 Microstructure and luminescence

State-of-the-art organic light-emitting diodes (OLEDs),[120, 121] organic photovoltaics (OPVs),[122–124] and organic light-emitting field-effect transistors (OLEFETs)[125] typically employ multiple materials and layers which separately optimise photon absorption and emission, charge separation and recombination, or bipolar charge transport.

The external efficiency of such devices is determined by the quantum efficiency (QE) of the constituent processes that occur during operation. Efficient OPVs require fast exciton migration to interfaces.[126] Efficient OLEDs require that the rate of radiative exciton decay is fast compared to the total rate of all non-radiative decay processes.[127] A convenient proxy for the efficiency of this process is the photoluminescence (PL) QE, and efforts to maximise the PLQE of materials are common in the literature.[128–131]

Concurrently, high-mobility amorphous polymers have attracted significant attention owing to the tunability of the energy gap,[132–134] high solubility,[134, 135] and operational stability,[135, 136] despite lacking long-range crystalline order.[26, 27, 117] Recently, a family of donor-*co*-acceptor polymers; indacenodithiophene-*alt*-benzothiadiazole (IDT-BT), has been shown to have disorder-free MOSFET-like transport and field-effect mobilities exceeding 2 cm^2/Vs at room-temperature, owing to a low degree of energetic disorder.[136,137] Such high-mobility materials typically exhibit a very low film PLQE, although precisely why this is the case is poorly understood. IDT-BT derivatives could be a model system to understand the interplay between mobility and PLQE. Some applications, including OLEFETs and single-layer OLEDs, rely directly on materials that combine a high PLQE with a high charge-carrier mobility.[138,139] Recent strategies to circumvent the problem of low PLQE in these polymers enlist low concentration doping with high PLQE emitters for fluorescence,[140] and capitalise on the typically large exciton diffusion coefficient in high-mobility polymers.

Polymers in the donor-*alt*-acceptor family tend to exhibit a relatively low energy gap. This is due to a strong internal charge-transfer (ICT) absorption between fused donor and acceptor moieties.[141, 142] The energy gap law links low PLQEs to low energy gaps, as strong wavefunction overlap (which decreases with increasing energy gap) of excited- and ground-states leads to fast non-radative decay in low-bandgap systems.[143] Additional non-radiative pathways arise from intermolecular coupling. These include energy transfer to weakly-luminescent excitonic species - either intermolecular themselves, or stabilised by environments with a higher dielectric constant,[37] which can be provided by chain packing. Inter-system crossing is also possible, and relies on proximity of multiple chromophores in some materials.[144] Internal conversion is also possible when potential energy surfaces intersect,[145, 146] leading to competing non-radiative pathways from the excited surface to the ground-state.[147] In general, this is thermally activated, and sometimes referred to as the thermally-accessible

Marcus-inverted intersection.[148, 149] The efficiency of these pathways, and hence their quantum yields, depend heavily on the inter-chain coupling strength.[150]

4.2 Introduction

In this chapter we compare the mobility of various materials in the IDT-BT family with their optical and structural properties. The difficulty of this is two-fold. Firstly, accurate measurement of the mobility from thin-film transistors (TFTs) - as described in Section 3.2.3 - can be challenging; in particular, the interpretation of data which deviates from the ideal MOSFET formulation. However, a comprehensive optimisation of our devices gives us confidence in our results. Below, we present a sketch of this optimisation for a particular IDT-BT derivative. Secondly, for amorphous polymers, direct measurement of small changes in microstructure is hard to resolve with bulk-sensitive X-ray crystallographic techniques. In this chapter, we focus on sensitive steady-state spectroscopic techniques and time-resolved photoluminescence measurements alongside X-ray crystallography measurements and density functional theory (DFT) calculations to probe the packing microstructure and degree of energetic disorder. Using this framework, we evaluate the benefit of sidechain substitution, backbone elongation, the degree of donor-acceptor character, and torsional rigidity on the mobility for this family of amorphous donor-acceptor polymers.

4.3 Sidechain substitution of IDT-BT

In this chapter, we analyse polymers in the IDT-BT family, whose backbone is shown in Figure 3.1. In particular, we delineate between the well-documented IDT-BT derivative with *n*-hexadecyl sidechains: $(C_{16}H_{33})_4$IDT-BT (hereunder C_{16}IDT-BT),[151] and another derivative with *p*-hexadecylbenzyl sidechains: $(C_6H_4\text{-}C_{16}H_{33})_4$IDT-BT (hereunder Ph$C_{16}$IDT-BT). The structures of these two derivatives are also shown explicitly in Figure 5.1.

Owing to the benzyl group close to the backbone, we expect two major differences. Firstly, we expect the degree of sterical hindrance due to the sidechain to inhibit packing of polymer chains in film. However, owing to their tilted configuration in the out-of-backbone-plane direction, we do not expect their own aromatic π-systems to

mix strongly with that of the backbone. Density function theory (DFT) calculations of molecular orbitals (MOs) of a single repeat unit support this assertion, and geometry optimised structures have dihedral angles of $\sim$ 85 $^{\circ}$ between the two π-systems. Concomitantly, we calculate low electron density on the sidechains for both derivatives, particularly in important MOs for charge transport; including the highest occupied (HO) and lowest unoccupied (LU) MOs. The role of sterical hindrance in backbone-backbone coupling is one of the key focuses of this chapter, and we discuss this at length below.

A second consideration involves the environmental stability of the two derivatives. Oxidative cleavage of the sidechains can result in defects on the polymer backbone. Ketone defects in poly(9,9-dioctylfluorene) (PFO),[48] which has a similar chemistry to IDT, lead to decreased transport and a redshifted emission pathway, which can be formed in situ under UV irradiation.[152] Our IDT-BT derivatives are also susceptible to this form of degradation, and we observe that our thin films change in colour from blue to red (and decrease in solubility) with irradiation over time. Qualitatively, we observe that C_{16}IDT-BT degrades much faster timescales than PhC_{16}IDT-BT, and while the mechanism for the degradation of the former most likely involves a S_N1-type reaction (like for PFO[153]), the latter may involve a slower electrophilic aromatic substitution.

4.4 Solution processing

The effects of solution processing on charge transport in TFTs is profound. In order to ensure good transport, an optimised production procedure must first be formulated to ensure reproducibility and meaningful extraction of the field-effect mobility (hereunder, mobility). In this section, we evaluate the importance of solvent choice, molecular weight, and thickness of PhC_{16}IDT-BT films in producing high performance devices.

4.4.1 Choice of solvent

We find that while our polymers were highly soluble in many solvents, the device performance is highly dependent on the solvent choice. Within the set of aromatic solvents in Figure 4.1, high solubility affords very smooth films and highly reproducible

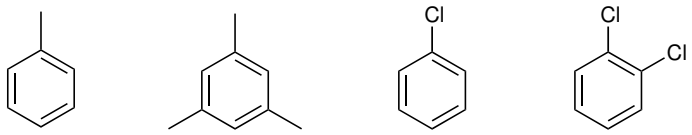

Figure 4.1 Solvents used in study (left to right): toluene (methylbenzene; MB), mesitylene (1,3,5-trimethylbenzene; TMB), chlorobenzene (CB), and 1,2-dichlorobenzene (DCB).

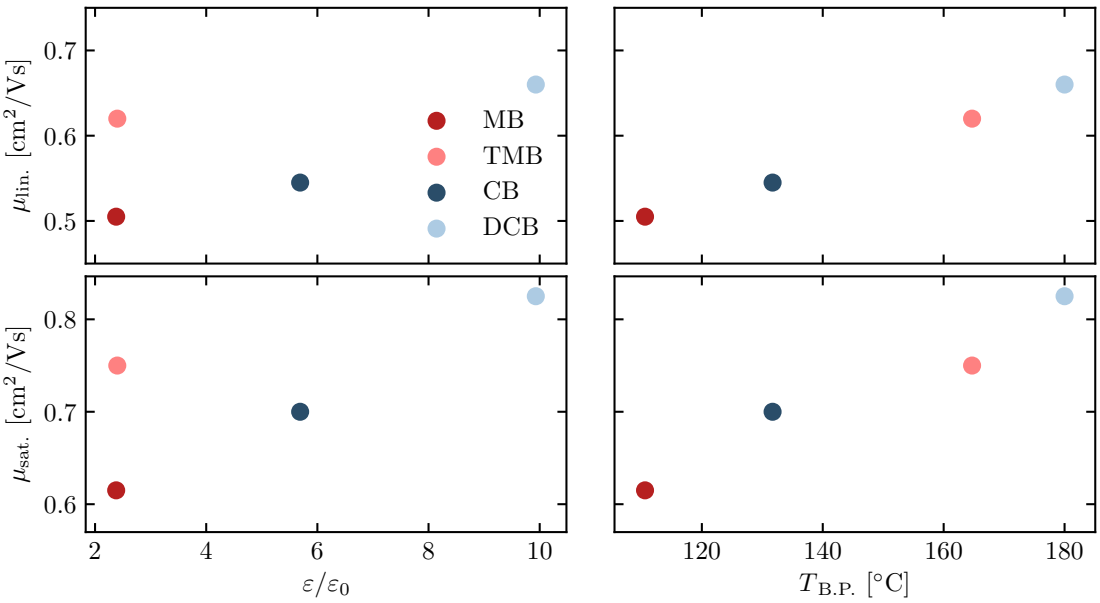

Figure 4.2 Mobility of $PhC_{16}IDT\text{-}BT$, as cast from various solvents: $\mu_{\text{lin.}}$ (top) $\mu_{\text{sat.}}$ (bottom) expressed as a function of the relative permattivity of the solvent (ε_r; left) and its boiling point ($T_{\text{B.P.}}$; right).

devices using $PhC_{16}IDT\text{-}BT$. In Figure 4.2, we parametrise extracted linear and saturation mobilities by the relative permittivity of the solvent and its boiling point. Expressing deviation from MOSFET behaviour as uncertainty in the mobility allows us to quickly identify the reliability of the device and extraction, and this procedure uses Equations 3.3 and 3.4.[1] Strong agreement between the linear and saturation mobility suggests reasonable extraction in good devices.

We see strong correlation between the mobility and solvent boiling point. It has been observed previously that the incorporation of molecular additives - in this case,

[1]In this chapter, where mobility has been expressed with uncertainties, the uncertainty values are extracted in the same way. This methodology, along with the ideal MOSFET equations, is discussed in Section 3.2.3.

solvent molecules - leads to high operational stability in polymer TFTs, particularly for amorphous semiconductors. Nikolka and coworkers argue that displacement of atmospheric species such as water within voids in the polymer microstructure leads to increased and prolonged performance.[136] Concomitantly, evaporation of the solvent molecules from the film allows for water permeation and can lead to increased trapping, lower mobilities, and the suppression of MOSFET-like ideal behaviour. Since the fraction of additive molecules remaining in the film increases with solvent boiling point, we observe increasing mobility and ideality for devices processed with DCB over MB. This highlights the importance of prompt measurement of devices after fabrication.

By contrast, we see only weak correlation between mobility and the dielectric constant of the solvent. Strong dependency of mobility on the dielectric environment has been observed in graphene,[154] but this effect is not important here.

4.4.2 Doping, additives, and anti-solvents

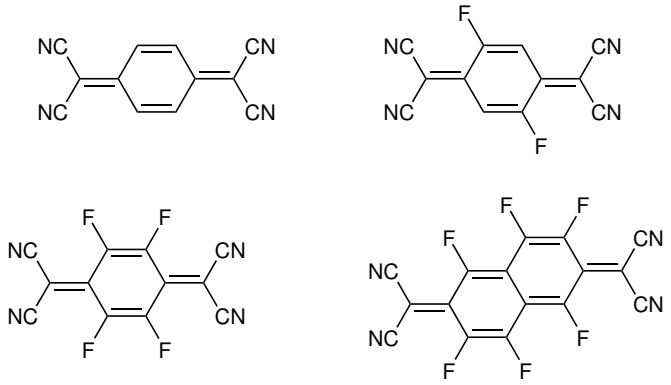

Figure 4.3 Additives used in this study (left to right, top to bottom): TCNQ, F_2-TCNQ, F_4-TCNQ, and F_6-TCNNQ.

For long-term environmental stability, we disperse a solid-phase molecular additive in the polymer film, as described previously.[136] For $PhC_{16}IDT$-BT, we measure a relatively deep HOMO energy of -5.4 eV by ultraviolet photoemission spectroscopy, which means that the small molecules in the TCNQ family (Figure 4.3) are convenient for performing an additive role with tuneable doping. TCNQ has a LUMO of -4.5 eV, and leads to neglibile doping, shown by the low off-current (I_{DS} near $V_{GS} = 0$ V) in Figure 4.4 (left) with a loading of 5 % by weight. F_4-TCNQ has a LUMO of -5.2

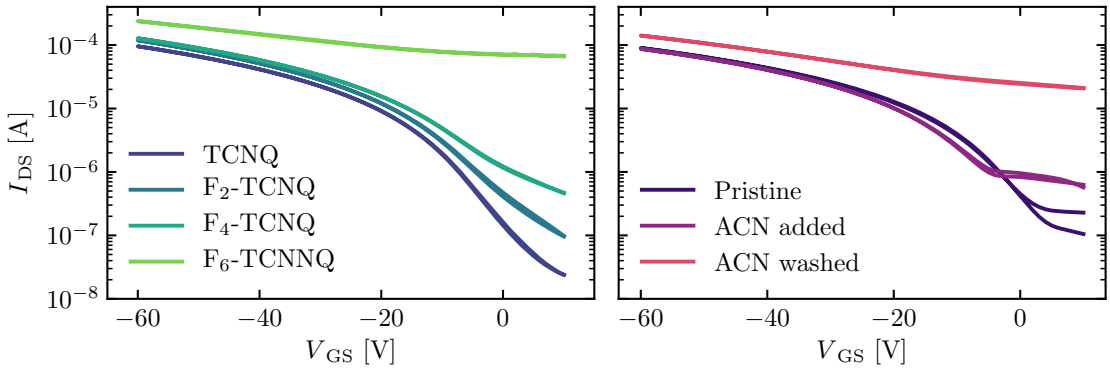

Figure 4.4 Transfer characteristics of $PhC_{16}IDT$-BT in saturation ($V_{DS} = -60$ V) for different additives (left) and ACN processing conditions (right).

eV, and we see stronger doping character with an off-current $\sim 50\times$ higher at the same loading. Finally, F_6-TCNNQ has a deeper LUMO of −5.4 eV,[155] and very strong doping leads to a conductive FET channel at the same loading. While it is not the primary focus of this chapter, we note that all of these devices retain a high environmental stability on the order of months.

We also consider the extra solvent molecular additives to improve device performance. Using acetonitrile (ACN, $T_{B.P.} = 82$ °C) in which IDT-BT derivatives have poor solubility, we (i) add small volumes of ACN to the polymer DCB precursor solution, and (ii) washed the polymer surface with ACN before spin-drying, and compared these with a pristine device in Figure 4.4 (right). We observe that treatment with ACN leads to an increase in the off-current consistent with doping, but ACN cannot itself participate in p-type (n-type) doping due to its high LUMO (deep HOMO) of 1.1 eV (−8.7 eV) as suggested by DFT results. We observe separately that spin-casting similar polymers from poor solvents such as tetrahydrofuran - giving unfavourable aggregation in films - can also lead to high off-currents. We therefore attribute this behaviour to a partial (but poor) solubility of $PhC_{16}IDT$-BT in ACN. This explanation is consistent with an increased threshold potential compared to the pristine device for the sample with ACN added, and modulation of the microstructure at the interface and accumulation region upon washing with ACN, where top-gated OFETs are particularly sensitive.

4.4.3 Choice of polymer molecular weight

Table 4.1 Molecular weight dependence of mobility in $PhC_{16}IDT$-BT.

Fraction	$\mu_{lin.}$ [cm^2/Vs] ($r_{lin.}$)	$\mu_{sat.}$ [cm^2/Vs] ($r_{sat.}$)
1	0.61 (0.60)	0.63 (0.57)
2	0.62 (0.61)	0.63 (0.62)
$5-11$	0.71 (0.55)	0.72 (0.62)
Tail	0.22 (0.29)	0.17 (0.20)

In Table 4.1, we compare the mobility and ideality of different molecular weight fractions separated by gel permeation chromatography. Polymer chains with the shortest elution times are on average shorter in length, and have a low molecular weight compared with longer chains, which have a higher molecular weight, and whose path through the gel column is therefore impeded to a greater degree. The lowest molecular weight samples (eluted in fractions 1 and 2) have suppressed mobilities, and greater relative deviation from MOSFET-like ideality compared to the higher molecular weight fractions ($5-11$). Therefore, we see marginal improvement of the mobility with increasing molecular weight of the polymer chain molecular weight. The origin of this is unclear, but this behaviour is similar to semicrystalline polymers where chains have a high degree of polymerisation.[156–158] On the one hand, this may be explained by the model proposed by Salleo and coworkers for semicrystalline materials; where the mobility no longer increases with chain polymerisation because the paracrystallinity tends to saturate at high molecular weights.[80] On the other hand, perhaps this behaviour requires a more amorphous picture, and the rate-limiting step in charge conduction is the barrier to hopping between chains, which increased polymerisation does little to help. By comparison, the tail fraction has the lowest mobility and most profound deviation from ideal behaviour in saturation since it is likely to contain both the highest molecular weight chains and also any impurities with longer elution times.

4.4.4 Choice of polymer thickness

We observe a dependency of mobility on the thickness of the polymer layer. With thicker polymer films, the device performance increases monotonically between $< 5-35$ nm, with the mobility increasing by $> 2\times$, and deviation from MOSFET-like ideality decreasing to ~ 5 %. The mobility is extracted saturation, and summarised in

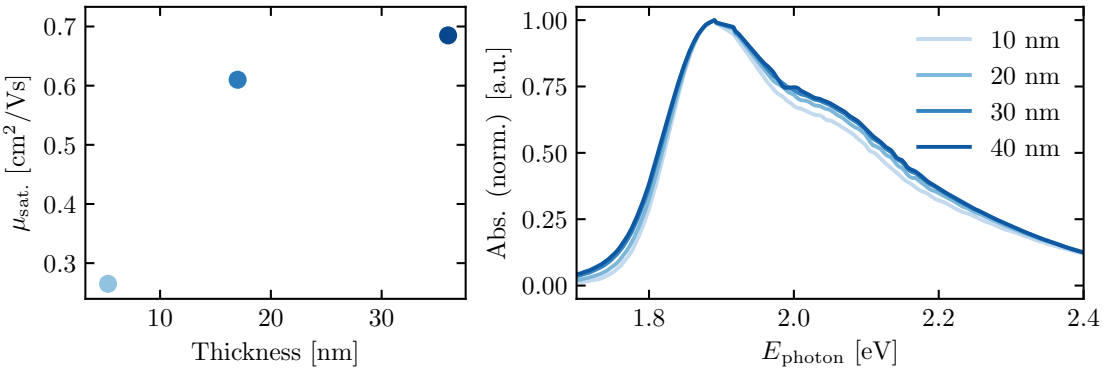

Figure 4.5 Thickness dependence of $PhC_{16}IDT$-BT on the mobility (left) and abor-bance spectra (right).

Figure 4.5 (left). The thickness of the polymer is determined using ellipsometry, and applying Cauchy's equations for reflection from a transparent surface[159] as described previously.[160, 161] We attribute this difference to a thickness dependent morphology at the dielectric interface in our top-gated TFT devices.

Scattering-corrected absorption spectra of films of various thicknesses, shown in Figure 4.5 (right), support this hypothesis: the absorption spectrum of donor-acceptor polymers is dominated by the low bandgap transition to an internal charge transfer (ICT) species.[162, 163] Owing to its chemistry, this behaves largely as a J-aggregate,[38] and has a vibronic progression with decreasing intensity at higher energies. The absorption shoulder at 2.05 eV arises from the $S_1(\nu = 0) \rightarrow S_0(\nu = 1)$ (hereunder 0-1) vibronic transition.[2] With increasing thickness, the intensity of the 0-1 increases relative to the 0-0 transition, suggesting a greater degree of H-aggregation for polymer chains further away from the substrate, which may be mediated by a more face-on correlation of polymer chains. Such a microstructure leads to higher mobilities and more ideal behaviour.

4.5 Tuning microstructure by annealing

The ability to tune the polymer microstructure is powerful, and may lead to improved charge transport. In this section, we investigate the relationship between annealing

[2]The nomenclature $S_m(\nu = n)$ is used to denote the nth vibrational quantum overtone in the mth highest singlet potential energy surface.

and structural changes in morphology of $PhC_{16}IDT$-BT, and how this correlates to transport. We consider both (i) conventional X-ray scattering techniques and (ii) time-resolved photoluminescence (PL) spectroscopy for a more sensitive microscopic probe of inter-chain interactions.

4.5.1 Correlating average microstructure with mobility

In Figure 4.7 (left) we compare the mobility (top) and contact resistance (bottom) of $PhC_{16}IDT$-BT devices. We observe that the extracted mobility decreases with increasing annealing temperature ($T_{\text{ann.}}$). However, due to deviation from ideal behaviour particularly in saturation, robust extraction of mobility with $T_{\text{ann.}} \geq 200$ °C is not possible. We attribute this behaviour largely to an evaporation of the solvent in the thin film, leading to the decreased performance discussed earlier in Section 4.4.1, since thermal degradation is negligible in this range. The temperature at which degradation is appreciable is $T_{\text{ann.}} > 300$ °C, as determined by a tandem differential scanning calorimetry and thermogravimetric analysis measurement, shown in Figure 4.6. Here the loss of mass is negligible until this point, and the heat flow is constant, indicating no phase transitions.

Consistent with this, the threshold voltage increases monotonically in this series to -25 V for $T_{\text{ann.}} = 300$ °C. Effort was made to decouple the solvent effect from measurement of the true mobility, and devices (with semiconductor thickness of 25 nm) were cast from a high boiling-point solvent (DCB; $T_{\text{B.P.}} = 182$ °C) had short anneal times (4 mins.).[3]

Annealing with $T_{\text{ann.}} \leq 100$ °C gives good devices. Nonetheless, we observe a decrease in mobility (in both linear and saturation regimes) between samples annealed at 25 and 100 °C, shown in Figure 4.7 (top left). Concomitantly, a proportional decrease in the saturated on-current (I_{DS} at $V_{\text{GS}} = V_{\text{DS}} = -60$ V) is observed in the output characteristic (bottom left). Since $T_{\text{B.P.}} \gg T_{\text{ann.}} = 100$ °C, we do not expect significant evaporation of the solvent from the film; supported by only a marginal change to the reliability of the device. Therefore, we conclude that the reduction in mobility observed upon annealing below 100 °C is instead due to the changing

[3]We also considered TCNQ as an additive for this comparison, although decreased device stability and changes in film morphology suggest aggregation of TCNQ upon high temperature annealing.

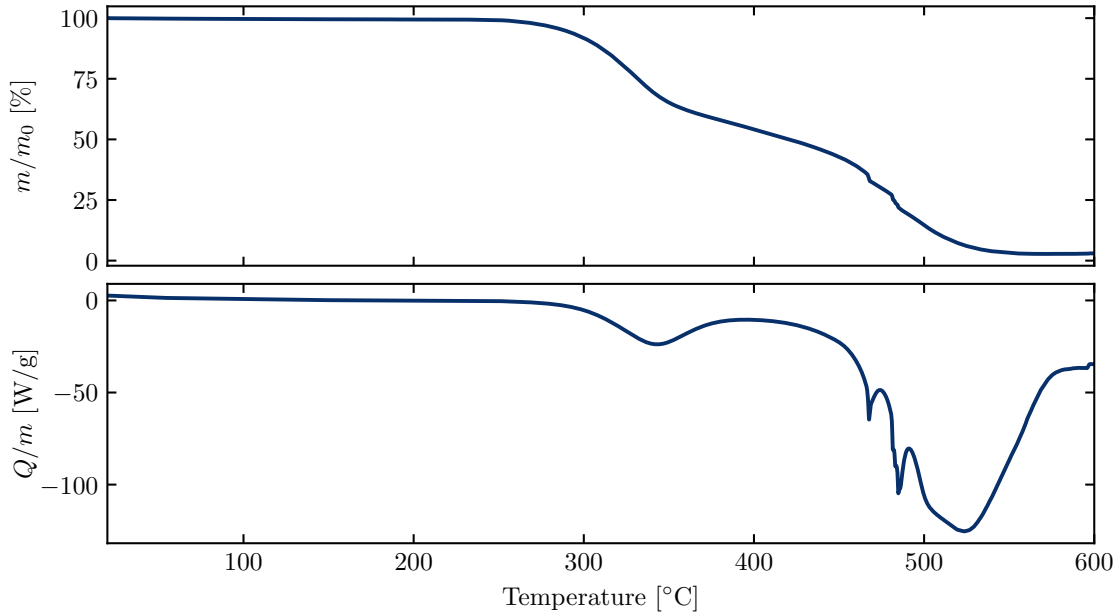

Figure 4.6 Tandem thermogravimetric analysis (top) and differential scanning calorimetry (bottom) for a $PhC_{16}IDT$-BT powder sample.

microstructure. Annealing with $T_{\text{ann.}} \geq 200$ °C gives poor devices. We observe a large contact resistance leading to unfavourable sigmoidal character in the output curves at the same accumulation (V_{GS}). This decreases the on-current in saturation, and leads to an underestimation of the real mobility.

With the same annealing conditions, we observed a systematic change to the packing microstructure. Using X-ray diffraction (XRD) to probe the out-of-(substrate-)plane (z) direction, we find that annealing leads to the formation of a peak around $q_z = 0.26$ Å^{-1} ($d_z = 3.8$ Å) with increasingly strong intensity at higher temperatures up to 250 °C. This is shown in Figure 4.7 (top right). This agrees well with the picture presented by Zhang and coworkers for $C_{16}IDT$-BT of a persisting out-of-plane packing motif involving a backbone tilted with respect to the substrate[137] and we therefore assign this to the (100) reflection. The uniformity of this structural motif increases as this peak grows with annealing temperature. By 300 °C, the polymer melts, adopting a more edge-on and less tilted configuration (with decreased crystalline strain) with a (narrower) peak at $q_z = 0.24$ Å^{-1} ($d_z = 4.2$ Å).

However, using grazing incidence wide-angle X-ray scattering (GIWAXS) to probe the in-(substrate-)plane (xy) direction, we do not see a substantial change in the

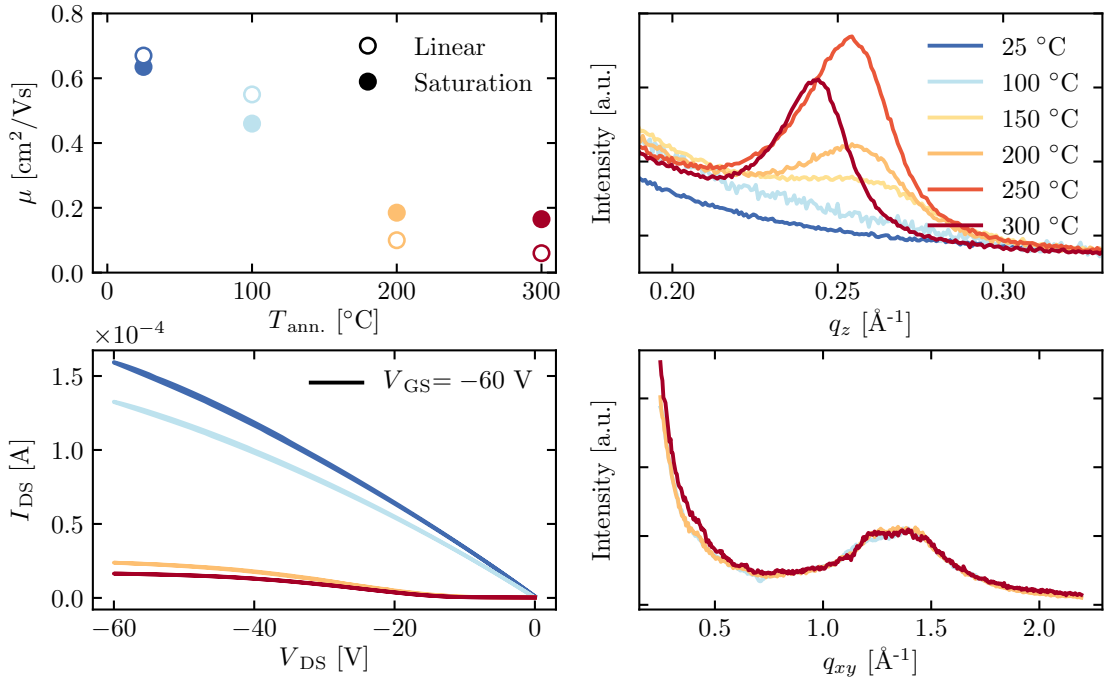

Figure 4.7 Annealing temperature dependency of charge transport (left) and structural properties (right) in PhC$_{16}$IDT-BT. Mobility (top left) and output transconductance (bottom left), normalised XRD (top right) and GIWAXS (bottom right) line-outs. Unlabelled curves have the same colour scale defined in the top left panel.

average structure. This is shown in Figure 4.7 (bottom right). For a full treatment, a more extensive GIWAXS study would be required, but by comparison with published diffractograms for C$_{16}$IDT-BT, we assign reflections with $q_{xy} = 1.2 - 1.6$ to (003) and broad (h10) and (h01) reflections. From the latter, we extract a π-π stacking distance of 0.48 ± 0.4 nm, greater than 0.38 nm for C$_{16}$IDT-BT[137] owing to the bulky sidechains in PhC$_{16}$IDT-BT. Importantly, we did not resolve additional peaks due to macroscopic π-π stacking, even for samples annealed above 300 °C. We conclude that increased order in the out-of-plane direction does not correlate with in-plane order. Macroscopically, polymer chains do not become collinear, and appear to remain largely amorphous in-plane.

4.5.2 Photoluminescence as a structural probe

X-ray structural characterisation is only sensitive to electron densities which are periodic in space.[164] This presents a serious limitation on our ability to carefully study small changes in microstructure in disordered systems. PL spectroscopy

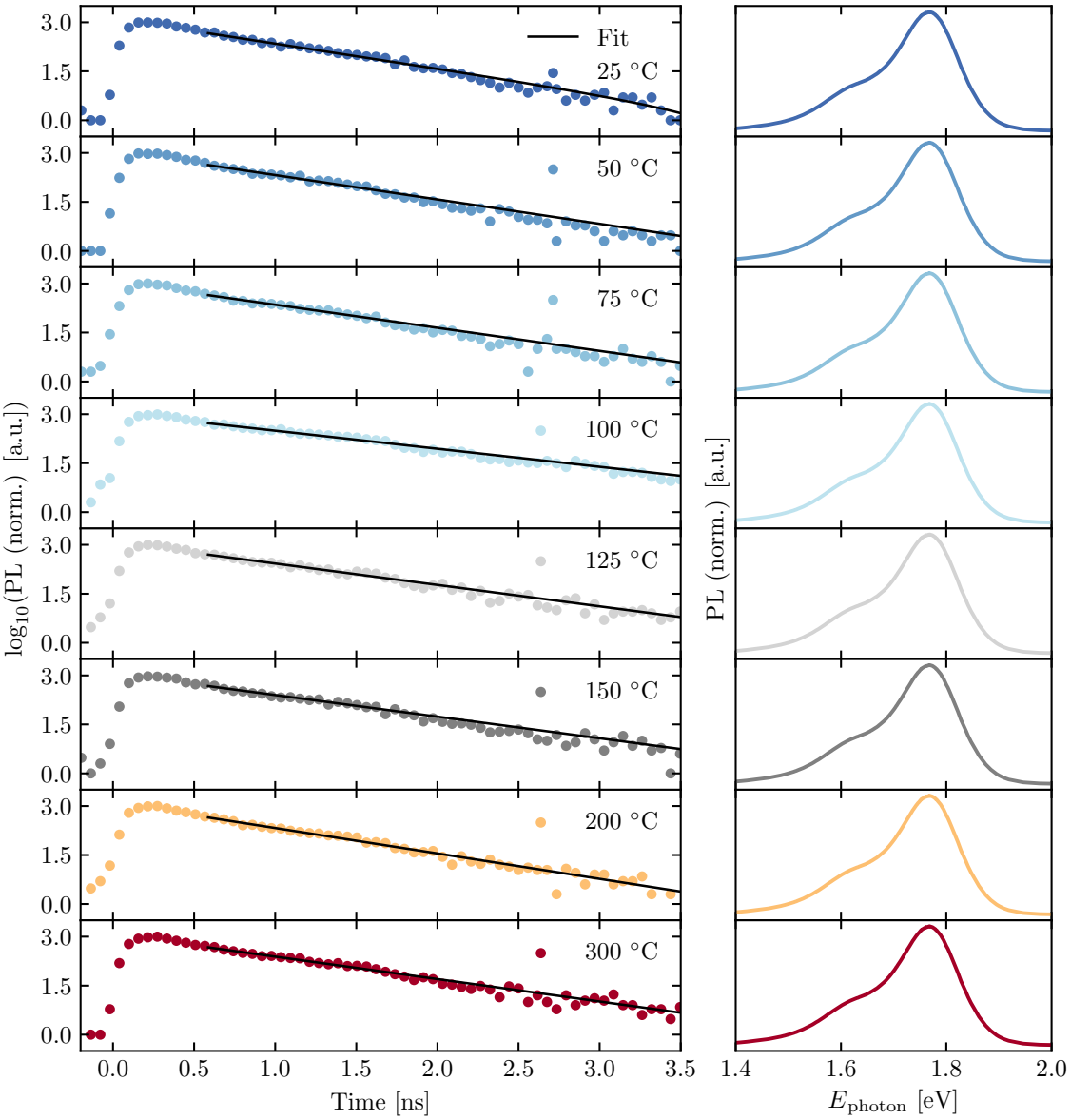

Figure 4.8 Annealing temperature dependency of luminescence decay kinetics (left) spectrum (right) in $PhC_{16}IDT$-BT annealed at different temperatures. Monomolecular fits are also shown (grey).

is more selective. Combining Kasha's rule[165] with the potentially long exciton diffusion lengths (> 10 nm) in organic polymers,[166] we expect excitons to sample large areas of microstates, but emit preferentially from those with the lowest bandgap. Since (i) chain packing typically leads to a lower bandgap, and (ii) the degree and nature of interchain coupling is intimately related to the radiative and non-radiative rates of (exciton) decay, we can use this as a se-

lective probe for the the most aggregated microstructures in otherwise amorphous films.

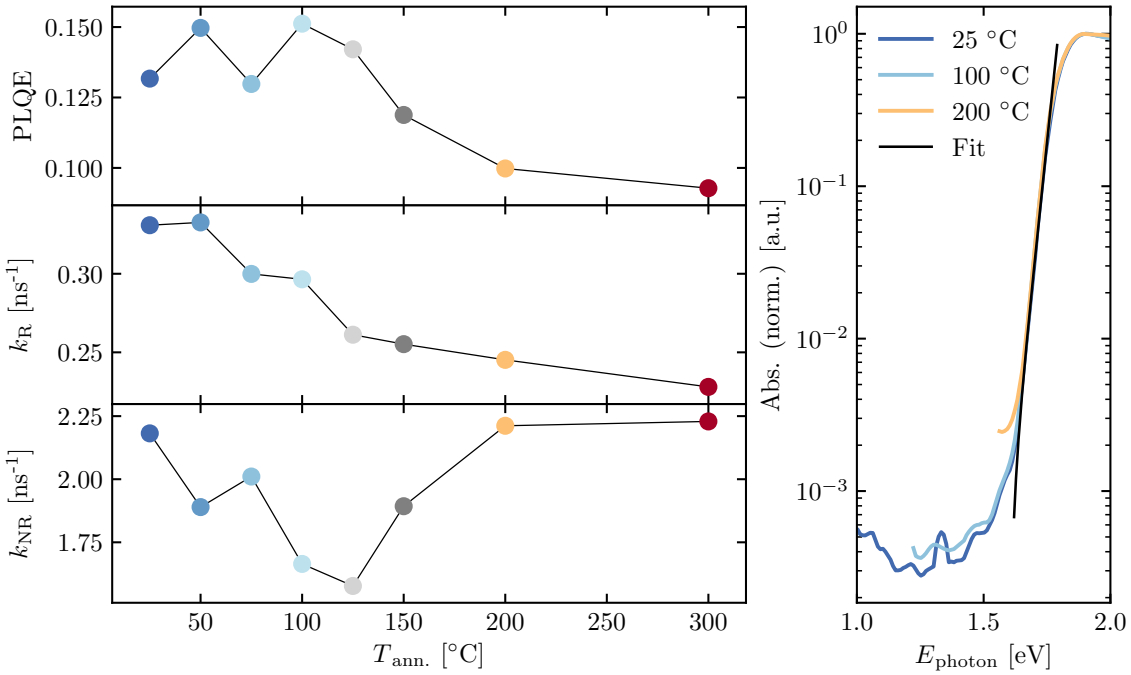

Figure 4.9 Annealing temperature dependency of optical properties in $PhC_{16}IDT$-BT. The optical parameters (left, top to bottom); PLQE, the radiative rate of decay (k_R), and the non-radiative rate of decay (k_{NR}), and the normalised absorption near the band-edge, fit for extraction of the Urbach energy.

To improve our macroscopic picture with microscopic detail, we measure the spectra and decay kinetics of the PL with different annealing temperatures in Figure 4.8. Any spectral differences due to annealing are subtle, however we see a greater change in fitted monomolecular decay rate (k_{PL}). In addition, the PL quantum efficiency (QE) changes with different annealing temperatures, and this is summarised in Figure 4.9 (top left). For annealing between $25 - 125$ °C, the PLQE is high, exceeding 15 % in some cases. However, the PLQE decreases monotonically to < 10 % at higher annealing temperatures. To explain this, we measure the PL decay kinetics to extract the radiative and non-radiative rates of decay, as described in Section 3.3.3.5. These measurements used a low pump fluence (f_{pump}) of 2.5 µJ/cm^2 to determine the decay kinetics, which corresponded to the regime where the response of the material was (nearly) linear with fluence. This idea is discussed at length in the following chapter for this material. Therefore, measurements at lower fluence still did not decrease the

extracted k_{PL} by more than ~ 5 %. This is shown in Figure 4.10.

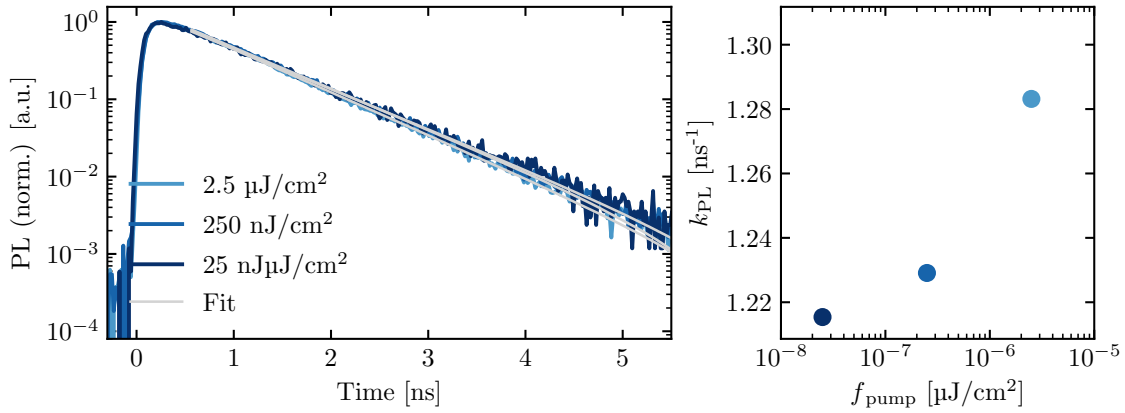

Figure 4.10 Fluence dependence of the PL decay kinetics in $PhC_{16}IDT$-BT near the detection limit: decay kinetics with monomolecular fit (left), and extracted k_{PL} (right).

Both radiative and non-radiative rates (of decay) are highly sensitive to the the nature of chromophore packing. The radiative rate is sensitive to both proximity of chromophores, and the alignment of adjacent transition electric dipole moments. J-aggregates, such as any donor-acceptor polymer chain in isolation, have transition electric dipole moments that stack end-to-end, which leads to an enhancement of the radiative rate of decay.[38] On the other hand, close edge-on packing of polymer chains with parallel transition electric dipole moments, such as in P3HT, can lead to the suppression of the radiative rate. The origin of non-radiative rates can be more unclear to assign, since non-radiative internal conversion can proceed via many different pathways. Briefly, it is thought that close packing of chromophores leads to enhanced non-radiative rates both (i) directly, via additional non-radiative intermolecular quenching pathways and (ii) indirectly since increased exciton delocalisation increases the potency of existing non-radiative quenching sites. This is discussed further in Section 2.3.4.

We determine the radiative and non-radiative rates of decay for each annealing temperature in Figure 4.9 (middle left) and (bottom left) respectively. We find that there are two regimes: (i) for $T_{ann.} \leq 125$ °C, the radiative and non-radiative rates each decrease, but are coupled, leading to an approximately stable PLQE ~ 14 %, and (ii) for $T_{ann.} \geq 150$ °C, radiative and non-radiative rates become decoupled, and as the radiative rate continues to decrease, the non-radiative rate increases, leading to a

decreasing PLQE.

By comparison with crystallographic structural data in Figure 4.7 (top right), we assign these low and high annealing temperature ranges to regimes of gradual and rapid structural changes respectively. In the low-temperature limit, we do not observe a substantial change to the macroscopic out-of-plane crystal structure. However, the reduction of the radiative rate of decay over this range implies a microscopic increase in the H-like aggregation character of chromophores. Importantly, the coupled reduction in the decay rates over this temperature range suggests that the degree of aggregation is approximately constant, but that the nature of the existing aggregation changes to become more H-aggregated. It follows that in this regime, there is no long-range reorganisation of the chains, but chromophores with close contact points modulate their inter-chain geometry to become more face-on on average, while retaining a high degree of structural disorder. Comparison with extracted in-plane mobilities in this range in Figure 4.7 (top left) suggest that this microscopic reorganisation of polymer chains may lead to a small decrease in the observed mobility.

In the high annealing temperature range, crystallography reveals greater out-of-plane structural changes, and chains are both more closely H-aggregated and structurally uniform in the out-of-plane direction. This leads to both a reduction of the radiative rate, consistent with the earlier discussion. Here, we also see a large increase in the non-radiative rate, as additional internal conversion pathways due to increased aggregation become more important. While this may add additional charge carrier transport pathways, we are unable to comment on how structural changes in this regime modulate the mobility.

Finally, the absorption spectrum near the band edge is shown in Figure 4.9 (right) for annealed films. Importantly, there is no observable difference to the energetic disorder of the joint density of states (JDOS) for $T_{\text{ann.}} \leq 200$ °C, and the Urbach energy is constant at 25 ± 2 meV. In all likelihood, the energetic disorder in this polymer arises due to torsion on the backbone,[27] and complementary design of the chemistry of the IDT and BT leads to a high torsion potential about this bridging single bond (from the IDT beta carbon). This implies that the origin of energetic disorder in PhC_{16}IDT-BT is (to an extent) decoupled from its morphology, and that

this polymer is torsionally rigid whatever its microstructure.

4.6 Modulating sidechain chemistry

To investigate the formation of these close crossing points further, we compare the transport and optical properties of sidechain-modulated variants of IDT-BT. It has been shown previously that there is a strong dependency of the transport properties of a polymer on its sidechain length, and that longer alkyl sidechains lead to higher mobilities in IDT-BT FET devices.[167] While this is thought to involve different degrees of aggregation due to differences in solubility, the precise reason behind this observation is unclear. In this section, we compare three IDT-BT derivatives shown in Figure 4.11. For clarity, each IDT-BT derivative is referred to by its sidechain regiochemistry in this section; C_{16}IDT-BT is referred to as 'linear', PhC_{16}IDT-BT is referred to as 'benzyl', and the 3,7,11-trimethyldodecyl derivative is referred to as 'branched'. These each have long sidechains and high solubility, and we anticipate that the aggregation properties of backbones in films are mostly determined by the sterical hindrance conferred by the sidechain, and not small differences in backbone solubility.

4.6.1 Room temperature charge transport

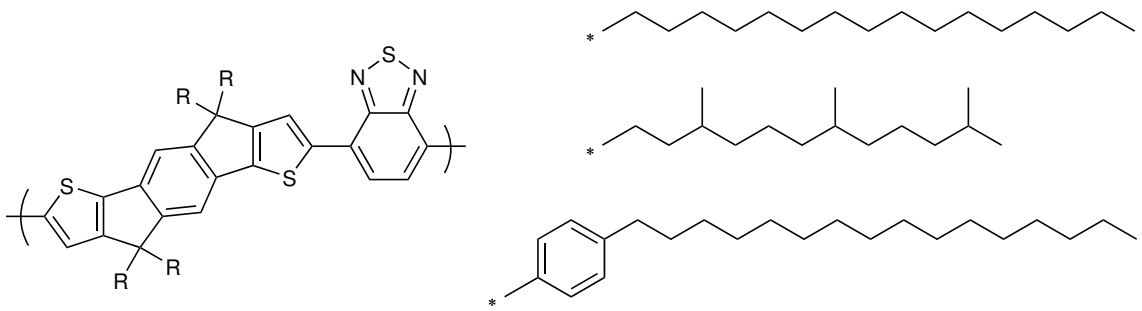

Figure 4.11 IDT-BT backbone structure (left) and sidechains (R; right) used in the study (top to bottom): linear (*n*-hexadecyl), branched (3,7,11-trimethyldodecyl), and benzyl (*p*-hexadecylbenzyl).

The transfer characteristics of devices with the three derivatives are shown in Figure 4.12 in linear (top left) and saturation (centre) regimes with extracted mobility below. Linear IDT-BT devices have largest on-currents $\sim 10^{-4}$ A in the

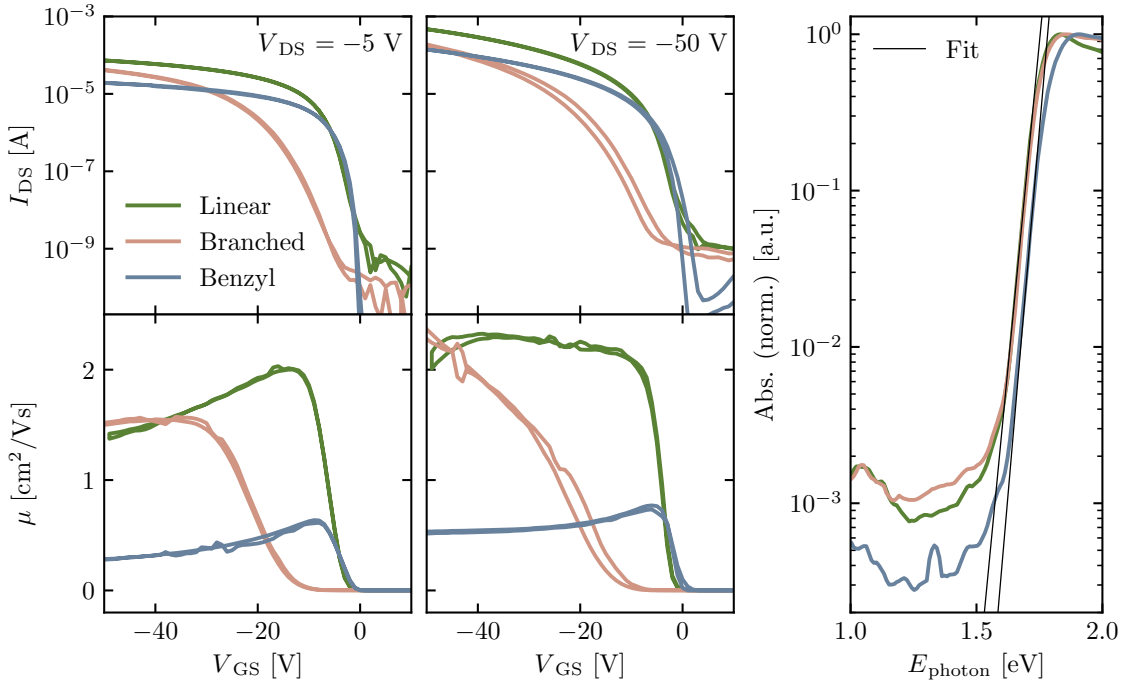

Figure 4.12 Transfer characteristics (top) and mobility extraction (bottom) for sidechain-substituted IDT-BT derivatives in the linear (left) and saturation (centre). Absorption near the band-edge, fit to extract the Urbach energy (right).

linear regime, and approaching $\sim 10^{-3}$ A in saturation. Summarised in Table 4.2, we observe a on:off-current ratio (I_{on}/I_{off}) approaching six orders of magnitude, a low threshold voltage (V_{Th}),[4] and small sub-threshold swing (S).[5] Together with the absence of hysteresis, this indicates good high-performance devices free from trapping, burning, or current crowding effects which might otherwise lead to overestimation of the mobility of the linear IDT-BT. The extraction of the mobility as a function of charge carrier accumulation (V_{GS}) is shown in Figure 4.12 (bottom left and centre). In linear IDT-BT, the measured mobility does not depend on V_{GS} after switching on, indicated by a small fractional uncertainty in the saturation mobility quoted, and there is good agreement between mobility extracted in each V_{DS} regime. A high mobility > 2 cm^2/Vs was therefore extracted for this derivative.

Similarly, in benzyl IDT-BT, good on-currents, low threshold voltages, vanishing hysteresis, and a V_{GS}-independent mobility in saturation imply robust extraction of

[4]Throughout, this is determined in the saturation regime.

[5]Throughout, this is determined in the linear regime, and is defined as the gradient of the $\log(I_{DS}) - V_{GS}$ graph as the device switches on.

Table 4.2 Summary of device parameters for different IDT-BT sidechain derivatives.

Derivative	$\mu_{\text{lin.}}$ [cm^2/Vs] ($r_{\text{lin.}}$)	$\mu_{\text{sat.}}$ [cm^2/Vs] ($r_{\text{sat.}}$)	$I_{\text{on}}/I_{\text{off}}$	V_{Th} [V]	S [V/dec]
Linear	1.71 (0.91)	2.18 (0.92)	$\sim 5 \times 10^5$	-3.51	1.92
Branched	1.48 (0.67)	1.74 (0.59)	$\sim 2 \times 10^5$	-15.3	3.13
Benzyl	0.43 (0.91)	0.61 (0.97)	$\sim 3 \times 10^6$	0.60	0.55

a mobility > 0.5 cm^2/Vs. We attribute the difference observed in mobility between these materials to an increased π-π stacking distance arising from increased sterical hindrance due to the bulky sidechains in the benzyl IDT-BT derivative, and therefore suppressed inter-chain hopping of charge carriers. Notably, for benzyl IDT-BT, a very sharp device turn-on yielded a large $I_{\text{on}}/I_{\text{off}}$ and a smaller S by 4×, which can be attributed to a lower density of charge traps in PhC$_{16}$IDT-BT. Examination of the absorption spectrum in the sub-energy gap regime for these two derivatives in Figure 4.12 (right) reveals that the (normalised) absorption cross section reaches a lower level for PhC$_{16}$IDT-BT. While this may support our picture of decreased trap densities here, it may also arise from a decreased density of doping impurities with broad spectra; consistent with the difference in observed $I_{\text{on}}/I_{\text{off}}$ between the derivatives.

By comparison, branched IDT-BT gives poorer device performance. A large $V_{\text{Th}} \approx -15$ V, larger S, and clockwise hysteresis in saturation all point to a higher trap density than for the other derivatives. Meaningful extraction of the mobility from the saturation regime is challenging due to substantial deviation from MOSFET-like performance. However, the device behaves well in the linear regime, and mobility extracted here is gate-independent well above the threshold voltage. Additionally comparison of the on-currents in the linear regime corroborates the validity of the mobility extraction here, since the branched on-current lies between that of the linear and the benzyl derivatives. Therefore, we conclude that the branched IDT-BT has an intermediate sterical hindrance, and therefore an intermediate mobility, again limited by the ability of charge carriers to hop between adjacent chains. We note that in more crystalline systems, the structural origin of the carrier mobility can often be inferred from in-plane and out-of-plane X-ray scattering measurements, as discussed in the previous section. However here, the high degree of structural disorder - particularly when $T_{\text{ann.}} = 25$ °C and the TFT mobility is highest - makes this conventional analysis highly ambiguous, and was therefore not pursued to a high degree in this work. Much

of this thesis is concerned with finding more appropriate ways to determine important structural parameters.

One such methodology is quantifying the energetic disorder in the joint density of states, and, consistent with our interpretation, we observe in Figure 4.12 (right) that the substitution of sidechains does not make any difference to the observed Urbach energy, $E_{\mathrm{U}} \approx 25$ meV, as determined using Equation 3.6. Since the width of the JDOS arises from disorder in the absorbing chromophores, we conclude that tuning the backbone separation does not modulate the width of the distribution of microstates which broaden the energy gap edge. Instead, as we expect, the Urbach energy arises from the organisation of on-chain chromophores, and may be modulated particularly via torsion between IDT and BT subunits. This is the only (non-cyclic) single bond with rotational freedom in the polymer, and is likely therefore to be unchanged with sidechain substitution.[6]

4.6.2 Temperature dependence of charge transport

To confirm suppressed inter-chain hopping as the mechanism decreasing the mobility in the benzyl IDT-BT, we examine the temperature dependence of various transport parameters. In Figure 4.13 (top left), we measure a benzyl IDT-BT device in saturation between $120 - 300$ K, and the gate voltage dependency of the transconductance is shown from low to high temperatures (from black to yellow). Specifically, we explore the power law dependency of the current (I_{DS}) with carrier accumulation ($-V_{\mathrm{GS}}$) while the device is in saturation ($V_{\mathrm{DS}} = -60$ V). Straight lines in $\log - \log$ plots indicate good fitting to power law relations, and the decreasing gradient when varied between $120 - 300$ K indicates a decrease in the allometric fitting parameter with increasing temperature. While I_{DS} at any given V_{GS} is greater at a higher temperature (indicating a mobility which increases with temperature), the increase in I_{DS} with $|V_{\mathrm{GS}}|$ at a given temperature is smaller if the temperature is greater.

By fitting the relation $I_{\mathrm{DS}} \sim (V_{\mathrm{GS}} - V_{\mathrm{Th}})^{\gamma}$ for $|V_{\mathrm{GS}}| > 20$ V ($|V_{\mathrm{GS}} - V_{\mathrm{Th}}| \gg |V_{\mathrm{DS}}|$), we recover the allometric parameter (γ), and its temperature dependency is shown explicitly in Figure 4.13 (top right). The Vissenberg-Matters model for

[6]The role of backbone spacing in (i) blueshifting the absorption spectrum, and (ii) determining the sub-bandgap features are discussed in the following chapter.

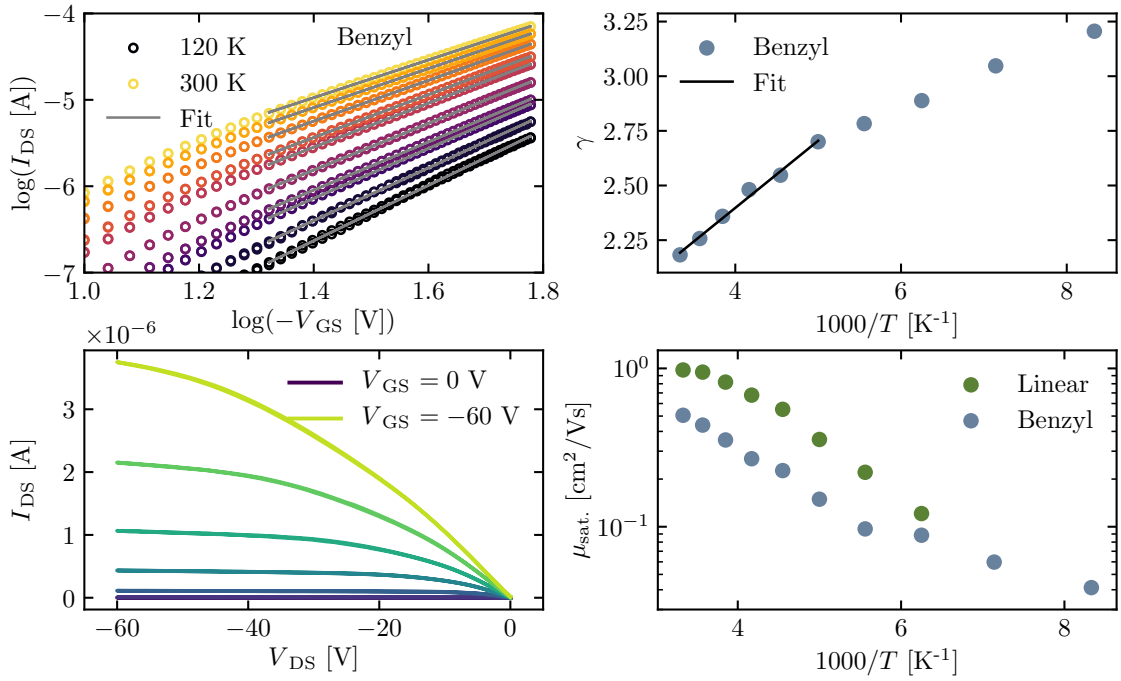

Figure 4.13 Low-temperature transport properties of linear and benzyl IDT-BT. Saturation transconductance characteristics ($V_{DS} = -60$ V) between $120 - 300$ K with 20 K increments and allometric fit (top left), and allometric fitting parameter (γ) at different temperatures, fit to 2D Vissenberg-Matters model near room-temperature (top right). Output transconductance at 120 K with V_{GS} between 0 and -60 V incrementing by -10 V (bottom left) and the temperature-dependency of the mobility extracted in saturation (bottom right).

amorphous organic transistors assumes percolation hopping of charge carriers in a three-dimensional exponential density of states, and requires a temperature dependency of the allometric parameter $\gamma_{VM} = T_0/T$, where T_0 is the characteristic width of the transport DOS.[91] This is discussed in Section 2.4.4. This does not agree well with our results in high temperature limit ($T > 200$ K) where we fit a linear relation (shown) with an intercept of 1.17.[7] Instead, recent work by Brondijk and coworkers show that in the case of charge carrier confinement in very thin semiconductors in (bottom-gated) TFTs, a two-dimensional carrier density profile with an exponential density of states describes the temperature evolution more appropriately: $\gamma_B = T_0/T + 1$.[92] Such a model agrees well with our observations in this system, despite our semiconductor being much thicker. For benzyl IDT-BT,

[7] This also does not explain the low-temperature transport physics observed, since a different fit for $T < 200$ K has an intercept > 1.5.

$T_0 = 307$ K $= 26.5$ meV, which agrees well with $E_U \approx 25$ meV extracted earlier. Just as for its low Urbach energy, benzyl IDT-BT has the amongst the lowest T_0 reported in the literature, compared to poly([N,N'-bis(2-octyldodecyl)-naphthalene-1,4,5,8-bis(dicarboximide)-2,6-diyl]-*alt*-5,5'-(2,2'-bithiophene)) (N2200; 366 K), P3HT (585 K), and poly(2,5-bis(3-tetradecylthiophen-2-yl)thieno[3,2-b]thiophene) (PBTTT; 670 K).[93]

It has been shown separately that linear IDT-BT does not behave in the same way. In work by Venkateshvaran *et al.*, it was observed that $\gamma = 2$ (the value for an ideal MOSFET with a no gate dependency of the mobility) in the range $200 - 300$ K. This is surprising, and implies a very narrow density of states, such that even at 200 K, charge carriers can still access the transport level, and suppressed hopping within the tail of the density of states does not limit the mobility.[27] By comparison, the high-temperature behaviour of benzyl IDT-BT has $\gamma \to 2$, consistent with the extraction of $T_0 > 295$ K.

In order to meaningfully extract the mobility at any given temperature, the output characteristics should show vanishing contact resistance. The contact resistance typically increases at low temperature in non-ideal devices. In Figure 4.13 (bottom left), the output characteristic at the lowest temperature of 120 K is shown. For different hole accumulation between $V_{GS} = 0$ V and $V_{GS} = -60$ V, we see Ohmic contact behaviour about $V_{DS} = 0$ V, and no sigmoidal shape indicative of injection problems. Furthermore, good saturation of I_{DS} suggests robust extraction of the mobility in the saturation regime.

The mobility in saturation is extracted for linear and benzyl IDT-BT FETs, and plotted for different temperatures in Figure 4.13 (bottom right). Both materials exhibit a temperature activated mobility, and fitting of the benzyl IDT-BT trend to an Arrhenius relation; $\mu \sim \exp(-E_A/k_BT)$ yields the 'activation energy' (E_A) or the characteristic energetic barrier to transport. This behaviour may be understood by using the framework of Marcus theory for electron transfer (Section 2.3.4.4), where E_A is the energy where bands intersect ($\Delta E^\dagger$). However, the reliability of E_A as a figure-of-merit to describe the barrier to conduction is limited by poor agreement between high- and low-temperature regimes. Nonetheless, in the high-temperature regime, benzyl IDT-BT has $E_A = 65 \pm 2$ meV. In the low-temperature limit, $E_A < 50$

meV. This behaviour implies that the energetic barrier to conduction in this IDT-BT derivative is small at low temperatures, possibly due to closer structural packing and decreased dynamic disorder below 200 K compared to 300 K. Comparison with γ for $T < 200$ K in Figure 4.13 (top right) supports this picture, and suggests that the geometry adopted by the charge accumulation is changing, consistent with a gradual structural change.

However, for linear IDT-BT, a comparable $E_A = 71 \pm 5$ meV is extracted between $160 - 220$ K. A gradual decrease in the temperature-activated mobility towards room temperature makes a meaningful E_A extraction in the high-temperature limit challenging, particularly since we also expect a similar structural change here. The precise reason for this levelling-off of the saturation mobility is not clear and requires further investigation. Yamashita *et al.* have recently claimed band-like transport[168] and the cross-over between hopping and band-like transport[169] in similar (but crystalline) donor-acceptor materials using a combination of four-point probe and Hall-effect measurements. However, devices in these studies suffer from large threshold voltages and low on-currents, and require better devices (such as in reference [170]) or transient photoconductivity measurements[171] to support this claim. It is possible that here we observe the cross-over between hopping and band-like transport regimes, but various thermal artefacts including those due to Joule heating must be ruled out to confirm this.

4.6.3 Aggregation dependency of morphology

Luminescence can be quenched by strong intermolecular coupling of chomophores. The origin of this can involve increased delocalisation of excitons to quenching sites, the formation of weakly emissive interchain species, or other non-radiative decay pathways arising directly from the packing.[8] In donor-acceptor polymers, increased aggregation typically leads to a lower PLQE. We can therefore use changes in the PLQE to qualitatively describe the degree of inter-chain coupling. In this section, we compare four IDT-BT derivatives, differing only in their sidechain chemistry. These are the three from the previous section, and a shorter variant of the branched derivative (with 2-ethylhexyl sidechains) hereunder referred to as 'short branched'.

[8] We quantitatively compare these pathways in the next chapter, and so they are not discussed in more detail here.

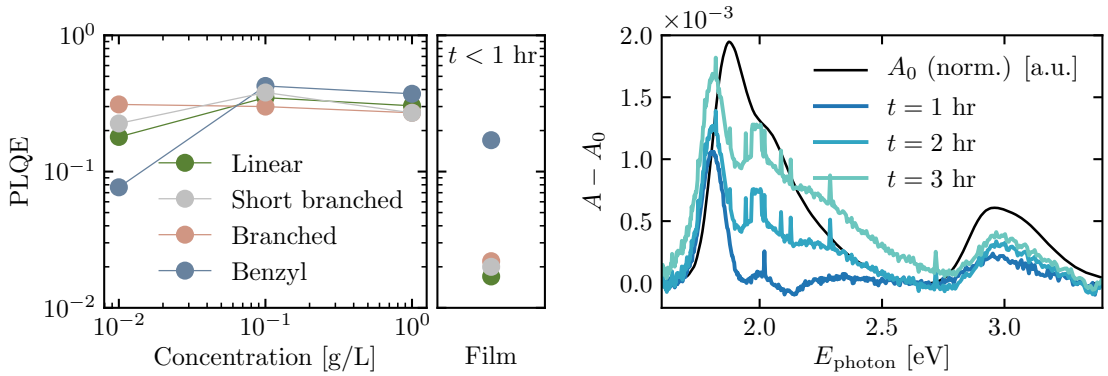

Figure 4.14 The effect of aggregation on the photophysics of IDT-BT. The PLQE at different concentrations in TMB and in film (left), and the differential change in the absorption spectrum of PhC_{16}IDT-BT (right) at different times after spin-casting (blues) with the normalised absorption spectrum (black).

At 0.1 g/L in mesitylene (TMB), the PLQE of benzyl IDT-BT is the highest, and exceeds 0.42, compared to $0.30 - 0.38$ for all other derivatives. This is summarised in Figure 4.14 (left). Since the chromophore for each derivative is identical, this indicates that some aggregation is occurring (even at low concentrations) and that benzyl IDT-BT is least quenched by this aggregation. This is likely to be due to decreased intermolecular interaction for benzyl IDT-BT compared to the branched and linear derivatives, owing to its sterical hindrance close to the backbone. Increasing the concentration to 1 g/L, we observe a reduction in the PLQE for each derivative, consistent with increased aggregation leading to faster non-radiative quenching. While the PLQE of the most sterically hindered (benzyl) IDT-BT decreases from 0.42 to 0.37, the greatest change due to aggregation is observed for short branched IDT-BT which decreases from 0.38 to 0.27. We conclude that this material forms stronger intermolecular interactions at higher concentrations, despite the (mild) sterical hindrance because of the short branched sidechain. This is likely due to its decreased solubility with shorter sidechains compared to the other derivatives.

The film PLQE constitutes the highest concentration of chromophores, and we infer the limit of exciton quenching due to aggregation. To mitigate any differences due to PL out-coupling, effort was made to ensure the films were similar in thickness (30 nm) and surface roughness. The film PLQE for each derivative is lower still than for the highest concentration solution measurement. In the high-aggregation limit, the length of the sidechain does not make a substantial difference to the PLQE, and the short

branched, branched, and linear derivatives (with increasing sidechain length) all have PLQEs in the range $0.017 - 0.022$. However, increasing the degree of sterical hindrance - which decreases the aggregation and aggregation-induced quenching non-radiative decay pathway - increases the PLQE. The film PLQE of benzyl IDT-BT is high, at $0.16 - 0.18$. We conclude that the strategy of sidechain variation, particularly the inclusion of phenyl groups close to the backbone, is very effective at tuning the degree of intermolecular coupling, giving us access to high film PLQEs even in low-bandgap polymers.

The PLQE behaviour below 0.1 g/L is curious. Quadruplicate measurements give us confidence in the decreasing PLQE at very low concentrations. Since mean distance between chromophores in solution ($\langle l \rangle$) scales with concentration as $\langle l \rangle \sim c^{1/3}$, it is possible that with $c = 0.01$ g/L, we enter a regime where chains interact much more weakly, and a greater distribution of geometries (including perhaps increased torsion due to decreased sterical hindrance between chains) leads to additional non-radiative decay pathways. Furthermore, we observe a strong dependency of the solution PLQE on the solvent used, and the PLQE in polar DCB at 0.1 g/L was 0.20 (0.23) for linear (benzyl) IDT-BT, compared to 0.35 (0.42) in mesitylene. Recent studies discuss this phenomenon in comparable systems, and suggest that charge-separated non-emissive intermolecular states - which have a low PLQE - can be stabilised by polar solvents and lead to a reduction in the observed solution PLQE via Kasha's rule.[37] This interpretation is consistent with our results.

Aggregation in IDT-BT derivatives is, to some extent, predetermined by the chemistry of sidechains, and manifests in solution. However, even after spin-casting a film, we observe a systematic change in the absorption spectrum in the following hours. In Figure 4.14 (right), we show the initial absorption spectrum (arbitrarily normalised, black), and the differential change in this spectrum with time (from dark to light blue) of benzyl IDT-BT. While the change is small, on the order of $\sim$ mOD, we observe a redshifted spectrum growing in with time. The lowest energy peak in differential spectrum shows this, and suggests increased exciton delocalisation leading to this redshift. Consistent with this, the peak at 3 eV continues to grow in, and this increasing optical density, indicating stronger oscillator strength and greater wavefunction overlap, is consistent with the picture of increased exciton delocalisation.[172] This implies structural change with time which leads to increased

delocalisation and greater wavefunction overlap. Furthermore, the vibronic shoulders near 2.0 and 2.2 eV increase in relative intensity compared to the lowest energy peak, indicating increasing face-on packing of chromophores leading to H-aggregate character. We reach a similar conclusion earlier when considering the effect of annealing on the radiative rate of decay. We conclude that similar physics is at play here, and that the lowest energy macrostate with greater wavefunction delocalisation - possibly within a more H-aggregated morphology - can require hours to reach after casting an unannealed amorphous polymer film.[9]

4.7 Increasing subunit length

In high mobility amorphous polymers, a low degree of energetic disorder is required for good transport. However, the DOS can be broadened by conformational disorder including torsion.[27] In our donor-acceptor systems, we make use of fused ring systems to planarise each subunit, and minimise the degree of torsion internally. However, there is still some conformational dihedral freedom around the single bond coupling donor and acceptor moieties, but Venkateshvaran *et al.* discuss resilience to torsion by promoting planarising electrostatic interactions between donor and acceptor subunits to lock in a favourable conformation.[173]

A similar strategy involves elongation of the repeating backbone unit to increase the planarised length, in order to decrease the energetic disorder per unit length of backbone. Efforts to elongate the popular IDT donor unit are common in the literature, but have mostly had limited success in achieving high charge-carrier mobilities.[174–178] Recently, however, reports of two elongated IDT-BT analogues have claimed promising mobilities > 1 cm^2/Vs.[179, 180] In this section, we explore backbone elongation as a strategy to improve charge transport in amorphous donor-acceptor polymers, and present a systematic study with comparable materials and appropriate solution processing.

[9] While we expect annealing to expedite this effect, and therefore help prevent further time-evolution of the film microstructure, a more detailed study is required to confirm this.

4.7.1 Polymers with PhC_{16}[Donor]-BT chemistry

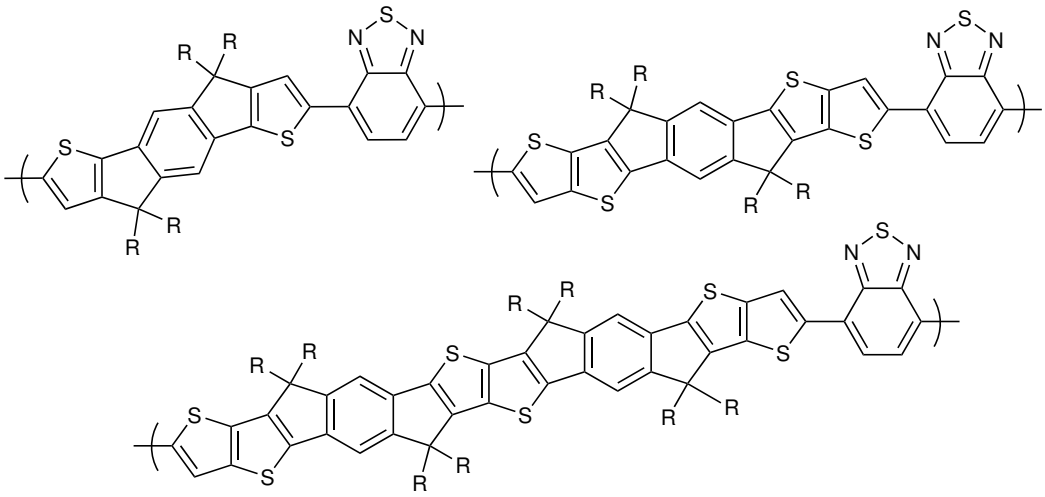

Figure 4.15 PhC_{16}[Donor]-BT polymers in the study: [Donor] = IDT (top left), IDTT (top right), and IDTIDTT (bottom). R = *p*-hexadecylbenzyl.

In Figure 4.15, we show the structures of IDT-BT, IDTT-BT, and IDTIDTT-BT, and we summarise the device performance in Figure 4.16 (top).[10] While IDT-BT and IDTIDTT-BT derivatives are solution processed using CB, poor device performance with a large threshold voltage ($V_{\mathrm{Th}} \approx -25$ V) is observed for the IDTT-BT when processed in the same way. Instead, the same processing except for DCB as the solvent choice yields much better devices. To compare the length of the polymer, we use calculated geometries[11] to estimate the repeat unit lengths of 1.64, 2.04, and 3.05 nm for IDT-BT, IDTT-BT, and IDTIDTT-BT backbones, respectively, while all materials have the same structural motif including torsional plananarity (or a dihedral angle $\theta_{\mathrm{dihed.}} \sim 0\ ^\circ$), and that the (HOMO) LUMO is (de)localised to a similar degree.

Between IDT-BT and IDTT-BT, we observe a modest increase to the mobility, followed by a substantial decrease between IDTT-BT and IDTIDTT-BT. This is summarised in Table 4.3 with other important device parameters. A comparison of the transconductance characteristics between materials in Figure 4.16 (top) shows that the turn-on for IDT-BT is the sharpest. With increasing backbone length, the turn-on becomes less steep (increasing S) and the V_{Th} increases in tandem. This is a clear

[10] This subsection only deals with materials with *p*-hexadecylbenzyl sidechain, and so the name is omitted for brevity.

[11] Our DFT calculation method is described in detail in Section 3.5.

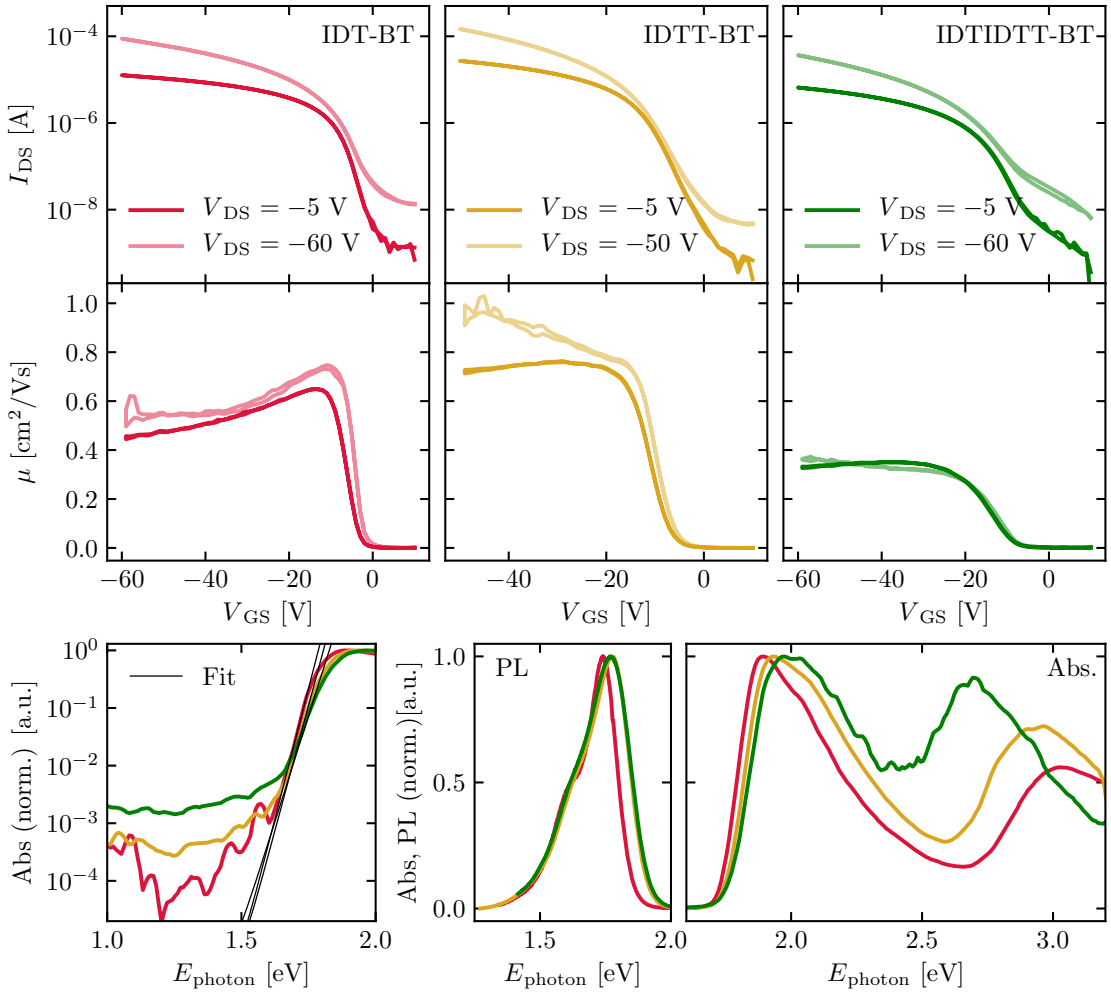

Figure 4.16 Effect of backbone elongation on PhC$_{16}$[Donor]-BT polymers: transfer characteristics in linear (top left) and saturation regimes (top right) with extracted mobility below. Normalised (PDS) absorption spectrum with Urbach extraction (bottom left and right) with the normalised PL spectrum (bottom centre).

indication of increased trapping with donor length in this set, since greater charge densities are required to fill localised states before appreciable conductivities can be measured.

Non-ideal behaviour emerges when comparing the mobility extracted in linear and saturation regimes. For IDT-BT devices, despite having the lowest $|V_{Th}|$ and S, the peak mobility is reached by $V_{GS} = -10$ V and the measured mobility seems to decrease with increased accumulation thereafter. The gated device architecture can lead to

Table 4.3 Summary of device parameters for PhC_{16}[Donor]-BT polymers.

[Donor]	$\mu_{\text{lin.}}$ [cm^2/Vs] ($r_{\text{lin.}}$)	$\mu_{\text{sat.}}$ [cm^2/Vs] ($r_{\text{sat.}}$)	$I_{\text{on}}/I_{\text{off}}$	V_{Th} [V]	S [V/dec]
IDT	0.56 (0.81)	0.64 (0.80)	$\sim 6 \times 10^3$	1.39	3.09
IDTT	0.74 (0.77)	0.86 (0.73)	$\sim 4 \times 10^4$	−6.57	4.42
IDTIDTT	0.34 (0.35)	0.33 (0.32)	$\sim 2 \times 10^3$	−8.75	5.52

a spurious increase in the transconductance, and comparison with ideal MOSFET equations can lead to a overestimation of the mobility.[94] However, by $V_{\text{GS}} = -40$ V, the saturation mobility plateaus, and we have confidence in the extracted mobility. It is for this reason that we report $V_{\text{Th}} > 0$ in this case, despite seeing no mobility at $V_{\text{GS}} = 0$ V. Interestingly, neither IDTT-BT nor IDTIDTT-BT suffer from the same type of injection problem. This discrepancy is most likely owing to the low trap density of IDT-BT compared to the IDTT-BT and IDTIDTT-BT, together with its marginally higher off-current; which may arise from impurity doping.

In the case of some polymers, the current in saturation increases as $I_{\text{DS}} \sim (V_{\text{GS}} - I_{\text{Th}})^{\gamma}$ where $\gamma > 2$. IDTT-BT behaves in this way, and leads to a saturation mobility which is dependent on accumulation. By itself, this behaviour is predicted within any variable range hopping transport model where a disordered density of states has a width greater than $k_B T$.[85, 91, 181] However, any such model also predicts similar behaviour in the linear regime. Here, the device behaves like an ideal MOSFET in the linear regime. It is worth mentioning that despite extensive solution processing optimisation - including doping the semiconductor - we find that the linear and saturation mobilities are irreconcilable. Furthermore, we observe separately that explicitly 'pinching off' the device channel with $V_{\text{GS}} = V_{\text{DS}}$ for all accumulations makes no difference to the shape of the saturation characteristic. This deviation from ideality summarises our preference for the mobility extraction in the linear regime which is well-behaved.

By comparison, IDTIDTT-BT gives highly ideal devices, allowing for meaningful extraction of the mobility in both regimes with a high degree of certainty. While the on-current exceeds 10^{-5} A, a high V_{Th} and S gives poor on-off switching, leading to a low $I_{\text{on}}/I_{\text{off}} \sim 10^3$.

Even after extracting mobilities with good precision, there is poor correlation between backbone length and mobility in this set. However closer inspection of the optical properties of the polymers in Figure 4.16 (bottom) clarifies this observation. Extraction of the Urbach energy near the absorption edge (left) shows an increasing energetic disorder in the joint density of states from 25 ± 2, to 27 ± 2, to 35 ± 4 meV for IDT-BT, IDTT-BT and IDTIDTT-BT respectively. Concomitantly, the broadness of the PL lineshape (centre) also increases with backbone length, indicating emission from a broader density of emissive microstates. The blueshift of the peak of this feature results directly from the increasing bandgap (right). We conclude that while increasing the backbone length can result in a higher mobility (in the case of IDTT-BT), this is unlikely to proceed from the suppression of torsion, since energetic disorder (in the JDOS) also increases with backbone length. Therefore, the trend in mobility we see with backbone length is likely to balance some underlying benefit received by increasing the backbone length, and the concomitant increase in the energetic disorder.

To elucidate the origin of the positive effect of increasing backbone length, we consider the sterical effects of the sidechains. As discussed earlier, since amorphous polymers do not have extended regions of strong interchain π-π interaction, they rely heavily on close contact points between chains for charges to hop with a low energetic barrier. Here our donors each have bulky *p*-hexadecylbenzyl sidechain substitutions close to the backbone, so we expect this system to be highly susceptible to changes in the sterical environment. If instead of considering the absolute length of the backbone repeat-unit, we consider the density of sidechains per unit backbone length, we recover that IDTIDTT-BT is the most sterically hindered polymer per unit length, followed by IDT-BT, then IDTT-BT, and this correlates well with the trend in extracted mobility. We propose that there is a compromise between an increased energetic disorder in longer chains and the degree of sterical hindrance conferred by the sidechain density; in bulky PhC_{16}[Donor]-BT polymers, this leads to an improved mobility for IDTT-BT.

4.7.2 Polymers with C_{16}[Donor]-BT chemistry

To explore this sterical hindrance argument further, we compare two polymers of different backbone length which have less bulky *n*-hexydecyl sidechains on the donor.

In Figure 4.17, we show the structure of IDT-BT and backbone-extended TIF-BT.[12] By insertion of aromatic 6-membered rings between the terminal thiophene and the unconjugated 5-membered rings, the backbone length is increased from 1.64 to 2.12 nm, as determined by DFT. This gives very different transport and optical properties, and these are summarised in Figure 4.18.

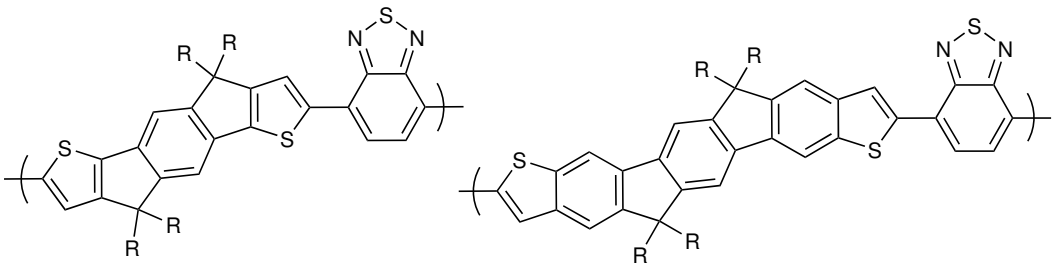

Figure 4.17 C_{16}[Donor]-BT polymers in the study (left to right): [Donor] = IDT, and TIF. R = *n*-hexadecyl.

Table 4.4 Summary of device parameters for different C_{16}[Donor]-BT polymers.

[Donor]	$\mu_{\text{lin.}}$ [cm^2/Vs] ($r_{\text{lin.}}$)	$\mu_{\text{sat.}}$ [cm^2/Vs] ($r_{\text{sat.}}$)	$I_{\text{on}}/I_{\text{off}}$	V_{Th} [V]	S [V/dec]
IDT	1.61 (0.89)	2.02 (0.84)	$\sim 4 \times 10^5$	−4.89	2.16
TIF	2.84 (0.81)	3.56 (0.68)	$\sim 5 \times 10^7$	−6.50	1.25

For IDT-BT, the transport is similar to that demonstrated earlier. High on-currents approaching $\sim 10^{-3}$ A indicate a high mobility (summarised in Table 4.4), and a good $I_{\text{on}}/I_{\text{off}} \sim 10^5$. A low degree of trapping gives a small V_{Th} and S and extraction of the mobility in linear and saturation regimes yields good agreement with one another and with ideal MOSFET equations. By comparison, TIF-BT is less well behaved in transistors, but very high on-current $\sim 10^{-3}$, an exceedingly large $I_{\text{on}}/I_{\text{off}}$, and a comparably small S indicate the absence of trapping, and suggest a mobility even higher than for IDT-BT. Extraction of the mobility in the linear regime is negatively affected by a barrier to injection presented by contact resistance. Therefore, we anticipate a slight overestimation of mobility extracted in the linear regime, giving us an upper bound on the true TIF-BT mobility.

[12]This subsection only deals with materials with *n*-hexadecyl sidechain, and so the name of the sidechain is omitted for brevity.

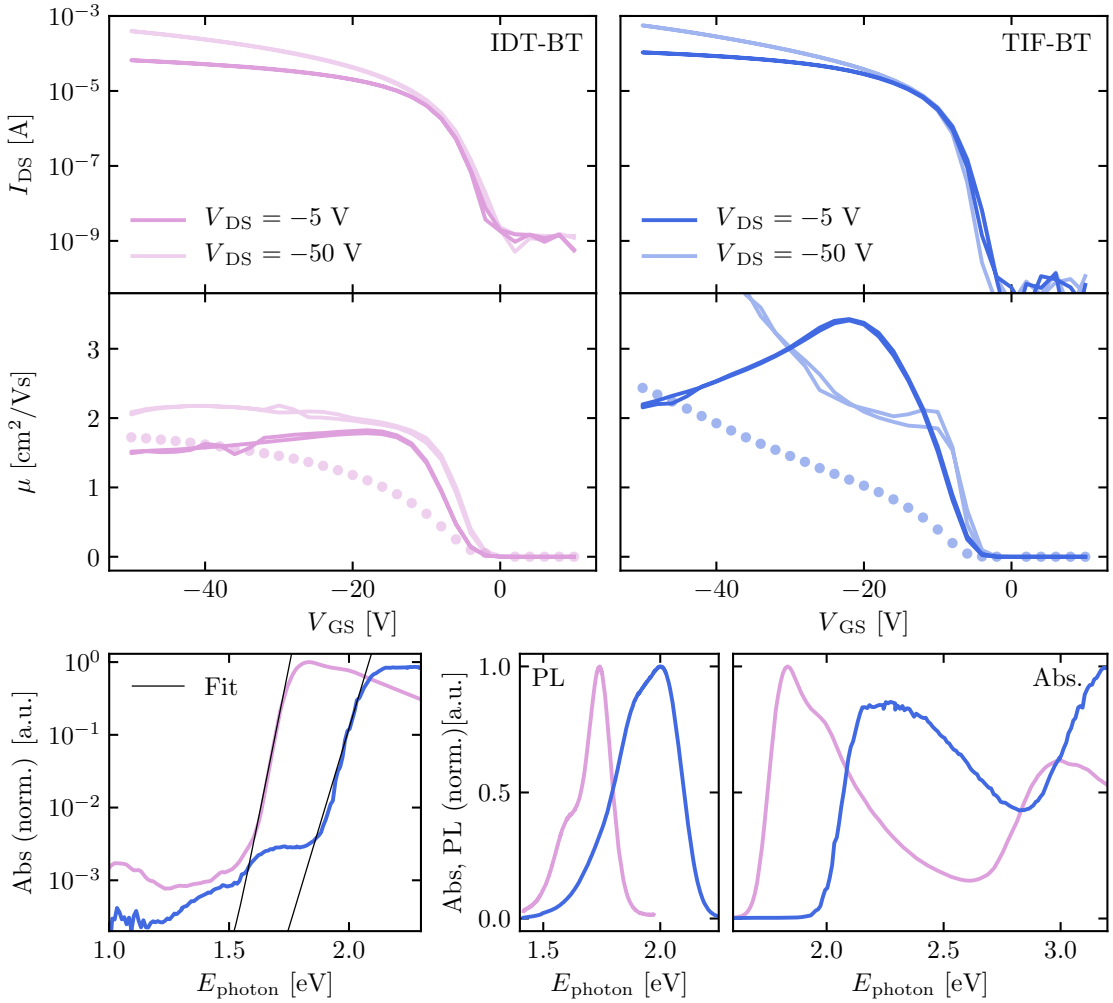

Figure 4.18 Effect of backbone elongation on C_{16}[Donor]-BT polymers: transfer characteristics in linear (top left) and saturation regimes (top right) with extracted mobility below ('instantaneous' mobility as circles). Normalised (PDS) absorption spectrum (bottom left and right) with the normalised PL spectrum (bottom centre).

We note that TIF-BT also has $\gamma > 2$ non-ideal behaviour in the saturation regime, making a precise extraction of V_{Th} challenging. In any case, a conservatively estimated V_{Th} is greater for TIF-BT than IDT-BT. This may be due to various difficulties encountered with this polymer including a deep ionisation potential of -5.7 eV and the low environmental device stability discussed by Chen and coworkers.[180] A meaningful extraction of the true saturation mobility is also challenging, since the mobility deviates substantially from the ideal equations. Instead, faced by the same non-ideal behaviour, Chen *et al.* calculate a lower-bound on the saturation mobility by

assuming a negligible threshold voltage and determine the 'instantaneous' mobility implied by the current (I_{DS}) at a single accumulation (V_{GS}). To do this, we use the one-to-one mapping of ($I_{\mathrm{DS}}, V_{\mathrm{GS}}$) tuples to $\mu_{\mathrm{sat.}}$ via the MOSFET Equation 2.33, and this methodology is discussed further in Section 3.2.3. We show this extraction as dots in the mobility plots of Figure 4.18. These dots are a lower bound on the real mobility. Therefore, at $V_{\mathrm{GS}} = -50$ V we conclude that $\mu_{\mathrm{sat.}} > 2.4$ cm^2/Vs, and the mobility of TIF-BT exceeds that of IDT-BT.

Consistent with our earlier observations, the energetic disorder in the JDOS increases with backbone length. This is what we expect, and can be thought of in two ways: (i) longer polymer chains with the same torsion probability per unit length are more likely to have a greater total degree of torsion, and (ii) the electrostatic interaction which is important in planarising the polymer backbone decreases with increased donor electron density; which also increases with backbone length. In Figure 4.18 (bottom left), the Urbach energy increases from 24 ± 2 meV for IDT-BT to 31 ± 3 meV for TIF-BT. Concomitantly, the PL lineshape (bottom centre) is substantially broader for TIF-BT, and again, the blueshifted PL spectrum arises directly from an increased bandgap, shown in the absorption spectrum (bottom right), resulting from a more electron-rich donor, and hence a decreasing push-pull character.

Similarly, in this series we observe the same correlation between decreasing sidechain density and increasing mobility. This effect is weaker here, since the bulkiness of *n*-hexadecyl sidechains is reduced compared to *p*-hexadecylbenzyl. It is likely that this observation is due to the need for a high density of close contact points between adjacent polymer chains for good transport, and that high sidechain density and bulkiness can disrupt this important packing. In this respect, increasing the length of the backbone subunit without increasing the total number of sidechains may lead to stronger interaction between adjacent chains, and ultimately the very high mobility observed for TIF-BT.

4.8 Tuning donor-acceptor character

Increasing the length of the backbone by using longer donor subunits also changes the amount of push-pull character. To verify our picture of sidechain sterics determining

the mobility, we must decouple the role of the push-pull character from sidechain density on the charge transport. Perfluorination of the benzothiadiazole (BT) acceptor, yielding F_2BT, increases the ionisation potential of the polymer (without substantially changing the LUMO energy) because of its electron-withdrawing properties.[182–184] On the other hand, substitution of BT for benzobisthiadiazole (BBT) increases the relative electron-widthdrawing strength of the acceptor dramatically.[185] However due to additional MOs in BBT, the LUMO energy is approximately −3.6 eV,[186] leading to exceedingly low bandgaps.[187, 188] In this section, we compare three polymers with the PhC_{16}IDTT-[Acceptor] motif with acceptors BT, F_2BT, and BBT. While IDTT-BT, IDTT-F_2BT, and IDTT-BBT have the same subunit length of 2.04 nm and sidechain density, they differ substantially in their push-pull character.[13] Using DFT, we calculate the permanent polarisation (dipole moment) in the direction of the repeat unit ($P_{\hat{r}}$) to be 1.68, 1.91, and 4.21 D respectively.[14]

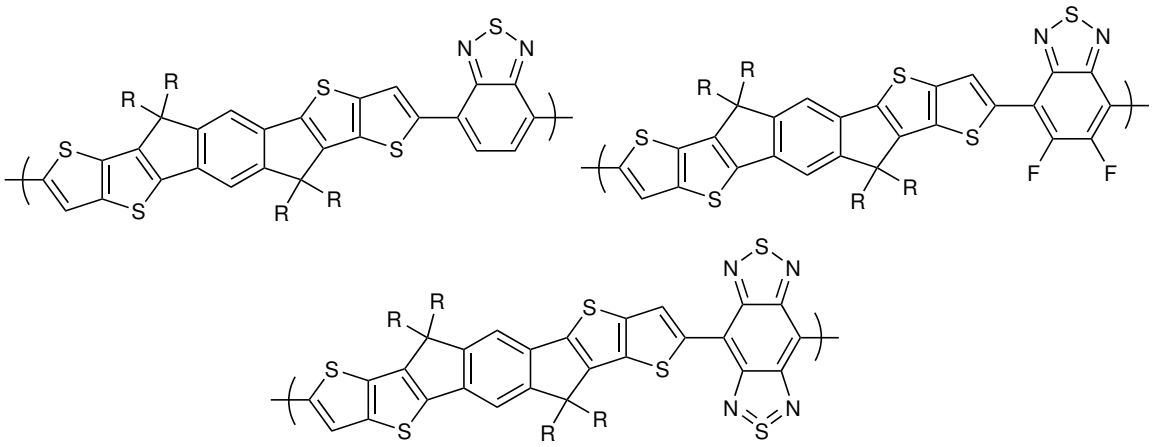

Figure 4.19 PhC_{16}IDTT-[Acceptor] polymers in the study: [Acceptor] = BT (top left), F_2BT (top right), and BBT (bottom). R = *p*-hexadecylbenzyl.

The transport properties of IDTT-BT and IDTT-F_2BT are similar. High on-currents, good I_{on}/I_{off}, and small S indicate the absence of appreciable trapping in these materials, and the FET characteristics are shown in Figure 4.20 (top). Key device parameters are summarised in Table 4.5. Nonetheless, both materials suffer

[13]This section only deals with materials with *p*-hexadecylbenzyl sidechain, and so the sidechain name is omitted for brevity.

[14]From DFT-optimised geometries, a readout of the converged electron density yields the permanent electric dipole moment vector ($\vec{\mu}_E$). We project this in the direction of the repeat unit ($\hat{r}$) to determine $P_{\hat{r}} = \vec{\mu}_E \cdot \hat{r}$.

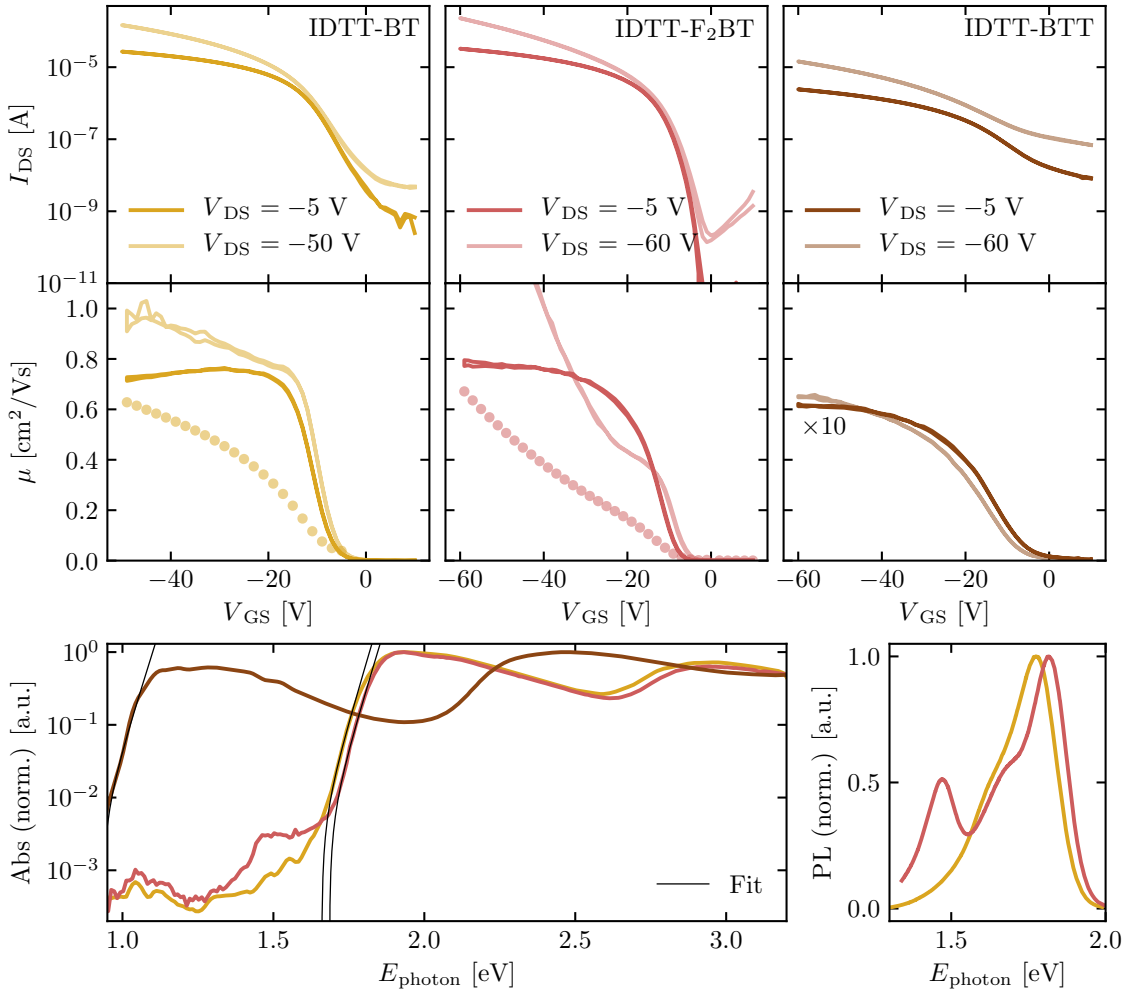

Figure 4.20 Effect of push-pull modulation on PhC_{16}IDTT-[Acceptor] polymers: transfer characteristics in linear (top left) and saturation regimes (top right) with extracted mobility below ('instantaneous' mobility as circles). Normalised (PDS) absorption spectrum with fit for Urbach extraction (bottom left) and normalised PL spectrum (bottom right).

from the aforementioned $\gamma > 2$ non-ideal behaviour in saturation. As for TIF-BT, both IDTT-BT and IDTT-F_2BT have near ideal MOSFET-like behaviour in the linear regime, as demonstrated (below), and this allows for the robust extraction of mobilities in this regime. As before, a proper extraction of V_{Th} in spite of this non-ideality is difficult, and independent of our extensive optimisation of the solution processing conditions. Similar to the previous section, we calculate a lower bound for the saturation mobility at each gate voltage for these non-ideal materials assuming a

Table 4.5 Summary of device parameters for different C_{16}IDTT-[Acceptor] polymers.

[Acceptor]	$\mu_{\text{lin.}}$ [cm^2/Vs] ($r_{\text{lin.}}$)	$\mu_{\text{sat.}}$ [cm^2/Vs] ($r_{\text{sat.}}$)	$I_{\text{on}}/I_{\text{off}}$	V_{Th} [V]	S [V/dec]
BT	0.74 (0.79)	0.86 (0.73)	$\sim 4 \times 10^4$	−6.57	4.42
F_2BT	0.75 (0.78)	1.28 (0.53)	$\sim 1 \times 10^6$	−9.91	1.24
BBT	0.055 (0.79)	0.051 (0.73)	$\sim 2 \times 10^2$	−5.97	12.5

negligible V_{Th}. We notice that at high gate voltages, this estimate approaches the linear mobility estimate from below, supporting its validity as a lower estimate of the true mobility, and the appropriateness of the linear mobility extraction. There is a slightly improved mobility upon BT perfluorination. This observation is difficult to interpret directly, and may arise from (i) an increased planarisation due to a greater barrier to torsion upon perfluorination of the BT, or (ii) direct involvement of push-pull character, perhaps electrostatically promoting closer packing between chains. There is little evidence in the literature to support closer π-π stacking distances between donors and acceptors on different chains with increased push-pull character,[26] and while 2D-nuclear magnetic resonance and GIWAXS strategies have been successful in analysing the packing in structurally related semicrystalline CDT-BTZ, this has even shown the opposite trend of strong donor-donor/acceptor-acceptor interaction.[189]

By comparison, IDTT-BTT has a substantially reduced mobility, but more ideal MOSFET-like behaviour gives good agreement between linear and saturation mobilities. The mobility in each of these regimes plateaus. A high off-current gave a poor $I_{\text{on}}/I_{\text{off}}$ and S, despite the on-current being appropriate for the low-mobility polymer and a low V_{Th}.

Comparing the steady-state optical properties of these materials in Figure 4.20 (bottom), we observe that for IDTT-BT and IDTT-F_2BT, there is a marginal increase in bandgap from 1.79 eV to 1.82 eV, but no resolvable change in energetic disorder; each having an Urbach energy of 27 ± 2 meV. Consistent with this, there is no difference in the PL broadening, but the blueshift in the PL of IDTT-F_2BT arises directly from the higher bandgap.[15] By comparison, IDTT-BBT has a very different absorption spectrum, a substantially reduced bandgap, and an increased Urbach

[15]The additional peak in the PL of this material below 1.5 eV and its corresponding absorption in the PDS spectrum is due to an additional emissive pathway from excitons spread between two adjacent chains. This is discussed in detail in another chapter.

energy of 37 ± 5 meV. We do not measure any PL from films (at low or high excitation density) owing to a vanishing PLQE, which is typical of very low-energy gap materials, and discussed at length in the following chapter.

An increase in the polarisation of the material may lead to a marginal improvement in the mobility, but it is difficult to truly disentangle this from a changing torsion potential with different electrostatic and sterical substitutions on the BT. However, the unchanging Urbach energy and width of PL lineshape between IDTT-BT and IDTT-F_2BT suggest that increasing the donor-acceptor polarisation can itself directly improve the mobility, potentially via improving close crossing between chains, although further investigation of this is required. However, this has its limitations, and IDTT-BBT has a disappointing mobility; irrespective of film formation or solution processing conditions. This is likely to be due to its high degree of energetic disorder, although it is unclear whether this disorder is itself due to a very high ground-state polarisation or another factor which is specific to BBT.

4.9 Minimising torsion-induced disorder

To determine which factors planarise the backbone in our amorphous donor-acceptor polymers, we evaluate the role of backbone elongation, push-pull character, and electrostatic interaction between donor and acceptor subunits, and the dielectric environment. In this section, we use DFT to calculate the equilibrium positions and gas-phase torsion potentials for the various polymers examined in this chapter.

In order to compare torsion potentials between materials, we calculate relaxed potential energy surfaces for our materials in Figure 4.21 (left). By fixing the dihedral angle between the planes of donor and acceptor moieties ($\theta_{\text{dihed.}}$), we optimise all bond lengths, bond angles, and all other dihedral angles to find the 'constrained' energetic minimum at each step.[16] We define lower energy coplanar configuration as having $\theta_{\text{dihed.}} = 0\ ^\circ$. For computational efficiency, we simulate each molecule as a single donor-acceptor repeat unit capped with methyl (-CH_3) groups, and also replacing the sidechain with methyl groups. Therefore, we do not distinguish here between the

[16] In this section, we iterate from $0 - 180\ ^\circ$ with $10\ ^\circ$ steps, and interpolate between the points for readability.

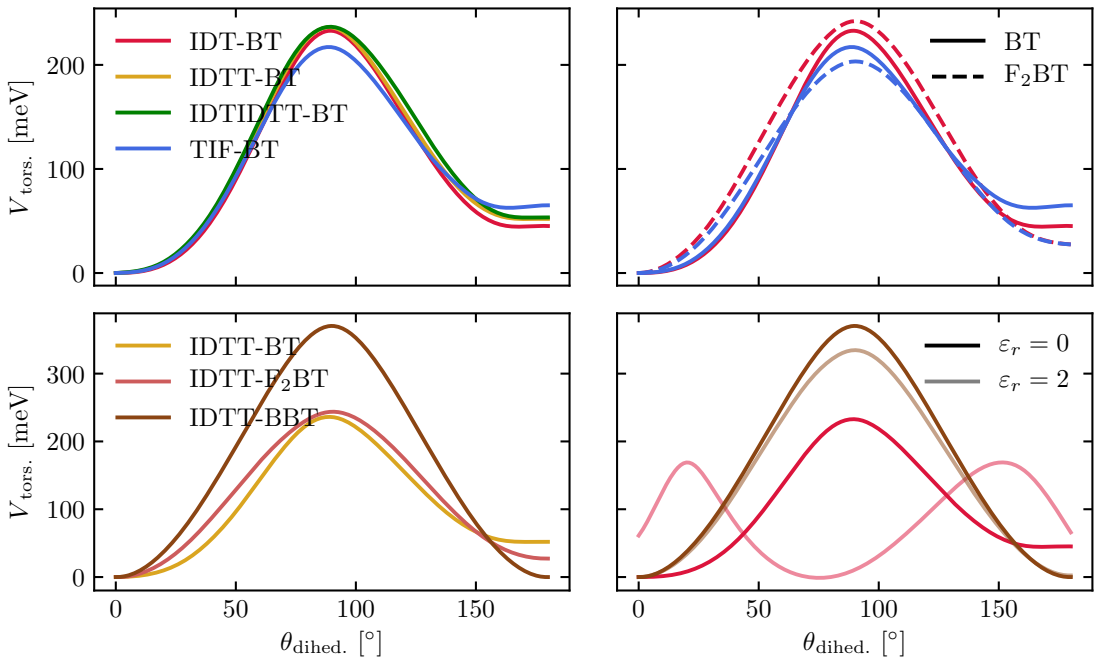

Figure 4.21 Calculated potential energy surface of torsion between donor and acceptor subunits for various polymers.

sidechains explored in this chapter, and only examine the electronic properties of the backbone.

In Figure 4.21 (top left), we assess the effects of backbone elongation on the torsion potential. Here we compare different [Donor]-BT polymers including IDT, IDTT, IDTIDTT, and TIF donors. Between all the polymers, we do not see a substantial change in the torsion potential, suggesting that the length of the backbone does not determine the barrier to torsion. Instead, the torsion potential seems to be determined by the chemistry of the rings flanking the donor, and their interaction with the acceptor. This is particularly clear for IDT, IDTT, and IDTIDTT where we see very little change. However, we observe a small reduction in the torsion potential for the TIF donor, consistent with its increased Urbach energy in films. We note that in general, many factors including dielectric environment (discussed below) and microstructure can contribute to the energetic disorder of a material, however we find in this family of polymers that the biggest contribution is from torsion due to the chemical properties of the backbone; and the sidechains discussed in Section 4.6.1

(that modulate both the aforementioned properties) do not seem to make a difference.

In Figure 4.21 (bottom left), we assess the effect of polarisation on the torsion potential, comparing different IDTT-[Acceptor] polymers with BT, F_2BT, and BBT acceptors. Here, we observe a greater change, but this is likely to result from the difference in polymer chemistry rather than polarisation explicitly. Comparing IDTT-BT with IDTT-F_2BT, we observe a marginal increase in the torsion potential upon perfluorination, including a steeper torsion potential about $\theta_{\text{dihed.}} = 0\ ^\circ$. This implies a greater restorative torque (since $\tau \sim \partial V_{\text{tors.}}/\partial\theta_{\text{dihed.}}$) and potentially a more rigid backbone. Conversely, perfluorination of the BT leads to stabilisation of the $\theta_{\text{dihed.}} = 180\ ^\circ$ conformation, as a repulsive hydrogen-hydrogen interaction is replaced by an attractive hydrogen-flourine interaction. Ultimately, however, the height of the potential energy surface, and hence thermodynamic properties due to torsion, do not change substantially with BT perfluorination. However, a big improvement is made to both the restorative torque and height of the surface for IDTT-BBT. Again, this is explained by the change in chemistry, and the symmetric BBT leads to a strong electrostatic attraction between the IDTT and the BBT in both coplanar dihedral conformations.

The effect of perfluorination on the BT is extended to IDT-BT (pink) and TIF-BT (blue) in Figure 4.21 (top right).[17] While perhydrogenated samples (solid lines) have shallow potential energy surfaces about the local minima, perfluorinated-BT analogues (dashed lines) have a steeper surface, indicating a greater restorative force. However, the thermodynamic energy barrier does not change in a consistent way for the two materials: while it increases marginally for the IDT (and IDTT) donor(s), it decreases for the TIF donor.

Our calculations therefore do not correlate well with observed Urbach energies. This is an important observation, since it highlights various limitations of this methodology. Most notably, when we measure the Urbach energy, we do so using a polymer thin film. On the other hand, our calculations simulate a polymer subunit in the gas phase. While we do not anticipate the single subunit methodology giving unreliable results,[18]

[17] These two polymers are included in an optical study later, and we include them in the discussion here for completeness.

[18] We anticipate a systematic error in the absolute torsion potential values due to the calculation, but we expect qualitative comparisons between similar polymer subunits to be robust.

we do not know the precise chemical environment of specific chromophores in our amorphous polymer films *a priori*, and we therefore neglect sterical effects which would act to increase the torsion potential, and dielectric stabilisation effects which would decrease the torsion potential.

To briefly explore this, we calculate the torsion potential of IDT-BT (pink) and IDTT-BBT (brown) in Figure 4.21 (bottom right), both in the gas phase (dark, $\varepsilon_r = 0$) and as a dilute guest in a non-interacting dielectric host (light, $\varepsilon_r = 2$).[19] For IDT-BT, the differences are profound: the dielectric environment reduces the overall barrier to torsion, and seems to shift the absolute energetic minimum towards a highly twisted conformation. A similar torsional change is observed when simulating individual interacting polar molecules.[136] While this is unlikely to be the case in a film where the sterics of face-on packing act to suppress such torsion, especially given the observed high mobility in IDT-BT polymers, it may be the origin of the low PLQE in very dilute solution, since dynamic dihedral torsion has been shown to mediate ultrafast internal conversion in similar PCDTBT.[191] On the other hand, IDTT-BBT, which has a substantially increased torsion potential compared to similar IDTT-BT, does not change its potential energy surface shape, but decreases its magnitude marginally in the presence of a dielectric medium. Therefore, while IDT-BT may rely on sterics to maintain planarity in films, IDTT-BBT is more likely to be locked in a rigid planar configuration by the chemistry of its acceptor-flanking units strongly interacting with electronegative nitrogen on the BBT subunit.

4.10 Summary

Through a detailed study of solution processing conditions, we show that PhC_{16}IDT-BT yields its highest mobilities and most ideal devices when processed with a high boiling point solvent. We attribute this to the displacement of atmospheric species, including water, which otherwise introduces non-idealities into the device, decreasing the mobility. A similar effect is seen upon incorporation of small concentrations of molecular additive - particularly in the TCNQ family - however increasing TCNQ fluorination leads to doping of the polymer at a constant dopant loading. Furthermore, an increased solubility of PhC_{16}IDT-BT over conventional C_{16}IDT-BT leads to

[19] We used the COSMO package for a polarisable van der Waals cavity here.[190]

difficulties with 'orthogonal' solvent post-treatement.

The structure can be robustly tuned using different annealing at different temperatures. Short annealing times and high boiling point solvents are preferred, because it can otherwise be difficult to accurately measure the mobility due to increased trapping and contact resistance - consistent with the removal of the solvent - degrading the transport properties. Nevertheless, annealing at increasing temperature leads to increasing polymer fraction with a more edge-on packing motif, compared to an amorphous face-on geometry for unnanealed polymer. Consistent with this, the photophysics indicates increasing H-type aggregation with increased annealing temperature, although annealing above 125 °C accelerates this process substantially, and leads to fast non-radiative decay as chains begin to pack more closely. Despite this, there is no change in the Urbach energy, suggesting that the energetic disorder is, at most, weakly dependent on the packing motif.

We explore the changing packing motif using sidechain substitution of the IDT-BT polymer. Bulky sidechains lead to increased π-stacking distances and lower mobilities, since we expect the close contact points between adjacent chains (which are highly important for charge transport in amorphous polymers) to be further apart for PhC_{16}IDT-BT compared to C_{16}IDT-BT. Consistent with this, there is no significant difference in the energetic disorder of these polymers, however, the temperature dependency of the transport suggests a broader transport density of states for PhC_{16}IDT-BT - indicated by the $\gamma(T) > 2$ behaviour - and an increased energy barrier to transport near room temperature, consistent with its increased distance between polymer chains. The aggregation of the polymers occurs (to an extent) even in solution, where the choice of solvent has a profound effect on the PLQE. Consistent with these results, PhC_{16}IDT-BT has the lowest degree of aggregation-induced quenching, however chains continue to evolve towards their energetic minimum for hours after spin-casting, as shown using differential absorption spectroscopy.

In order to achieve higher-performance materials than IDT-BT, we consider the role of dihedral torsion between donor and acceptor, and polymer repeat-unit length. Although we expect the energetic disorder to be directly related to the extent of dynamic torsion on the backbone, we observe poor correlation between increased backbone length (and therefore propensity for torsion per unit length

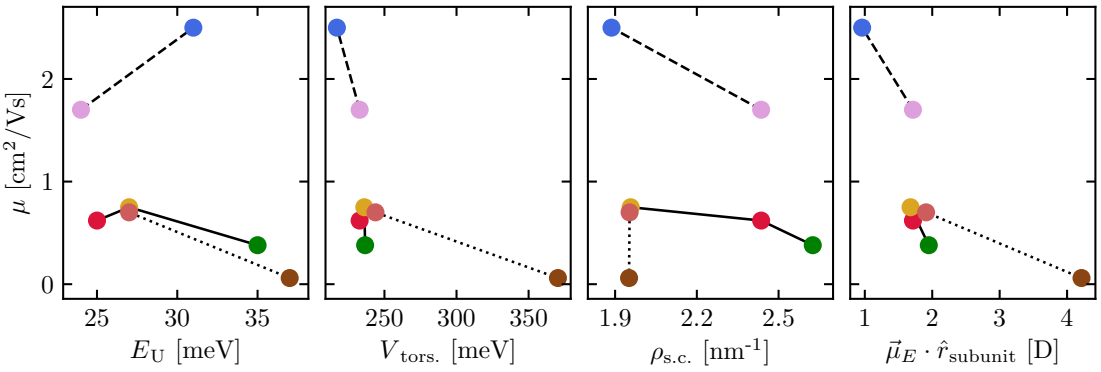

Figure 4.22 Correlating mobility with optical, electronic and structural parameters (left to right), $\mu_{\text{lin.}}$ against: the Urbach energy (E_{U}), the torsional barrier conformational flipping in a vacuum ($V_{\text{tors.}}$), the number of sidechains per unit length ($\rho_{\text{s.c.}}$), and the polarisation in the direction of the repeating unit ($\vec{\mu}_E \cdot \hat{r}_{\text{subunit}}$). *Point colours (series)*: Red/yellow/green (solid line) = PhC_{16}[Donor]-BT with IDT/IDTT/IDTIDTT; blue/pink (dashed line) = C_{16}[Donor]-BT with IDT/TIF; yellow/orange/rust (dotted line) = PhC_{16}IDTT-[Acceptor] with BT/F_2BT/BBT.

of backbone) and Urbach energy. While we see some correlation between Urbach energy and mobility in PhC_{16}[Donor]-BT derivatives, shown in Figure 4.22 (far left), we see that this does not correspond to changes in the calculated energy barrier to BT flipping in the gas phase, in Figure 4.22 (middle left). Furthermore, while the absolute repeat-unit backbone length does not correlate well with the observed mobility, when we consider the sterics of the sidechains, defining a number of sidechains per unit length of backbone ($\rho_{\text{s.c.}}$), we see much stronger correlation in Figure 4.22 (middle right). The importance of $\rho_{\text{s.c.}}$ is even clearer within our C_{16}[Donor]-BT series, since while the decreased sterical hindrance (per sidechain) leads to higher mobility, the trend is the same, and TIF-BT gives the highest mobility measured with the lowest value of $\rho_{\text{s.c.}}$. Importantly, polymers in the C_{16}[Donor]-BT series have the opposite trend in mobility with Urbach energy and torsion potential, supporting the weakness of this correlation in our family of high mobility polymers.

We show that increasing degree of polarisation (as estimated by $\vec{\mu}_E \cdot \hat{r}_{\text{subunit}}$) decreases the mobility. This trend, shown in Figure 4.22 (far right), holds true for all our materials - irrespective of sidechain choice. These results do not support the idea that increasing push-pull character leads to greater π-π interaction between chains leading to higher mobility, and in the low polarisation limit, TIF-BT has the highest mobility. Furthermore, extra data points in Figure 4.22 (far left and middle left)

continue to weaken the correlation between mobility and both Urbach energy and torsion potential.

4.11 Conclusions

Within our family of high mobility donor-acceptor polymers, all of the Urbach energies measured indicate among the lowest energetic disorder for any material - amorphous or crystalline,[80] and increased efforts to planarise the material do not seem to give higher mobilities. Instead, our results suggest that in order to increase the mobility further, polymers with decreased sidechain density and sterical hindrance should be considered. Such polymers with low $\rho_{\text{s.c.}}$ are likely to increase the closeness of close contact points between chains, which increases the mobility dependent on appropriate stacking of chains. However, further investigation of the precise chemical nature and geometry of these close contact points is required to explain the very high mobility in C_{16}IDT-BT and C_{16}TIF-BT. We investigate this in the following two chapters.

4.12 Contributions

Dr. Mark Nikolka developed the ACN washing protocol for C_{16}IDT-BT, shown in Figure 4.4 for PhC_{16}IDT-BT, and provided the device data for C_{16}IDT-BT and C_{16}TIF-BT in Figure 4.18 (top). Dr. Katharina Broch measured the GIWAXS data of PhC_{16}IDT-BT for different annealing temperatures shown in Figure 4.7 (bottom right). Dr. Aditya Sadhanala measured all the photothermal deflection spectroscopy spectra in this chapter.

Chapter 5

Chain coupling and luminescence in high-mobility amorphous polymers

5.1 Introduction

In this chapter, we investigate the extent to which the low PLQEs in the IDT-BT polymer family are related to the degree of inter-chain coupling, and by which mechanisms the inter-chain coupling leads to non-radiative decay. By using side-chain engineering to destabilise close IDT-BT backbone packing, we decouple high mobility from low PLQE and report the highest film PLQE of 18 % reported for a high-mobility amorphous material and propose a design strategy to avoid non-radiative pathways which arise across 200 fs−100 µs timescales.

In this work, we characterise the conjugated polymer IDT-BT electronically in devices, and photophysically on ultrafast to microsecond timescales. We use hexadecyl and hexadecylbenzyl sidechains to yield C_{16}IDT-BT and PhC_{16}IDT-BT respectively, hereunder M_0 and M_1. The structures are shown in Figure 5.1.

5.2 Electrical and optical characterisation

In an organic field-effect transistor (OFET) architecture, we interrogate the *p*-type conductivity of the derivatives as a function of hole-accumulation (V_{GS}) in saturation and linear device regimes. This is shown in Figure 4.12, and discussed in detail in

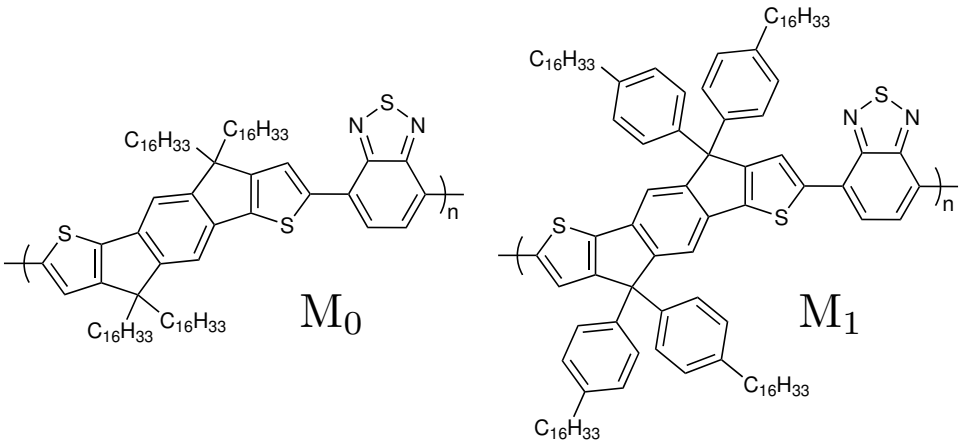

Figure 5.1 Structures of IDT-BT with hexadecyl sidechains; C_{16}IDT-BT (left), and with hexadecylbenzyl sidechains; PhC_{16}IDT-BT (right).

Section 4.6. Briefly, high on-currents approaching $I_{\text{on}} \sim 10^{-3}$ A yield a high field-effect mobility of $\mu_{\text{FET}} \sim 2$ cm^2/Vs for M_0 with good agreement between values extracted in linear and saturation regimes. A slightly lower but comparable mobility of $\mu_{\text{FET}} > 0.5$ cm^2/Vs is extracted for M_1. Both materials display ideal MOSFET-like operation with $I_{\text{DS}} \sim (V_{\text{GS}} - V_{\text{Th}})^2$, giving a constant mobility for accumulation above the threshold. The *n*-type conductivity was also measured, although device stability and batch-to-batch variation in our devices were found to be poor. This is possibly owing to a LUMO energy of approximately −3.6 eV, which leaves electron transport vulnerable to atmospheric trapping.[52] Owing to this difficulty, we do not consider *n*-type transport in our discussion here, but presume that it *p*- and *n*-type transport is improved by many of the same factors; including minimising the energetic disorder.

MOSFET-like operation indicates a narrow transport density of states (DOS) and suppressed energetic disorder.[192] The low energetic disorder we observe is owing to long-range homogeneity in backbone conformation.[80] The high degree of long-range uniformity is achieved not through crystallinity, but by a high potential barrier to torsion. Electrostatic attraction between the IDT thiophene proton and the BT sulfenamide nitrogen provides a deep energetic minimum of the dihedral torsion potential (which is discussed in Section 4.9), which stabilises a coplanar configuration.[27] Despite the well-defined planar backbone conformation which favours fast intra-chain transport along the polymer backbone, achieving high mobility over long distances also relies on efficient hole transfer between chains at close contact

points where chains aggregate strongly. Owing to the bulkiness of M_1 side-chains,[193] we observe an increased π-π stacking distance of 0.48 ± 0.4 nm (Figure I.1), compared to 0.38 nm in M_0 reported previously.[137] This is likely to be the origin for the slightly decreased mobility in M_1.

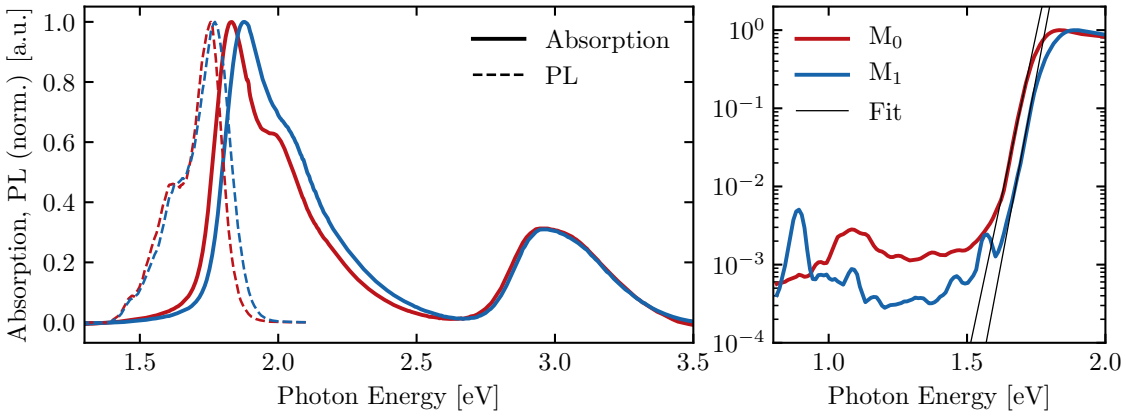

Figure 5.2 Steady-state optical characterisation of IDT-BT derivatives thin films. Absorption (solid line) and PL (dashed line) for M_0 (red) and M_1 (blue) thin films (left), with absorption and Urbach energy extraction determined by PDS near energy gap edge (right).

Energetic disorder can be quantified by the width of the joint density of states (JDOS) near the band-edge.[93] We fit the absorption tail near the energy gap edge to Equation 3.6 to recover the Urbach energy (E_U), a measure of the disorder in the JDOS. M_0 and M_1 have similar $E_U = 23 \pm 2$ meV and 25 ± 2 meV respectively, shown in Figure 5.2 (right). The similarity in E_U between the materials is an indication that energetic disorder along the backbone is similar (and very low), and that the side-chain substitution does not lead to changes in the conformation of the backbone in films. Furthermore, this energetic disorder is amongst the lowest reported in any polymer[27, 93, 194] despite its near-amorphous microstructure.

The absorption spectrum in Figure 5.2 (left) shows two spectrally-resolved absorbing species. By comparison with time-dependent (TD-) density functional theory (DFT) calculations, we assign three transistions. The bluer band, peaking at 2.91 eV are the $S_0 \rightarrow S_2$ and $S_0 \rightarrow S_3$ transitions, resulting in the skew lineshape. Due to their relative localisation on the IDT moiety, these are often referred to collectively as $\pi \rightarrow \pi^*$ transitions in the donor.[195] The redder band, peaking at 1.83 eV (1.88 eV)

for M_0 (M_1), defines the energy gap of the materials, and corresponds to an intra-chain charge-transfer state (ICT). Here, the exciton is stabilised through charge-transfer across fused donor and acceptor moieties.[196] This transition is strongly coupled to a vibronic progression with a frequency of 1430 cm^{-1}, which DFT results confirm corresponds to an in-plane C=C distortion with strong activity on the IDT subunit.

In the luminescence spectrum, we observe only one species. Resembling the ICT absorption in lineshape and energy, we conclude that emission proceeds only from the ICT, and not higher energy states, despite exciting the sample by pumping the $S_0 \rightarrow S_3$ transition with a photon energy of 3.10 eV. This is consistent with Kasha's rule, and confirms that cooling of the exciton wavefunction to the band edge proceeds much faster than luminescence. Separately, we find that emission of the ICT species is isotemporal across the emissive band, and independent of excitation wavelength, which we discuss further in Section I.2. Comparing the two materials, the PL spectra are very similar: they are nearly isoenergetic (peaking at 1.77 eV), vibronically coupled to the same intra-chain vibration (at 1270 cm^{-1}), and have the same transition linewidth and Huang-Rhys parameter. This is a clear indication that the emissive ICT is the same in the two materials. Positive solvatochromism accounts for the redshift of the absorption of M_0 compared to M_1. We expect that for M_1, suppressed backbone packing decreases the bulk dielectric constant[197] and DFT confirms that the LUMO is more localised than the HOMO, leading to a greater charge-transfer (CT) character for S_1 than S_0, which can be stabilised by a higher permittivity environment.[198] However, the PL does not redshift to the same degree as the absorption, leading to a difference in Stokes shift; 74.6 meV for M_0 and 107 meV for M_1.

This observation is important: M_1 undergoes a greater reorganisation than M_0 upon photo-excitation. This seems intuitive; M_1 is bulkier, and has more atoms per repeat unit, and may therefore require a greater reorganisation. However, DFT confirms that the sidechains do not participate in molecular orbitals near the energy gap, so excitons are confined to the backbone plane. We therefore expect reorganisation to be mostly limited to the backbone atoms, not changing substantially between the two materials. Instead, the difference in reorganisation is likely to be related to the microstructure, as closer packing increases dielectric constant of the film and also the sterical hindrance for any such reorganisation. As for all amorphous polymers in this family, it is not meaningful to talk about the precise packing microstructure since it is not well defined.

However, optical measurements of the bulk properties of these materials considers contributions from all occurring microstructures, and provides a structural handle on properties, including dynamic reorganisation, which are otherwise difficult to probe.

5.3 Polaron-pair formation

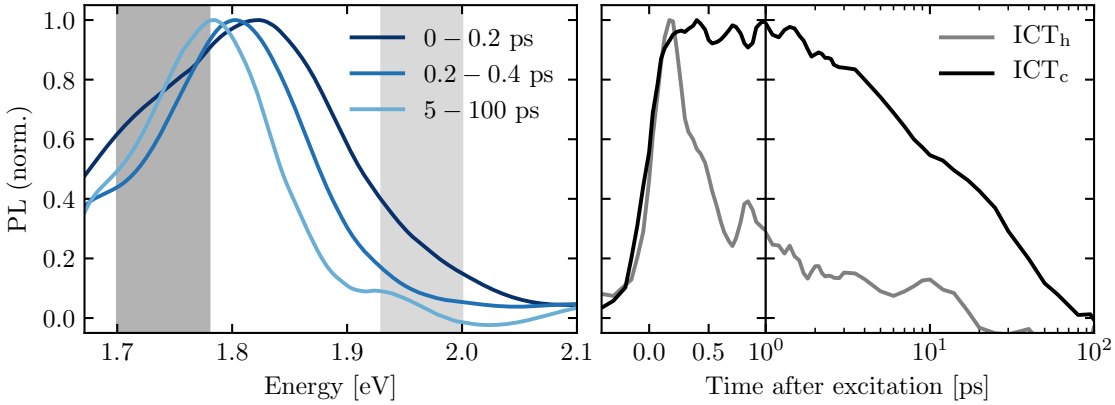

Figure 5.3 Ultrafast time-resolved PL of M_1 thin films. Normalised spectra integrated in the time domain (left) and normalised kinetics integrated in the energy domain shaded left (right).

To investigate the reorganisation we use ultrafast transient grating PL with a time resolution of < 200 fs. As before, we pump the IDT π-π^* transitions in M_1 thin films with an excitation energy (E_{pump}) of 3.10 eV at the fluence (f_{pump}) of 39 $\mu J/cm^2$, with pulses at 1 kHz to minimise any 'wrap-around' effects. In Figure 5.3 (left), we show the luminescence spectra averaged over various time intervals. At the earliest times, the spectrum (dark blue) peaks at 1.83 eV, and is very broad with a FWHM of 0.14 eV. At later times, the spectrum (light blues) redshifts to 1.79 eV and narrows to a FWHM of 0.07 eV. The spectrum at the earliest times resembles the steady-state absorption spectrum, which is characteristic of an unequilibrated, or 'hot', exciton population before reoganisation. By 5 ps, the PL spectrum resembles the steady-state emission spectrum, so the exciton population (and wavefunction) has cooled and the geometric reorganisation which confers the Stokes shift has occurred.

To determine the timescale of this cooling, we consider the decay kinetics of the hot and cooled exciton species. For good signal-to-noise while avoiding signal mixing from the two species, we integrate the kinetics over a spectral range (shaded). We

measure the kinetics on the high-energy (low-energy) edge of the prompt (delayed) ICT species to minimise signal mixing. We show the normalised kinetics in Figure 5.3 (right) in the same shades. The prompt component (grey) is the emission from the 'hot' ICT (ICT_h), and decays to zero by 500 fs, a timescale which is typical for dynamic reorganisation. The delayed component is the 'cooled' ICT (ICT_c), which decays to zero over the next 100 ps. We observe separately (and discuss below) that this cooling lifetime is independent of fluence, so here we use a moderate fluence which decreases the lifetime of ICT_c by bimolecular exciton-exciton annihilation processes.

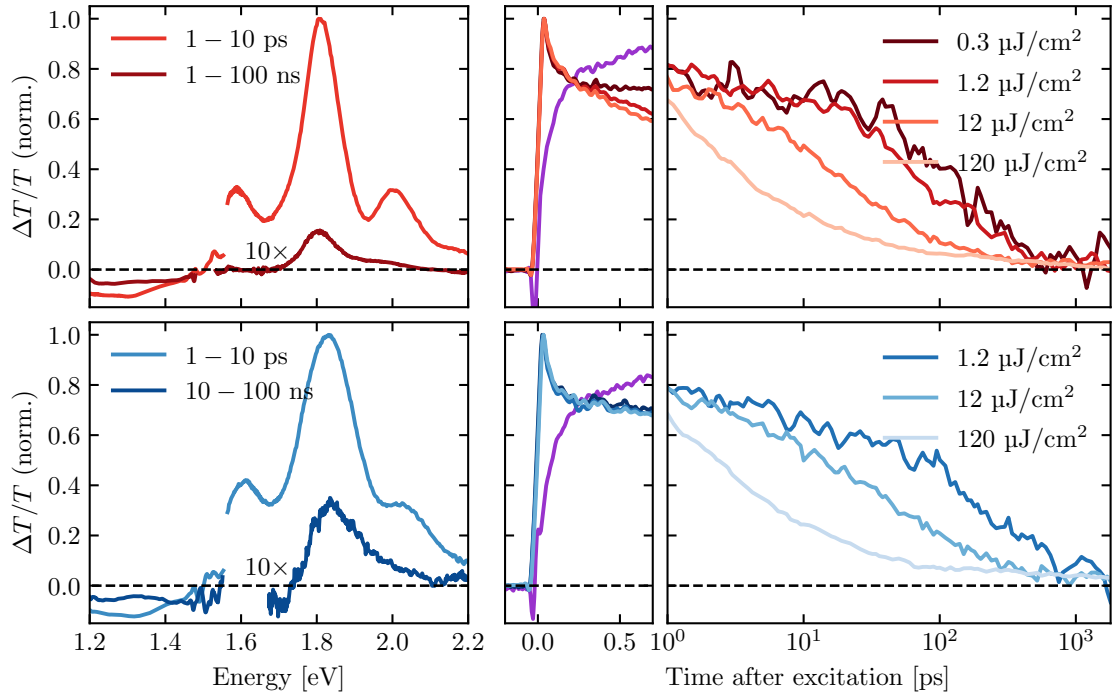

Figure 5.4 Ultrafast time-resolved TA of M_0 (red; top) and M_1 (blue; bottom) thin films. Normalised spectrum during (light) and after luminescence (dark, magnified 10×) (left). Normalised SE (violet; 5.9 µJ/cm²) and GSB kinetics before 1 ps with fluence 5.9, 24, 71 µJ/cm² (5.9, 16, 49 µJ/cm²) from dark to light for M_0 (M_1) (centre), and normalised GSB kinetics after 1 ps (right).

We observe the same physics in ultrafast transient absorption (TA) measurements. The TA experiment is described in detail in Section 3.3.2.3. We identify three spectral features in Figure 5.4 (left): (i) a ground-state bleach (GSB) of the strongly absorbing ICT between 1.8 – 2.2 eV by comparison with the steady-state absorption spectrum, (ii) stimulated emission (SE) of the same species between 1.5 – 1.8 eV by comparison with the steady-state PL spectrum, and (iii) broadband photo-induced absorption (PIA)

from transitions $S_1 \rightarrow S_n$ under the whole probe band, but increasing in intensity below 1.4 eV. The peak at 1.81 eV (1.83 eV) for M_0 (M_1) is composed of spectrally overlapping $GSB_{0\text{-}0}$ and $SE_{0\text{-}0}$ features.[1] We confirm this assignment by observing the suppression of the SE peaks at higher fluence where the PLQE is reduced by multi-exciton annihilation processes, shown in Figure I.4 (right). This leads to a narrowing and blueshifting of the mixed peak at higher fluence as it becomes increasingly dominated by the $GSB_{0\text{-}0}$ signal.

Furthermore, at early timescales, the mixed feature has a narrow spectral lineshape, shown in Figure I.4 (left). However, by 500 fs, we observe a broadening of the red-edge of this peak in tandem with a redshift of $SE_{0\text{-}1}$. This is the same wavefunction cooling and reorganisation which occurs on the prompt timescales in the ultrafast PL, and confirms the same cooling and reorganisation picture for both M_0 as M_1. This is discussed further in Section I.3. This physics has also been observed in various comparable low mobility donor-acceptor polymers on similar timescales.[199–201] The kinetics of the GSB (here, $GSB_{0\text{-}1}$ to minimise signal mixing) decrease by 25 % during cooling in Figure 5.4 (centre), indicating a reduction of the number of chromophores bleached by 1 in 4. We observe the same dynamics for both materials, and the exciton cooling proceeds on the same timescales. This cooling rate does not depend on fluence, and with sub-40 fs time resolution here, the kinetics in the first 300 fs are indistinguishable between the two materials. This is important for two reasons. Firstly, since the ratio of the GSB before and after reorganisation does not change between the two materials - in spite of the different intra-chain coupling - it follows that the ICT_h exciton is diffuse mainly in the plane of the backbone, and not in the out-of-plane direction or between adjacent chains. Over the same timescales, the SE signal (here, $SE_{0\text{-}1}$ in purple) grows in for both materials. Secondly, the isotemporal relaxation between the two materials disproves the hypothesis that M_1 undergoes a greater relaxation in the excited state, since we would expect such a relaxation to proceed over longer timescales. Instead, this reorganisation timescale is indistinguishable between the two materials, suggesting that the difference in Stokes shift discussed earlier is due to a flatter S_1 potential energy surface in M_0.

Over the following nanosecond, the GSB decays nearly to zero, and this occurs over shorter timescales for M_0 than M_1. This is shown in Figure 5.4 (right). For

[1] Here, the shorthand $GSB_{x\text{-}y}$ and $SE_{y\text{-}x}$ to denote the transition to the different vibrational states; $S_0(\nu = x)$ and $S_1(\nu = y)$.

M_0, we observe that this decay is monomolecular at the low fluence of 0.3 µJ/cm^2 (dark red). At higher fluence, the decay becomes faster due to increasing bimolecular recombination (lighter reds). For M_1, we are unable to measure good signal at the low fluence, and the kinetics at the higher fluences shown could not be fit by a single exponential for this reason. Interestingly, the decay of the GSB does not proceed to zero, and we observe a non-zero GSB signal even after emission from the ICT has finished. To investigate this, we compare the TA spectra during emission (light) with the spectrum after emission has finished (dark) for the two materials in Figure 5.4 (left). The two spectra differ only in that SE signal decays towards long times, and only a GSB and a broad PIA remain. This indicates the persistence of photoexcited species, and leads to a apparent blueshift of the largest peak and a decrease in the structure of the band below 1.5 eV as $SE_{0\text{-}2}$ disappears. The unchanged PIA suggests that the long-lived species likely resembles the emissive state to a degree, and is therefore unlikely to be a chemical flaw or defect which traps excitons for very long times. For M_0 (M_1), this long-lived species which has no luminescence is the fate of 1.5 % (3.5 %) of excitons in films. We turn our attention to the nature and formation of this species, hereunder referring to them as polaron-pairs (PPs).

To determine how the quantum yield of PPs depends on fluence, we determine the yield from the normalised GSB kinetic at 1 ns in Figure 5.4 (right). We observe that all the kinetics tend to the same non-zero value, which indicates that the quantum yield does not depend on fluence for either material. Even in the limit where bimolecular recombination is dominant (for high fluences of 120 µJ/cm^2), the formation yield of this state does not depend on any bimolecular recombination processes from interacting emissive excitons. Therefore, it follows that (approximately) all of these species must be formed on ultrafast timescales; either before or during cooling, and cannot be formed in appreciable yields afterwards without having a strong dependency on the bimolecular rate constant.

These long-lived PPs are different to ICT_c since they are non-emissive and persist for longer than 100 ns. A discussion of the spectral features and decay kinetics on this timescale is provided in Section I.4.1. Such a state has been observed in neat polymer systems before, and assigned to the formation of spatially extended excitons species - named CTs[202, 203] or polaron(-pairs)[53, 204–206] - whose oscillator strength is small. TA measurements in dilute solution in Section I.4.3 reveal that yield of

this species depends on polymer concentration (decreasing by a factor of two upon 10-fold dilution) but is unaffected by fluence, and it is therefore associated with the formation of inter-chain excitons. This species has monomolecular decay dynamics (shown in Figure I.7), indicating geminate recombination. A light-induced electron spin-resonance (LI-ESR) study, discussed in Section I.6, does not reveal photoinduced $s = 1/2$ or $s = 1$ species, ruling out generation of charges or triplets, and hence exciton dissociation or inter-system crossing over µs-timescales.[207] We also rule out the thermal artefact seen in pentacene,[208] and rr-P3HT,[209] since the spectrum does not resemble absorption spectrum plus its first derivative, and does not occur to the same extent in dilute solution. We therefore conclude that 1.5% (3.5%) of excitons in M_0 (M_1) films become non-interacting, tightly-bound PPs, which have a low oscillator strength, and are formed before 500 fs during cooling of the ICT_h.

5.4 Emissive state dynamics

To complete the kinetic picture, we match an excitation density for two TA experiments with 100 fs and 2 ns resolution in Figure 5.5 to measure the entire exciton decay. We use a moderate fluence giving initial excitation densities of 1.1×10^{17} cm^{-3} $\pm$ 10 % (8.3×10^{16} cm^{-3} $\pm$ 19 %) for M_0 (M_1) to achieve good signal over eight orders of magnitude in time. Using a genetic algorithm described elsewhere,[210] we decompose the TA map in energy and time (after 1 ps) into two independent spectra and their kinetics. The decomposed spectra are shown in Figure 5.5 (right) and their associated kinetics (lines, in the same colours) are overlaid with the measured GSB (black circles) and transient PL (grey circles) kinetic data (left) measured using excitation densities of $\sim 1 \times 10^{16}$ cm^{-3}. The decomposed kinetics represent the relative populations of the two species which have TA spectra shown right. For each material, we assign the (prompt) light trace to the ICT_c species and the (delayed) dark trace to the PP species. To verify this, for M_0 (reds), the decay kinetic of the fast species overlaps considerably with the PL kinetic, confirming its assignment as the emissive species. Concomitantly, the spectrum of this species contains SE signal, and its maximum peak is redshifted and broadened with respect to the PP species. The latter lacks SE signal and is therefore more blueshifted and narrower in linewidth, as discussed earlier. Before 100 ps, the GSB, PL, and decomposed ICT_c kinetics roughly overlap, however as this species decays towards zero, the PP species increases in relative

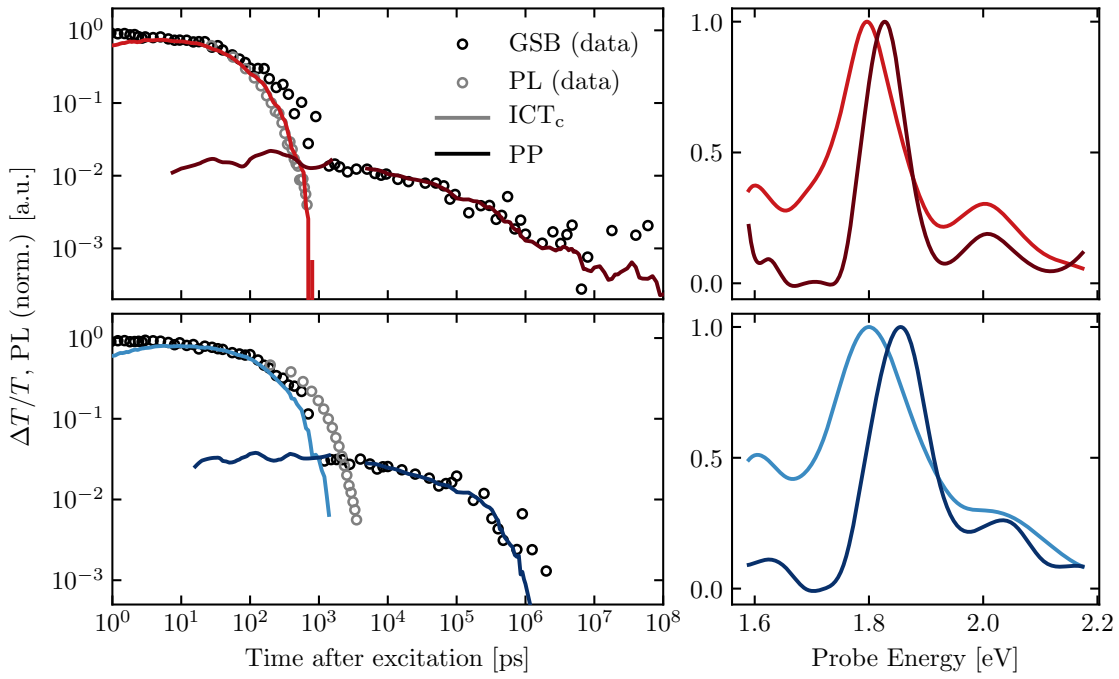

Figure 5.5 Two-species deconvolution of TA map for M_0 (top; red) and M_1 (bottom; blue) thin films in energy and time. Normalised kinetics of GSB and PL (dots) with kinetics of the deconvolved species overlaid (left). Prompt (light, ICT$_c$) and delayed (PP, dark) components are labelled. In the same colours, normalised spectra of the deconvolved species are shown (right).

population, elongating the GSB data towards 1 ns. After 1 ns, the ICT$_c$ decays to zero and the GSB follows the kinetic of the PPs for the rest of the decay. By 100 µs, the PPs decay to zero. By observing the complete decay kinetics of the two species we confirm that there are no additional states formed in this system with a measurable yield over the entire lifetime of the excitons. In addition, PL kinetic (for which our detection sensitivity exceeds that of TA by $\sim$ 100×) does not have any slow tail, indicating (i) the PPs have no PL, and (ii) there is no energy transfer from PPs to ICT$_c$.

For M_1 (blues), the behaviour is similar, except that it is more susceptible to bimolecular recombination at the same excitation density than M_0, and we are unable to measure TA at a fluence whose ICT$_c$ kinetic decomposition accurately overlays the PL kinetic (determined by TC-SPC measurements at a fluence of $\sim$ 2 µJ/cm^2). Nevertheless, we assign the fast species to the same ICT$_c$ which lives for a longer time and has a larger PLQE, suggested by the larger spectral SE signal around 1.6 eV. PPs are formed with a greater quantum yield in M_1, but are shorter-lived

and therefore perhaps more confined, and have a very similar TA spectrum to M_0. This confirms that the PPs in the two materials are similar in chemical environment.

Table 5.1 Decay rates and exciton diffusion parameters for M_0 and M_1

	Thin film		*Dilute solution*	
	M_0	M_1	M_0	M_1
PLQE	0.017	0.18	0.20	0.23
D [nm^2/ns]	1550	947	-	-
L_D [nm]	7.30	16.7	-	-
k_R [ns^{-1}]	0.203	0.263	0.148	0.137
k_{NR} [ns^{-1}]	11.6	1.15	0.593	0.485

To the best of our knowledge, M_1 has the highest PLQE of 18 % reported to date for a polymer film, amorphous or crystalline, with hole mobility exceeding that of amorphous silicon. Polymer films with higher PLQE, notably the fluorene family, have a much smaller p-type field-effect mobility; poly(9,9-dioctylfluorene) (F8; 67%,[211]; 5×10^{-3} cm^2/Vs,[212]), 9,9-dioctylfluorene-*alt*-benzothiadiazole (F8-BT; 51%,[213]; 1.8×10^{-3} cm^2/Vs,[214]), 9,9-dioctylfluorenyl-2,7-diyl-*alt*-[4,7-bis(3-hexylthiophen-5-yl)-benzothia- diazole]-2′,2″-diyl (F8-TBT; 27%,[215]; 5×10^{-4} cm^2/Vs,[216]). Using a procedure detailed in Section I.5, we estimate that M_1 has the lowest density of intrinsic exciton traps of 8.3×10^{15} cm^{-3} reported for any polymer. This is lower still than 7.8×10^{16} cm^{-3} for M_0, which agrees with the lower sub-energy gap floor for the former in Figure 5.2 (right). The larger exciton diffusion coefficient in M_0 compared to M_1 is indicative of increased exciton delocalisation of M_0 excited states, possibly owing to the closer chain packing. In spite of its smaller diffusion coefficient, M_1 has the largest exciton diffusion length of 16.7 nm for any reported high-mobility amorphous polymer, as estimated using the formalism in [51]. This is more than double that of M_0.[2] The long diffusion length of M_1 is owing to its much longer photoluminescence lifetime than M_0. These important optical parameters are summarised in Table 5.1. For suitability in optoelectronic devices, we need to design long exciton diffusion length, trap-free polymers, and M_1 is a promising candidate toward high-performance OLED and OLEFET applications.

[2]For comparison to work by Mikhnenko and coworkers,[51] we have assumed one-dimensional exciton transport ($Z = 1$) in this formalism.

The difference between M_0 and M_1 is the degree of inter-chain coupling. In dilute solution (*o*-DCB, 0.01 g/L), the two materials are very similar, and have the same PLQE. In each case, casting thin films from solutions leads to a decrease in the PLQE. While the PLQE of M_0 is reduced to 10 % of its former value, M_1 falls by only 20 % in thin films. This suggests an inter-chain component to the exciton decay pathway. By independent measurement of the PLQE and PL decay rate, we determine the radiative (k_R) and non-radiative (k_{NR}) rates of decay, as explained in Section 3.3.3.5. These values are summarised in Table 5.1. The PLQEs and PL decay rates differ only by a small amount in dilute solution, yielding similar values for k_R and k_{NR}. Thin films have an increased k_R, compared to solution, consistent with increased exciton delocalisation[217, 218] upon close chain packing. This is a measure of the oscillator strength which increases with exciton delocalisation, and M_0 excitons are more delocalised in films due to closer chain-packing. In film, k_{NR} increases starkly from the solution value; but this difference is greater for M_0 than for M_1. From solution to film, k_{NR} increases by 20× for M_0, but only 2× for M_1. Hereunder, we focus on understanding the origin of k_{NR} of ICT_c in M_0 and M_1 by decomposing it into intra- and inter-chain non-radiative components.

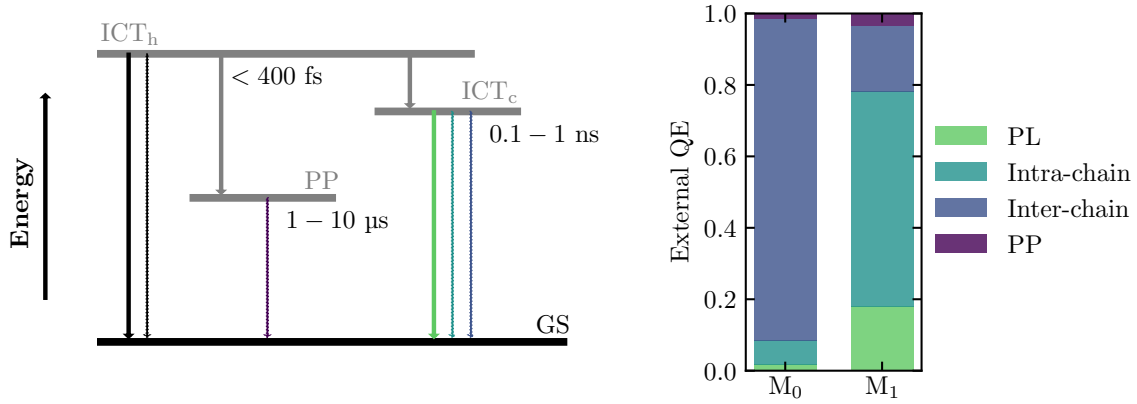

Figure 5.6 Exciton decay scheme and yields for M_0 and M_1. Energy level diagram (left) summarising radiative (solid) and non-radiative (dashed) decay (colour) and cooling processes (solid grey) from various states with arrows. In the same colours, external quantum efficiency of decay processes is shown (right).

The complete exciton dynamics are shown schematically in Figure 5.6 (left). To summarise, optical pumping results in the population of hot ICT states (ICT_h). On ultrafast timescales, the exciton population branches, and transfers either to cool ICT

states (ICT_c) or to polaron-pair states (PP). This proceeds on much faster timescales than radiative (black solid line) or non-radiative (black dashed line) decay to the ground state (GS), and also exciton-exciton interactions, and the branching yields are conferred by the microstructure. The PPs decay non-radiatively (dashed purple line) over long timescales. In tandem, the population of ICT_c excitons also decay to the ground-state. This can can proceed radiatively (solid green line) leading to PL, or non-radiatively (dashed blue lines). The non-radiative quenching pathway can be deconvolved into its intra- and inter-chain contributions: and we write a non-radiative rate due to intra-chain quenching which is also present in solution (dashed light blue line), and the additional non-radiative rate that arises from aggregation (dashed dark blue line).

5.5 Coherent oscillations

To discuss the origin of the difference in PLQE in films, we estimate the intra- and inter-chain components of k_{NR}, and full details are provided in Section I.6. In brief, we anticipate intra-chain quenching; including that due to defects, to be fast in films owing to the increased exciton delocalisation discussed earlier. To estimate this conservatively, we use the ratio of k_R in film and solution to scale up the intra-chain (solution) k_{NR}, and attribute any excess k_{NR} in film to inter-chain non-radiative pathways. The external QEs of the different decay processes in films are shown in Figure 5.6 (right). For M_0, the inter-chain non-radiative QE dominates, and over 80 % of excitons decay through this pathway. This is the factor which really decreases the PLQE, and not a high PPQE which is relatively small by comparison. On the other hand, M_1 has a much lower inter-chain non-radiative QE owing to its suppressed intermolecular interaction, and PLQE is high because this pathway is slow.

The temperature evolution of the PLQE indicates that the inter-chain non-radiative rate is thermally activated. We observe that the PLQE of M_0 at 4 K increases to 3.5× its value at 300 K, shown in Figure I.9. This cannot be explicitly assigned to a decreased inter-chain k_{NR} at low temperatures, since we also expect the intra-chain k_{NR} to change as the spectrum redshifts at low temperature. However, k_{NR} in M_1, whose intra-chain non-radiative temperature evolution should be similar to M_0, increases by only 2.7× at 4 K. This implies thermal activation of the inter-chain non-radiative rate,

although quantifying the activation energy meaningfully would require a more detailed investigation.

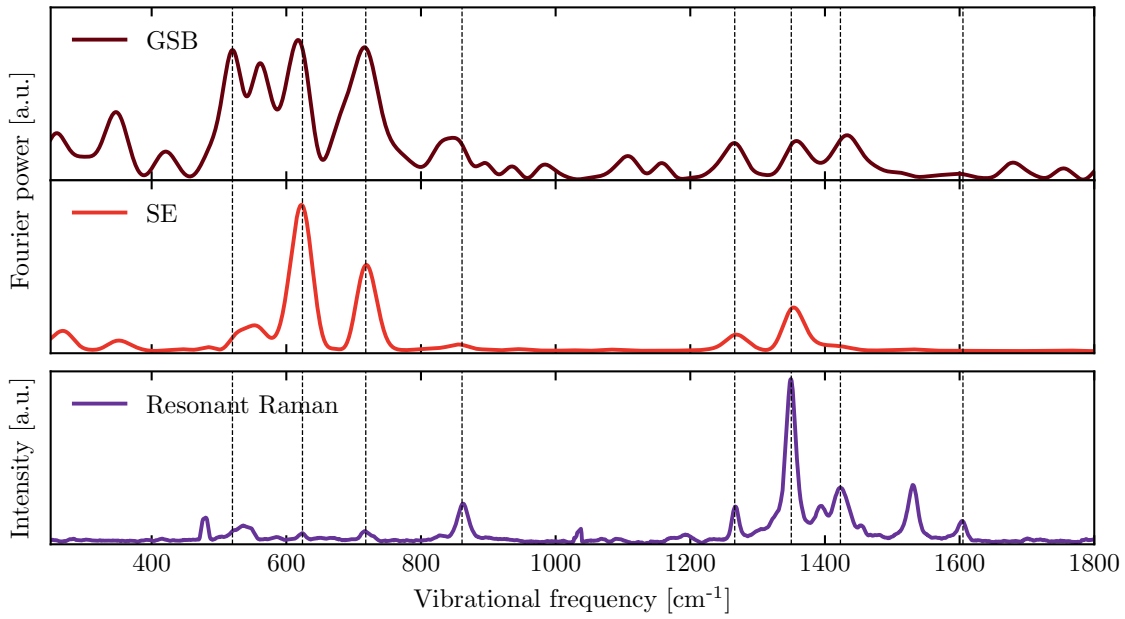

Figure 5.7 Vibrations in M_0. Fourier power of coherent oscillations (top) in GSB (dark red) and SE (light red) spectral domains, determined by ultrafast TA, and resonant Raman intensity (violet; below). Various modes present in both ground- and excited-states are highlighted by vertical dashed lines.

It has been shown in other systems that strong exciton-phonon coupling in the excited state can lead to very fast non-radiative decay.[219, 220] In order to determine the strength of any such coupling, we use temporally-compressed optical pulses with (sub-40 fs) duration shorter than the oscillation period of most phonons to search for coherent oscillations in ultrafast TA decay kinetics. Subtracting the decay signal and taking a Fourier transform of the residual, we observe that various modes are strongly active during decay. These modes have a strong electron-phonon coupling, and it is likely that non-radiative decay is mediated via these modes. We resolve the different Fourier power spectrum in the GSB and SE features in Figure 5.7 (top).[221] The SE power spectrum shows strong exciton coupling to various excited-state phonons, and the GSB shows strong coupling to a combination of ground- and excited-state phonons. Interestingly, the excited-state exciton wavefunction couples strongly to modes in two bands: (i) low ($520 - 827$ cm^{-1}) and (ii) high energy ($1265 - 1430$ cm^{-1}). Various modes in these bands are highlighted in Figure 5.7 by dashed vertical lines. By comparison

with ground-state vibrational DFT calculations, we assign the low energy modes to atomic deformations of the polymer backbone in the out-of-sp^2-plane direction, whereas the high energy modes are the in-plane Peierls distortions. Concomitantly, the latter is strongly Raman-active, but the former is more IR-active and couples more strongly to a transition electric dipole moment. It is likely that these modes are responsible for the fast non-radiative decay observed here. Interestingly, these coherent oscillations are extremely weak in M_1, shown in Figure I.10, and this observation is discussed in Section I.8 in more detail.

The precise mechanism of the inter-chain non-radiative decay is not the focus of this chapter, although we speculate that it may proceed via conical intersections of S_1 and S_0 bands which are thermally accessible in the case of closer packing in M_0. This interpretation is consistent with our observations that k_{NR} is increasing with greater polymer chain interaction, with temperature, and with strong exciton-phonon coupling in the excited state. These observations cannot be explained by the formation of polaron-pairs or triplets, which are each formed in small yields in this polymer.

5.6 Conclusions

The photophysical decay processes and charge transport of hexadecyl- and the novel hexadecylbenzyl-substituted IDT-BT are nearly the same, despite the difference in observed film PLQE. Disorder-free transport and a high mobility > 0.5 cm^2/Vs in M_1 are observed alongside the highest film PLQE of 18 % reported for any polymer semiconductor with such a high mobility. Additionally, we observe the largest exciton diffusion length of 16.7 nm reported for any donor-*alt*-acceptor polymer.

Upon excitation, long-lived ($s = 0$) inter-chain polaron-pairs are formed promptly (before 500 fs) with a small yield less than 4 %, and do not limit the PLQE substantially. Instead, the non-radiative component of the emissive species increases substantially with inter-chain coupling. This internal conversion is likely to be mediated by a combination of in-sp^2-plane Raman-active bond deformations and out-of-sp^2-plane IR-active modes, and is strongly temperature-dependent. The substitution of bulky sidechains substantially increases the optical suitability of this class of material for OLED and OPV devices, rendering it promising for amorphous polymer optoelectronic applications.

5.7 Contributions

Dr. Jasmine Rivett and Mr. Qifei Gu measured the TA data, Drs. Johannes Richter and Chaw-Keong Yong measured the ultrafast PL and Dr. Aditya Sadhanala measured the PDS spectra. Dr. David Harkin, together with this author, designed the experiments, and helped measure the PLQEs, PL lifetimes, and the exciton diffusion length. Mr. Sam Schott assisted with the LI-ESR measurement and Dr. Katharina Broch measured and analysed the X-ray crystallography data.

Chapter 6

High mobility highly luminescent amorphous polymers

6.1 Introduction

Developing our discussion in Section 4.1, amorphous polymer semiconductors have attracted significant attention in recent years, and materials which combine a high charge carrier mobility (μ) and a high fluorescence quantum efficiency (Φ) are highly sought after for optoelectronic applications.[138, 222–224] Amorphous polymer organic light-emitting diodes (OLEDs) and organic photovoltaic devices (OPVs) benefit from the tuneability of the energy gap,[132–134] high solubility,[134, 135] and operational stability[135, 136] of amorphous polymers, however materials in state-of-the-art devices are usually selected for their individually optimised Φ or μ values.[225] Materials which have both high Φ and μ are uncommon. This has hampered efforts to simplify device architectures,[212] and to achieve high brightness OLEDs towards electrically driven organic lasing applications.[226] There is an apparent trade-off between these two desirable properties.

Central to this trade-off is the degree of inter-chain interaction. Strong electronic coupling between chains, mediated by close chain packing, is thought to be crucial for realising high μ in amorphous systems where charge transport is limited by the ability to hop between adjacent chains.[80, 227] However, strong inter-chain interactions have been shown to lead to low Φ. Studies have attributed this to (i) increased exciton diffusion to pre-existing chemical defects or exciton quenching 'trap' sites[32, 51] and (ii) to an additional density of inter-chain states with low oscillator

strength,[32, 150, 205, 206, 228] or (iii) additional fast non-radiative decay channels arising from intersecting bands,[145, 146, 148] and (iv) the suppression of radiative decay pathways in some cases.[38] The relative quantum efficiency (QE) of each pathway is highly morphology dependent, making meaningful comparisons between studies challenging.[150]

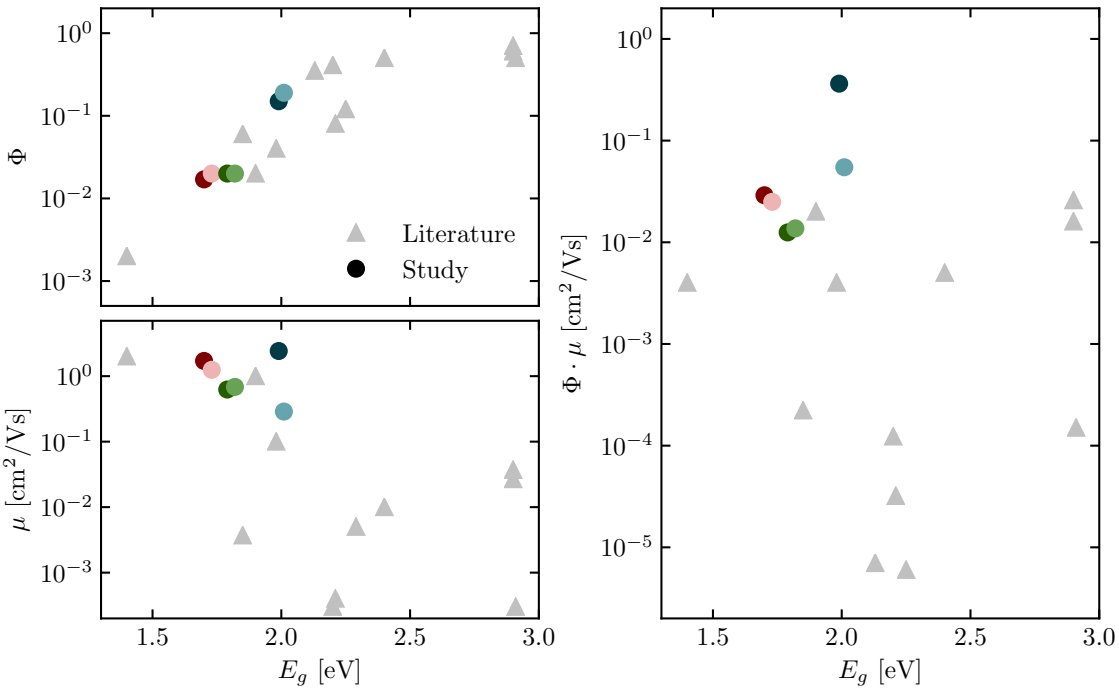

Figure 6.1 Scope of study and summary of literature. Φ (top left) and μ (bottom left) against E_g, and $\Phi \cdot \mu$ (right) against E_g. Literature values (triangles) and this study (circles).

Another aspect of the trade-off is the energy gap (E_g) of the polymer. Φ generally increases with E_g, and this trend is shown for various polymers in Figure 6.1 (top left). For Φ, the energy gap law predicts fast non-radiative decay in low E_g materials,[46] and the rate of radiative (spontaneous) emission increases with E_g.[229] Therefore, polymers with $E_g < 1.8$ eV typically have low Φ, and the most fluorescent polymers - including poly(9,9-di-n-octylfluorenyl-2,7-diyl) (F8, $\Phi = 0.65$, $E_g = 3.0$ eV[230]) and poly(9,9-dioctylfluorene-*alt*-benzothiadiazole) (F8-BT, $\Phi = 0.5$, $E_g = 2.5$ eV[213]) - have $E_g > 2.0$ eV. These polymers are also amorphous. On the other hand, in Figure 6.1 (bottom left), μ seems to decrease with increasing E_g, but this trend is less clear. Concomitantly, while F8 and F8-BT have low $\mu < 10^{-2}$ cm^2/Vs,

polymers with $\mu > 1$ cm^2/Vs such as diketopyrrolopyrrole-derivatives,[8, 66, 106] and poly(bis(3-alkylthiophen-2-yl)thienothiophene) (pBTTT)[27] have $E_g < 1.8$ eV and low Φ. While a high E_g can lead to limitations in charge injection and increased charge carrier trapping due to atmospheric species,[26, 52] this behaviour does not seem to hold for small molecule semiconductor systems, where high E_g, μ, and Φ have been observed simultaneously.[231]

To evaluate materials, we define a new figure of merit, the product of Φ and μ shown in Figure 6.1 (right) combining the highest published values for polymers with the materials in this study. All of the materials studied here have $\Phi \cdot \mu \sim 10^{-2} - 10^{-1}$ cm^2/Vs, comparable to the highest reported $\Phi \cdot \mu$ of 2.6×10^{-2} cm^2/Vs for a F8 derivative.[138] One polymer, C_{16}TIF-BT has a higher $\Phi \cdot \mu = 0.38$ cm^2/Vs by more than an order of magnitude, owing to a high $\Phi = 0.15$ and μ in thin films. To the best of our knowledge, C_{16}TIF-BT is the only polymer reported so far with $\mu > 1$ cm^2/Vs and $E_g > 2.0$ eV.

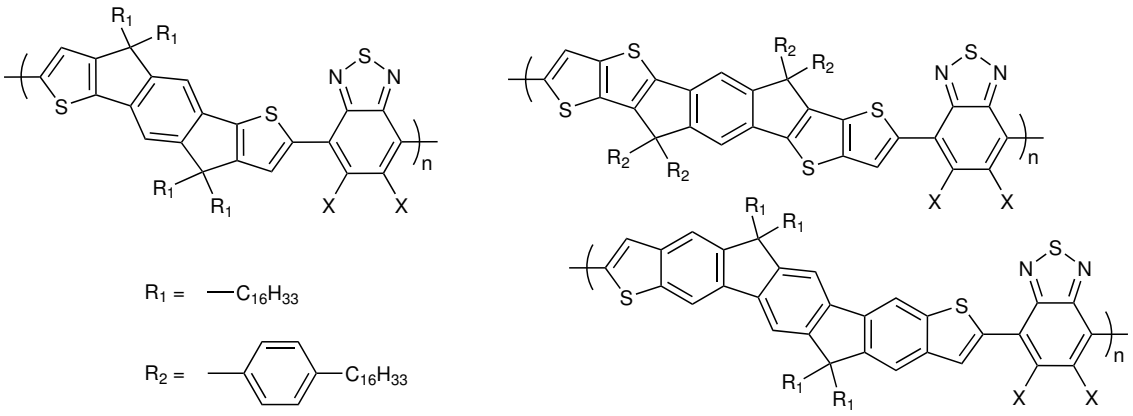

Figure 6.2 Structures in this study; IDT-X$_2$BT with hexadecyl sidechains (top left), IDTT-X$_2$BT with hexadecylbenzyl sidechains (top right), and TIF-X$_2$BT with hexadecyl sidechains (bottom right). X = H, F.

In this chapter, we extend the understanding developed by the previous two chapters of the interplay between carrier mobility and fluorescence. By extending the backbone of C_{16}IDT-BT via of a thiophene or benzene ring yields C_{16}IDTT-BT and C_{16}TIF-BT respectively. Substitution of hexadecylbenzyl sidechains on C_{16}IDTT-BT yields PhC_{16}IDTT-BT, and the chemical structures of these polymers are shown in Figure 6.2. In this chapter, these materials, together with the perfluorinanted-benzothiadiazole

(F_2BT) analogues, are characterised electrically and photophysically.[1] Here, we explore the interplay between the μ, Φ, and nature of the aggregation in amorphous donor-acceptor polymers, and how the two figures of merit are not really mutually exclusive. By inserting fused rings, we show how increasing the electron density on the donor subunit can lead to increased inter-chain wavefunction overlap, and a higher μ in amorphous polymers, while simultaneously increasing E_g and Φ.

6.2 Electrical characterisation

We use organic field-effect transistor (OFET) devices to confirm that all these materials have a high p-type mobility comparable to (or exceeding) that of amorphous-Si.[232] In our devices, we observe that contact resistance and threshold voltages are closely related to appropriate solution processing of these materials, and care was taken not to overestimate the mobility of our optimised devices where they deviate from MOSFET behaviour. Meaningful extraction of the mobility in this work is discussed in detail in Section II.1, where we show all the transfer, output, and mobility characteristics for the polymers in this work in Figure II.1. A detailed comparison of the two highest performing materials IDT-H_2BT (pink) and TIF-H_2BT (blue) in linear (dark) and saturation (light) regimes, is shown in Figure 4.18, and discussed in detail in Section 4.7.2.

To summarise briefly, low threshold voltages ($|V_{\mathrm{Th}}|$), sharp subthreshold swings and on:off-current ratios $\sim 10^5 - 10^7$ indicate good injection into the polymers with low trap densities for both materials, and high on-currents approaching 1 mA suggest high μ.[2] For IDT-H_2BT, there is little deviation from MOSFET behaviour, and it shows a field-effect mobility exceeding 1.7 cm^2/Vs independent of hole accumulation in the linear and saturation regime.[3] TIF-H_2BT is less ideal in the OFET architecture, and there is a strong dependency of the field-effect mobility on the gate voltage. Additionally, increased contact resistance due to a deeper-lying highest occupied molecular orbital

[1] In this chapter, only the C_{16}IDT-X_2BT, PhC_{16}IDTT-X_2BT, and C_{16}TIF-X_2BT sidechain derivatives are considered, and so we hereunder refer to them as IDT-X_2BT, IDTT-X_2BT, and TIF-X_2BT (with X = H, F) for brevity.

[2] The OFET aspect ratio is 50 and gate capacitance of 37 $\mu F/m^2$.

[3] In this chapter, for simplicity, the mobility values reported are the conservatively estimated effective mobilities, as defined in Equation 3.5.

(HOMO) energy leads to an inflated value of the mobility where $|V_{GS}| \approx 20 > |V_{Th}|$ and the linear and saturation extractions converge to 2.4 cm^2/Vs in the regime where $|V_{GS}| \gg |V_{Th}|$. However, the contact resistance is small, and the output transconductance characteristics in Figure II.1 lack a sigmoidal artefact near $V_{DS} = 0$ V.

The increasing mobility of TIF-H_2BT, or superlinear $\sqrt{I_{DS}} - V_{GS}$ behaviour at high accumulations, is curious. While this has been attributed to a broad transport density of states,[91, 233, 234] or a Coulomb effect in semicrystalline polymers,[235] its origin in these low-disorder near-amorphous polymers is unclear. We note that conventional extraction using a linear fit to $\sqrt{I_{DS}} - V_{GS}$ is inappropriate here, and yields $\mu > 6$ cm^2/Vs which is inconsistent with the increase of only ~ 50 % in on-current values between IDT-H_2BT and TIF-H_2BT in saturation. Instead, $\mu = 2.5$ cm^2/Vs is in superior agreement.

By comparison, we observe a moderate decrease in μ to $\sim$ 1.1 cm^2/Vs for IDT-F_2BT. Additionally, IDTT-H_2BT and IDTT-F_2BT have similar $\mu \sim 0.75 - 0.80$ cm^2/Vs, and the lower μ here is owing to an unfavourable increased chain stacking distance due to increased sterical hindrance from hexadecylbenzyl sidechains, seen before for IDT-H_2BT.[6] Finally, we observe a substantial decrease in μ between TIF-H_2BT and TIF-F_2BT, and the latter has lowest $\mu < 0.4$ cm^2/Vs. However, the high ionisation potential of TIF-F_2BT (of 5.8 eV) leads to increased contact resistance, and also leaves holes particularly vulnerable to deep atmospheric trap states.[180] The OFET data for these materials and the extraction are shown in Figure II.1.

6.3 Optical characterisation

Absorption spectra are shown in Figure 6.3 (left). Using a scattering-free photothermal deflection method described separately,[236] we measure the absorption coefficient (α) over orders of magnitude in intensity. In donor-acceptor polymers, the E_g is defined where α decreases quickly by a factor of $10^2 - 10^3$, and (approximately) corresponds in energy to the on-chain (internal) charge transfer state (ICT) where the hole is localised on the donor and the electron is localised on the acceptor.[237] We observe that increasing the donor electron density from IDT-H_2BT (top) to IDTT-H_2BT (middle) to TIF-H_2BT (bottom) increases the E_g as it decreases the relative push-pull character

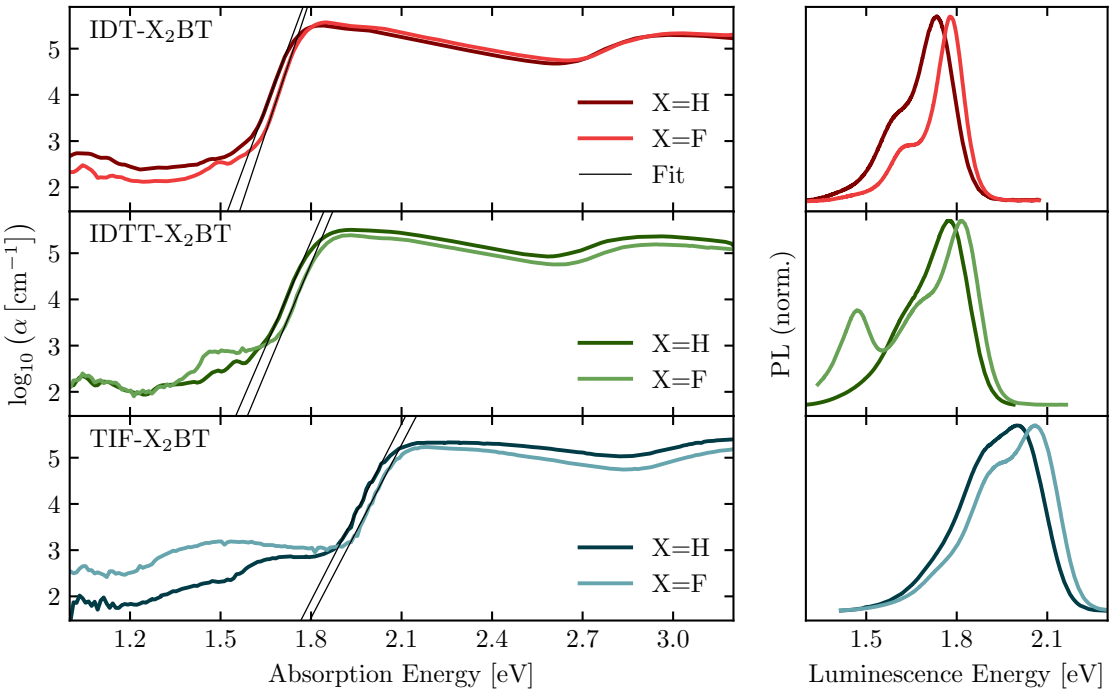

Figure 6.3 Absorption (left, determined by PDS; with Urbach energy extraction) and PL spectra.

of the repeat unit. Furthermore, substitution of H_2BT (dark) for F_2BT (light) slightly increases E_g for each polymer, and has been shown to increase the ionisation potential of the polymer (because of its electron-withdrawing properties) without substantially changing the lowest unoccupied molecular orbital (LUMO) energy.[182–184] Using photoluminescence (PL), we optically pump well above the E_g-edge ($E_{\text{pump}} = 3.05$ eV) and measure time-integrated spectra using very low fluence ($f_{\text{pump}} \sim 2$ µJ/cm^2). These spectra are normalised to their maximum in Figure 6.3 (right). The materials all had a low Stokes shift $\sim$ 100 meV, so the trends in spectral shifts were as for the E_g. By fitting the α tail over the E_g edge (using Equation 3.6), we extract the Urbach energies of E_U from 25 ± 2 meV for IDT-H_2BT, to 27 ± 2 meV for IDTT-H_2BT and 31 ± 3 meV for TIF-H_2BT. These values did not change upon substitution of F_2BT.

The differences observed in Φ are profound, and follow the energy gap law. While IDT-H_2BT has the lowest $\Phi = 0.017$, elongation of the backbone and substitution of F_2BT increases Φ monotonically to the high values of 0.15 and 0.19 for TIF-H_2BT and TIF-F_2BT respectively. The optical transitions in conjugated organic materials often couple strongly to C=C ring stretching modes ($\sim 1200 - 1400$ cm^{-1}

$\sim 0.15 - 0.20$ eV), and we observe a vibronic progression of decreasing PL intensity arising from $S_1(\nu = 0) \rightarrow S_0(\nu = m)$ transitions (hereunder $I_{0\rightarrow m}$) with $m = 0, 1, 2$ centred at 1.73, 1.59, and 1.44 eV in IDT-H_2BT and 1.99, 1.85, and 1.70 eV in TIF-H_2BT respectively. In the absence of inter-chain interactions, the Franck-Condon model applies,[35] and the vibronic progression is given by Equation 2.26. However, $I_{0\rightarrow 0}/I_{0\rightarrow 1}$ can be suppressed by both exciton localisation[238] and H-aggregation.[38] A comparison of $I_{0\rightarrow 1}/I_{0\rightarrow 2}$ yields similar values of $S = 0.37 \pm 0.05$ for IDT-H_2BT and TIF-H_2BT, however, $I_{0\rightarrow 0}/I_{0\rightarrow 1}$ is considerably suppressed in the latter. Separately, we estimate the exciton diffusion length to be 12.8 ± 1.9 nm in TIF-H_2BT using a method described in Section I.5;[51] a modest improvement over 7.1 ± 1.1 nm for IDT-H_2BT. Therefore, increased exciton localisation for TIF-H_2BT is unlikely compared to increased H-aggregate character. A similar comparison has been made in poly(2-methoxy-5-(2-ethylhexyloxy)-1,4-phenylenevinylene) (MEH-PPV),[239] and poly(3-hexylthiophene-2,5-diyl) (P3HT).[240]

6.4 Emissive inter-chain states

In some polymers, we observe luminescence which does not come from the ICT. This is immediately clear in IDTT-F_2BT where the additional PL peak below 1.5 eV cannot be explained by the vibronic progression of the ICT. This redshifted emission pathway is not present in dilute solution measurements, but rises upon addition of non-solvent precipitating suspended aggregates in solution.[241] It is also strongly decreased upon blending the polymer with a PMMA matrix. We are confident that the origin of this luminescence is not a defect, otherwise we would expect it to be also present in solution, and only weakly modulated in intensity when blended with PMMA. We can also tune the electroluminescence ratio of the two pathways with current densities in IDTT-H_2BT OLED architectures, and further information is discussed in Section II.2. This suggests an emissive species localised over multiple chains. While the formation of inter-chain charge transfer species (CTs) has been observed before in both neat polymer systems,[205, 228, 242–244] it is uncommon for them to be emissive. Luminescence from inter-molecular CTs in OPV systems is also uncommon,[245, 246] however it has been used as a tool to probe the bulk heterojunction interfaces.[247] This additional luminescence has a corresponding sub-E_g absorption feature at 1.50 eV which is not present for IDTT-H_2BT.

Much broader sub-E_g features are observed in TIF-H_2BT and TIF-F_2BT. In the $1.3 - 1.9$ eV range, these absorptions have a similar α for IDTT-F_2BT and TIF-H_2BT, but $\sim 2\times$ stronger for TIF-F_2BT, extending deep into the energy gap. It is unclear whether unintentional doping due to impurities leads to the stronger sub-energy gap absorption, or whether these materials have a host of absorbing inter-chain CTs, and that for TIF-H_2BT and TIF-F_2BT, different conformations with a non-zero oscillator strength lead to the large bandwidth. We evaluate these premises at length in the following discussion.

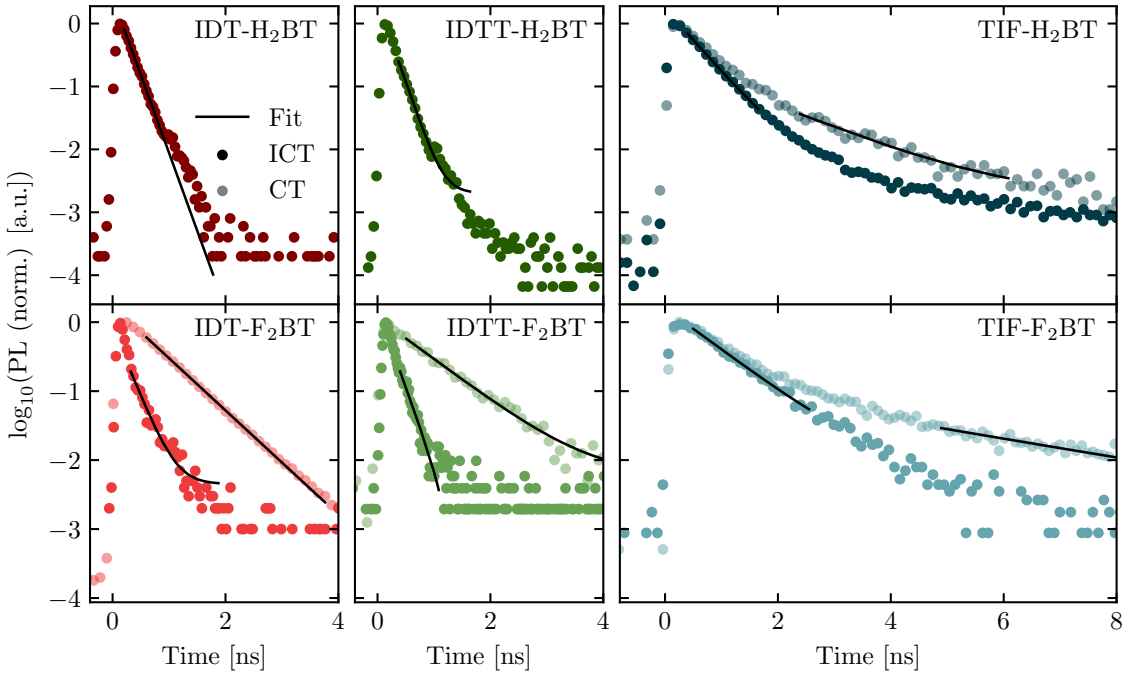

Figure 6.4 PL kinetics of materials with emission from two states; ICT (dark) and CT (light).

To confirm this picture, we use transient PL to search for inter-chain CT emission signatures in the materials. Since inter-chain CTs are likely to have a larger radius, they should also have longer decay lifetimes than for the ICTs, consistent with decreased wavefunction overlap. Using time-correlated single photon counting (TC-SPC; $E_{\text{pump}} = 3.05$ eV, $f_{\text{pump}} \sim 2$ µJ/cm^2), we measure the decay kinetics of the PL over the emissive band at different detection wavelengths. For IDTT-F_2BT, we observe that the inter-chain CT has a long lifetime (τ_{CT}) of 760 ps compared to the ICT (τ_{ICT}) which is faster than the 250 ps instrument response. This allows for

the spectral deconvolution of the two species based on their different kinetics, and uses a previously described genetic algorithm.[210] This data is summarised in Figure 6.4. This analysis is robust even when the two luminescent species have overlapping spectra, and this procedure is repeated for IDT-F_2BT ($\tau_{CT} = 560$ ps, $\tau_{ICT} < 250$ ps), TIF-H_2BT ($\tau_{CT} = 1.9$ ns, $\tau_{ICT} = 560$ ps) and TIF-F_2BT ($\tau_{CT} = 3.0$ ns, $\tau_{ICT} = 700$ ps), whose normalised spectra are shown in Figure 6.5. A limitation of this methodology is that we are unable to distinguish ICT and CT luminescence when τ_{ICT} and τ_{CT} are both less than 250 ps. So, while we do not observe luminescent CTs in IDT-H_2BT and IDTT-H_2BT using this strategy, we note that previously reported materials similar to IDT-H_2BT have $\tau_{ICT} < 250$ ps.[53] In fact, a small fluence dependency of the luminescence spectra of IDT-H_2BT confirms the presence of luminescent inter-chain CTs, and this is discussed further in Section II.2.2.

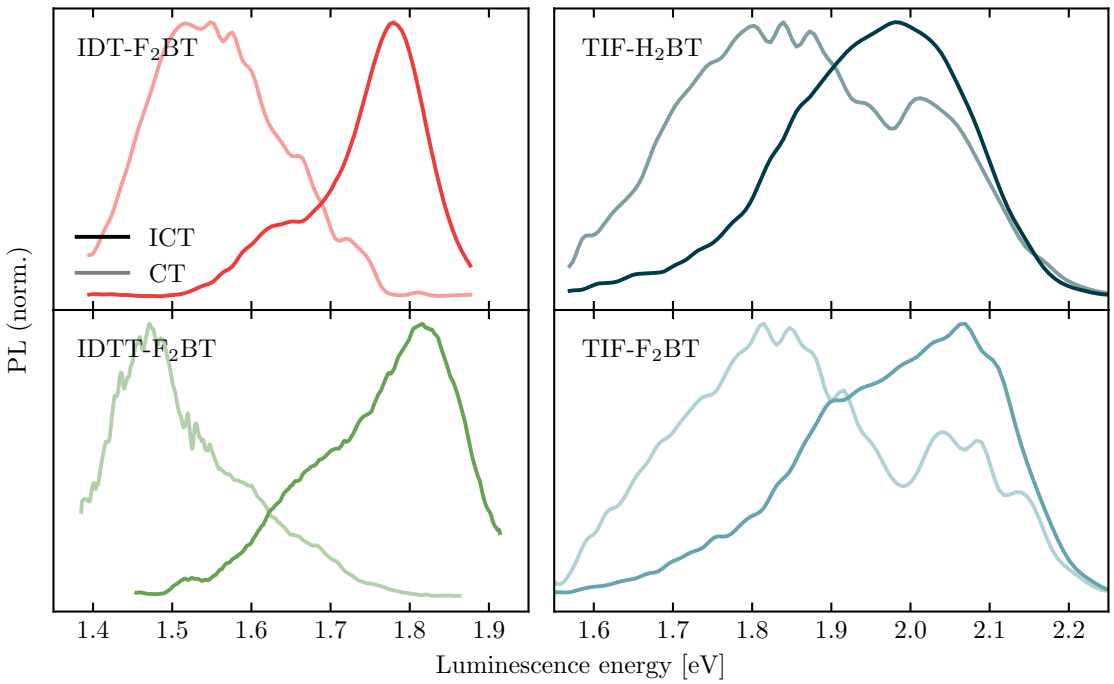

Figure 6.5 Decoupled PL spectra of materials with emission from two states; ICT (dark) and CT (light).

The photoluminescence lifetimes increase with E_g, predicted by the energy gap law. There is also strong variation in the spectral linewidth of the inter-chain CT luminescence between the materials. TIF-H_2BT and TIF-F_2BT have the broadest inter-chain CT transitions with a FWHM of $0.40 - 0.45$ eV, compared to < 0.2 eV

in IDTT-F_2BT. The FWHM of a PL transition is related to the width of JDOS weighted by the oscillator strength, and the broadband luminescence of TIF-H_2BT and TIF-F_2BT suggest a large distribution of luminescent packing microstates compared to IDTT-F_2BT. By comparison with sub-E_g absorption, this suggests that only packing microstates leading to high energy inter-chain CT transitions are luminescent, and those below 1.5 eV rather lead to non-radiative decay.

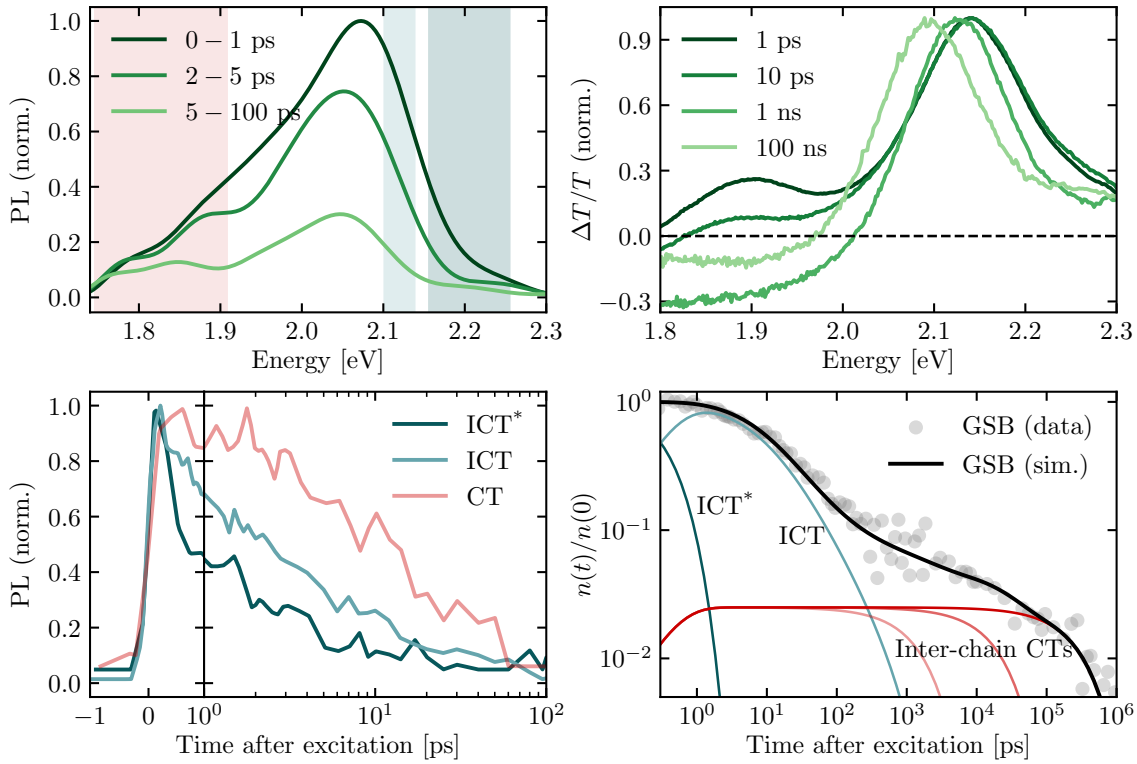

Figure 6.6 Transient optical characterisation: ultrafast PL spectra integrated over various time domains, and normalised to the maximum of the first time-slice (top left), kinetics of the ultrafast PL integrated over the energy domains shaded above (bottom left). TA spectra normalised to the maximum at various times (top right), and kinetics of GSB with population fits normalised to the maximum.

To complete the picture of inter-chain CT luminescence, we determine the timescales of inter-chain charge transfer. Using ultrafast transient grating PL (E_{pump} = 2.34 eV, f_{pump} = 25 µJ/cm^2, giving an excitation density $n_0 = 5 \times 10^{18}$ cm^{-3}), we measure the PL decay of TIF-H_2BT between 200 fs (the temporal resolution of the experiment) and 100 ps in Figure 6.6 (top left). In the first 1 ps after excitation, the broad PL spectrum peaks at 2.08 eV. Over the next 5 ps, the spectrum narrows,

decaying and redshifting to 2.04 eV, but the band below 1.85 eV does not decrease in intensity. Over the following 95 ps, the spectral maximum decays by a further 50 %, but the low-energy edge of the emission decays substantially less. At the earliest times, the ICT population we observe is not equilibrated - and is 'hot' (ICT^*) - overlapping in energy with the maximum of the absorption band, and yielding a small Stokes shift. However, by 5 ps, the thermalisation of excitons is complete and the ICT population has transferred to the luminescent intra-chain ICT population. We observe similar dynamics separately for IDT-H_2BT, discussed in detail in Section 5.3. At the earliest times, the luminescence band below 1.85 eV which contains the inter-chain CT luminescence maximum is already formed, and does not redshift during ICT population transfer. By integrating the shaded spectral windows, we show the normalised decay kinetics of three colour-corresponding energy bands in Figure 6.6 (bottom left). The bands are chosen to minimise signal mixing, and correspond to the 'hot' ICT (dark blue), 'equilibrated' ICT (light blue), and CT (light red) luminescence. To within 100 fs, all three bands rise at the same time. The decay of the hot ICT with a lifetime of 400 fs tracks the depopulation of the ICT^* state. After 1 ps, this converges to the ICT decay kinetic which decreases over the following 100 ps. The inter-chain CT decays with a longer lifetime than ICT. Importantly, this state has emission at very early times, and since the CT kinetic of decay deviates within 400 fs from the ICT, we conclude that the inter-chain CTs must be formed at least as fast as the ICT^* relaxation. This ultrafast charge transfer has been observed in other neat polymer systems.[199, 200, 248–252]

In general, we also expect charge transfer from the intra chain ICT to the inter-chain CT on timescales > 1 ps. To determine the yield of this transfer, we use ultrafast transient absorption spectropscopy (TA). Representative normalised TA spectra for TIF-H_2BT ($E_{\text{pump}} = 2.34$ eV, $f_{\text{pump}} = 25$ µJ/cm^2, $n_0 = 5 \times 10^{18}$ cm^{-3}) are shown in Figure 6.6 (top right), but all six materials behave in the same way. In the spectra, there are three spectroscopic features: (i) a ground-state bleach (GSB) above 2.0 eV, (ii) stimulated emission (SE) below 2.2 eV, and (iii) a broad photoinduced absorption over the entire probe band but increasing at low energies (PIA), with a full discussion in Section II.3.1. In brief, on the timescales of ICT luminescence, the signal is composed of all three spectroscopic features. By ~ 2 ns, the SE decays to zero, leaving a GSB which persists to $\sim$ µs, and a PIA continues to evolve over this time. While there is SE, the exciton population is mostly ICT excitons. However, when

SE is depleted, only inter-chain CTs (which have only weak SE) are left; leading to the persisting GSB. For this reason, in systems where τ_{CT} exceeds τ_{ICT} by more than $\sim 2\times$, the approximate yield of inter-chain CTs (ϕ_{CT}) can be estimated by the fraction of GSB remaining after SE has finished. A more accurate extraction methodology is discussed in Section II.3.3. In addition to the luminescent inter-chain CT with τ_{CT}, there exist several additional non-emissive inter-chain states which recombine on longer timescales. These have different absorption spectra, and leading to the PIA evolution long after τ_{CT}. This agrees well with the large bandwidth of α in the sub-E_g regime.

This kinetic picture was summarised in Figure 6.6 (bottom right) for TIF-H_2BT. The transient populations of the various exciton species are shown are simulated from coupled ODEs using measured parameters $\tau_{\mathrm{ICT}^*} = 400$ fs, τ_{ICT} and τ_{CT} for the different polymers. As discussed, additional non-emissive inter-chain CT species with $\tau > \tau_{\mathrm{CT}}$ are required to give a good GSB fit to 1 µs, and the total inter-chain CT formation quantum efficiency (ϕ_{CT}) did not vary substantially with the choice of non-emissive CT yield and lifetime. Full details of the simulation and are given in Section II.3.3 with tabulated parameters. In these materials, we observe a $\phi_{\mathrm{CT}} \sim 0.048 - 0.75$ except for TIF-H_2BT which has a higher $\phi_{\mathrm{CT}} = 0.084$. These values are in line with reported ϕ_{CT} determined in a similar way.[150]

For all of the materials in this study, ϕ_{CT} is independent of the pump fluence. While we observe that τ_{ICT} is considerably shortened with increased fluences as exciton-exciton (bimolecular) annihilation occurs, the GSB converges to the same value after SE has finished, shown in the supplementary information for all our materials. The independency of ϕ_{CT} on fluence indicates that inter-chain CTs persisting after ICTs have recombined are (i) formed linearly with excitation density, (ii) non-interacting and likely trapped, and (iii) not formed in appreciable yields indirectly from the ICT state, which is depleted by bimolecular recombination at high excitation densities. This observation is discussed in more detail in Section II.3.2.[4] Furthermore, in these systems, neither ϕ_{CT} nor τ_{ICT} depend on the wavelength of the pump (E_{pump}), and the photophysics after exciton cooling by ~ 10 ps is the same.

[4]This is also discussed in Section 5.3 in the context of IDT-H_2BT.

6.5 Exciton dynamics

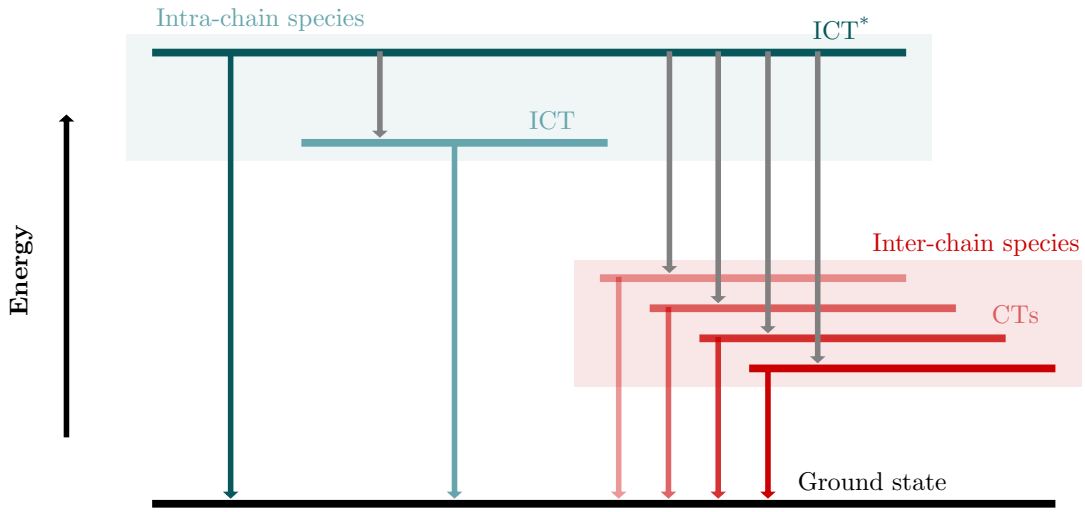

Figure 6.7 Energy level diagram: Intra-chain species (ICT* and ICT) are shaded in blue, and inter-chain species (CTs) in red. Grey arrows indicate cooling processes, whereas coloured arrows represent decay; which has, in general, a radiative and a non-radiative component.

We summarise the exciton dynamics from 200 fs−1 µs timescales in Figure 6.7. Nascent excitons initially populate an unequilibrated (or 'hot') intra-chain charge transfer state (ICT*). Over the first $\sim$ 400 fs, some excitons undergo charge transfer to form inter-chain CTs with quantum yield ϕ_{CT}, where the ϕ_{CT} is likely to depend strongly on the inter-chain morphology, but not E_{pump} or n_0. Excitons which are not transferred to inter-chain states thermalise to the 'cooled' intra-chain ICT where they decay to the ground state via radiative and non-radiative pathways (and bimolecularly in the case of higher f_{pump}). In tandem, each inter-chain species decays directly to the ground state, since a cascade to lower energy states is made impossible by the occupancy of lower-energy inter-chain CTs which are formed early and live longer. This is due to a weaker wavefunction overlap in these states. Finally, after the luminescent inter-chain CTs decay, non-emitting CTs with longer lifetimes decay on longer timescales until there are no more photoexcited states.

In this system, Φ can be expressed in terms of the quantum efficiencies of (i) transfer ($\phi_{i\to j}$ from state i to j) and (ii) PL ($\phi_{i\to 0}$ from state i to the ground state). In the limit that $\phi_{\mathrm{ICT}^*\to 0}$ and $\phi_{\mathrm{ICT}\to\mathrm{CT}}$ are small, $\phi_{\mathrm{ICT}^*\to\mathrm{CT}} \to \phi_{\mathrm{CT}}$, the total quantum efficiency

for inter-chain CT formation defined earlier, and

$$\Phi = (1 - \phi_{\mathrm{CT}}) \cdot \phi_{\mathrm{ICT}\to 0} + \phi_{\mathrm{CT}} \cdot \phi_{\mathrm{CT}\to 0} \tag{6.1}$$

in the case of negligible up-conversion. Furthermore, the ratio of $\phi_{i\to 0}$ for i luminescent states can be expressed in terms of the spectrally integrated PL intensities (I_i) and decay lifetimes (τ_i) assuming first-order dynamics

$$\frac{\phi_{\mathrm{ICT}\to 0}}{\phi_{\mathrm{CT}\to 0}} = \frac{I_{\mathrm{ICT}}}{I_{\mathrm{CT}}} \cdot \frac{\phi_{\mathrm{CT}}}{1 - \phi_{\mathrm{CT}}} \tag{6.2}$$

Therefore, independent measurement of I_i and Φ, τ_i, and ϕ_{CT} from PL spectra and decay kinetics, and TA spectroscopy respectively allows for the extraction of the PLQEs (ϕ_{PL}) of both the intra-chain ICT and inter-chain CT luminescence pathways. Full details of the methodology are given in Section II.3.3.2. We note, however, that due to our inability to distinguish between luminescent and 'dark' inter-chain CTs, we underestimate the true ϕ_{PL} of the emissive inter-chain CTs, and hereunder present a lower-bound on the ϕ_{PL} of the inter-chain CT luminescence.

6.6 Luminescence quantum efficiencies

In Figure 6.8 (top), we show the dependency of the intra-chain ICT and inter-chain CT ϕ_{PL} on the energy gap of the transition (determined by the energy of the PL spectral maximum). The trend is clear, and for intra-chain species, the ϕ_{PL} increases with energy gap, consistent with the energy gap law. We note that the fluorination of the acceptor results (in most cases) in the increase in the ϕ_{PL}, but it also increases the intra-chain ICT energy gap. It is therefore not clear whether explicitly decreasing the concentration of high-frequency C-H stretches (thought to be important for exciton quenching[253, 254]) or the increase to the energy gap upon fluorination is responsible for the increase in ϕ_{PL}; although both results are explained by different interpretations of the energy gap law. This trend also holds for inter-chain CT species, and both ICT and inter-chain CT ϕ_{PL} follow the same quasi-exponential relation with the transition energy gap. Accordingly, we see good agreement between $\phi_{\mathrm{PL}} \sim 0.02$ of the ICT of the polymers with IDT-H_2BT (dark red), IDT-F_2BT (light red) and IDTT-H_2BT (dark green), IDTT-F_2BT (light green), and the inter-chain CT of TIF-H_2BT (dark blue),

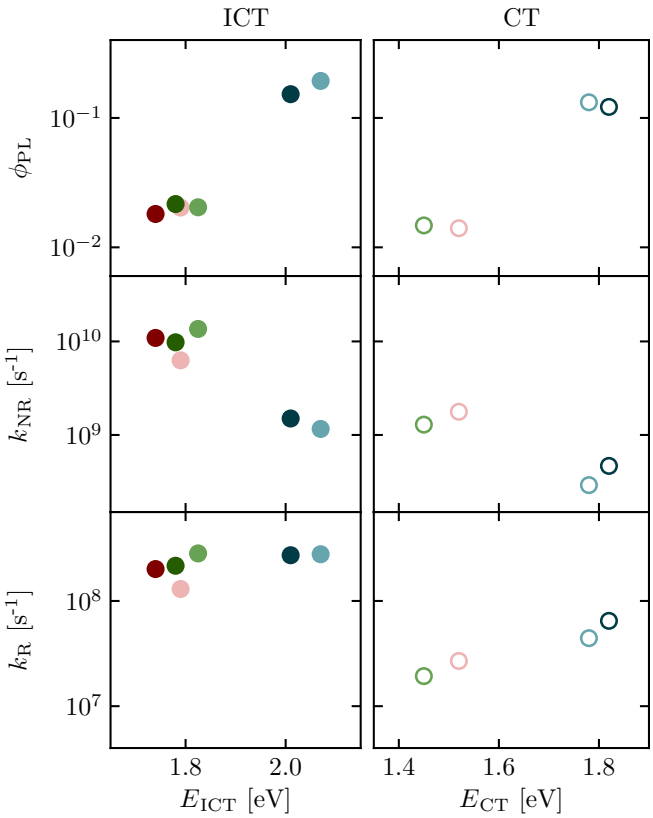

Figure 6.8 Extracted decay parameters: Intra- (left) and inter-chain (right) excitons parametrised in terms of the luminescence energy E. The PLQE of the transition (top), the non-radiative rate of decay of the state (middle) and the radiative rate of decay (bottom).

each with luminescence centred near 1.8 eV.

To unpick this observation, we determine the radiative (k_R) and non-radiative (k_{NR}) rates of exciton decay. In the absence of further energy transfer, decay kinetics are first-order, and Equation 3.12 applies. We plot k_{NR} against the luminescence energy in Figure 6.8 (middle). In intra-chain ICTs, k_{NR} is generally high. This is particularly pronounced for transitions below 1.9 eV, and is responsible for the short τ_{PL} and low ϕ_{PL}. As the PL energy increases, k_{NR} decreases by an order of magnitude for transitions at $\sim$ 2.0 eV. This behaviour is predicted by the energy gap law, as strong wavefunction overlap with the ground state at low energy gaps manifests as a high k_{NR}. By comparison, k_{NR} for inter-chain CTs are very low at an equivalent energy of transition. Around 1.8 eV, the k_{NR} of the inter-chain CTs for TIF-H_2BT and TIF-F_2BT (light blue) is $\sim 25\times$ slower than for intra-chain ICT PL near 1.8 eV.

This indicates a strong dependency of the non-radiative decay rate on the exciton geometry, and suggests that the inter-chain CT wavefunction has decreased coupling to high energy stretches which quench excitons. This assertion is also supported by the smaller decrease in k_{NR} for inter-chain CTs with increasing energy than for the intra-chain ICTs. Nonetheless, the energy gap law still applies for inter-chain CT transitions, and explains the decrease in non-radiative rate seen when moving from NIR to red transitions.

We show k_{R} in Figure 6.8 (bottom). For intra-chain ICTs, k_{R} is nearly independent of transition energy. The radiative rate is approximately constant at $\sim 10^8$ s^{-1}. For excitons, k_{R} arises directly from the degree overlap of hole and electron wavefunction. An unchanging k_{R} implies that for all the donor-acceptor systems studied here, the wavefunctions overlap to a similar degree. The HOMO and LUMO wavefunctions in these donor-acceptor polymers have the same geometric motif: the HOMO is diffuse and delocalised over the coherence length of the backbone, and the LUMO wavefunction is localised on the acceptor unit. Therefore, k_{R} is determined by the donor-acceptor chemistry, and it is unsurprising that it did not vary with the transition energy.

For inter-chain CTs, k_{R} is determined by the same physics. If k_{R} is small, there is a low wavefunction overlap between electron and hole, and if k_{R} is fast, it is because the wavefunctions overlap strongly. For all inter-chain CTs, k_{R} is lower than for ICTs, since CTs involve a HOMO and LUMO on separate chains which are further apart. We measured a radiative rate of TIF-H_2BT which is substantially higher than for IDT-F_2BT and IDTT-F_2BT, and higher even than TIF-F_2BT.

Since it arises directly from wavefunction overlap, we can use the inter-chain CT k_{R} as a powerful probe for the degree of electronic coupling at close-crossing points. Since close spacing is likely to result in the most luminescent CTs, our treatment of CTs is most sensitive to points in the polymer microstructure which are likely to mediate charge transport between chains. This suggests that TIF-H_2BT has a greater electronic mixing between chains at close crossing points than the other polymers in this study, rather than simply a higher density of close-crossing points. This is likely to be the origin of the superior μ observed in TIF-H_2BT over IDT-H_2BT and IDTT-H_2BT. This increased inter-chain wavefunction mixing seems to (i) increase with the length of the backbone between IDT-F_2BT and TIF-H_2BT and (ii) decrease

with increased push-pull polarisation between TIF-H_2BT and TIF-F_2BT, which suggest that increased donor electron density contributes to increased wavefunction delocalisation between chains. Also, (iii) this effect is hampered by sidechain sterical hindrance, which we speculate contributes to the lower k_R observed in IDTT-F_2BT.

While ~ 20 % of the PL proceeds from the inter-chain CT pathway, the high Φ in TIF-H_2BT arises from the high $\phi_{PL} > 0.16$ of the ICT. Since ICT luminescence efficiency is determined by the suppression of k_{NR} rather than increased k_R, its high Φ is owing to the energy gap law with $E_g \sim 2.0$ eV. The increased E_g is achieved by increasing the electron density on the donor, which decreases the overall polarisation of the polymer repeat unit. Concomitantly, the elongated repeat unit allows for a higher degree of wavefunction overlap at close-crossing points between chains, giving an improved inter-chain CT k_R and therefore μ. Ultimately, for a system with redshifted inter-chain CT luminescence (with $\phi_{PL} \sim 0.03$), increasing ϕ_{CT} decreases Φ. However, a near-amorphous TIF-H_2BT benefits from a generally low ϕ_{CT} compared to $\phi_{CT} > 0.3$ in semicrystalline polymers that contain lamellae.[150] This allows for the simultaneous improvement of Φ and μ, since aggregation-induced non-radiative effects are limited in the absence of long-range crystalline order and a high ϕ_{CT}.

6.7 Conclusions

We report three materials with the highest $\Phi \cdot \mu$ for conjugated polymers. By solving the rate equations governing exciton dynamics, we report that all amorphous donor-acceptor systems studied here form inter-chain states with $\phi_{CT} < 0.1$, and that some of these states are luminescent with $\phi_{PL} > 0.03$. We observe that k_{NR} for red and NIR transitions is typically fast for intra-chain excitons, but much slower for inter-chain excitons where exciton coupling to quenching on-chain vibrations is likely to be weaker. We use k_R of inter-chain CT luminescence as a probe to show strong wavefunction mixing at close-contact points, and suggest this as the origin for the highest mobility in TIF-H_2BT compared to IDT-H_2BT. We demonstrate how low mobility can be decoupled from E_g, and propose backbone elongation leading to increased inter-chain wavefunction overlap and a higher E_g as a design rule to increase Φ and μ together.

6.8 Contributions

Dr. David Harkin measured the exciton diffusion length, and together with this author measured the PLQEs and decay lifetimes. Dr. Mark Nikolka fabricated and measured FETs together with this author, and Mr. Alexander Gillett measured TA together with this author. Dr. Aditya Sadhanala measured the PDS, and Dr. Johannes Richter measured the ultrafast transient grating PL in this chapter. Dr. Hu Chen and Prof. Iain McCulloch provided IDT-H_2BT, TIF-H_2BT, and TIF-F_2BT, and Dr. Aurélie Morley and Merck Chemicals Ltd. provided IDT-F_2BT, IDTT-H_2BT, and IDTT-F_2BT.

Chapter 7

Vibrations in organic emitters

7.1 Design of TADF materials

Organic emitters which show thermally-activated delayed fluorescence (TADF) have emerged as a strategy to harness the 75 % triplet yield following charge recombination in organic light-emitting diodes (OLEDs) for emission.[22, 255] Unlike phosphorescent materials, the efficiency of TADF materials relies on reverse intersystem crossing (rISC) to repopulate the more emissive singlet state, and phosphorescence is not often observed at room temperature.[256] In this respect, the photophysics of these 'third generation' OLED materials differs substantially from materials which maximise phosphorescence, introduced in Section 1.2. In the case of TADF emitters, highly efficient luminescence requires rISC, or $T_1 \rightarrow S_1$ up-conversion, and therefore, that the singlet-triplet energy gap $\Delta E_{\mathrm{ST}} = E(S_1) - E(T_1)$ is smaller than $\sim k_B T$.[257] Several all-organic emitters have been reported recently whose high fluorescence QE and TADF properties lead to very high electroluminescence quantum efficiencies in OLEDs, in some cases between $19 - 37$ %.[21, 258]

7.1.1 Design rules

Efficient luminescence in TADF materials has two facets; (i) decay of the singlet should be strongly emissive, and (ii) rISC should be fast. For decay of the singlet exciton to be emissive, the radiative rate of the singlet $k_{\mathrm{R}}(S_1)$ should substantially outcompete the singlet and triplet non-radiative rates, $k_{\mathrm{NR}}(S_1)$ and $k_{\mathrm{NR}}(T_1)$. From the energy gap law, the high energy gap in blue emitters ensures a low $k_{\mathrm{NR}}(S_1)$. However,

$k_{\mathrm{R}}(S_1)$ is directly related to the oscillator strength ($f_{\mathrm{osc.}}$), and is only fast in the case of strong wavefunction overlap of highest occupied (HO) and lowest unoccupied (LU) molecular orbitals (MOs). For rISC to be fast, ΔE_{ST} should be small to minimise the energy barrier to upconversion, since $\ln(k_{\mathrm{rISC}}) \sim \Delta E_{\mathrm{ST}}/k_B T$. However, even when the T_1 and S_1 are degenerate, the conservation of the spin angular momentum presents a problem. It is surprising that ISC and rISC occur efficiently in the absence of heavy elements, and the mechanism is thought to involve a combination of the hyperfine interaction (~ 0.1 µeV) and spin-orbit coupling ($\sim 10 - 100$ µeV),[259, 260] although the latter is likely to dominate.[261]

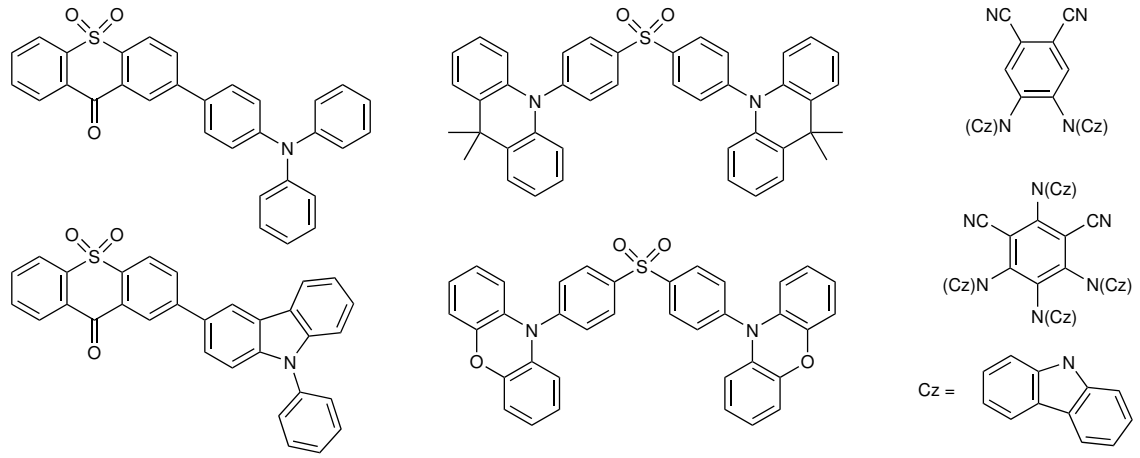

Figure 7.1 Structure of various TADF materials: donor-acceptor class (left; TXO-TPA top, TXO-PhCz bottom), donor-acceptor-donor class (centre; DMAC-DPS top, PXZ-DPS bottom), and 'Adachi' materials (right; 2CzPN top, 4CzIPN bottom).

7.1.2 Charge transfer motif

All reported TADF materials have a similar structural motif. Some of these are shown in Figure 7.1. Electron-withdrawing units, typically sulfonyl, carbonyl and nitrile groups, are substituted onto the acceptor subunit, and electron-donating systems, typically based on carbazole, phenazine, phenoxazine and triphenylamine are used as the donor subunit. Donor and acceptor subunits are linked, usually by a σ-bridge, to yield a polarised small molecule whose excitons have strong intramolecular charge-transfer (CT) character. To a great extent, this partitions the hole and electron over donor and acceptor respectively.[262] Loosely, there are three classes of TADF small molecules; the (i) donor-acceptor, including materials TXO-TPA and TXO-PhCz,

(ii) donor-acceptor-donor, including DMAC-DPS and DMAC-PXZ, and (iii) the 'Adachi' materials (including 4CzIPN) which are centred around a benzene ring, which can show character of both.[263]

In the limit that an exciton is pure CT, the exchange energy (which increases with HOMO and LUMO overlap, as discussed in Section 2.2.6) vanishes, and singlet and triplet excitons become degenerate: $\Delta E_{\mathrm{ST}} \to 0$. However, since $f_{\mathrm{osc.}}$ depends on the same quantity via Fermi's golden rule, CT excitons also have vanishing luminescence. This is the reason for the low $k_{\mathrm{R}}(S_1) \sim 10^7$ s^{-1} observed in the best TADF materials, whereas even donor-*alt*-acceptor polymer systems routinely have higher k_{R} values by an order of magnitude. Furthermore, assuming SOC as the prevailing mechanism for (r)ISC, $k_{\mathrm{(r)ISC}} \sim \langle T_1|\hat{H}_{\mathrm{SOC}}|S_1\rangle$ where $\hat{H}_{\mathrm{SOC}}$ is the SOC perturbation to the spinless hamiltonian for the system. El-Sayed's empirical rules forbid a change of spin angular momentum for electronic states with a similar nature,[264] and for π-π^* CT states, this matrix element, and $k_{\mathrm{(r)ISC}}$, should vanish.[264, 265]

This presents a fundamental trade-off. Fine-tuning CT character of the emitter can lead to maximisation of k_{rISC} by optimising ΔE_{ST} and $\langle T_1|\hat{H}_{\mathrm{SOC}}|S_1\rangle$ towards the CT extreme. This comes at the expense of $k_{\mathrm{R}}(S_1)$.

7.1.3 Vibrational coupling

In this chapter, we consider the effect of dynamic dihedral torsion, and its role in tuning $k_{\mathrm{(r)ISC}}$ and $k_{\mathrm{NR}}(T_1)$. To ensure high TADF device QEs, (i) $k_{\mathrm{NR}}(S_1)$ should be slow compared to $k_{\mathrm{R}}(S_1)$ and k_{ISC}, and (ii) $k_{\mathrm{NR}}(T_1)$ should be slow compared to k_{rISC}. The rule that non-radiative decay should be suppressed is obvious, but potentially affords freedom to circumvent the low $k_{\mathrm{R}}(S_1)$ problem. This clarifies the first design rule in Section 7.1.1 that the decay of the singlet should be strongly emissive. As discussed earlier, $k_{\mathrm{NR}}(S_1)$ is slow, particularly for blue emitters, since the energy gap law predicts decreasing wavefunction overlap between S_1 and high energy vibrational states of S_0 with increasing energy gap.

Unlike for $k_{\mathrm{NR}}(S_1)$, to conserve angular momentum during non-radiative decay of the triplet, $k_{\mathrm{NR}}(T_1)$ typically requires second-order processes. Theoretical approaches to explain measured $k_{\mathrm{NR}}(T_1)$ values in organic materials usually rely on perturbations

to the molecular geometry which are achieved by low frequency vibrations. 'Phonon field theory',[266] and the time-independent theory[267] explicitly consider the transition dipole matrix element, and how it varies with vibrational degrees of freedom to explain the exceedingly slow phosphorescence rate of $\sim 5.9 \times 10^{-2}$ s^{-1} in perdeuterionaphthalene.[264] The observation that $k_{NR}(T_1)$ is slow presents an opportunity for TADF materials. In the limit that $k_{NR}(T_1)/k_{rISC} \to 0$, the external QE approaches $k_R(S_1)/[k_R(S_1) + k_{NR}(S_1)]$. In other words, if $k_{NR}(T_1)$ is sufficiently low, any triplets formed are ultimately recycled into singlets, and the external QE is that of the singlet pathway. It is by this mechanism that weakly phosphorescent materials (with $k_R(T_1) \to 0$) can luminesce on the timescale of phosphorescence without a substantial change in their luminescence spectrum.

Most TADF materials separate donor and acceptor subunits by a C−C single bond, and have a low barrier to dihedral torsion ($\sim 0.1 - 1$ meV), estimated by our density functional theory (DFT) results (discussed later). Additionally, $k_{NR}(T_1)$ is strongly related to the low-energy vibrations in the system. Recent studies highlight the importance of low frequency vibrations to increase $k_R(S_1)$,[268] and $k_{(r)ISC}$ via SOC.[265, 269]

7.2 Molecular rotations in TADF materials

Raman spectroscopy is an important probe for low frequency vibrations in molecular systems. By measuring a shift in the scattered energy of a monochromatic source, vibrations as low as ~ 5 cm^{-1} (~ 0.15 THz) can be resolved.[270] Furthermore, using a monochromatic light source with a photon energy much lower than the energy gap, non-resonant Raman spectroscopy directly probes the electron-phonon coupling in the ground state.[271] Modes which have strong electron-phonon coupling, and therefore strong Raman activity, can form channels leading to fast non-radiative decay.[271] Consistent with this, torsional modes have been linked to fast non-radiative decay in various materials.[272–274] Importantly, the vibrational coordinate which links S_0 and S_1 equilibrium positions always has a strong electron-phonon coupling,[275] and we expect the non-resonant Raman activity to be strong at this energy.

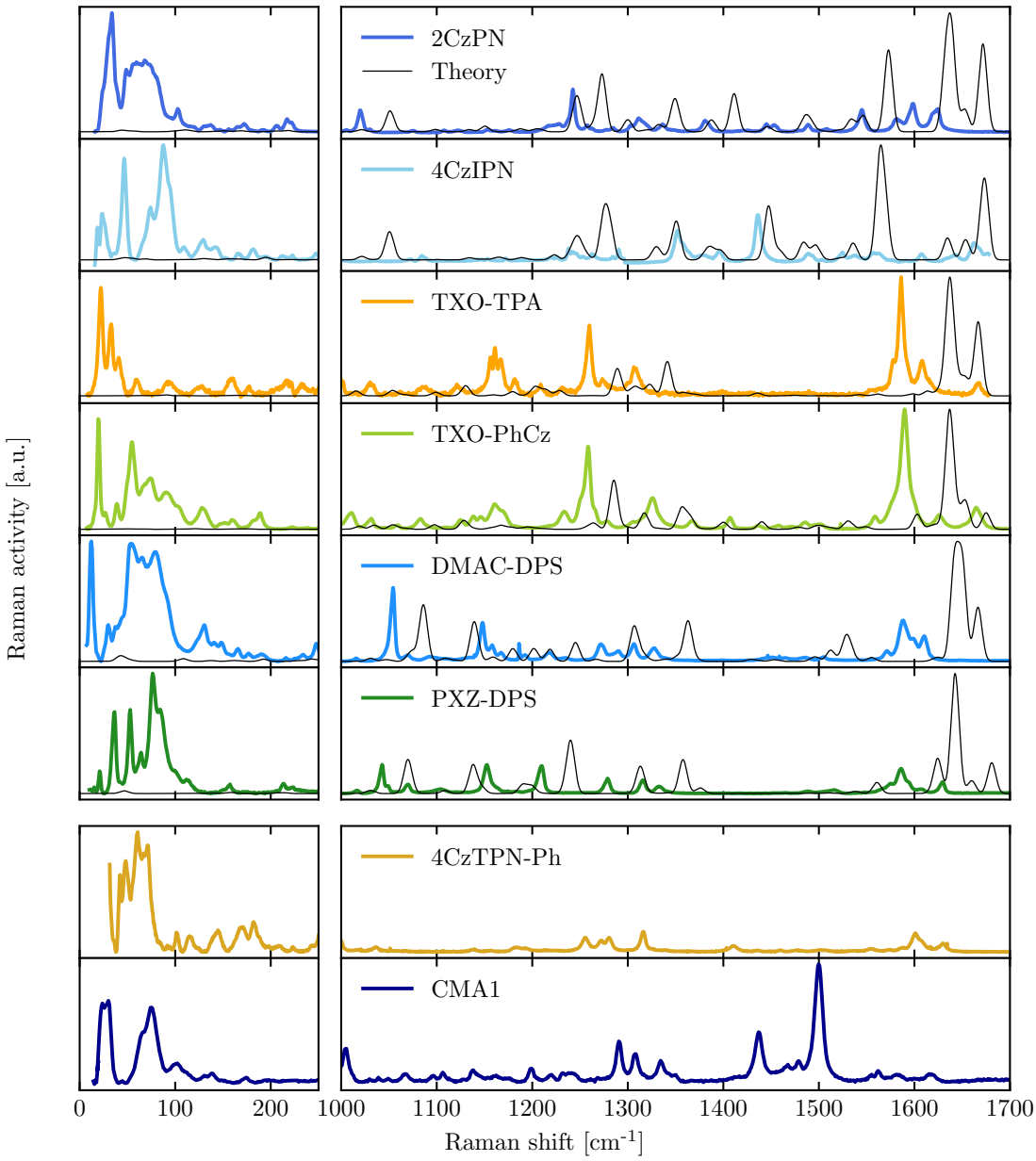

Figure 7.2 Non-resonant Raman spectra of TADF materials (colour) with calculated spectra (black).

The non-resonant Raman spectrum for a selection of TADF materials is shown in Figure 7.2. The structures of 4CzTPN-Ph and CMA1 can be found in Figure III.1. Backscattering a line which is far from resonance for all material presented here, the Raman spectrum of powders of TADF materials is observed to low frequencies, as described in Section III.1. Without exception, we observe that the electron-phonon

coupling is very strong for modes below 100 cm^{-1}. These modes are characteristic of large-scale dihedral rotations of molecular moieties, typically about C-C single bonds. In the case of 2CzPN, 4CzIPN, DMAC-DPS and PXZ-DPS, and 4CzTPN-Ph, the Raman activity is much stronger than even the cluster of modes around 1500 cm^{-1} which comprise C=C and C−N ring deformations and themselves are typically strong in π-delocalised systems.[120, 276]

Theoretical non-resonant Raman spectra in the gas phase have been calculated from the optimised S_0 geometry using DFT and B3LYP/6-31G(d). These are also plotted for some TADF materials in Figure 7.2. While the vibrations in the $1000-1700$ cm^{-1} range are systematically blueshifted compared to experimental results, there is generally a good agreement between Raman peak intensities in theory and experiment. However, this breaks down for the low frequency vibrations, which DFT confirms to belong to different types of dihedral rotational motion between donor and acceptor subunits, and DFT substantially underestimates the Raman activity here. The DFT Raman calculation considers only the S_0 potential energy surface, and therefore underestimates electron-phonon coupling of any modes which connect the equilibrium geometries of S_0 and S_1 electronic states.[275] This experiment is a clear indication that there is strong electron-phonon coupling for low frequency torsional modes in these systems which is likely to be linked to the non-radiative decay channels, particularly $k_{\mathrm{NR}}(T_1)$.

This behaviour is not unique to TADF materials. High Raman activity of low frequency vibrations is seen more generally in all the materials we studied which have dihedral angle rotational freedom. This is summarised for various polymer (top) and small molecule (bottom) host materials in Figure III.2. Together with the TADF results, this suggests the need for a more dynamic picture to explain the photophysics in these materials.

7.3 Restricting rotational freedom

We compare the photophysics of various TADF emitters between dilute solution and in a host-guest film. In solution, we expect rotational relaxation to be unhindered, whereas in a host-guest system, the resistance to internal torsional motion is determined

by the shear viscosity of the host.[277] Therefore, the selection of high molecular weight (1 MDa) atactic polystyrene (PS) with a high glass transition temperature $T_g \sim 95$ °C affords resistance against large-scale conformational relaxation.[278] Equally important in determining the photophysics is the dielectric rearrangement of the solvatochromic environment.[279] Since this is not intended to be the focus here, in this chapter we minimise this effect in amorphous PS with a low dielectric constant of $\varepsilon_r = 2.4 - 2.7$ and choose our solvent to match this value. Toluene has a comparable $\varepsilon_r = 2.38$, and bears close resemblance on a molecular level to PS. This helps ensure a similar contribution to potential energy landscape of S_0 from the chemical environment of the emitter, both in solution and film samples. To minimise contributions due to aggregation of the emitter, we use dilute solutions of 0.1 g/L in toluene, and drop-cast thick films prepared using 5 %w precursor solution to ensure a high optical density and low molar concentrations.

7.3.1 Rotations and external parameters

Table 7.1 PLQE of TADF materials with and without rotational freedom.

Material	Φ_{solution}	$\Phi_{\text{PS film}}$	$\Phi_{\text{UGH2 film}}$
2CzPN	0.31	0.20	-
4CzIPN	0.74	0.73	0.91
DMAC-DPS	0.19	0.42	-
PXZ-DPS	0.16	0.43	-
TXO-TPA	0.27	0.40	0.35

In Table 7.1, we show the photoluminescence (PL) QE (Φ) in solution and PS films for various TADF materials spanning the three classes. For 2CzPN, we observe a substantial decrease in Φ in film compared to solution of 0.11. For 4CzIPN, we do not observe a substantial change between PS film and solution, and in the case of DMAC-DPS, PXZ-DPS, and TXO-TPA, we observe a substantial increase to Φ in film compared to solution of $0.13 - 0.27$. This discrepancy in Φ is interesting, and is the focus of this section. However, we note that the observed Φ in solution is substantially lower than reported literature values of 0.94 at the same concentration in toluene.[21] This is concerning, since while significant efforts were made to ensure calibration of the instrument, and importantly to exclude oxygen during the measurement, it suggests that quenching of T_1 leads

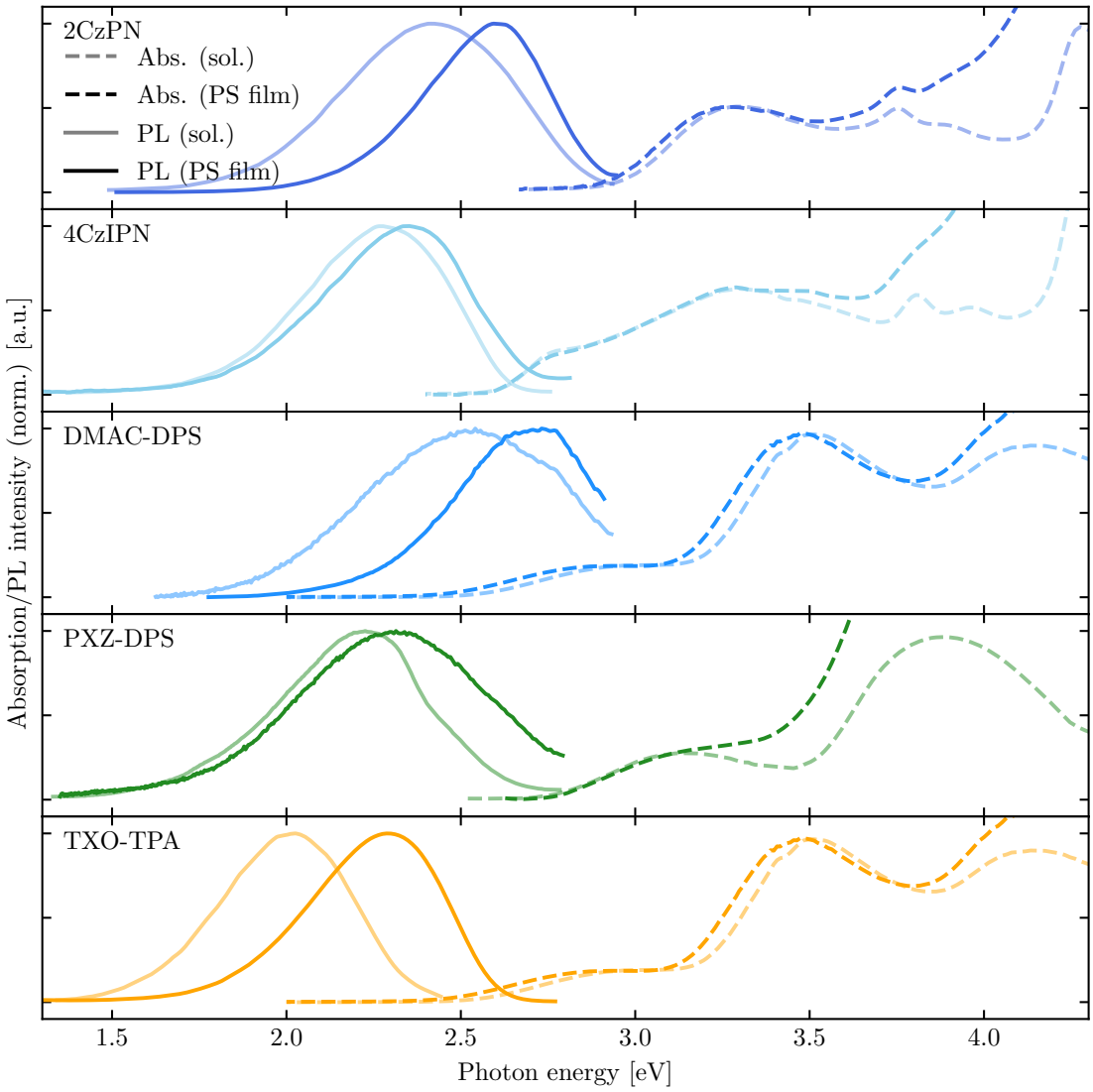

Figure 7.3 Absorption (dashed) and PL (solid) of solution (light) and PS film (dark) for 2CzPN (top), 4CzIPN (centre), and TXO-TPA (bottom).

to this lower Φ_{solution}. However, this measurement was made using a quartz-sealed tube, degassed by multiple freeze-pump-thaw cycles, and agrees with separate measurements which employed cuvette suba-seals and an over-pressure balloon of argon.

Furthermore, to validate the picture of a low degree of aggregation, we also measure host-guest films using *p*-bis(triphenylsilyl)benzene (UGH2) co-evaporated

with 4CzIPN and TXO-TPA respectively at a concentration of 10 %w.[1] This, in both cases, leads to a higher Φ than observed in solution. UGH2 is less rigid with respect to torsional motion than PS, and has a $T_g < 53$ °C,[280] and we therefore expect $\Phi_{\text{UGH2 film}} < \Phi_{\text{PS film}}$. However, since additional measurements of Φ employing atactic 10 kDa PS (which we expect also to be less rigid) yield the same values as for the heavier PS, we conclude that the discrepancy between PS and UGH2 films here is due to weak aggregation of 4CzIPN in the solution-processed films. This is not observed for TXO-TPA, which may aggregate more weakly, and $\Phi_{\text{solution}} < \Phi_{\text{UGH2 film}} < \Phi_{\text{PS film}}$, as we expect.

Comparison of steady-state absorption and PL spectra in Figure 7.3 confirms the picture of vibrational restriction in PS films. Without exception, the PL of the materials (solid lines) is blueshifted in film (dark) compared to solution (light). This contrasts with the absorption spectrum (dashed lines), which shows at most a small shift between solution and film. This leads to a decreased Stokes shift in the films, which cannot be explained in terms of a solvatochromic shift in solution compared to film, since $\varepsilon_r(\text{toluene}) < \varepsilon_r(\text{PS})$. Instead, this is direct evidence of the restriction of the conformational relaxation available in films compared to solution, and is discussed further in Section 2.3.4.4. In addition, a comparison of the difference in Stokes shifts suggests the degree to which this low frequency rotational motion is involved in the relaxation of S_1, and hence the photophysics of luminescence. Qualitatively, TXO-TPA and 2CzPN have the largest difference in Stokes shift, and also amongst the largest change in Φ between solution and film.

7.3.2 Rotations and time-resolved parameters

To explore this further, time-resolved luminescence measurements were performed for the materials in Figure 7.4. The PL in solution (black circles) has similar behaviour between the materials. Without exception, all of the materials show both prompt and delayed components to the PL, and the spectra (discussed in more detail below) do not change with time after excitation between 2 ns (the resolution of the experiment) and $\sim 10^5$ ns, when the delayed PL component decays fully. This is a hallmark of TADF materials, and indicates that rISC (rather than phosphorescence, for whom

[1] This sample is evaporated at a rate of 2 Å/s. The concentration used is rather high, although this is necessary to ensure that the sample has a sufficiently high optical density. We expect that the co-evaporation with UGH2 leads to minimal aggregation of the emitter.

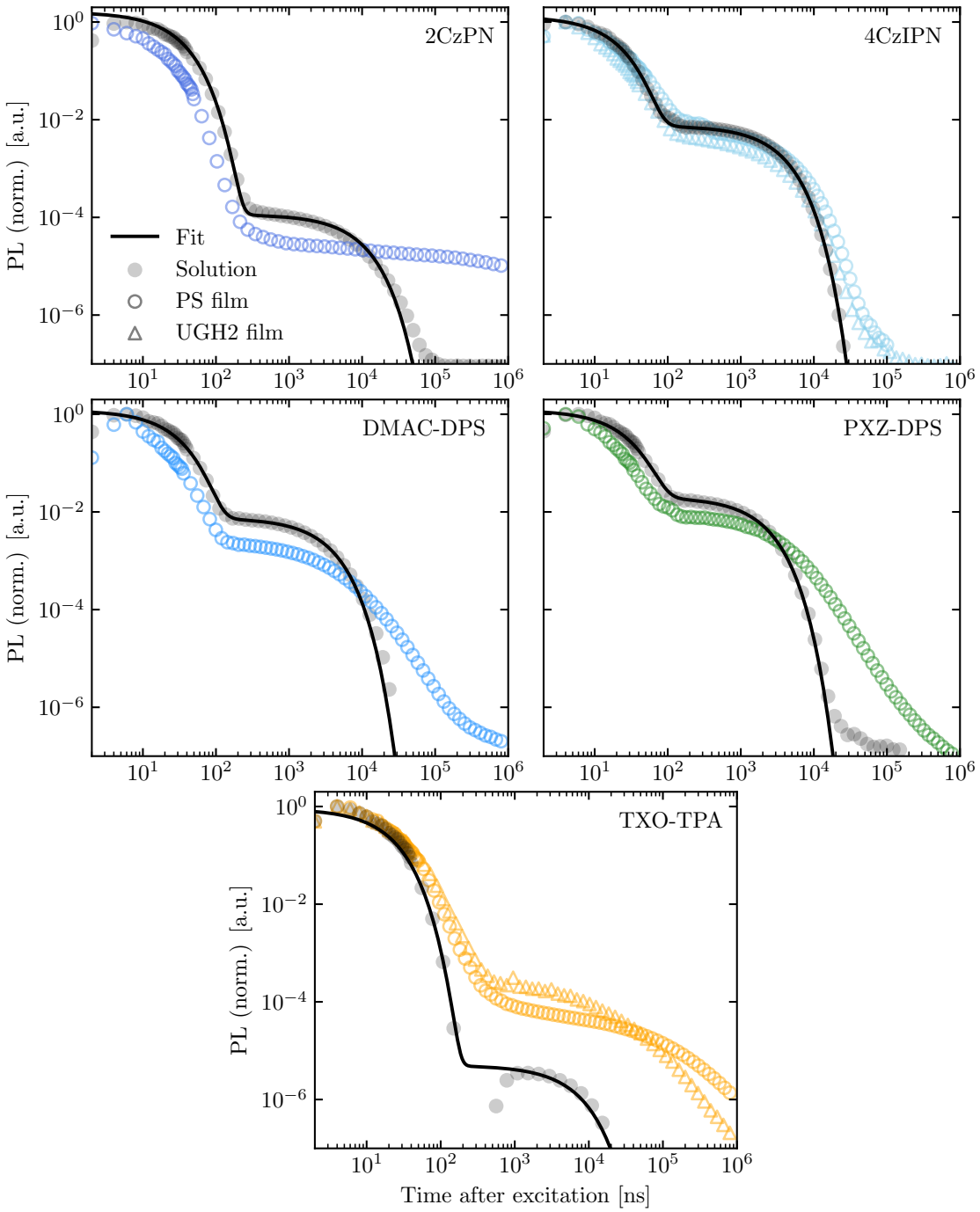

Figure 7.4 PL kinetics of TADF emitters in solution (black circles) with a bi-exponential fit (black line), in PS films (coloured circles), and also UGH2 films (coloured triangles) for some materials.

the luminescence spectrum is in general different) is the mechanism for delayed luminescence. Furthermore, a bi-exponential model (black line) yielded a good fit for all of the materials, and allowed for meaningful evaluation of the number of photons decaying through prompt and delayed luminescence pathways, and hence the PLQE of each of these pathways such that $\Phi = \Phi_{\text{prompt}} + \Phi_{\text{delayed}}$. For 4CzIPN, DMAC-DPS, and PXZ-DPS, the prompt and delayed PL contribute approximately equally to Φ. For 2CzPN and TXO-TPA, the delayed PL is suppressed, and $\Phi \approx \Phi_{\text{prompt}}$. This is true despite that the rates of prompt and delayed PL, k_{prompt} and k_{delayed}, are comparable between the various solutions. This data is summarised in Figure 7.5. The low Φ_{delayed} in these materials may arise from either a low $k_{\text{rISC}}/k_{\text{NR}}(T_1)$ ratio, indicating either fast non-radiative decay (compared to rISC), slow rISC (compared to non-radiative decay) perhaps due to a larger $\Delta E_{\text{ST}} > k_B T$, or a suppressed k_{ISC} decreasing the triplet yield.

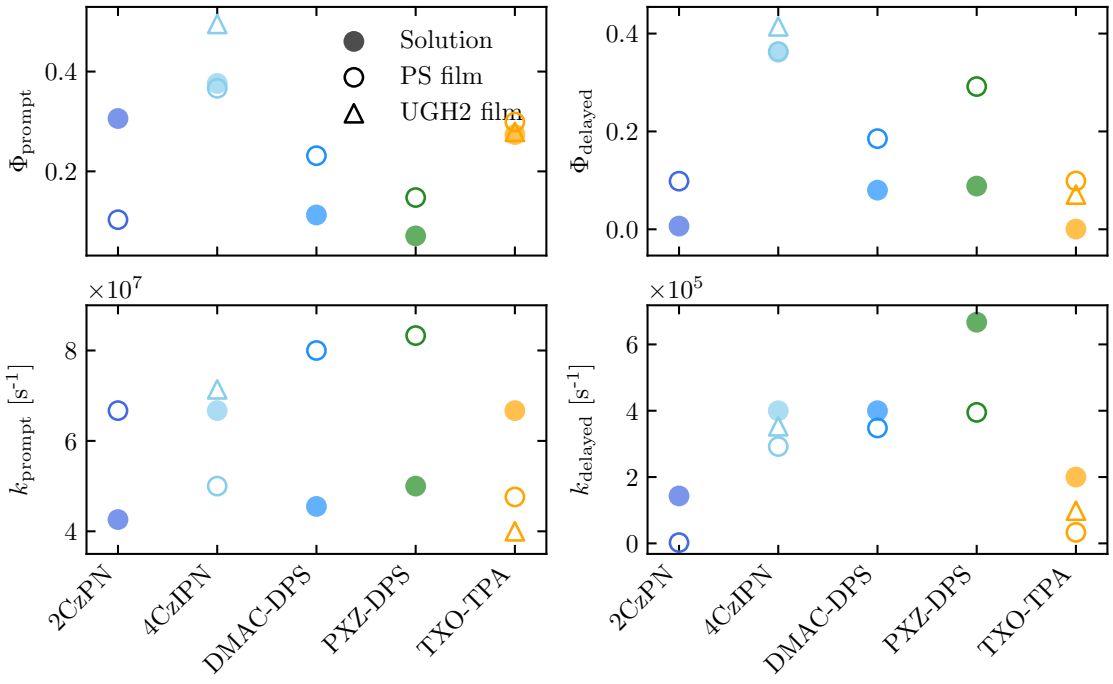

Figure 7.5 QE of prompt (top left) and delayed (top right) PL, and rates of prompt (bottom left) and delayed (bottom right) PL for TADF emitters in solution (full circles), in PS films (empty circles), and UGH2 films (triangles).

By comparison, the film luminescence (coloured points) behaves differently to solution. This leads to changes in both prompt and delayed luminescence components.

Without exception, k_{delayed} is slower in film than solution.[2] While this difference is small (< 25 %) for 4CzIPN and DMAC-DPS, a comparison of the delayed PL kinetic tails in Figure 7.4 confirms that this is clearly the case. This is unlikely to arise from a better encapsulation from an atmospheric oxygen in films, since k_{delayed} for 4CzIPN is nearly the same between solution and film (despite the difference in Φ values). Instead, this seems to be a general rule. Furthermore, without exception, the delayed decay is no longer well-fit by single exponential relation, indicating a change in the exciton dynamics between solution and film. With the exception of TXO-TPA, k_{prompt} increases for films compared to solution, which could arise from an increase in any combination of k_{ISC}, $k_{\text{R}}(S_1)$, and $k_{\text{NR}}(S_1)$. Integration under this curve for prompt and delayed components leads to a meaningful estimate of Φ_{prompt} and Φ_{delayed} in lieu of a fit, and leads to a much more equal partition of luminescence through prompt and delayed pathways for films with $\Phi_{\text{prompt}}/\Phi_{\text{delayed}} \sim 1$ for the materials, summarised in Figure 7.5. In this way, the strongest change is observed for TXO-TPA, whose Φ_{delayed} increases to 0.071 in UGH2, and to 0.099 in PS, correlating with the longevity of the delayed component in an increasingly rigid environment. This observation illustrates an important point - if Φ_{delayed} increases with rigidity, and so does the longevity of the triplet state, the Φ_{delayed} (which goes up in all cases in film) is likely to be limited by $k_{\text{NR}}(T_1)$ in solution. However, the SOC may also be different in the case that conformational rigidity is important in mediating singlet-triplet mixing. This is predicted by calculations,[265] so we also expect k_{ISC} and k_{rISC} to differ between solution and film in general. Further investigation of these dynamics is therefore required. If $k_{\text{NR}}(T_1)$ is decreasing in a rigid environment, this poses an opportunity to increase Φ in the materials that have fast k_{rISC} in spite of a reduced vibrational freedom.

To confirm this assertion, we use a more quantitative analysis following the methodology presented by Adachi and coworkers.[281] Here, first-order decay is assumed, and

$$k_{\text{prompt}} = k_{\text{ISC}} + k_{\text{R}}(S_1) + k_{\text{NR}}(S_1) \tag{7.1}$$

$$k_{\text{delayed}} = k_{\text{NR}}(T_1) + \left(1 - \frac{k_{\text{ISC}}}{k_{\text{ISC}} + k_{\text{R}}(S_1) + k_{\text{NR}}(S_1)}\right) k_{\text{rISC}} \tag{7.2}$$

[2] Upper bounds on k_{prompt} and k_{delayed} were estimated by comparing the half-life to an exponential model.

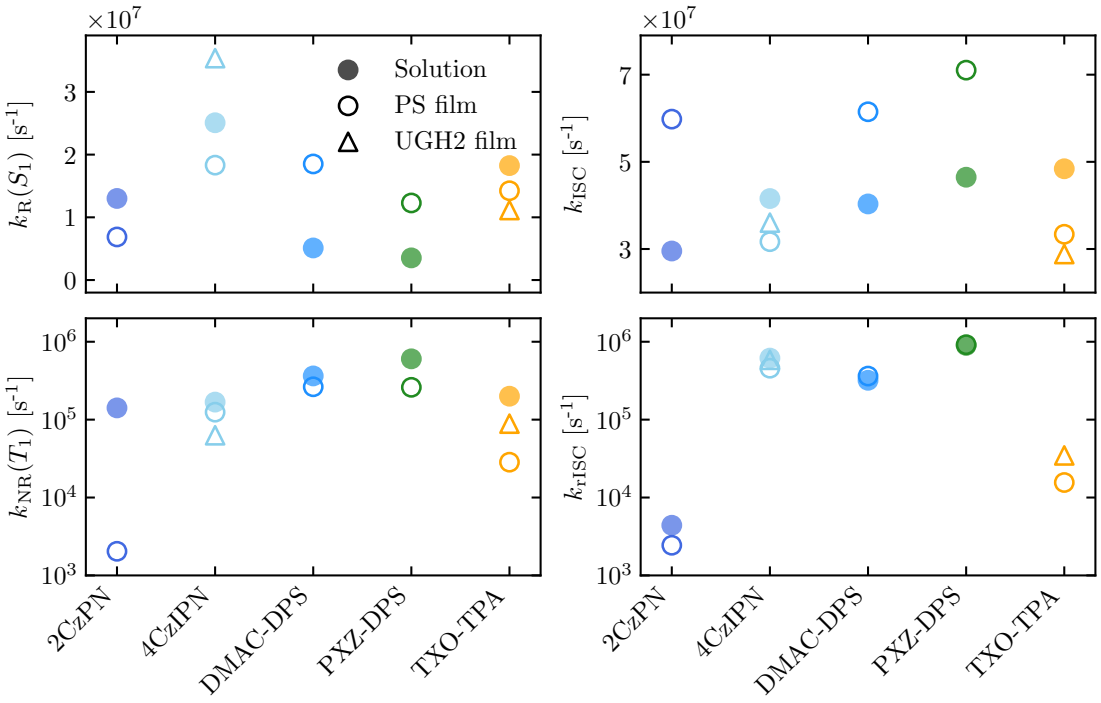

Figure 7.6 Singlet radiative (top left), ISC (top right), triplet non-raditive (bottom left) and rISC (bottom right) rates for TADF emitters in solution (full circles), in PS films (empty circles), and UGH2 films (triangles).

by comparison to an energy transfer model.[282] By defining

$$\Phi_{\text{prompt}} = \frac{k_R(S_1)}{k_{ISC} + k_R(S_1) + k_{NR}(S_1)} \tag{7.3}$$

$$\Phi_{ISC} = \frac{k_{ISC}}{k_{ISC} + k_R(S_1) + k_{NR}(S_1)} \tag{7.4}$$

and Φ_{rISC} as the QE of rISC, then

$$\Phi = \sum_{i=0}^{\infty} \left(\Phi_{ISC}\Phi_{rISC}\right)^i \Phi_{\text{prompt}} \tag{7.5}$$

and from these equation, they deduce that

$$k_{rISC} = \frac{\Phi_{\text{delayed}}}{\Phi_{\text{prompt}}} \frac{k_{\text{prompt}} k_{\text{delayed}}}{k_{ISC}} \tag{7.6}$$

Adachi and coworkers make the assumption that $k_{NR}(S_1) = 0$, and that all the non-radiative deactivation occurs via the $k_{NR}(T_1)$ pathway. This assumption is dubious, but nonetheless has been published (at least) three times.[257, 263, 283] To

justify this, they invoke the energy gap law for blue-green emitters, and corroborate this with evidence that $k_{\mathrm{NR}}(S_1)$ has a vanishing dependency on temperature. For the sake of comparison, and since the 'Adachi' materials studied hereunder are in common with these published studies, we follow this approach to extract k_{ISC}, k_{rISC}, and $k_{\mathrm{NR}}(T_1)$ in solution and film in Figure 7.6.

Using this methodology, no clear trend emerges in $k_{\mathrm{R}}(S_1)$ between solution and film. While PS film increases the radiative rate for the donor-acceptor-donor materials DMAC-DPS and PXZ-DPS, this rate decreases from solution in the other materials. Similarly, any trend in k_{ISC} is complicated, and while the donor-acceptor-donor class together with 2CzPN show faster ISC in film, this is slower by ~ 50 % in TXO-TPA and unchanged in 4CzIPN.

However, the difference between solution and film is more profound when considering the exciton dynamics of the triplet. In particular, as stated earlier, for all the materials, we observe a strong decrease in $k_{\mathrm{NR}}(T_1)$ in films, and for TXO-TPA, this follows the trend of structural rigidity of the host. This observation is strongest in the case of 2CzPN, whose $k_{\mathrm{NR}}(T_1)$ decreases by $\sim 100\times$ in PS film. This discrepancy is important, and we unpick this big change in the following section. We find that $k_{\mathrm{NR}}(T_1)$ can be substantially decreased by limiting the torsional freedom of the emitter. This supports our earlier assertion that $k_{\mathrm{NR}}(T_1)$ is strongly related to low frequency vibrations which are hindered in a rigid host film. Importantly, k_{rISC} also decreases with decreased rotational freedom, with the exception of PXZ-DPS whose k_{rISC} is approximately unchanged in film. From this experiment alone, it is not possible to comment meaningfully on whether the mechanism of ISC/rISC itself requires vibrational freedom, since there is poor agreement between the trends in k_{ISC} and k_{rISC} in solution and films. However, due to the longer k_{rISC} in torsionally hindered films, and assuming $\ln(k_{\mathrm{rISC}}) \sim \Delta E_{\mathrm{ST}}/k_B T$, the activation energy of rISC (here related to the exchange energy), seems to be reduced where these vibrations are freer; leading to the clear requirement of rotational freedom for fast k_{rISC}.

7.3.3 Theoretical considerations

To explore this idea further, we use DFT and time-dependent (TD-) DFT to explore S_0 and S_1 geometries respectively. For 2CzPN and 4CzIPN from the Adachi class, the simplest and highest performing materials respectively, we observe a striking

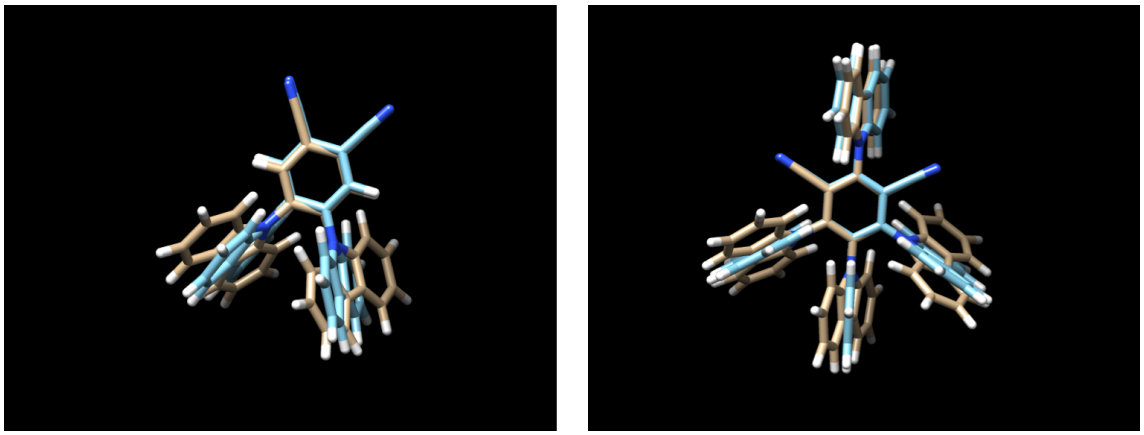

Figure 7.7 Optimised S_0 geometry (orange) superimposed on optimised S_1 geometry (blue) for 2CzPN (left) and 4CzIPN (right).

conformational change between the ground and first excited singlet states involving a rotation of the carbazole units. This is shown in Figure 7.7. In both cases, the optimised S_0 geometry has carbazole units tilted with respect to the substituted benzene, making dihedral angles of $\sim 50\,^{\circ}$. This geometry balances the energetic effects of π-conjugation of the benzene group and carbazoles, and the sterical interaction between carbazoles towards coplanarity. This geometry has C_2 symmetry. By contrast, the optimised S_1 geometry has increased carbazole dihedral angles of $\sim 90\,^{\circ}$. This leads to localisation of the HOMO on the carbazole units, and the LUMO on the substituted benzene, and hence a CT-like exciton wavefunction. This wavefunction geometry minimises the exchange energy (which otherwise increases the energy of the singlet excited state) in its geometry with higher C_{2v} symmetry.[3]

Qualitatively, dihedral torsion in these materials mediates CT and local-exciton (LE) wavefunction mixing, and is therefore important in determining both $k_R(S_1)$ and ΔE_{ST}. A recent theoretical study by Olivier and Beljonne suggest that $\langle S_1|\hat{H}_{SOC}|T_1\rangle$ also depends heavily on vibrations (although not exclusively low frequency rotations), and molecular dynamics simulations suggest a pseudolinear relationship between $\langle S_1|\hat{H}_{SOC}|T_1\rangle$ and ΔE_{ST} for microstates of 2CzPN and 4CzIPN in various degrees of vibrational disorder.[265] In Figure 7.8, we calculate the dependency of the singlet and triplet energies, $E(S_1)$ and $E(T_1)$ respectively, on the

[3]For 4CzIPN, the symmetry of the relaxed S_1 state is strictly C_2, owing to torsion of the carbazole in the 4- position. However, similar to 2CzPN, the carbazoles in 1,2,6- positions (1,2- positions for 2CzPN) become coplanar, and orthogonal to the benzene. Therefore, while 4CzIPN has a higher symmetry approaching C_{2v}, it remains C_2.

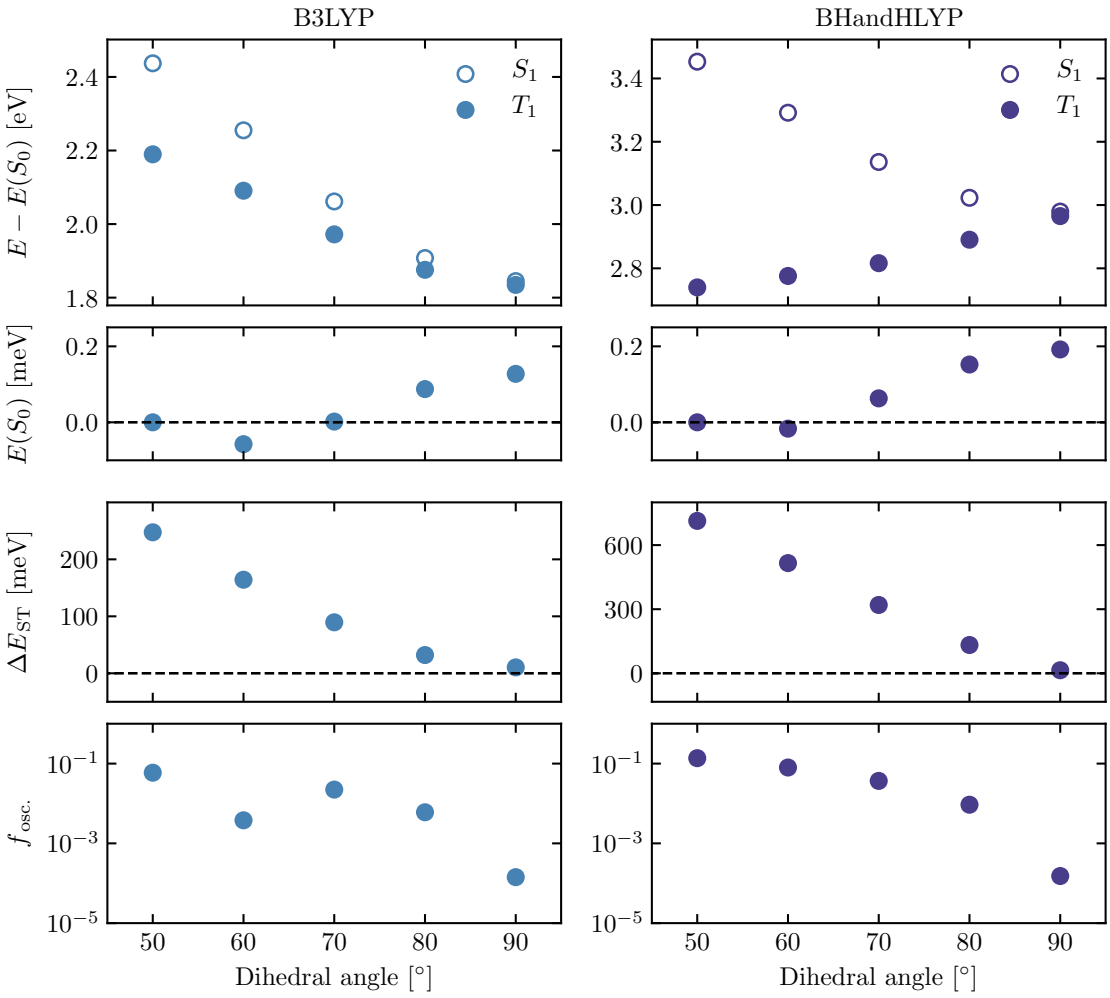

Figure 7.8 Relaxed dihedral potential energy surface for 2CzPN: comparison of B3LYP (left) and BHandHLYP (right) level of theory on the 6-31G(d) basis. From top to bottom, the energy of S_1 and T_1 levels above the respective S_0 is shown (top) with the absolute change in S_0 energy (below). Then, ΔE_{ST} is shown, and $f_{osc.}$ below.

dihedral angle in 2CzPN. To do this, we use the popular functional/basis combination B3LYP/6-31G(d) (left) to optimise the S_0 geometry for fixed dihedral angles, and calculate the S_1 and T_1 energies using TD-DFT. To a good approximation, this maps the first excited-state potential energy surfaces (PESs) as a function of dihedral rotation.

This reveals the important physics that the energy of the ground state, $E(S_0)$, does not depend strongly on dihedral angle, and we expect torsion to be approximately free for the ground-state electronic configuration. It also confirms that both ΔE_{ST} and

$f_{\text{osc.}}$ are minimised towards a dihedral angle of 90 °, in the limit that the geometry approaches C_{2v} symmetry, the exciton wavefunction has the greatest CT-character (and the least CT-LE mixing), and $\Delta E_{\text{ST}} \to 0$. However, a cursory comparison with steady-state absorption and PL spectra in Figure 7.3 reveals that this protocol does not reproduce the expected absorption energy gap > 3.2 eV, or the PL energy gap > 2.7 eV. It also fails to predict that increasing the dihedral angle should raise $E(T_1)$, and that $f_{\text{osc.}}$ should be monotonically decreasing. At this stage, we note that care must be taken when selecting the level of theory for TD-DFT calculations, as the degree of CT wavefunction character is closely related to how the exchange energy is estimated.[284] When poorly chosen, this can lead to an artificial minimum of a twisted geometry.[285] However, the integrity can be recovered by using functionals with 50 % Hartree-Fock (HF) exchange.[285, 286] Indeed, repeating the calculations with BHandHLYP (with explicitly 50 % HF exchange) in Figure 7.8 (right) shows similar $C_2 \to C_{2v}$ relaxation of S_1, and superior agreement with 2CzPN absorption and PL energies in the region of $2.7 - 3.4$ eV compared to highly underestimated values of $1.8 - 2.4$ eV with B3LYP (20 % HF exchange), and overestimated values of > 4.5 eV with 100 % HF exchange) observed separately.

Table 7.2 Calculated parameters for various TADF emitters (using BHandHLYP/6-31G(d).

Material	$\Delta E_{\text{ST}}(S_0)$ [meV]	$\Delta E_{\text{ST}}(S_1)$ [meV]	$f_{\text{osc.}}(S_0)/f_{\text{osc.}}(S_1)$
2CzPN	690	13.6	2580
4CzIPN	219	15.6	77.2
DMAC-DPS	16.9	17.3	60.2
PXZ-DPS	17.8	17.3	0.971
TXO-TPA	574	474	1.30

For all materials, we use DFT and TD-DFT to calculate the equilibrium geometries of S_0 and S_1 respectively, and then calculate ΔE_{ST} at these two points using the same BHandHLYP/6-31G(d) protocol. These calculations simulate the geometries relevant for absorption and luminescence, together with important parameters indicating CT-LE wavefunction mixing in these vibrational extrema in the absence of any restriction of vibrational freedom. This is slightly different to the redundant potential energy surface scan shown earlier, since here we do not fix any dihedral angles. Instead, the optimisation protocol gives the system total freedom to relax, and these results are

summarised in Table 7.2.

For 2CzPN and 4CzIPN, owing to a large ΔE_{ST} of the equilibrium S_0 geometry, the calculation suggests that rISC is unlikely to proceed from this rotational configuration, even if $\langle S_1|\hat{H}_{\mathrm{SOC}}|T_1\rangle$ is large here. Instead, the observation of TADF at all in these materials is likely to involve a geometry which is much closer to the twisted CT microstate which minimises ΔE_{ST}, even where $\langle S_1|\hat{H}_{\mathrm{SOC}}|T_1\rangle$ is weak. Accordingly, our calculated values for ΔE_{ST} at both conformational extremes fall on either side of measured values of 40 meV and 200 meV for 2CzPN and 4CzIPN respectively.[263] On the other hand, ISC may be faster in the case that the S_0 geometry is locked in, since when rotational freedom is conferred, we expect even slow molecular motion to be much faster than k_{ISC}. Furthermore, we see a strong dependency of the oscillator strength on the geometry, and the $f_{\mathrm{osc.}}(S_0)/f_{\mathrm{osc.}}(S_1) \sim 10^1 - 10^3$. In solution, owing to a low barrier to dihedral torsion, we expect to have a dynamic distribution of dihedral conformational microstates, however in casting a film, we expect to 'lock in' this distribution.

The picture for the other materials is seemingly different, and only small changes between ground- and excited-state geometry are calculated. Because of this, ΔE_{ST} and $f_{\mathrm{osc.}}$ are approximately constant between the two geometries, with the exception of DMAC-DPS whose $f_{\mathrm{osc.}}$ is higher for the S_0 geometry. The latter calculations do not agree well with experiments. In particular, a high $\Delta E_{\mathrm{ST}} \sim 0.5$ eV for TXO-TPA is unrealistic. This is possibly owing to the aforementioned problem when dealing with exchange energy in TD-DFT which we have optimised somewhat during our treatment of 2CzPN and 4CzIPN. These values should therefore not be compared directly to the other materials, but only qualitatively between the two geometries. We conclude that TXO-TPA is likely behave in the same way as the 'Adachi' materials, with ΔE_{ST} decreasing towards the S_1 equilibrium position, but that DMAC-DPS and PXZ-DPS perhaps undergo less of a rearrangement, leading to a small and comparable ΔE_{ST} in the S_0 and S_1 geometries.

7.4 Measurement of rotations

To confirm our picture, we look for direct spectroscopic evidence of dynamic rotations in TADF materials. Using a combination of transient absorption (TA) and PL, we highlight the differences in the photophysics between solution and film samples on timescales

between 300 fs−800 µs. For brevity, herein we focus on a detailed understanding of 2CzPN and 4CzIPN, but highlight where observations are more general.

7.4.1 Transient absorption

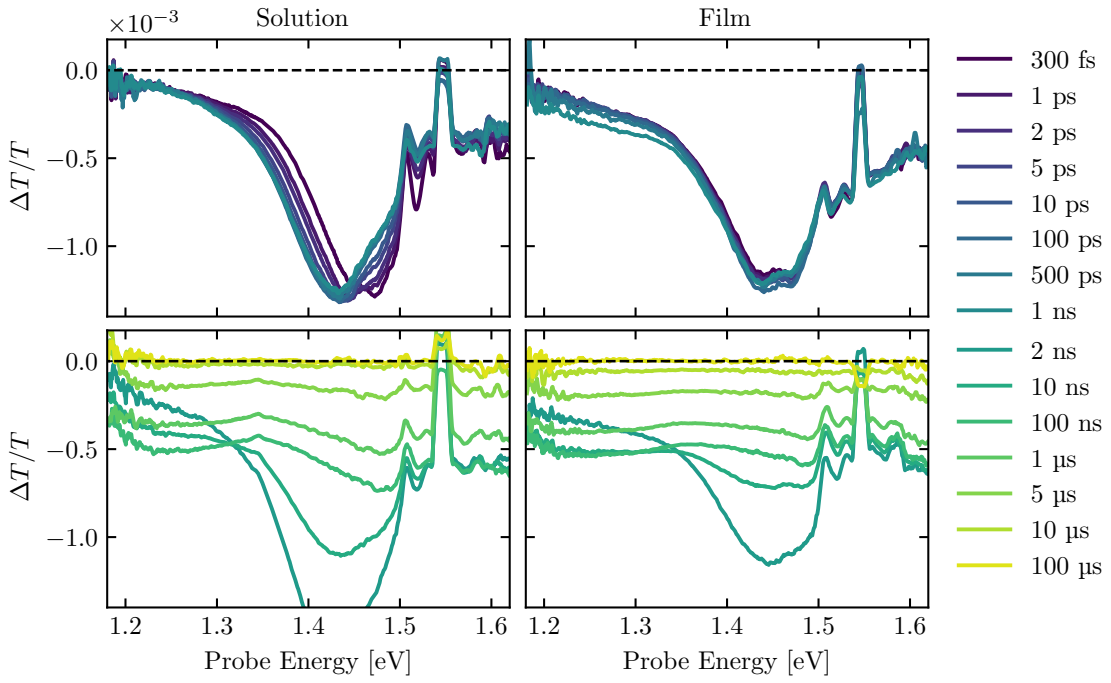

Figure 7.9 NIR TA spectra of 4CzIPN in solution (left) and film (right).

In Figure 7.9, we measure the TA spectra of 4CzIPN solution (left) and PS film (right) in the near-infrared (NIR) region. Specifically, we observe the evolution of the photo-induced absorption (PIA) after 300 fs with a time resolution ∼ 100 fs (top, $E_{\text{pump}} = 3.10$ eV) and ∼ 2 ns (bottom, $E_{\text{pump}} = 3.49$ eV) and the fluence (f_{pump}) is summarised in Table III.1. In solution, between the earliest times and 100 ps, we observe a fast redshift of the PIA from 1.48 to 1.42 eV. Since this is not coupled to a decay of the PIA, we infer that this is most likely to be an energy transfer process, and analysis of the ground-state bleach (GSB) (which follows) allows us to make this statement with more certainty. Over the following 1 ns after this shift is complete, the PIA does not change substantially in shape or magnitude until ∼ 2 ns when it begins to decay. Over the following 100 ns, this decay proceeds, and in tandem, an additional flat and broadband PIA over the entire probe window begins to rise, becoming obvious below 1.30 eV. This peak shape does not change after 1 µs, and the broad PIA decays

until 100 µs when it goes to zero. By comparison to the timescales of $1/k_{\text{prompt}}$ and $1/k_{\text{delayed}}$, we assign the broadband rising < 1.3 eV to the PIA of T_1 states, and the peak at ~ 1 ns to a relaxed S_1 configuration. The ultrafast redshift is interesting, since it proceeds much faster than k_{prompt}. With a timescale ~ 10 ps, this shift occurs on the same timescales as the period of various low frequency rotations as determined by Raman spectroscopy and DFT. Therefore, since this process appears to involve energy transfer rather than decay to the ground state, we propose that the shift is a conformational change where some 'activated' S_1 geometry cools to the equilibrated S_1; $S_1^* \rightarrow S_1$.

To support this picture, we analyse the spectral evolution of 4CzIPN in a PS film. In this case, while the decay picture of the assigned S_1 and T_1 is the same as solution after 2 ns, we do not observe an ultrafast redshift in the peak near 1.45 eV. If the PS host film confers conformational rigidity, we expect carbazole rotation in 4CzIPN molecules (in a PS film) to proceed on much longer timescales. Indeed, the absence of the shift from the ultrafast timescales confirms the $S_1^* \rightarrow S_1$ picture in solution, and that such a rotational relaxation is not possible in film. Interestingly, the PIA near 1.45 eV has a mixed character of S_1^* and S_1 by comparison to the solution measurement. This suggests that while 4CzIPN in PS films are unable to dynamically reorganise, casting the PS 'locks in' an ensemble of fixed geometry microstates between the two rotational extremes, consistent with the shallow S_0 potential energy surface predicted by DFT for 2CzPN. This observation is general, and the same behaviour is observed in 2CzPN and TXO-TPA, whose TA spectra are shown in Figures III.4 and III.5.

7.4.2 Photoluminescence

PL spectra of 4CzIPN in solution (left) and PS film (right) are shown in Figure 7.10. Ultrafast transient grating PL (top, normalised to the $0-1$ ps spectral maximum) shows the same shifting behaviour in solution. Over the same timescales, the spectrum redshifts from a broad peak centred near 2.5 eV towards 2.4 eV which we assign to the luminescence of S_1^* and S_1 respectively by comparison with the TA results. By ~ 50 ps, this shift is mostly complete, and the luminescent species (S_1) does not undergo further spectral evolution before it decays to zero.[4] 4CzIPN in a PS film

[4]We note that due to a high noise level in this experiment, interpretation of the data (dots) is aided by low-pass (Fourier) smoothing (lines). However, this treatment leads to small bump artefacts which should be ignored.

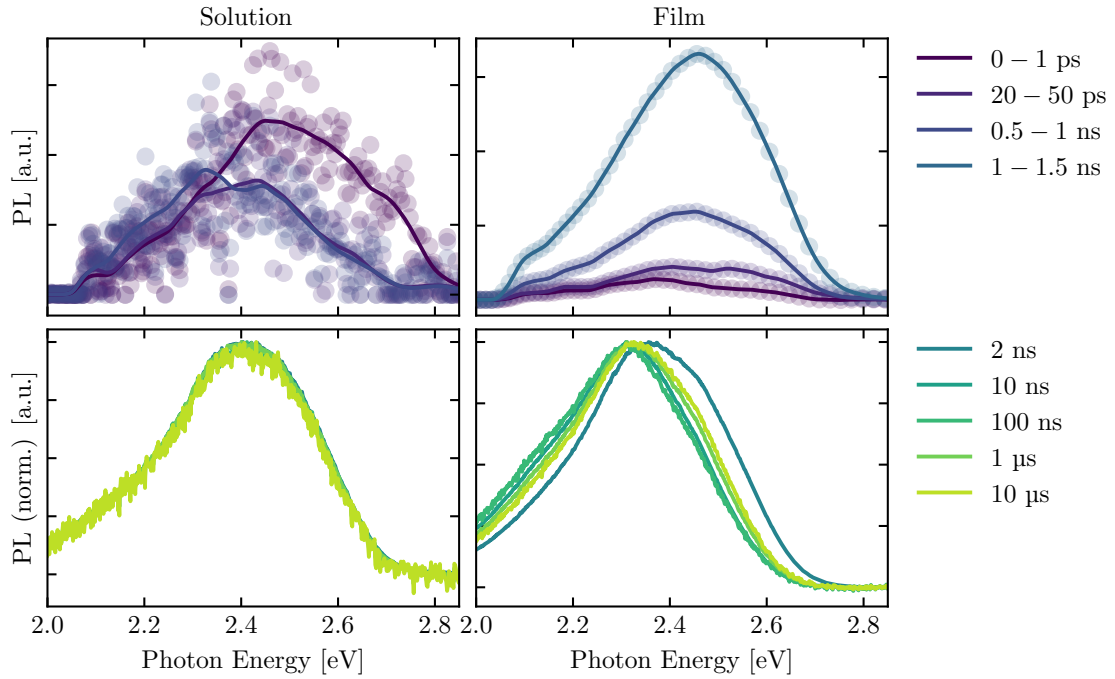

Figure 7.10 PL spectra of 4CzIPN in solution (left) and film (right).

behaves differently. Before 1 ps, the luminescence is very weak and does not change substantially in magnitude by 50 ps. By 500 ps, the luminescence grows very quickly, and is only maximised after 1 ns. During this time, the spectrum does not change substantially, and resembles the S_1^* luminescence observed in solutions at early times. This very unusual behaviour was also verified for 4CzIPN films using time-correlated single photon counting.

In Figure 7.11, we show the normalised kinetics of the GSB and PL (bottom) of 4CzIPN in solution (grey) and PS film (light blue), and 2CzPN in solution (dark blue). First, comparing the ultrafast PL (bottom right), we observe that the 'growing in' behaviour occurs both in 4CzIPN solution and PS film. In the latter, this behaviour leads to a very fast rise in the PL towards 1 ns, whereas the rise in solution occurs more slowly, and begins on earlier timescales towards $\sim$ 100 ps. Interestingly, this is true for both 4CzIPN and 2CzPN solutions, and the rise after $\sim$ 100 ps is comparable to between the two materials. Before 100 ps, both solutions show the ultrafast shift, shown here as a decay in the PL, which is consistent with a high degree of rotational freedom afforded by dilute solution. This is not observed for 4CzIPN in thin film, whose luminescence rise is slow after excitation, and approximately constant in

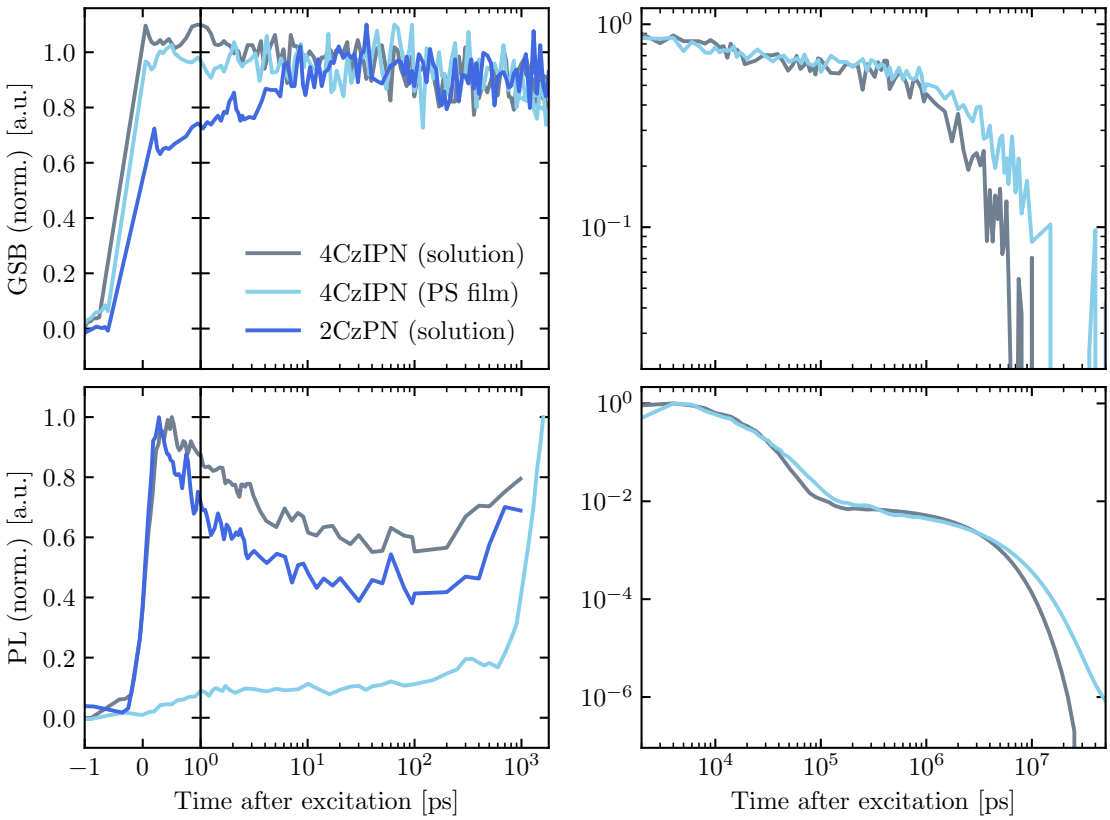

Figure 7.11 GSB (top) and PL (bottom) kinetics of 4CzIPN in solution (grey) and PS film (light blue), and 2CzPN in solution (dark blue).

magnitude before 500 ps. Despite this, measurement of normalised $\Delta T/T$ over the GSB band (top left) over the same timescales reveals that very few excitons decay before 1 ns in any of the samples, and appreciable decay is first observed over $1/k_{\text{prompt}}$ timescales (top right).[5] The PL decay kinetics after 1 ns is similar between 4CzIPN solution and PS film, but the spectral behaviour is interesting, and is discussed below.

This behaviour is predicted by our dynamic S_1 model, and improves our understanding of S_1^* and S_1. Since the S_0 potential energy surface has a minimum with a twisted carbazole dihedral arrangement but that of S_1 is minimised by a greater dihedral angle towards 90 °, then excitation leads to the formation of an activated S_1^* microstate. Upon excitation, the electronic state ungergoes $S_0 \rightarrow S_1^*$ within the Born-Oppenheimer approximation, where S_1^* has mixed CT-LE wavefunction character

[5]Due to weak signals and measuring with low noise in the UV band, high fluences between $120-200$ µJ/cm^2 and $270-420$ µJ/cm^2 were used for solution and PS film measurements respectively.

and blueshifted luminescence with respect to the S_1 equilibrium position. The excess energy $\Delta E_{\text{ex.}} = E(S_1^*) - E(S_1)$ is dissipated as the wavefunction relaxes to a CT-like wavefunction which minimises the exchange energy, and this is mediated by a rotation of the carbazoles. However, since a CT-like S_1 has a low $f_{\text{osc.}}$, emission relies on the re-mixing of CT-LE wavefunction character which can be mediated by the same (partial) carbazole rotation. Therefore, luminescence rises on the timescale of $S_1 \rightarrow S_1^*$ up-conversion (on substantially shorter timescales than $T_1 \rightarrow S_1$), which is determined by the steepness of the S_1 potential energy surface, or $\Delta E_{\text{ex.}}$. This leads to the curious rising PL after 100 ps timescales. 2CzPN and 4CzIPN, having similar molecular structure and geometric sterics in dilute solution, have a similar potential energy surface, so luminescence rises on comparable timescales. For the same reason, 4CzIPN in a rigid PS film has a steeper S_1 PES, leading to luminescence rising on longer timescales.

Finally, we turn our attention to the interesting spectral evolution of 4CzIPN in PS films on timescales longer than ~ 1 ns. Normalised spectra are shown in Figure 7.10 (bottom right). At ~ 2 ns, there is good agreement between the spectra measured here, and in the last spectrum at ~ 1 ns measured by ultrafast transient grating PL (above). In the following 100 ns, we see a strong redshifting of the spectrum as the PL decays, and this leads to a spectrum which more closely resembles the S_1 spectrum seen for solutions (left). Thereafter, on the timescales of rISC, this peak continuously shifts back towards the spectrum at ~ 1 ns (but never reaching it), and this occurs over very long timescales to 10 µs.

This behaviour is also predicted by our model in the case that rotational vibrational disorder (induced by a shallow S_0 PES) is locked in upon casting the PS film, leading to an ensemble of static rotational configurations. In this case, geometries with the smallest dihedral angle giving the greatest $f_{\text{osc.}}$ emit first, but these also have the greatest $E_{\text{ex.}}$ with respect to the solution phase S_1 equilibrium geometry, and the bluest luminescence. Over increasingly long timescales, more twisted microstates (leading to greater CT-exciton character) emit, and as $E_{\text{ex.}} \rightarrow 0$, the spectrum redshifts. After the prompt emission is finished, for excitons which have found their way onto the T_1 manifold, the more twisted microstates (for whom ΔE_{ST} is small) undergo rISC first, leading to the delayed fluorescence. Finally, on the longest timescales, rISC occurs for the less twisted geometries with a large ΔE_{ST}, leading to an increasing blueshift as these microstates luminesce. Of course, rISC also depends on $\langle T_1 | \hat{H}_{\text{SOC}} | S_1 \rangle$ which

also depends heavily on dihedral angle, and it is for this reason that the blueshift towards ~ 1 µs does not extend all the way to the microstates emitting towards ~ 1 ns. In these materials, rISC must balance a large $\langle T_1|\hat{H}_{\mathrm{SOC}}|S_1\rangle$ and small ΔE_{ST}, both mediated by carbazole rotation, and this leads to a smaller distribution of possible microstates near the solution S_1 potential energy surface minimum with which rISC occurs with a unique rate and PL energy.

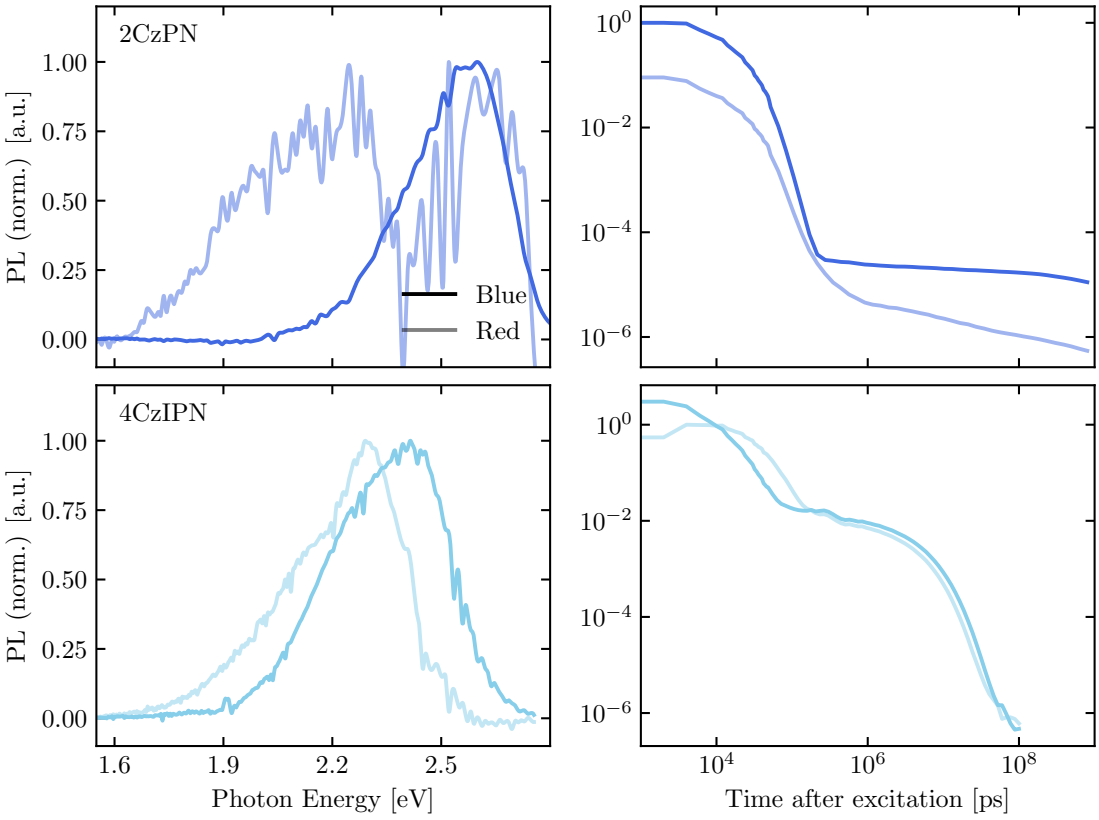

Figure 7.12 PL spectra (left) and kinetics (right) for prompt (dark) and delayed (light) luminescence species in 2CzPN (top) and 4CzIPN (bottom) in film.

This behaviour is ubiquitous, and in all our materials in PS film, we observe shifting of the luminescence spectra on both prompt and delayed PL timescales. This is summarised for 2CzPN (top) and 4CzIPN (bottom) in Figure 7.12. Using a genetic algorithm described elsewhere,[210] we temporally deconvolve the PL map to recover two spectra (left) and their kinetics (right). The 'bluer' spectral component (dark), corresponding to microstates with greater LE-exciton character, decays faster, leaving the 'redder' component with more CT-exciton character, to decay over longer timescales.

During the delayed luminescence, the blueshift can be expressed in terms of a mixture of the two extrema, and the spectral evolution is given by changing ratio as the twisted microstructures leading to CT-exciton microstructure undergo rISC followed by the less twisted CT-LE mixed state.

7.5 Conclusions

We show that $k_{\mathrm{NR}}(T_1)$ is strongly related to dynamic low frequency torsion motion, and both are reduced in the presence of a rigid host matrix for various TADF materials for which we do not see phosphorescence. However, we also highlight the importance of rotational freedom in determining $f_{\mathrm{osc.}}$, ΔE_{ST}, and $\langle S_1|\hat{H}_{\mathrm{SOC}}|T_1\rangle$, which, in the absence of a rigid host, mediates the strong emissive properties in these materials. Therefore, suppressing dynamic motion can strongly modulate the photophysics of these materials, and lead to an increase in Φ particularly in lower energy gap materials PXZ-DPS and TXO-TPA. Using 2CzPN and 4CzIPN as an exemplar, we show the need for a dynamic picture to explain the high k_{ISC} and k_{rISC} in spite of a good $k_{\mathrm{R}}(S_1)$ for TADF materials, and present an intuitive model relying on low frequency vibrations which predicts the highly unusual luminescent behaviour on both short and long timescales.

7.6 Contributions

This project was completed in close collaboration with Dr. Emrys Evans and Mr. Alexander Gillett. Measurements of Φ and time-resolved (ns) PL were conducted together. Alexander Gillett performed the TA spectroscopy, and Dr. Johannes Richter and Mr. Sascha Feldmann measured the ultrafast transient grating PL.

Chapter 8

Conclusions and outlook

In order to summarise this work, we clarify the mechanism for charge and exciton transport in various disordered organic semiconductors, and formulate a number of design rules to improve materials for optoelectronic applications. By breaking this problem down into two parts, we focus on separately improving charge transport and fluorescence through enhancement of the two figures of merit: the charge carrier mobility (μ), and the fluorescence quantum efficiency (Φ).

In the first part, we consider a family of alternating donor-acceptor polymers which show high μ despite lacking long-range crystalline order. With the prototype system indacenodithiophene-*alt*-benzothiadiazole, we show how the solution processing procedure of the material, using high boiling point solvents, low-temperature annealing, and molecular additives to fill voids in the polymer microstructure, can each lead to metal oxide semiconductor field-effect transistor behaviour in the material. We also show that by annealing of the semiconductor layer, we can tune the structure such that a predominantly face-on configuration can be tilted towards an edge-on packing motif. We show that the packing motif is particularly important in achieving high μ, and the solubilising sidechains are crucial in determining the inter-chain packing, and a high density of close-contact points.

We develop this understanding further by considering other polymers in the same family. We show that insertion of fused rings elongating the donor subunit only increases the mobility when the number of sidechains per repeat unit is decreasing. To this end, linear *n*-hexadecyl sidechains should replace bulky *p*-hexadecylbenzyl, since this acts to separate backbones and reduce μ. However, it is important to disentangle

this observation from other chemical effects upon repeat-unit elongation. High μ, particularly in amorphous polymers, is highly dependent on a low degree of energetic torsional disorder between donor and acceptor subunits. Despite this, we observe that so long as the design motif of donor thiophene proton and the BT sulfenamide nitrogen remains, this design strategy provides a deep energetic minimum of the dihedral torsion potential in the coplanar configuration. This leads to a small energetic disorder in the polymer, and is partially responsible for its high μ. Our results support the assertion that push-pull character in our donor-acceptor polymers does not lead to a substantial improvement in the mobility, and our highest performing materials are more weakly push-pull in character. In fact, we do not see any evidence to suggest that increased intermolecular interaction is mediated by this polarisation, but rather that a decreasing density of sidechains (leading to decreased sterical hindrance between polymer chains) is the only factor which reliably improves μ in our disordered materials.

This discovery leads to the second part of our work where we seek to improve Φ. We show that this can be achieved in two ways; by (i) explictly decreasing the electronic interaction between polymer chains, and (ii) increasing the energy gap of the material. For the first strategy, we can use aforementioned bulky sidechains for sterical hindrance. In the same polymer mentioned earlier, we break open the mechanism by which excitons can be quenched non-radiatively on ultrafast timescales, and show that the largest contribution to non-radiative decay pathways is intrinsically linked to the degree of aggregation between polymer chains. In addition to its sensitivity to inter-chain coupling, this decay is also thermally activated, and mediated by various in-plane and out-of-plane vibrations which have strong electron-phonon coupling. By contrast, neutral excitations spread across chains are formed with a low quantum yield. These polaron pairs have a high degree of charge transfer (CT) character, and low oscillator strength. These are formed only on ultrafast timescales, and ultimately lead to non-radiative decay. Comparing the polymer with bulky sidechains with the benchmark sterically unhindered polymer, we observe a reduction in μ by $\sim 4\times$, but an improvement in Φ by $> 10\times$. The substitution of bulky sidechains as design modification strategy is appropriate for improving luminescence from high mobility, low energy gap materials with vanishing Φ.

The second strategy for improving Φ is not at the expense of μ. This is particularly important towards realising high-efficiency red and near infrared emitter applications.

By elongating the backbone as described earlier, an increased electron density of the donor decreases the degree of push-pull character. This increases the energy gap, and therefore decreases the wavefunction mixing of ground- and excited-states, according to the energy gap law. This is responsible for directly achieving $\Phi > 0.15$ in polymer semiconductor films, even when the electronic mixing between chains is strong. This presents an opportunity, and some polymers with low sidechain sterical hindrance due to their elongated backbone have a very high μ and Φ simultaneously. In order to link these observations causally, we determine the quantum yield of inter-chain CTs and its rate of decay, which in the case of high energy gap polymers has a luminescent signature. By solving the rate equations governing exciton dynamics developed in the previous section, we determine the radiative rate of decay of inter-chain excitons. This is an optical probe of close-contact points between polymer chains, and we observe substantially larger inter-chain wavefunction overlap for materials with low sidechain density. Therefore, while these inter-chain species ultimately provide a secondary decay pathway with a lower fluorescence quantum efficiency, they provide a valuable tool to study the close-contact points and show how increased aggregation in higher energy gap materials can lead to the simultaneous improvement of μ and Φ in disordered polymer materials. Further improvement to these materials may be achieved through longer elongation of the backbone repeat unit without changing the number of solubilising sidechains, or the development of less sterically hindered sidechains to promote greater wavefunction mixing between chains.

Finally, we turn our attention to improving Φ in organic emitting materials which display thermally activated delayed fluorescence (TADF). The design of all TADF materials involves strong intermolecular push-pull character which partitions HOMO and LUMO wavefunctions on donor and acceptor moieties respectively. Despite the characteristically slow radiative decay $k_{\mathrm{R}}(S_1)$ due to the CT exciton wavefunction character, significant luminescence quantum efficiencies (Φ) are realised by slow non-radiative rates $k_{\mathrm{NR}}(S_1)$ and $k_{\mathrm{NR}}(T_1)$. In particular, $k_{\mathrm{NR}}(T_1)$ is typically mediated by vibrational processes with strong electron-phonon coupling, such as low frequency torsion. This rate can be reduced in rigid environment where such motion can be suppressed, and hence presents an opportunity to increase Φ in some materials. We show that $k_{\mathrm{NR}}(T_1)$ is strongly related to dynamic low frequency torsion motion, and both are reduced in the presence of a rigid host matrix for various TADF materials across different classes. However, we also highlight the importance of

rotational freedom in determining the oscillator strength, the exchange energy, and the spin-orbit coupling matrix element, which, in the absence of a rigid host, mediate the luminescence in these materials. Therefore, suppressing dynamic motion can strongly modulate the photophysics of these materials. This leads to an improvement in Φ particularly in lower energy gap materials, although we show the need for a dynamic picture to explain the high k_{ISC} and k_{rISC} in spite of a good $k_{\mathrm{R}}(S_1)$ for TADF materials.

With respect to future work and the broader context, this work is particularly relevant towards the production of improved emitters for optoelectronic device applications. We develop the design rules according to our current understanding of the photophysics of luminescent organic materials, and fabricating and optimising OLED, OPV, and OLEFET devices with improved operating efficiencies is the next step. We have presented detailed investigations into some of the exciton decay mechanisms present in these materials, which we expect to fundamentally limit device performance. Indeed, those mechanisms which quench optically injected excitons in OPVs are likely also to limit the device efficiencies of OLEDs and OLEFETs. We find that, with proper control of the degree and nature of intermolecular coupling and the reduction of certain degrees of torsional freedom, (or equally via the use of higher E_g materials) we recover a very high Φ in some materials which are seldom thought appropriate for such applications. For polymer materials which are the focus of this work, if high μ and Φ can be achieved simultaneously, this is a key step towards the reduction in complexity of OPV device architectures, which can improve device efficiency and reduce fabrication restraints. However, the most important point is the potential, therefore, for such materials to achieve solid-state organic lasing, a milestone in organic electronics which has hitherto proved elusive; and this ambitious goal should be the focus of future work.

Bibliography

[1] Chiang, C. K. *et al.* Electrical Conductivity in Doped Polyacetylene. *Phys. Rev. Lett.* **39**, 1098–1101 (1977).

[2] Eley, D. D. Phthalocyanines as Semiconductors. *Nature* **162**, 819 (1948).

[3] Forrest, S. R. The path to ubiquitous and low-cost organic electronic appliances on plastic. *Nature* **428**, 911–918 (2004).

[4] Burroughes, J. H., Jones, C. A. & Friend, R. H. New semiconductor device physics in polymer diodes and transistors. *Nature* **335**, 137–141 (1988).

[5] Garnier, F., Horowitz, G., Peng, X. & Fichou, D. An all-organic 'soft' thin film transistor with very high carrier mobility. *Adv. Mater.* **2**, 592–594 (1990).

[6] Chen, Z. *et al.* High-Performance Ambipolar Diketopyrrolopyrrole-Thieno[3,2-b]thiophene Copolymer Field-Effect Transistors with Balanced Hole and Electron Mobilities. *Adv. Mater.* **24**, 647–652 (2012).

[7] Minemawari, H. *et al.* Inkjet printing of single-crystal films. *Nature* **475**, 364–367 (2011).

[8] Kang, I., Yun, H.-J., Chung, D. S., Kwon, S.-K. & Kim, Y.-H. Record High Hole Mobility in Polymer Semiconductors via Side-Chain Engineering. *J. Am. Chem. Soc.* **135**, 14896–14899 (2013).

[9] Sirringhaus, H. *et al.* High-Resolution Inkjet Printing of All-Polymer Transistor Circuits. *Science* **290**, 2123–2126 (2000).

[10] Pope, M., Kallmann, H. P. & Magnante, P. Electroluminescence in Organic Crystals. *The Journal of Chemical Physics* **38**, 2042–2043 (1963).

[11] Helfrich, W. & Schneider, W. G. Recombination Radiation in Anthracene Crystals. *Phys. Rev. Lett.* **14**, 229–231 (1965).

[12] Burroughes, J. H. *et al.* Light-emitting diodes based on conjugated polymers. *Nature* **347**, 539–541 (1990).

[13] Greenham, N. C., Moratti, S. C., Bradley, D. D. C., Friend, R. H. & Holmes, A. B. Efficient light-emitting diodes based on polymers with high electron affinities. *Nature* **365**, 628–630 (1993).

[14] Grice, A. W. *et al.* High brightness and efficiency blue light-emitting polymer diodes. *Appl. Phys. Lett.* **73**, 629–631 (1998).

[15] Yang, Y., Pei, Q. & Heeger, A. J. Efficient blue polymer light-emitting diodes from a series of soluble poly(paraphenylene)s. *Journal of Applied Physics* **79**, 934–939 (1996).

[16] Zhang, Q. *et al.* Efficient blue organic light-emitting diodes employing thermally activated delayed fluorescence. *Nat. Photonics* **8**, 326–332 (2014).

[17] Adachi, C., Baldo, M. A., Thompson, M. E. & Forrest, S. R. Nearly 100% internal phosphorescence efficiency in an organic light-emitting device. *Journal of Applied Physics* **90**, 5048–5051 (2001).

[18] Baldo, M. A., Thompson, M. E. & Forrest, S. R. High-efficiency fluorescent organic light-emitting devices using a phosphorescent sensitizer. *Nature* **403**, 750–753 (2000).

[19] Baldo, M. A. *et al.* Highly efficient phosphorescent emission from organic electroluminescent devices. *Nature* **395**, 151–154 (1998).

[20] Schmidbauer, S., Hohenleutner, A. & König, B. Chemical Degradation in Organic Light-Emitting Devices: Mechanisms and Implications for the Design of New Materials. *Adv. Mater.* **25**, 2114–2129 (2013).

[21] Uoyama, H., Goushi, K., Shizu, K., Nomura, H. & Adachi, C. Highly efficient organic light-emitting diodes from delayed fluorescence. *Nature* **492**, 234–238 (2012).

[22] Endo, A. *et al.* Thermally Activated Delayed Fluorescence from Sn4+–Porphyrin Complexes and Their Application to Organic Light Emitting Diodes — A Novel Mechanism for Electroluminescence. *Adv. Mater.* **21**, 4802–4806 (2009).

[23] Friend, R. H. *et al.* Electroluminescence in conjugated polymers. *Nature* **397**, 121–128 (1999).

[24] Tsujimura, T. *OLED Display Fundamentals and Applications* (John Wiley & Sons, 2017).

[25] Luo, Z. & Wu, S.-T. OLED versus LCD: Who wins. *Opt Photonics News* 19–21 (2015).

[26] Sirringhaus, H. 25th Anniversary Article: Organic Field-Effect Transistors: The Path Beyond Amorphous Silicon. *Adv. Mater.* **26**, 1319–1335 (2014).

[27] Venkateshvaran, D. *et al.* Approaching disorder-free transport in high-mobility conjugated polymers. *Nature* **515**, 384–388 (2014).

[28] Atkins, P. W. & Friedman, R. S. *Molecular Quantum Mechanics* (Oxford University Press, 2005), 4 edn.

[29] Köhler, A. & Bässler, H. *Electronic Processes in Organic Semiconductors: An Introduction* (John Wiley & Sons, 2015).

[30] Griffiths, D. J. *Introduction to Quantum Mechanics* (Cambridge University Press, 2016).

[31] Aldrich, C. & Bajaj, K. K. Binding energy of a Mott-Wannier exciton in a polarizable medium. *Solid State Communications* **22**, 157–160 (1977).

[32] Pope, M. & Swenberg, C. E. *Electronic Processes in Organic Crystals and Polymers* (Oxford University Press, 1984).

[33] Knupfer, M. Exciton binding energies in organic semiconductors. *Appl. Phys. A* **77**, 623–626 (2003).

[34] Foot, C. J. *Atomic Physics* (Oxford University Press, 2005).

[35] Clark, J., Silva, C., Friend, R. H. & Spano, F. C. Role of Intermolecular Coupling in the Photophysics of Disordered Organic Semiconductors: Aggregate Emission in Regioregular Polythiophene. *Phys. Rev. Lett.* **98**, 206406 (2007).

[36] Ho, P. K. H., Kim, J.-S., Tessler, N. & Friend, R. H. Photoluminescence of poly(p-phenylenevinylene)–silica nanocomposites: Evidence for dual emission by Franck–Condon analysis. *The Journal of Chemical Physics* **115**, 2709–2720 (2001).

[37] Hu, Z. *et al.* An insight into non-emissive excited states in conjugated polymers. *Nat. Commun.* **6**, 8246 (2015).

[38] Spano, F. C. & Silva, C. H- and J-Aggregate Behavior in Polymeric Semiconductors. *Annu. Rev. Phys. Chem.* **65**, 477–500 (2014).

[39] Brown, P. J. *et al.* Effect of interchain interactions on the absorption and emission of poly(3-hexylthiophene). *Phys. Rev. B* **67**, 064203 (2003).

[40] Spano, F. C. Modeling disorder in polymer aggregates: The optical spectroscopy of regioregular poly(3-hexylthiophene) thin films. *The Journal of Chemical Physics* **122**, 234701 (2005).

[41] Yang, X., Dykstra, T. E. & Scholes, G. D. Photon-echo studies of collective absorption and dynamic localization of excitation in conjugated polymers and oligomers. *Phys. Rev. B* **71**, 045203 (2005).

[42] Dykstra, T. E., Kovalevskij, V., Yang, X. & Scholes, G. D. Excited state dynamics of a conformationally disordered conjugated polymer: A comparison of solutions and film. *Chemical Physics* **318**, 21–32 (2005).

[43] Stoneham, A. M. Non-radiative transitions in semiconductors. *Rep. Prog. Phys.* **44**, 1251 (1981).

[44] Kovalenko, S. A., Schanz, R., Farztdinov, V. M., Hennig, H. & Ernsting, N. P. Femtosecond relaxation of photoexcited para-nitroaniline: Solvation, charge transfer, internal conversion and cooling. *Chemical Physics Letters* **323**, 312–322 (2000).

[45] Wild, W., Seilmeier, A., Gottfried, N. H. & Kaiser, W. Ultrafast investigations of vibrationally hot molecules after internal conversion in solution. *Chemical Physics Letters* **119**, 259–263 (1985).

[46] Englman, R. & Jortner, J. The energy gap law for radiationless transitions in large molecules. *Mol. Phys.* **18**, 145–164 (1970).

[47] Di Pietro, R. *et al.* Synthesis of High-Crystallinity DPP Polymers with Balanced Electron and Hole Mobility. *Chem. Mater.* **29**, 10220–10232 (2017).

[48] Kuik, M. *et al.* The Effect of Ketone Defects on the Charge Transport and Charge Recombination in Polyfluorenes. *Adv. Funct. Mater.* **21**, 4502–4509 (2011).

[49] Bolis, S. *et al.* Optical gain from polyfluorene keto defects in a liquid crystal mixture. *Chem. Commun.* **51**, 9686–9689 (2015).

[50] Gong, X., Moses, D., Heeger, A. J. & Xiao, S. White Light Electrophosphorescence from Polyfluorene-Based Light-Emitting Diodes: Utilization of Fluorenone Defects. *J. Phys. Chem. B* **108**, 8601–8605 (2004).

[51] Mikhnenko, O. V. *et al.* Trap-Limited Exciton Diffusion in Organic Semiconductors. *Adv. Mater.* **26**, 1912–1917 (2014).

[52] Nicolai, H. T. *et al.* Unification of trap-limited electron transport in semiconducting polymers. *Nat. Mater.* **11**, 882–887 (2012).

[53] Dimitrov, S. D. *et al.* Polaron pair mediated triplet generation in polymer/fullerene blends. *Nat. Commun.* **6**, 6501 (2015).

[54] Haug, A. Carrier density dependence of Auger recombination. *Solid-State Electronics* **21**, 1281–1284 (1978).

[55] Bessière, A. *et al.* Storage of Visible Light for Long-Lasting Phosphorescence in Chromium-Doped Zinc Gallate. *Chem. Mater.* **26**, 1365–1373 (2014).

[56] Köhler, A. & Bässler, H. Charges and Excited States in Organic Semiconductors. In *Electronic Processes in Organic Semiconductors*, 87–191 (Wiley-VCH Verlag GmbH & Co. KGaA, 2015).

[57] Marcus, R. A. On the Theory of Oxidation-Reduction Reactions Involving Electron Transfer. I. *The Journal of Chemical Physics* **24**, 966–978 (1956).

[58] Grancini, G. *et al.* Hot exciton dissociation in polymer solar cells. *Nat. Mater.* **12**, 29–33 (2013).

[59] Brédas, J.-L., Beljonne, D., Coropceanu, V. & Cornil, J. Charge-Transfer and Energy-Transfer Processes in π-Conjugated Oligomers and Polymers: A Molecular Picture. *Chem. Rev.* **104**, 4971–5004 (2004).

[60] Troisi, A. Charge transport in high mobility molecular semiconductors: Classical models and new theories. *Chem. Soc. Rev.* **40**, 2347–2358 (2011).

[61] Tsutsui, Y. *et al.* Unraveling Unprecedented Charge Carrier Mobility through Structure Property Relationship of Four Isomers of Didodecyl[1]benzothieno[3,2-b][1]benzothiophene. *Adv. Mater.* **28**, 7106–7114 (2016).

[62] Tsutsui, Y. *et al.* Evaluation of the intrinsic charge carrier transporting properties of linear- and bent-shaped π-extended benzo-fused thieno[3,2- b]thiophenes. *Phys. Chem. Chem. Phys.* **17**, 9624–9628 (2015).

[63] Choi, H. H., Cho, K., Frisbie, C. D., Sirringhaus, H. & Podzorov, V. Critical assessment of charge mobility extraction in FETs. *Nat. Mater.* **17**, 2–7 (2017).

[64] Chang, J.-F. *et al.* Hall-Effect Measurements Probing the Degree of Charge-Carrier Delocalization in Solution-Processed Crystalline Molecular Semiconductors. *Phys. Rev. Lett.* **107**, 066601 (2011).

[65] Senanayak, S. P., Ashar, A. Z., Kanimozhi, C., Patil, S. & Narayan, K. S. Room-temperature bandlike transport and Hall effect in a high-mobility ambipolar polymer. *Phys. Rev. B* **91**, 115302 (2015).

[66] Kang, K. *et al.* 2D coherent charge transport in highly ordered conducting polymers doped by solid state diffusion. *Nat Mater* **15**, 896–902 (2016).

[67] Herlogsson, L. *Electrolyte-Gated Organic Thin-Film Transistors*. Ph.D. thesis, Linköping University (2011).

[68] Köhler, A. & Bässler, H. Fundamentals of Organic Semiconductor Devices. In *Electronic Processes in Organic Semiconductors*, 307–388 (Wiley-VCH Verlag GmbH & Co. KGaA, 2015).

[69] Mas-Torrent, M. & Rovira, C. Tetrathiafulvalene derivatives for organic field effect transistors. *J. Mater. Chem.* **16**, 433–436 (2006).

[70] Shahid, M. *et al.* Low band gap selenophene – diketopyrrolopyrrole polymers exhibiting high and balanced ambipolar performance in bottom-gate transistors. *Chem. Sci.* **3**, 181–185 (2012).

[71] Sirringhaus, H. Device Physics of Solution-Processed Organic Field-Effect Transistors. *Adv. Mater.* **17**, 2411–2425 (2005).

[72] Bürgi, L., Richards, T. J., Friend, R. H. & Sirringhaus, H. Close look at charge carrier injection in polymer field-effect transistors. *Journal of Applied Physics* **94**, 6129–6137 (2003).

[73] Holstein, T. Studies of polaron motion: Part I. The molecular-crystal model. *Annals of Physics* **8**, 325–342 (1959).

[74] Beljonne, D. *et al.* Optical Signature of Delocalized Polarons in Conjugated Polymers. *Adv. Funct. Mater.* **11**, 229–234 (2001).

[75] Horowitz, G. Organic field-effect transistors. *Adv. Mater.* **10**, 365–377 (1998).

[76] O'Donnell, K. P., Martin, R. W. & Middleton, P. G. Origin of Luminescence from InGaN Diodes. *Phys. Rev. Lett.* **82**, 237–240 (1999).

[77] Sirringhaus, H. *et al.* Two-dimensional charge transport in self-organized, high-mobility conjugated polymers. *Nature* **401**, 685–688 (1999).

[78] Blackman, J. A. & Sabra, M. K. Interchain coupling and optical absorption in degenerate and nondegenerate polymers. *Phys. Rev. B* **47**, 15437–15448 (1993).

[79] Troisi, A. Prediction of the Absolute Charge Mobility of Molecular Semiconductors: The Case of Rubrene. *Adv. Mater.* **19**, 2000–2004 (2007).

[80] Noriega, R. *et al.* A general relationship between disorder, aggregation and charge transport in conjugated polymers. *Nat Mater* **12**, 1038–1044 (2013).

[81] Fröhlich, H. On the theory of dielectric breakdown in solids. *Proc. R. Soc. Lond. A* **188**, 521–532 (1947).

[82] Cohen, M. H., Fritzsche, H. & Ovshinsky, S. R. Simple Band Model for Amorphous Semiconducting Alloys. *Phys. Rev. Lett.* **22**, 1065–1068 (1969).

[83] Mott, N. The mobility edge since 1967. *J. Phys. C: Solid State Phys.* **20**, 3075 (1987).

[84] Shur, M. & Hack, M. Physics of amorphous silicon based alloy field-effect transistors. *Journal of Applied Physics* **55**, 3831–3842 (1984).

[85] Horowitz, G., Hajlaoui, R. & Delannoy, P. Temperature Dependence of the Field-Effect Mobility of Sexithiophene. Determination of the Density of Traps. *J. Phys. III France* **5**, 355–371 (1995).

[86] Horowitz, G., Hajlaoui, M. E. & Hajlaoui, R. Temperature and gate voltage dependence of hole mobility in polycrystalline oligothiophene thin film transistors. *Journal of Applied Physics* **87**, 4456–4463 (2000).

[87] Spear, W. E. & Le Comber, P. G. Investigation of the localised state distribution in amorphous Si films. *Journal of Non-Crystalline Solids* **8-10**, 727–738 (1972).

[88] Mott, N. F. Conduction in non-crystalline materials. *Philos. Mag. J. Theor. Exp. Appl. Phys.* **19**, 835–852 (1969).

[89] Conwell, E. M. Impurity Band Conduction in Germanium and Silicon. *Phys. Rev.* **103**, 51–61 (1956).

[90] Miller, A. & Abrahams, E. Impurity Conduction at Low Concentrations. *Phys. Rev.* **120**, 745–755 (1960).

[91] Vissenberg, M. C. J. M. & Matters, M. Theory of the field-effect mobility in amorphous organic transistors. *Phys. Rev. B* **57**, 12964–12967 (1998).

[92] Brondijk, J. J. *et al.* Two-Dimensional Charge Transport in Disordered Organic Semiconductors. *Phys. Rev. Lett.* **109**, 056601 (2012).

[93] Kronemeijer, A. J. *et al.* Two-Dimensional Carrier Distribution in Top-Gate Polymer Field-Effect Transistors: Correlation between Width of Density of Localized States and Urbach Energy. *Adv. Mater.* **26**, 728–733 (2014).

[94] Bittle, E. G., Basham, J. I., Jackson, T. N., Jurchescu, O. D. & Gundlach, D. J. Mobility overestimation due to gated contacts in organic field-effect transistors. *Nat. Commun.* **7**, 10908 (2016).

[95] de Mello, J. C., Wittmann, H. F. & Friend, R. H. An improved experimental determination of external photoluminescence quantum efficiency. *Adv. Mater.* **9**, 230–232 (1997).

[96] Yong, C. K. *et al.* Strong Carrier Lifetime Enhancement in GaAs Nanowires Coated with Semiconducting Polymer. *Nano Lett.* **12**, 6293–6301 (2012).

[97] Schmid, S. A. *et al.* Analyzing the Molecular Weight Distribution in Supramolecular Polymers. *J. Am. Chem. Soc.* **131**, 17696–17704 (2009).

[98] Neese, F. The ORCA program system. *WIREs Comput Mol Sci* **2**, 73–78 (2012).

[99] Lee, C., Yang, W. & Parr, R. G. Development of the Colle-Salvetti correlation-energy formula into a functional of the electron density. *Phys. Rev. B* **37**, 785–789 (1988).

[100] Becke, A. D. Density-functional thermochemistry. III. The role of exact exchange. *The Journal of Chemical Physics* **98**, 5648–5652 (1993).

[101] Ditchfield, R., Hehre, W. J. & Pople, J. A. Self-Consistent Molecular-Orbital Methods. IX. An Extended Gaussian-Type Basis for Molecular-Orbital Studies of Organic Molecules. *The Journal of Chemical Physics* **54**, 724–728 (1971).

[102] Tirado-Rives, J. & Jorgensen, W. L. Performance of B3LYP Density Functional Methods for a Large Set of Organic Molecules. *J. Chem. Theory Comput.* **4**, 297–306 (2008).

[103] Bouzzine, S. M., Bouzakraoui, S., Bouachrine, M. & Hamidi, M. Density functional theory (B3LYP/6-31G*) study of oligothiophenes in their aromatic and polaronic states. *Journal of Molecular Structure: THEOCHEM* **726**, 271–276 (2005).

[104] Sortur, V., Yenagi, J., Tonannavar, J., Jadhav, V. B. & Kulkarni, M. V. Vibrational assignments for 7-methyl-4-bromomethylcoumarin, as aided by RHF and B3LYP/6-31G* calculations. *Spectrochimica Acta Part A: Molecular and Biomolecular Spectroscopy* **71**, 688–694 (2008).

[105] Arjunan, V. & Mohan, S. Fourier transform infrared and FT-Raman spectra, assignment, ab initio, DFT and normal co-ordinate analysis of 2-chloro-4-methylaniline and 2-chloro-6-methylaniline. *Spectrochimica Acta Part A: Molecular and Biomolecular Spectroscopy* **72**, 436–444 (2009).

[106] Li, J. *et al.* A stable solution-processed polymer semiconductor with record high-mobility for printed transistors. *Sci. Rep.* **2**, 754 (2012).

[107] Noh, Y.-Y., Zhao, N., Caironi, M. & Sirringhaus, H. Downscaling of self-aligned, all-printed polymer thin-film transistors. *Nat. Nanotechnol.* **2**, 784–789 (2007).

[108] Back, J. Y. *et al.* Investigation of Structure–Property Relationships in Diketopyrrolopyrrole-Based Polymer Semiconductors via Side-Chain Engineering. *Chem. Mater.* **27**, 1732–1739 (2015).

[109] Oosterbaan, W. D. *et al.* On the Relation between Morphology and FET Mobility of Poly(3-alkylthiophene)s at the Polymer/SiO2 and Polymer/Air Interface. *Adv. Funct. Mater.* **24**, 1994–2004 (2014).

[110] Olivier, Y. *et al.* 25th Anniversary Article: High-Mobility Hole and Electron Transport Conjugated Polymers: How Structure Defines Function. *Adv. Mater.* **26**, 2119–2136 (2014).

[111] Sirringhaus, H., Tessler, N. & Friend, R. H. Integrated Optoelectronic Devices Based on Conjugated Polymers. *Science* **280**, 1741–1744 (1998).

[112] Bao, Z., Dodabalapur, A. & Lovinger, A. J. Soluble and processable regioregular poly(3-hexylthiophene) for thin film field-effect transistor applications with high mobility. *Appl. Phys. Lett.* **69**, 4108–4110 (1996).

[113] Chang, J.-F. *et al.* Molecular-weight dependence of interchain polaron delocalization and exciton bandwidth in high-mobility conjugated polymers. *Phys. Rev. B* **74**, 115318 (2006).

[114] Lei, Y. *et al.* Solution-Processed Donor-Acceptor Polymer Nanowire Network Semiconductors For High-Performance Field-Effect Transistors. *Sci. Rep.* **6**, 24476 (2016).

[115] Takacs, C. J. *et al.* Remarkable Order of a High-Performance Polymer. *Nano Lett.* **13**, 2522–2527 (2013).

[116] Kim, J.-S. *et al.* Optoelectronic and Charge Transport Properties at Organic-Organic Semiconductor Interfaces: Comparison between Polyfluorene-Based Polymer Blend and Copolymer. *J. Am. Chem. Soc.* **130**, 13120–13131 (2008).

[117] Veres, J., Ogier, S., Lloyd, G. & de Leeuw, D. Gate Insulators in Organic Field-Effect Transistors. *Chem. Mater.* **16**, 4543–4555 (2004).

[118] Veres, J., Ogier, S., Leeming, S., Cupertino, D. & Mohialdin Khaffaf, S. Low-k Insulators as the Choice of Dielectrics in Organic Field-Effect Transistors. *Adv. Funct. Mater.* **13**, 199–204 (2003).

[119] Street, R. A. Unraveling Charge Transport in Conjugated Polymers. *Science* **341**, 1072–1073 (2013).

[120] Di, D. *et al.* High-performance light-emitting diodes based on carbene-metal-amides. *Science* **356**, 159–163 (2017).

[121] Reineke, S. *et al.* White organic light-emitting diodes with fluorescent tube efficiency. *Nature* **459**, 234–238 (2009).

[122] Cnops, K. *et al.* 8.4% efficient fullerene-free organic solar cells exploiting long-range exciton energy transfer. *Nat. Commun.* **5**, 3406 (2014).

[123] Dou, L. *et al.* Tandem polymer solar cells featuring a spectrally matched low-bandgap polymer. *Nat Photon* **6**, 180–185 (2012).

[124] Han, T.-H. *et al.* Extremely efficient flexible organic light-emitting diodes with modified graphene anode. *Nat Photon* **6**, 105–110 (2012).

[125] Capelli, R. *et al.* Organic light-emitting transistors with an efficiency that outperforms the equivalent light-emitting diodes. *Nat Mater* **9**, 496–503 (2010).

[126] Brédas, J.-L., Norton, J. E., Cornil, J. & Coropceanu, V. Molecular Understanding of Organic Solar Cells: The Challenges. *Acc. Chem. Res.* **42**, 1691–1699 (2009).

[127] Achermann, M., Petruska, M. A., Koleske, D. D., Crawford, M. H. & Klimov, V. I. Nanocrystal-Based Light-Emitting Diodes Utilizing High-Efficiency Nonradiative Energy Transfer for Color Conversion. *Nano Lett.* **6**, 1396–1400 (2006).

[128] Barkhouse, D. A. R., Pattantyus-Abraham, A. G., Levina, L. & Sargent, E. H. Thiols Passivate Recombination Centers in Colloidal Quantum Dots Leading to Enhanced Photovoltaic Device Efficiency. *ACS Nano* **2**, 2356–2362 (2008).

[129] Campbell, A. R. *et al.* Low-Temperature Control of Nanoscale Morphology for High Performance Polymer Photovoltaics. *Nano Lett.* **8**, 3942–3947 (2008).

[130] Xia, R., Heliotis, G., Hou, Y. & Bradley, D. D. Fluorene-based conjugated polymer optical gain media. *Org. Electron.* **4**, 165–177 (2003).

[131] Noel, N. K. *et al.* Enhanced Photoluminescence and Solar Cell Performance via Lewis Base Passivation of Organic–Inorganic Lead Halide Perovskites. *ACS Nano* **8**, 9815–9821 (2014).

[132] Xie, T. Tunable polymer multi-shape memory effect. *Nature* **464**, 267–270 (2010).

[133] Aiyar, A. R., Hong, J.-I., Nambiar, R., Collard, D. M. & Reichmanis, E. Tunable Crystallinity in Regioregular Poly(3-Hexylthiophene) Thin Films and Its Impact on Field Effect Mobility. *Adv. Funct. Mater.* **21**, 2652–2659 (2011).

[134] Yiu, A. T. *et al.* Side-Chain Tunability of Furan-Containing Low-Band-Gap Polymers Provides Control of Structural Order in Efficient Solar Cells. *J. Am. Chem. Soc.* **134**, 2180–2185 (2012).

[135] Katz, H. E. *et al.* A soluble and air-stable organic semiconductor with high electron mobility. *Nature* **404**, 478–481 (2000).

[136] Nikolka, M. *et al.* High operational and environmental stability of high-mobility conjugated polymer field-effect transistors through the use of molecular additives. *Nat Mater* **16**, 356–362 (2017).

[137] Zhang, X. *et al.* Molecular origin of high field-effect mobility in an indacenodithiophene–benzothiadiazole copolymer. *Nat. Commun.* **4**, 2238 (2013).

[138] Yap, B. K., Xia, R., Campoy-Quiles, M., Stavrinou, P. N. & Bradley, D. D. C. Simultaneous optimization of charge-carrier mobility and optical gain in semiconducting polymer films. *Nat Mater* **7**, 376–380 (2008).

[139] Gwinner, M. C. *et al.* Highly Efficient Single-Layer Polymer Ambipolar Light-Emitting Field-Effect Transistors. *Adv. Mater.* **24**, 2728–2734 (2012).

[140] Harkin, D. J. *et al.* Decoupling Charge Transport and Electroluminescence in a High Mobility Polymer Semiconductor. *Adv. Mater.* **28**, 6378–6385 (2016).

[141] Han, J. *et al.* Low-bandgap donor–acceptor polymers for photodetectors with photoresponsivity from 300 nm to 1600 nm. *J. Mater. Chem. C* **5**, 159–165 (2017).

[142] Steckler, T. T. *et al.* Very Low Band Gap Thiadiazoloquinoxaline Donor–Acceptor Polymers as Multi-tool Conjugated Polymers. *J. Am. Chem. Soc.* **136**, 1190–1193 (2014).

[143] Zulkarnaen Bisri, S., Takenobu, T. & Iwasa, Y. The pursuit of electrically-driven organic semiconductor lasers. *J. Mater. Chem. C* **2**, 2827–2836 (2014).

[144] Lukman, S. *et al.* Tuning the role of charge-transfer states in intramolecular singlet exciton fission through side-group engineering. *Nat. Commun.* **7**, ncomms13622 (2016).

[145] Horio, T., Fuji, T., Suzuki, Y.-I. & Suzuki, T. Probing Ultrafast Internal Conversion through Conical Intersection via Time-Energy Map of Photoelectron Angular Anisotropy. *J. Am. Chem. Soc.* **131**, 10392–10393 (2009).

[146] Fidder, H., Rini, M. & Nibbering, E. T. J. The Role of Large Conformational Changes in Efficient Ultrafast Internal Conversion: Deviations from the Energy Gap Law. *J. Am. Chem. Soc.* **126**, 3789–3794 (2004).

[147] Brazard, J., Bizimana, L. A., Gellen, T., Carbery, W. P. & Turner, D. B. Experimental Detection of Branching at a Conical Intersection in a Highly Fluorescent Molecule. *J. Phys. Chem. Lett.* **7**, 14–19 (2016).

[148] Benduhn, J. *et al.* Intrinsic non-radiative voltage losses in fullerene-based organic solar cells. *Nat. Energy* **2**, 17053 (2017).

[149] Marcus, R. A. Electron transfer reactions in chemistry. Theory and experiment. *Rev. Mod. Phys.* **65**, 599–610 (1993).

[150] Sheng, C.-X., Tong, M., Singh, S. & Vardeny, Z. V. Experimental determination of the charge/neutral branching ratio η in the photoexcitation of π-conjugated polymers by broadband ultrafast spectroscopy. *Phys. Rev. B* **75**, 085206 (2007).

[151] Zhang, W. *et al.* Indacenodithiophene Semiconducting Polymers for High-Performance, Air-Stable Transistors. *J. Am. Chem. Soc.* **132**, 11437–11439 (2010).

[152] List, E., Guentner, R., Scanducci de Freitas, P. & Scherf, U. The Effect of Keto Defect Sites on the Emission Properties of Polyfluorene-Type Materials. *Adv. Mater.* **14**, 374–378 (2002).

[153] Scherf, U. & List, E. Semiconducting Polyfluorenes—Towards Reliable Structure–Property Relationships. *Adv. Mater.* **14**, 477–487 (2002).

[154] Chen, F., Xia, J., Ferry, D. K. & Tao, N. Dielectric Screening Enhanced Performance in Graphene FET. *Nano Lett.* **9**, 2571–2574 (2009).

[155] Karpov, Y. *et al.* Molecular Doping of a High Mobility Diketopyrrolopyrrole–Dithienylthieno[3,2-b]thiophene Donor–Acceptor Copolymer with F6TCNNQ. *Macromolecules* **50**, 914–926 (2017).

[156] Yan, H. *et al.* A high-mobility electron-transporting polymer for printed transistors. *Nature* **457**, 679–686 (2009).

[157] Chang, J.-F., Sirringhaus, H., Giles, M., Heeney, M. & McCulloch, I. Relative importance of polaron activation and disorder on charge transport in high-mobility conjugated polymer field-effect transistors. *Phys. Rev. B* **76**, 205204 (2007).

[158] Tong, M. *et al.* Higher Molecular Weight Leads to Improved Photoresponsivity, Charge Transport and Interfacial Ordering in a Narrow Bandgap Semiconducting Polymer. *Adv. Funct. Mater.* **20**, 3959–3965 (2010).

[159] Hall, A. C. A century of ellipsometry. *Surface Science* **16**, 1–13 (1969).

[160] Franquet, A. *et al.* Determination of the thickness of thin silane films on aluminium surfaces by means of spectroscopic ellipsometry. *Thin Solid Films* **384**, 37–45 (2001).

[161] Aspnes, D. E. Spectroscopic ellipsometry — Past, present, and future. *Thin Solid Films* **571**, 334–344 (2014).

[162] Tsutsumi, J., Matsuzaki, H., Kanai, N., Yamada, T. & Hasegawa, T. Charge Separation and Recombination of Charge-Transfer Excitons in Donor–Acceptor Polymer Solar Cells. *J. Phys. Chem. C* **117**, 16769–16773 (2013).

[163] Banerji, N. *et al.* Breaking Down the Problem: Optical Transitions, Electronic Structure, and Photoconductivity in Conjugated Polymer PCDTBT and in Its Separate Building Blocks. *J. Phys. Chem. C* **116**, 11456–11469 (2012).

[164] Warren, B. E. X-Ray Diffraction in Random Layer Lattices. *Phys. Rev.* **59**, 693–698 (1941).

[165] Kasha, M. Characterization of electronic transitions in complex molecules. *Discuss. Faraday Soc.* **9**, 14–19 (1950).

[166] Mikhnenko, O. V., Blom, P. W. M. & Nguyen, T.-Q. Exciton diffusion in organic semiconductors. *Energy Env. Sci* **8**, 1867–1888 (2015).

[167] Bronstein, H. *et al.* Indacenodithiophene-co-benzothiadiazole Copolymers for High Performance Solar Cells or Transistors via Alkyl Chain Optimization. *Macromolecules* **44**, 6649–6652 (2011).

[168] Yamashita, Y. *et al.* Mobility Exceeding 10 cm$2̂$/(V·s) in Donor–Acceptor Polymer Transistors with Band-like Charge Transport. *Chem. Mater.* **28**, 420–424 (2016).

[169] Yamashita, Y. *et al.* Transition Between Band and Hopping Transport in Polymer Field-Effect Transistors. *Adv. Mater.* **26**, 8169–8173 (2014).

[170] Podzorov, V. *et al.* Intrinsic Charge Transport on the Surface of Organic Semiconductors. *Phys. Rev. Lett.* **93**, 086602 (2004).

[171] Ostroverkhova, O. *et al.* Bandlike transport in pentacene and functionalized pentacene thin films revealed by subpicosecond transient photoconductivity measurements. *Phys. Rev. B* **71**, 035204 (2005).

[172] Vezie, M. S. *et al.* Exploring the origin of high optical absorption in conjugated polymers. *Nat. Mater.* **15**, 746–753 (2016).

[173] Lee, T. W. *et al.* Heteroarene-fused π-conjugated main-chain polymers containing 4,7-bis(4-octylthiophen-2-yl)benzo[c][1,2,5]thiadiazole or 2,5-bis(4-octylthiophen-2-yl)thiazolo[5,4-d]thiazole and their application to photovoltaic devices. *J. Polym. Sci. A Polym. Chem.* **48**, 5921–5929 (2010).

[174] Schroeder, B. C. *et al.* Synthesis of novel thieno[3,2-b]thienobis(silolothiophene) based low bandgap polymers for organic photovoltaics. *Chem. Commun.* **48**, 7699–7701 (2012).

[175] Bronstein, H. *et al.* Synthesis of a Novel Fused Thiophene-thieno[3,2-b]thiophene-thiophene Donor Monomer and Co-polymer for Use in OPV and OFETs. *Macromol. Rapid Commun.* **32**, 1664–1668 (2011).

[176] Cheng, Y.-J. *et al.* Carbazole-Based Ladder-Type Heptacylic Arene with Aliphatic Side Chains Leading to Enhanced Efficiency of Organic Photovoltaics. *Chem. Mater.* **23**, 2361–2369 (2011).

[177] Chang, C.-Y. *et al.* Combination of Molecular, Morphological, and Interfacial Engineering to Achieve Highly Efficient and Stable Plastic Solar Cells. *Adv. Mater.* **24**, 549–553 (2012).

[178] Wu, J.-S. *et al.* Dithienocarbazole-Based Ladder-Type Heptacyclic Arenes with Silicon, Carbon, and Nitrogen Bridges: Synthesis, Molecular Properties, Field-Effect Transistors, and Photovoltaic Applications. *Adv. Funct. Mater.* **22**, 1711–1722 (2012).

[179] Zhang, W. *et al.* A Novel Alkylated Indacenodithieno[3,2-b]thiophene-Based Polymer for High-Performance Field-Effect Transistors. *Adv. Mater.* **28**, 3922–3927 (2016).

[180] Chen, H. *et al.* Dithiopheneindenofluorene (TIF) Semiconducting Polymers with Very High Mobility in Field-Effect Transistors. *Adv. Mater.* **29**, n/a–n/a (2017).

[181] Brown, A. R., Jarrett, C. P., de Leeuw, D. M. & Matters, M. Field-effect transistors made from solution-processed organic semiconductors. *Synthetic Metals* **88**, 37–55 (1997).

[182] Li, W. *et al.* Mobility-Controlled Performance of Thick Solar Cells Based on Fluorinated Copolymers. *J. Am. Chem. Soc.* **136**, 15566–15576 (2014).

[183] Zhang, Y. *et al.* Increased open circuit voltage in fluorinated benzothiadiazole -based alternating conjugated polymers. *Chem. Commun.* **47**, 11026–11028 (2011).

[184] You, J. *et al.* A polymer tandem solar cell with 10.6% power conversion efficiency. *Nat. Commun.* **4**, 1446 (2013).

[185] Yuen, J. D. *et al.* High Performance Weak Donor–Acceptor Polymers in Thin Film Transistors: Effect of the Acceptor on Electronic Properties, Ambipolar Conductivity, Mobility, and Thermal Stability. *J. Am. Chem. Soc.* **133**, 20799–20807 (2011).

[186] Yuen, J. D. *et al.* Ambipolarity in Benzobisthiadiazole-Based Donor–Acceptor Conjugated Polymers. *Adv. Mater.* **23**, 3780–3785 (2011).

[187] Steckler, T. T. *et al.* A Spray-Processable, Low Bandgap, and Ambipolar Donor-Acceptor Conjugated Polymer. *J. Am. Chem. Soc.* **131**, 2824–2826 (2009).

[188] Fan, J. *et al.* High-Hole-Mobility Field-Effect Transistors Based on Co-Benzobisthiadiazole-Quaterthiophene. *Adv. Mater.* **24**, 6164–6168 (2012).

[189] Niedzialek, D. *et al.* Probing the Relation Between Charge Transport and Supramolecular Organization Down to Ångström Resolution in a Benzothiadiazole-Cyclopentadithiophene Copolymer. *Adv. Mater.* **25**, 1939–1947 (2013).

[190] Klamt, A. & Schüürmann, G. COSMO: A new approach to dielectric screening in solvents with explicit expressions for the screening energy and its gradient. *J. Chem. Soc., Perkin Trans. 2* **0**, 799–805 (1993).

[191] Fazzi, D. *et al.* Ultrafast internal conversion in a low band gap polymer for photovoltaics: Experimental and theoretical study. *Phys. Chem. Chem. Phys.* **14**, 6367–6374 (2012).

[192] Kalon, G., Jun Shin, Y., Giang Truong, V., Kalitsov, A. & Yang, H. The role of charge traps in inducing hysteresis: Capacitance–voltage measurements on top gated bilayer graphene. *Appl. Phys. Lett.* **99**, 083109 (2011).

[193] Wu, J.-S., Cheng, S.-W., Cheng, Y.-J. & Hsu, C.-S. Donor–acceptor conjugated polymers based on multifused ladder-type arenes for organic solar cells. *Chem. Soc. Rev.* **44**, 1113–1154 (2015).

[194] Kim, N.-K. *et al.* Solution-Processed Barium Salts as Charge Injection Layers for High Performance N-Channel Organic Field-Effect Transistors. *ACS Appl. Mater. Interfaces* **6**, 9614–9621 (2014).

[195] Zhang, M., Guo, X., Wang, X., Wang, H. & Li, Y. Synthesis and Photovoltaic Properties of D–A Copolymers Based on Alkyl-Substituted Indacenodithiophene Donor Unit. *Chem. Mater.* **23**, 4264–4270 (2011).

[196] McCulloch, I. *et al.* Design of Semiconducting Indacenodithiophene Polymers for High Performance Transistors and Solar Cells. *Acc. Chem. Res.* **45**, 714–722 (2012).

[197] Schaller, R. D. *et al.* The Nature of Interchain Excitations in Conjugated Polymers: Spatially-Varying Interfacial Solvatochromism of Annealed MEH-PPV Films Studied by Near-Field Scanning Optical Microscopy (NSOM). *J. Phys. Chem. B* **106**, 9496–9506 (2002).

[198] Jenekhe, S. A., Lu, L. & Alam, M. M. New Conjugated Polymers with Donor-Acceptor Architectures: Synthesis and Photophysics of Carbazole-Quinoline and Phenothiazine-Quinoline Copolymers and Oligomers Exhibiting Large Intramolecular Charge Transfer. *Macromolecules* **34**, 7315–7324 (2001).

[199] Banerji, N., Cowan, S., Leclerc, M., Vauthey, E. & Heeger, A. J. Exciton Formation, Relaxation, and Decay in PCDTBT. *J. Am. Chem. Soc.* **132**, 17459–17470 (2010).

[200] Banerji, N. Sub-picosecond delocalization in the excited state of conjugated homopolymers and donor–acceptor copolymers. *J. Mater. Chem. C* **1**, 3052–3066 (2013).

[201] Roy, P. *et al.* Ultrafast bridge planarization in donor-π-acceptor copolymers drives intramolecular charge transfer. *Nat. Commun.* **8**, 1716 (2017).

[202] Keivanidis, P. E. *et al.* Delayed Luminescence Spectroscopy of Organic Photovoltaic Binary Blend Films: Probing the Emissive Non-geminate Charge Recombination. *Adv. Mater.* **22**, 5183–5187 (2010).

[203] Johnson, K. *et al.* Control of Intrachain Charge Transfer in Model Systems for Block Copolymer Photovoltaic Materials. *J. Am. Chem. Soc.* **135**, 5074–5083 (2013).

[204] Montanari, I. *et al.* Transient optical studies of charge recombination dynamics in a polymer/fullerene composite at room temperature. *Appl. Phys. Lett.* **81**, 3001–3003 (2002).

[205] Yan, M., Rothberg, L. J., Papadimitrakopoulos, F., Galvin, M. E. & Miller, T. M. Spatially indirect excitons as primary photoexcitations in conjugated polymers. *Phys. Rev. Lett.* **72**, 1104–1107 (1994).

[206] Frankevich, E. L. *et al.* Polaron-pair generation in poly(phenylene vinylenes). *Phys. Rev. B* **46**, 9320–9324 (1992).

[207] Segal, M. Excitonic singlet-triplet ratios in molecular and polymeric organic materials. *Phys. Rev. B* **68** (2003).

[208] Rao, A., Wilson, M. W. B., Albert-Seifried, S., Di Pietro, R. & Friend, R. H. Photophysics of pentacene thin films: The role of exciton fission and heating effects. *Phys. Rev. B* **84**, 195411 (2011).

[209] Albert-Seifried, S. & Friend, R. H. Measurement of thermal modulation of optical absorption in pump-probe spectroscopy of semiconducting polymers. *Appl. Phys. Lett.* **98**, 223304 (2011).

[210] Gélinas, S. *et al.* The Binding Energy of Charge-Transfer Excitons Localized at Polymeric Semiconductor Heterojunctions. *J. Phys. Chem. C* **115**, 7114–7119 (2011).

[211] Endo, T., Kobayashi, T., Nagase, T. & Naito, H. Preparation and Optical Properties of Aligned β-Phase Polyfluorene Thin Films. *Jpn. J. Appl. Phys.* **46**, L1093 (2007).

[212] Muccini, M. A bright future for organic field-effect transistors. *Nat. Mater.* **5**, 605–613 (2006).

[213] Kim, Y. *et al.* Organic Photovoltaic Devices Based on Blends of Regioregular Poly(3-hexylthiophene) and Poly(9,9-dioctylfluorene-co-benzothiadiazole). *Chem. Mater.* **16**, 4812–4818 (2004).

[214] Gwinner, M. C., Jakubka, F., Gannott, F., Sirringhaus, H. & Zaumseil, J. Enhanced Ambipolar Charge Injection with Semiconducting Polymer/Carbon Nanotube Thin Films for Light-Emitting Transistors. *ACS Nano* **6**, 539–548 (2012).

[215] Yan, H. *et al.* Correlating the Efficiency and Nanomorphology of Polymer Blend Solar Cells Utilizing Resonant Soft X-ray Scattering. *ACS Nano* **6**, 677–688 (2012).

[216] Zaumseil, J. *et al.* Quantum efficiency of ambipolar light-emitting polymer field-effect transistors. *Journal of Applied Physics* **103**, 064517 (2008).

[217] Lim, S.-H., Bjorklund, T. G., Spano, F. C. & Bardeen, C. J. Exciton Delocalization and Superradiance in Tetracene Thin Films and Nanoaggregates. *Phys. Rev. Lett.* **92**, 107402 (2004).

[218] Ahn, T.-S. *et al.* Experimental and theoretical study of temperature dependent exciton delocalization and relaxation in anthracene thin films. *The Journal of Chemical Physics* **128**, 054505 (2008).

[219] Jagtap, A. M., Khatei, J. & Rao, K. S. R. K. Exciton–phonon scattering and nonradiative relaxation of excited carriers in hydrothermally synthesized CdTe quantum dots. *Phys. Chem. Chem. Phys.* **17**, 27579–27587 (2015).

[220] Lin, M.-F. *et al.* Ultrafast non-radiative dynamics of atomically thin MoSe 2. *Nat. Commun.* **8**, 1745 (2017).

[221] Musser, A. J. *et al.* Evidence for conical intersection dynamics mediating ultrafast singlet exciton fission. *Nat Phys* **11**, 352–357 (2015).

[222] Kim, H., Schulte, N., Zhou, G., Müllen, K. & Laquai, F. A High Gain and High Charge Carrier Mobility Indenofluorene-Phenanthrene Copolymer for Light Amplification and Organic Lasing. *Adv. Mater.* **23**, 894–897 (2011).

[223] Mu, C. *et al.* High-Efficiency All-Polymer Solar Cells Based on a Pair of Crystalline Low-Bandgap Polymers. *Adv. Mater.* **26**, 7224–7230 (2014).

[224] Baldo, M. A., Holmes, R. J. & Forrest, S. R. Prospects for electrically pumped organic lasers. *Phys. Rev. B* **66**, 035321 (2002).

[225] Zhao, W. *et al.* Molecular Optimization Enables over 13% Efficiency in Organic Solar Cells. *J. Am. Chem. Soc.* **139**, 7148–7151 (2017).

[226] Tessler, N. Lasers Based on Semiconducting Organic Materials. *Adv. Mater.* **11**, 363–370 (1999).

[227] Troisi, A. The speed limit for sequential charge hopping in molecular materials. *Organic Electronics* **12**, 1988–1991 (2011).

[228] Yan, M., Rothberg, L. J., Kwock, E. W. & Miller, T. M. Interchain Excitations in Conjugated Polymers. *Phys. Rev. Lett.* **75**, 1992–1995 (1995).

[229] Hilborn, R. C. Einstein coefficients, cross sections, f values, dipole moments, and all that. *American Journal of Physics* **50**, 982–986 (1982).

[230] Hassaan, M. U. *et al.* Highly Efficient Energy Transfer in Light Emissive Poly(9,9-dioctylfluorene) and Poly(p-phenylenevinylene) Blend System. *ACS Photonics* **5**, 607–613 (2018).

[231] Liu, J. *et al.* High mobility emissive organic semiconductor. *Nat. Commun.* **6**, 10032 (2015).

[232] Wu, C. C. *et al.* Integration of organic LEDs and amorphous Si TFTs onto flexible and lightweight metal foil substrates. *IEEE Electron Device Lett.* **18**, 609–612 (1997).

[233] Dimitrakopoulos, C. D., Purushothaman, S., Kymissis, J., Callegari, A. & Shaw, J. M. Low-Voltage Organic Transistors on Plastic Comprising High-Dielectric Constant Gate Insulators. *Science* **283**, 822–824 (1999).

[234] Horowitz, G., Hajlaoui, R., Fichou, D. & El Kassmi, A. Gate voltage dependent mobility of oligothiophene field-effect transistors. *Journal of Applied Physics* **85**, 3202–3206 (1999).

[235] Di Pietro, R. *et al.* Coulomb Enhanced Charge Transport in Semicrystalline Polymer Semiconductors. *Adv. Funct. Mater.* **26**, 8011–8022 (2016).

[236] Sadhanala, A. *et al.* Preparation of Single-Phase Films of CH3NH3Pb(I1–xBrx)3 with Sharp Optical Band Edges. *J. Phys. Chem. Lett.* **5**, 2501–2505 (2014).

[237] Gibson, G. L., McCormick, T. M. & Seferos, D. S. Atomistic Band Gap Engineering in Donor–Acceptor Polymers. *J. Am. Chem. Soc.* **134**, 539–547 (2012).

[238] Spano, F. C. & Yamagata, H. Vibronic Coupling in J-Aggregates and Beyond: A Direct Means of Determining the Exciton Coherence Length from the Photoluminescence Spectrum. *J. Phys. Chem. B* **115**, 5133–5143 (2011).

[239] Köhler, A., Hoffmann, S. T. & Bässler, H. An Order–Disorder Transition in the Conjugated Polymer MEH-PPV. *J. Am. Chem. Soc.* **134**, 11594–11601 (2012).

[240] Paquin, F. *et al.* Two-dimensional spatial coherence of excitons in semicrystalline polymeric semiconductors: Effect of molecular weight. *Phys. Rev. B* **88**, 155202 (2013).

[241] Luo, J. *et al.* Aggregation-induced emission of 1-methyl-1,2,3,4,5-pentaphenylsilole. *Chem. Commun.* **0**, 1740–1741 (2001).

[242] Dyakonov, V., Rösler, G., Schwoerer, M. & Frankevich, E. L. Evidence for triplet interchain polaron pairs and their transformations in polyphenylenevinylene. *Phys. Rev. B* **56**, 3852–3862 (1997).

[243] Tautz, R. *et al.* Structural correlations in the generation of polaron pairs in low-bandgap polymers for photovoltaics. *Nat. Commun.* **3**, 970 (2012).

[244] Di Nuzzo, D. *et al.* Enhanced Photogeneration of Polaron Pairs in Neat Semicrystalline Donor–Acceptor Copolymer Films via Direct Excitation of Interchain Aggregates. *J. Phys. Chem. Lett.* **6**, 1196–1203 (2015).

[245] Sariciftci, N. S., Smilowitz, L., Heeger, A. J. & Wudl, F. Photoinduced Electron Transfer from a Conducting Polymer to Buckminsterfullerene. *Science* **258**, 1474–1476 (1992).

[246] Vacar, D., Maniloff, E. S., McBranch, D. W. & Heeger, A. J. Charge-transfer range for photoexcitations in conjugated polymer/fullerene bilayers and blends. *Phys. Rev. B* **56**, 4573–4577 (1997).

[247] Tvingstedt, K. *et al.* Electroluminescence from Charge Transfer States in Polymer Solar Cells. *J. Am. Chem. Soc.* **131**, 11819–11824 (2009).

[248] Westerling, M. *et al.* Photoexcitation dynamics in an alternating polyfluorene copolymer. *Phys. Rev. B* **75**, 224306 (2007).

[249] Miranda, P. B., Moses, D. & Heeger, A. J. Ultrafast photogeneration of charged polarons in conjugated polymers. *Phys. Rev. B* **64**, 081201 (2001).

[250] Miranda, P. B., Moses, D. & Heeger, A. J. Ultrafast photogeneration of charged polarons on conjugated polymer chains in dilute solution. *Phys. Rev. B* **70**, 085212 (2004).

[251] Soci, C., Moses, D., Xu, Q.-H. & Heeger, A. J. Charge-carrier relaxation dynamics in highly ordered poly(p-phenylene vinylene): Effects of carrier bimolecular recombination and trapping. *Phys. Rev. B* **72**, 245204 (2005).

[252] Xu, Q.-H., Moses, D. & Heeger, A. J. Direct observation of a time-delayed intermediate state generated via exciton-exciton annihilation in polyfluorene. *Phys. Rev. B* **68**, 174303 (2003).

[253] Shafirovich, V. Y., Courtney, S. H., Ya, N. & Geacintov, N. E. Proton-coupled photoinduced electron transfer, deuterium isotope effects, and fluorescence quenching in noncovalent benzo [a] pyrenetetraol-nucleoside complexes in aqueous solutions. *J. Am. Chem. Soc.* **117**, 4920–4929 (1995).

[254] Shizuka, H. & Tobita, S. Proton-induced quenching and hydrogen-deuterium isotope-exchange reactions of methoxynaphthalenes. *J. Am. Chem. Soc.* **104**, 6919–6927 (1982).

[255] Zhang, Q. *et al.* Design of Efficient Thermally Activated Delayed Fluorescence Materials for Pure Blue Organic Light Emitting Diodes. *J. Am. Chem. Soc.* **134**, 14706–14709 (2012).

[256] Dias, F. B., Penfold, T. J. & Monkman, A. P. Photophysics of thermally activated delayed fluorescence molecules. *Methods Appl. Fluoresc.* **5**, 012001 (2017).

[257] Endo, A. *et al.* Efficient up-conversion of triplet excitons into a singlet state and its application for organic light emitting diodes. *Appl. Phys. Lett.* **98**, 083302 (2011).

[258] Lin Ting-An *et al.* Sky-Blue Organic Light Emitting Diode with 37% External Quantum Efficiency Using Thermally Activated Delayed Fluorescence from Spiroacridine-Triazine Hybrid. *Advanced Materials* **28**, 6976–6983 (2016).

[259] Bobbert, P. A., Nguyen, T. D., van Oost, F. W. A., Koopmans, B. & Wohlgenannt, M. Bipolaron Mechanism for Organic Magnetoresistance. *Phys. Rev. Lett.* **99**, 216801 (2007).

[260] Wu, Y., Xu, Z., Hu, B. & Howe, J. Tuning magnetoresistance and magnetic-field-dependent electroluminescence through mixing a strong-spin-orbital-coupling molecule and a weak-spin-orbital-coupling polymer. *Phys. Rev. B* **75**, 035214 (2007).

[261] Ogiwara, T., Wakikawa, Y. & Ikoma, T. Mechanism of Intersystem Crossing of Thermally Activated Delayed Fluorescence Molecules. *J. Phys. Chem. A* **119**, 3415–3418 (2015).

[262] Sato, K. *et al.* Organic Luminescent Molecule with Energetically Equivalent Singlet and Triplet Excited States for Organic Light-Emitting Diodes. *Phys. Rev. Lett.* **110**, 247401 (2013).

[263] Hosokai, T. *et al.* Evidence and mechanism of efficient thermally activated delayed fluorescence promoted by delocalized excited states. *Sci. Adv.* **3**, e1603282 (2017).

[264] Lower, S. K. & El-Sayed, M. A. The triplet state and molecular electronic processes in organic molecules. *Chem. Rev.* **66**, 199–241 (1966).

[265] Olivier, Y. *et al.* Nature of the singlet and triplet excitations mediating thermally activated delayed fluorescence. *Phys. Rev. Materials* **1**, 075602 (2017).

[266] Gouterman, M. Radiationless Transitions: A Semiclassical Model. *The Journal of Chemical Physics* **36**, 2846–2853 (1962).

[267] Robinson, G. W. & Frosch, R. P. Electronic Excitation Transfer and Relaxation. *The Journal of Chemical Physics* **38**, 1187–1203 (1963).

[268] Swalina, C. & Maroncelli, M. Nonradiative Deactivation in Benzylidene Malononitriles. *J. Phys. Chem. C* **114**, 5602–5610 (2010).

[269] Etherington, M. K., Gibson, J., Higginbotham, H. F., Penfold, T. J. & Monkman, A. P. Revealing the spin–vibronic coupling mechanism of thermally activated delayed fluorescence. *Nat. Commun.* **7**, 13680 (2016).

[270] Duval, E., Boukenter, A. & Champagnon, B. Vibration Eigenmodes and Size of Microcrystallites in Glass: Observation by Very-Low-Frequency Raman Scattering. *Phys. Rev. Lett.* **56**, 2052–2055 (1986).

[271] O'Neill, L. & Byrne, H. J. Structure-Property Relationships for Electron-Vibrational Coupling in Conjugated Organic Oligomeric Systems. *J. Phys. Chem. B* **109**, 12685–12690 (2005).

[272] Allen, B. D., Benniston, A. C., Harriman, A., Llarena, I. & Sams, C. A. How the Central Torsion Angle Affects the Rates of Nonradiative Decay in Some Geometrically Restricted p-Quaterphenyls. *J. Phys. Chem. A* **111**, 2641–2649 (2007).

[273] Yu, W., Zhou, J. & Bragg, A. E. Exciton Conformational Dynamics of Poly(3-hexylthiophene) (P3HT) in Solution from Time-Resolved Resonant-Raman Spectroscopy. *J. Phys. Chem. Lett.* **3**, 1321–1328 (2012).

[274] Oelkrug, D. *et al.* Tuning of Fluorescence in Films and Nanoparticles of Oligophenylenevinylenes. *J. Phys. Chem. B* **102**, 1902–1907 (1998).

[275] Rumi, M., Zerbi, G., Müllen, K., Müller, G. & Rehahn, M. Nonlinear optical and vibrational properties of conjugated polyaromatic molecules. *The Journal of Chemical Physics* **106**, 24–34 (1997).

[276] Ehrenfreund, E., Vardeny, Z., Brafman, O. & Horovitz, B. Amplitude and phase modes in trans-polyacetylene: Resonant Raman scattering and induced infrared activity. *Phys. Rev. B* **36**, 1535–1553 (1987).

[277] Elich, K., Kitazawa, M., Okada, T. & Wortmann, R. Effect of S1 Torsional Dynamics on the Time-Resolved Fluorescence Spectra of 9,9'-Bianthryl in Solution. *J. Phys. Chem. A* **101**, 2010–2015 (1997).

[278] Lukman, S. *et al.* Tuneable Singlet Exciton Fission and Triplet–Triplet Annihilation in an Orthogonal Pentacene Dimer. *Adv. Funct. Mater.* **25**, 5452–5461 (2015).

[279] Han, C., Duan, C., Yang, W., Xie, M. & Xu, H. Allochroic thermally activated delayed fluorescence diodes through field-induced solvatochromic effect. *Sci. Adv.* **3**, e1700904 (2017).

[280] Sun, D., Ren, Z., R. Bryce, M. & Yan, S. Arylsilanes and siloxanes as optoelectronic materials for organic light-emitting diodes (OLEDs). *J. Mater. Chem. C* **3**, 9496–9508 (2015).

[281] Goushi, K., Yoshida, K., Sato, K. & Adachi, C. Organic light-emitting diodes employing efficient reverse intersystem crossing for triplet-to-singlet state conversion. *Nat. Photonics* **6**, 253–258 (2012).

[282] Baldo, M. A. & Forrest, S. R. Transient analysis of organic electrophosphorescence: I. Transient analysis of triplet energy transfer. *Phys. Rev. B* **62**, 10958–10966 (2000).

[283] Masui, K., Nakanotani, H. & Adachi, C. Analysis of exciton annihilation in high-efficiency sky-blue organic light-emitting diodes with thermally activated delayed fluorescence. *Organic Electronics* **14**, 2721–2726 (2013).

[284] Harbach, P. H. P. & Dreuw, A. The Art of Choosing the Right Quantum Chemical Excited-State Method for Large Molecular Systems. In Comba, P. (ed.) *Modeling of Molecular Properties*, 29–47 (Wiley-VCH Verlag GmbH & Co. KGaA, 2011).

[285] Plötner, J. & Dreuw, A. Pigment Yellow 101: A showcase for photo-initiated processes in medium-sized molecules. *Chemical Physics* **347**, 472–482 (2008).

[286] Plötner, J., Tozer, D. J. & Dreuw, A. Dependence of Excited State Potential Energy Surfaces on the Spatial Overlap of the Kohn-Sham Orbitals and the Amount of Nonlocal Hartree-Fock Exchange in Time-Dependent Density Functional Theory. *J. Chem. Theory Comput.* **6**, 2315–2324 (2010).

[287] Zhang, X. *et al.* Molecular Packing of High-Mobility Diketo Pyrrolo-Pyrrole Polymer Semiconductors with Branched Alkyl Side Chains. *J. Am. Chem. Soc.* **133**, 15073–15084 (2011).

[288] Smyder, J. A. *et al.* The influence of continuous vs. pulsed laser excitation on single quantum dot photophysics. *Phys. Chem. Chem. Phys.* **16**, 25723–25728 (2014).

[289] Park, K. B. *et al.* High Electrical Performance of Wet-Processed Indium Zinc Oxide Thin-Film Transistors. *IEEE Electron Device Lett.* **31**, 311–313 (2010).

[290] Sandanayaka, A. S. D., Yoshida, K., Matsushima, T. & Adachi, C. Exciton Quenching Behavior of Thermally Activated Delayed Fluorescence Molecules by Charge Carriers. *J. Phys. Chem. C* **119**, 7631–7636 (2015).

Appendix I

Supplementary information: Chain coupling and luminescence in high-mobility amorphous polymers

I.1 Crystallographic characterisation

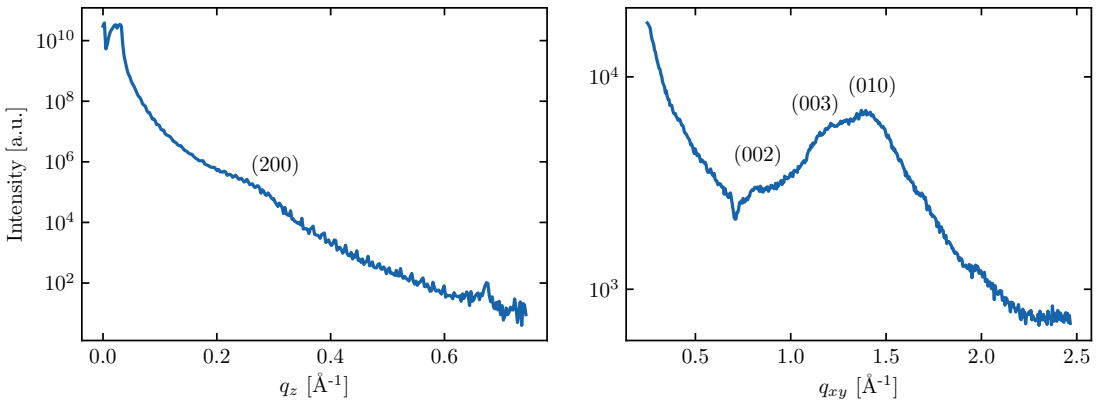

Figure I.1 X-ray crystallographic data for M_1 films: X-ray reflection (left) and grazing incidence (right).

X-ray crystallography is undertaken to determine π-π stacking distances for M_1. The assignment of peaks was made by comparison to the published data for M_0.[287]

I.2 Parametric dependencies of luminescence

In order to determine the number of emissive species, we analyse the transient decay of the film PL and the dependency of the PL spectrum on excitation wavelength (or E_{pump}) in this section. As discussed below, time-resolved studies for M_0 films are non-trivial (owing to its very short luminescence lifetime) and accurate determination of luminescence decay lifetimes require specialised techniques, discussed later.

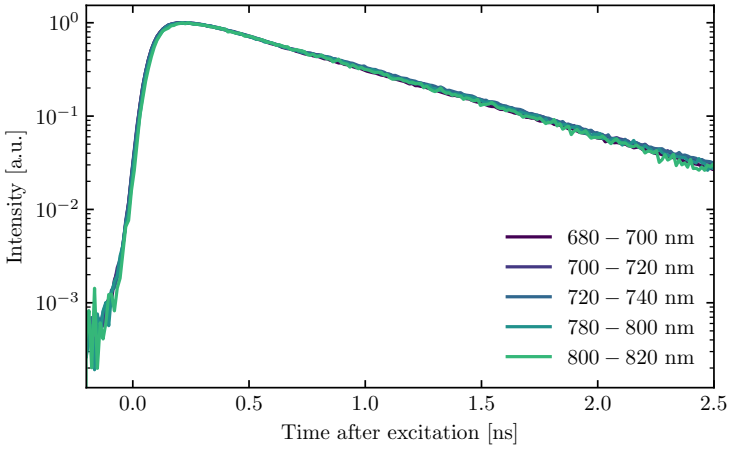

Figure I.2 PL decay kinetics of M_1 thin films at different detection wavelengths.

Using TC-SPC (described in Section 3.3.3.4) we observe that there is no dependency of the detection wavelength on the decay kinetics in M_1. This is shown in Figure I.2, where we use excitation energy of $E_{\text{pump}} = 3.05$ eV and a low fluence of $f_{\text{pump}} = 2$ µJ/cm^2. We note that we deliberately exclude the band $740 - 780$ nm due to the presence of a reflection artefact in the setup; manifesting as another pump pulse arriving ~ 1 ns later. The exponential decay confirms first order decay, and the same lifetime over the entire luminescence band confirms a single luminescent species in M_1. We are unable to verify that this is also the case for M_0 films, since its short PL lifetime calls for specialised detection techniques (described in Section 3.3.3.7) requiring high f_{pump}, which we observe separately decreases the PLQE by exciton-exciton annihilation to below the detection limit.

Additionally, we compare the steady-state PL spectra in Figure I.3 for M_0 (left) and M_1 (right) for different values of E_{pump}. This is measured in an integrating sphere. We note that the difference in M_1 PL when exciting with a 647 nm pump is due to the use of a different grating to give finer spectral resolution in order to exclude pump scatter

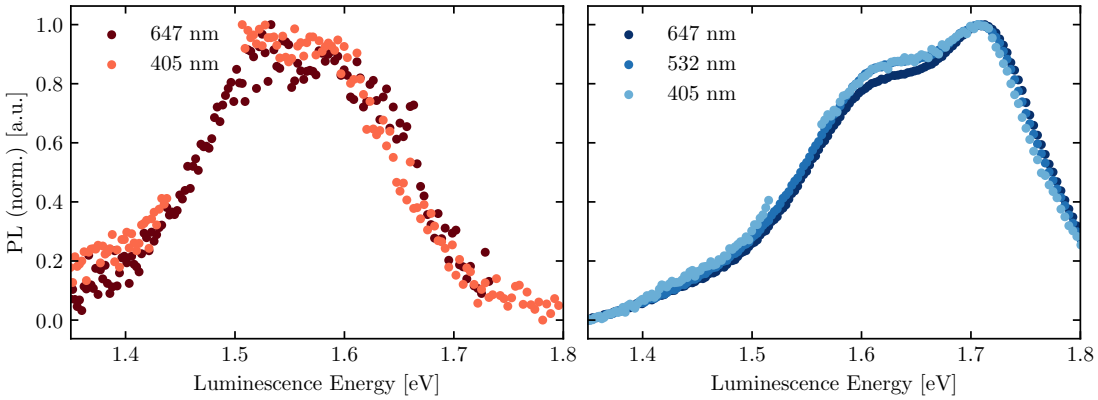

Figure I.3 PL spectrum of M_0 (left) and M_1 (right) films with different excitation wavelengths.

close to the blue-edge of the PL. While there are small differences to the spectra, no systematic difference emerges due to excitation wavelengths used.

I.3 Observation of ultrafast cooling

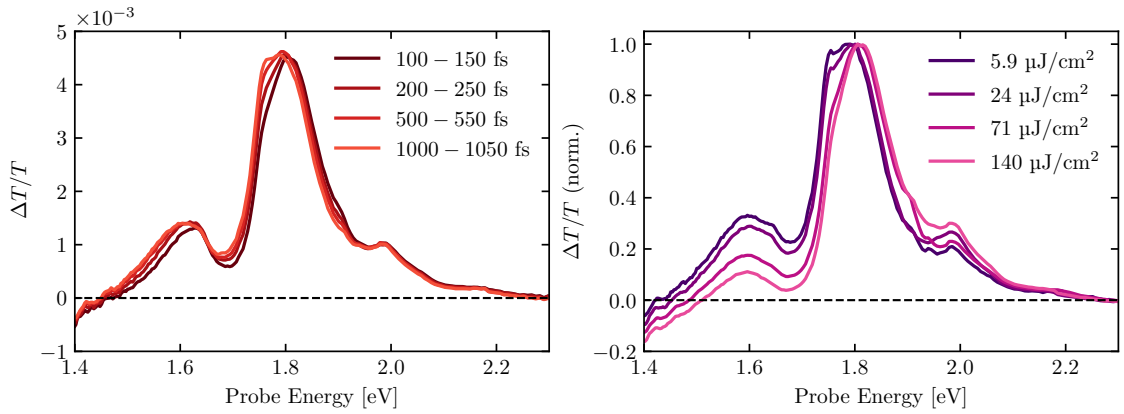

Figure I.4 TA spectra of M_0 thin films: evolution of spectrum in time using $f_{\text{pump}} = 5.9$ µJ/cm^2 (left), and at different f_{pump} integrated over $5 - 10$ ps (right), both using $E_{\text{pump}} = 2.34$ eV.

In order to verify the assignment of the ground-state bleach (GSB) and stimulated emission (SE) spectral features in TA, and corroborate the ultrafast cooling picture, we observe the spectrum evolve in the first 1 ps after excitation in Figure I.4 (left). In this experiment, we use pulses shorter than 40 fs in length. At the earliest times, the GSB and SE are close to mirror-images of each other about the central peak

near 1.80 eV. As time progresses, the 0-1 vibronic peak of the SE ($SE_{0\text{-}1}$) peak grows and redshifts. The $SE_{0\text{-}0}$ peak also redshifts, and becomes a spectral shoulder on the peak near 1.8 eV by 500 fs. The shift of the SE signal agrees well with the picture of exciton cooling of the luminescent species which we see in the ultrafast PL.

Further to this, in Figure I.4 (right), we show the difference in spectrum (integrated between $5 - 10$ ps) for different fluences. By normalising the spectra to the maximum, we observe a suppression of the SE signal, and a larger PIA (which we discuss later is associated with both the luminescent species and the inter-chain species) which makes the SE negative below 1.5 eV. This is consistent with increased exciton-exciton (bimolecular) non-radiative decay at high f_{pump} which decreases the PLQE and also the SE. This increases the yield of inter-chain states relative to the luminescent state by $5 - 10$ ps, and therefore increases the relative intensity of the PIA of the inter-chain species. We also deduce from this that the inter-chain species is less prone to bimolecular recombination, indicating more localised species.

I.4 Nature of polaron-pairs

I.4.1 Recombination kinetics of polaron-pairs

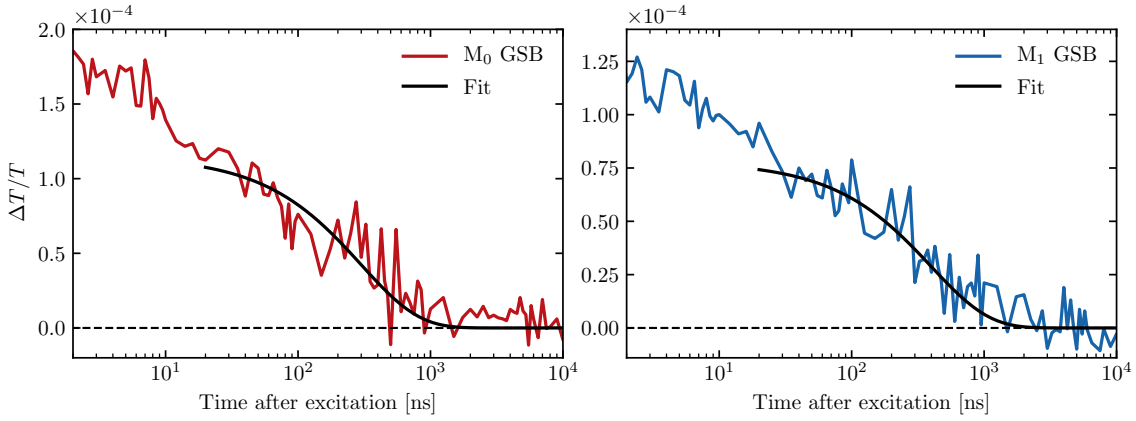

Figure I.5 Decay kinetics for M_0 (red) and M_1 (blue) thin films: PIA (top) and GSB with monoexponential fit (bottom).

In the regime where SE has decayed to zero and the only remaining species is the PP, we examine the decay kinetics of the GSB after 2 ns in Figure I.5. The low oscillator strength leads to small differential transmissions $\Delta T/T < 10^{-4}$ and

considerable noise. Therefore, directly comparing $\dot{n}$ with n to determine an allometric relation is not feasible. However, a single exponential decay over this time domain gives the best fit, indicating first-order geminate recombination.

I.4.2 LI-ESR investigation of polaron-pairs

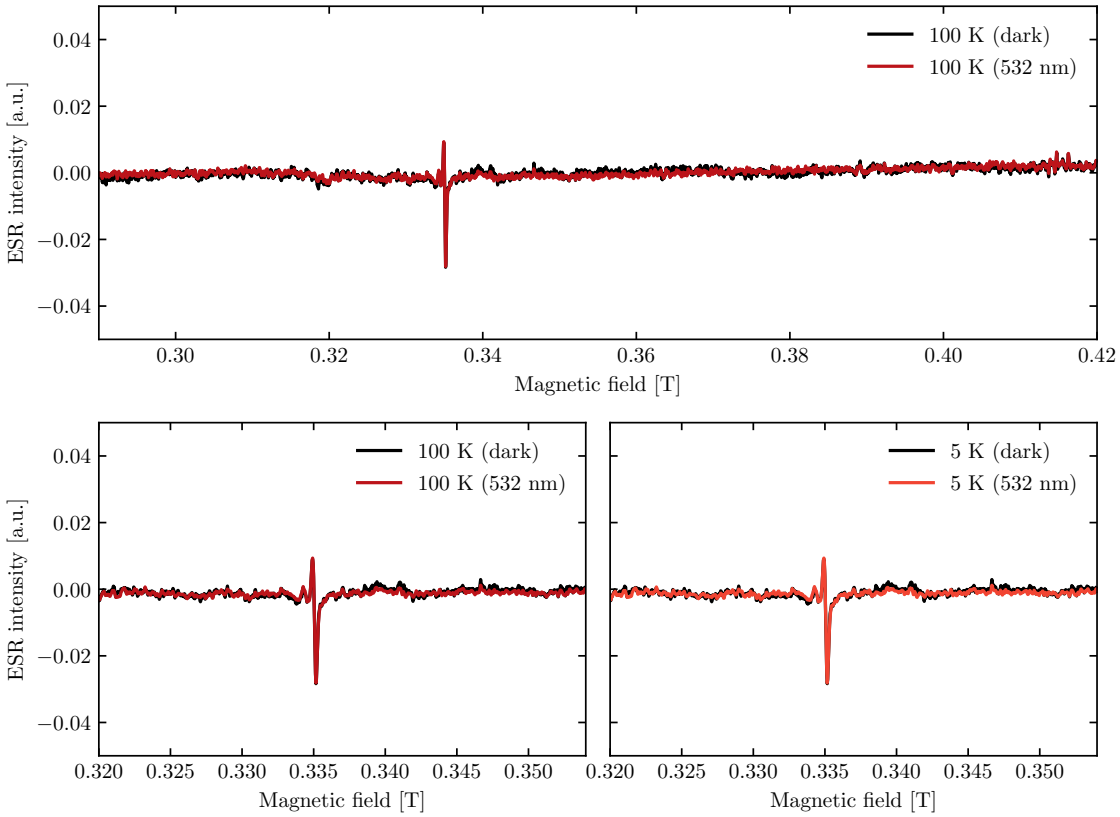

Figure I.6 LI-ESR of M_0 films with (red) and without (black) CW illumination. Wide scan at 100 K (top), high resolution scans at 100 K (bottom left) and 5 K (bottom right).

To verify this picture, we use light-induced (LI-) electron spin resonance (ESR) to rule out the formation of charges (with $s = 1/2$) or triplets (with $s = 1$) as a decay mechanism with an appreciable quantum efficiency in M_0. Using the formalism given in [288], we estimate the time-averaged number of polaron-pairs to be $\langle p \rangle \sim 6 \times 10^{11}$ under 532 nm (5 mW) CW illumination. To estimate this, we assume a PP formation quantum yield of ~ 1.5 % (discussed later).

Briefly, about the instrument, all ESR spectra are recorded on a Bruker E500 X-band spectrometer with a Bruker ER 4122SHQE microwave cavity between $9.4 - 9.7$ GHz at low-microwave powers of $6 - 60$ µW to prevent power saturation and the linewidth broadening. The external magnetic field is modulated at 100 kHz and the spectra are locked-in, giving a sensitivity limit of $\sim 1 \times 10^{10}$ mT^{-1}. We expect the sensitivity limit for detection of charges to be $\sim 10^8$ spins, and triplets to be $\sim 10^{11}$ spins. Therefore, we expect the time-averaged number of photogenerated species to be above the sensitivity limit for triplets and charges.

We measure the ESR spectrum of a thick M_0 film with and without illumination using a 532 nm CW laser. Over the temperature range $5 - 300$ K, we do not observe any change between the two spectra. Representative spectra are shown in Figure I.6, where red (black) traces denote spectra with (without) laser excitation. At 100 K, we expect long spin dephasing times. Here, we deliberately underestimate $\langle p \rangle$, since we expect the decay of these long-lived states to be slower at low-temperature. Notwithstanding, we are unable to resolve any change between the two measurements over a wide detection window (top) or with high resolution (bottom left). The same is true at 5 K (bottom right). We therefore conclude that neither charges nor triplets are formed in appreciable yields under illumination.

I.4.3 Intermolecular origin of polaron-pairs

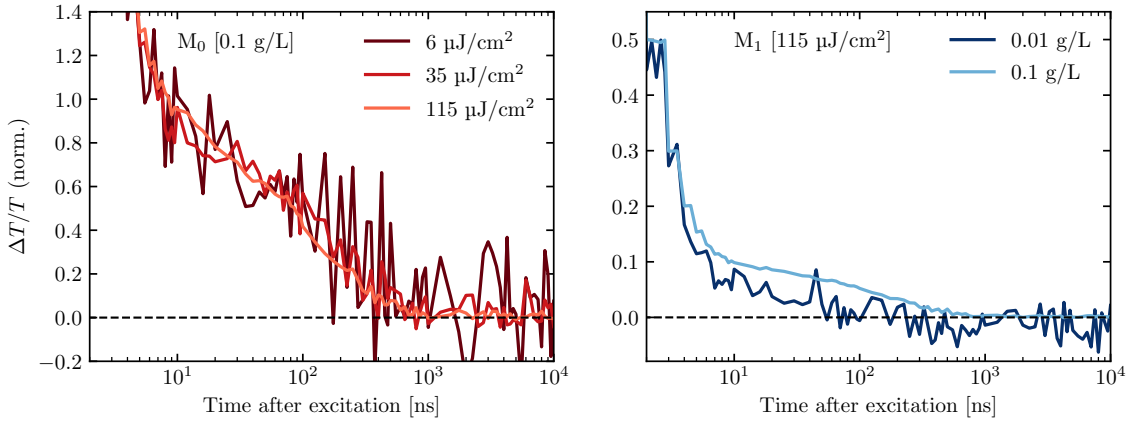

Figure I.7 Normalised GSB kinetics of M_0 (red) solutions at different f_{pump} (left), and of M_1 (blue) solutions at different concentrations (right) with $E_{pump} = 3.10$ eV.

Solution TA measurements on longer timescales 2 ns demonstrate that PPs are inter-chain species. This is true because the formation yield is decreased in increasingly dilute solution. In a solution of 1,2-dichlorobenzene, we show the GSB decay of M_1 in dilute (0.01 g/L, dark blue) and more concentrated (0.1 g/L, light blue) solutions in Figure I.7 (right). Normalised at the maximum value, the long-lived GSB decreased in magnitude from 12 % to 5 % at 10 ns upon 10-fold dilution. This is a clear indication that the formation of these PPs requires aggregation, and that in the absence of chain-packing, these states do not form. It also suggests that even at 0.01 g/L, there is still some chain aggregation in solution.

To confirm that this observation is not simply due to the increasing excitation density with a greater concentration solution, we measure the f_{pump} dependency of this species in a solution of M_0. This is shown in Figure I.7 (left), and we use a 0.1 g/L solution in the same solvent. We observe no dependency of the normalised signal on the fluence over more than an order of magnitude. This indicates that the yield of PPs (as indicated by the persisting GSB) is linear in fluence, and the quantum yield is instead determined (on shorter timescales) by the degree of aggregation.

I.5 Exciton diffusion length and trap density

We follow the method presented in reference [51]. Here, Mikhnenko and coworkers compare the quenching efficiency of the polymer PL as a function of added [6,6]-phenyl C_{61}-butyric acid methyl ester (PCBM) concentration. PCBM is known to efficiently quench luminescence, and the quenching of the polymer PL is determined by the ability of the excitons to diffuse to these sites. By measuring the PL lifetime, these authors apply the Stern-Volmer equation:

$$\frac{1}{\tau_c} = \frac{1}{\tau_0} + 4\pi r D c \tag{I.1}$$

We begin with a derivation of this result, and consider the PLQE (ϕ) both in the absence (ϕ_0) and in the presence (ϕ_c) of PCBM. Without PCBM, the PLQE is defined as in the previous section:

$$\phi_0 = \frac{k_{\mathrm{R}}}{k_{\mathrm{R}} + k_{\mathrm{NR}}} = \frac{k_{\mathrm{R}}}{k_0} \tag{I.2}$$

where k_{R} (k_{NR}) is the (non-)radiative rate of exciton decay. Treatment of this equation upon addition of PCBM requires only an extra non-radiative term, since the radiative rate of decay is unchanged:

$$\phi_c = \frac{k_{\mathrm{R}}}{k_0 + k_q} = \frac{k_{\mathrm{R}}}{k_c} \tag{I.3}$$

and therefore,

$$\frac{\phi_0}{\phi_c} = 1 + \tau_0 k_q \tag{I.4}$$

for monomolecular recombination. By assuming diffusion-limited exciton quenching, we can substitute the well-known rate for quenching:

$$k_q = 4\pi r D c \tag{I.5}$$

where D is the exciton diffusion coefficient, r is the exciton-capture radius (we use $r = 1$ nm), and c is the concentration of added PCBM. In the case that the radiative rate is the same with and without PCBM (i.e., the addition of PCBM does not lead to an additional PL pathway), then:

$$\phi_0 k_0 = \phi_c k_c \tag{I.6}$$

and we can write,

$$\frac{\tau_0}{\tau_c} = 1 + 4\pi r D \tau_0 c \tag{I.7}$$

In our systems, since accurate measurement of short PL lifetimes is difficult, we deviate from the methodology proposed by Mikhnenko and coworkers and instead compare the PL intensity (I) as a function of PCBM added rather than the PL lifetime. This is equivalent for monomolecular recombination of the emissive species since

$$\tau_{\mathrm{PL}} \propto \int_0^\infty I_{\mathrm{PL}}(t)dt = I \tag{I.8}$$

and therefore,

$$\frac{I_0}{I_c} = 1 + 4\pi r D \tau_0 c \tag{I.9}$$

It is convenient to define the exciton-quenching efficiency η_q,

$$\eta_q(c) = 1 - \frac{I_c}{I_0} = \frac{1}{1/(4\pi r D \tau_0 c) + 1} \tag{I.10}$$

and η_q is plotted against increasing number density of PCBM (c) in Figure I.8. Triplicate measurements yielded statistics on these reported vales, and a fit of these data with independently measured τ_0 yielded the value of the diffusion coefficient reported in the main text. The exciton diffusion length (L_D) can be calculated using its definition, assuming one-dimensional ($Z = 1$) exciton diffusion,

$$L_D^2 = 2ZD\tau_0 \tag{I.11}$$

and these values were also reported in the main text.

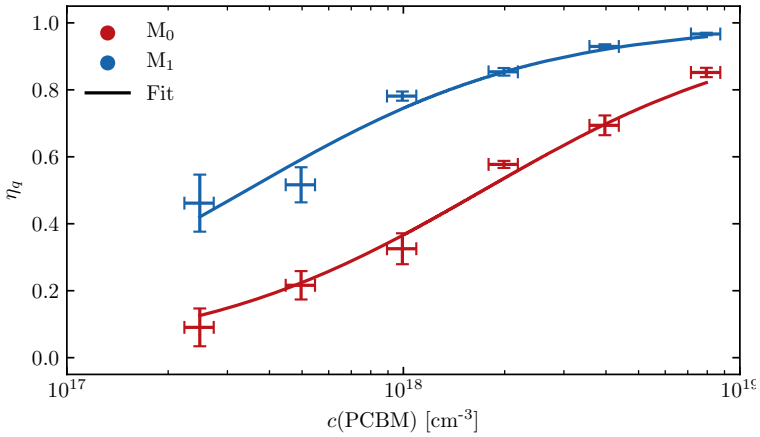

Figure I.8 Exciton quenching efficiency of M_0 (red) and M_1(blue) films at different concentration of PCBM quencher, and a fit to the model.

In order to determine the relative density of exciton traps which arise upon casting a film (c_0), Mikhnenko and coworkers compare neat film measurements (with no PCBM) with dilute solution. By applying the same formalism in Equation I.1, substitution of $\tau_c \to \tau_0$ and $\tau_0 \to \tau_s$ (where τ_s is the photoluminescence lifetime in dilute solution) can be used to determine c_0. Rearranging, we write

$$c_0 = \frac{1}{4\pi r D}\left(\frac{1}{\tau_0} - \frac{1}{\tau_s}\right). \tag{I.12}$$

Of course, we note that this treatment assumes implicitly that the increase to non-radiative decay between dilute solution and film is due to exciton diffusion to quenching sites with the same capture radius (of 1 nm) as PCBM. This offers a helpful framework to compare materials on the same scale, but is insensitive to the mechanism

Material	c_0 [cm^{-3}]
M_1	8.3×10^{15}
M_0	7.8×10^{16}
F8BT*	$\sim 1 \times 10^{17}$
PCPDTBT*	$\sim 7 \times 10^{17}$
MEH-PPV*	$\sim 8 \times 10^{17}$
P3HT*	$\sim 2 \times 10^{18}$

Table I.1 Intrinsic film exciton-trap density for various materials measured in this study. *Data from reference [51].

of this non-radiative quenching. Values for c_0 determined in this study are compared with published values in Table I.1.

I.6 Estimating k_{NR} due to inter-chain interactions

It is valuable to disentangle the k_{NR} observed in film into parts - (i) the intrinsic quenching k_{NR} which occurs in dilute solution, including that due to chemical defects, and (ii) the additional k_{NR} which arises directly from inter-chain interactions in a film. We have assumed in these low-disorder polymers that the casting of the film does not itself lead to a greater density of defects. The values for inter-chain contribution to the observed film k_{NR} reported in the main text are estimated in the following way.

First, we assume that in dilute solution (0.01 g/L in *o*-DCB), inter-chain coupling is extremely weak, and results in a vanishing inter-chain k_{NR}. In the absence of other chains, k_{NR} in dilute solution, hereunder $k_{\mathrm{NR\ (sol)}}$, is entirely determined by intra-chain processes, and we can write

$$k_{\mathrm{NR\ (intra\text{-}chain)}} = k_{\mathrm{NR\ (sol)}}. \tag{I.13}$$

Second, we assume that the film k_{NR}, hereunder $k_{\mathrm{NR\ (film)}}$, is the sum of $k_{\mathrm{NR\ (intra\text{-}chain)}}$ and any additional decay pathways arising directly from the inter-chain coupling. We call this additional rate $k_{\mathrm{NR\ (inter\text{-}chain)}}$. It follows that, by subtracting $k_{\mathrm{NR\ (sol)}}$ from $k_{\mathrm{NR\ (film)}}$, we recover an estimate for the non-radiative rate due to inter-chain coupling:

$$k_{\mathrm{NR\ (inter\text{-}chain)}} = k_{\mathrm{NR\ (film)}} - k_{\mathrm{NR\ (intra\text{-}chain)}} \tag{I.14}$$

To estimate $k_{\mathrm{NR\ (inter\text{-}chain)}}$ conservatively, we consider that $k_{\mathrm{NR\ (intra\text{-}chain)}}$ is related to the degree of exciton delocalisation, and increasing exciton delocalisation should

result in an increased $k_{\text{NR (intra-chain)}}$. To take this into account, we modify the equation for estimating $k_{\text{NR (intra-chain)}}$ to deal with the increased exciton delocalisation observed in film over dilute solution:

$$k_{\text{NR (intra-chain)}} = \frac{k_{\text{R (film)}}}{k_{\text{R (sol)}}} \cdot k_{\text{NR (sol)}} \tag{I.15}$$

where here we use k_{R} in solution ($k_{\text{R (sol)}}$) and film ($k_{\text{R (film)}}$) as a proxy for the degree of exciton delocalisation. Using this substitution, we apply Equation I.14, and recover a lower-bound for the inter-chain component to the decay rate.

I.7 PL intensity as a function of temperature

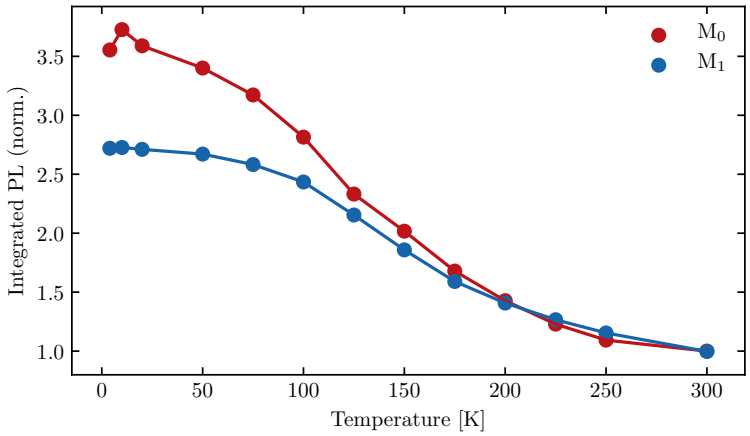

Figure I.9 Integrated PL of M_0 (red) and M_1 (blue) films at different temperatures normalised to 300 K.

Observing the temperature evolution of the PL intensity is a convenient proxy for how the PLQE scales with temperature. Direct measurement of the PLQE (using an integrating sphere) within a cryostat is not feasible, and instead, the PL intensity is evaluated by integrating in time and luminescence energy. We show this temperature evolution in Figure I.9, normalising the integrated PL to the respective value at 300 K. This indicates that while the PLQE increases for both M_0 and M_1 films, the PLQE of M_0 increases more substantially. This discrepancy is consistent with the picture of a thermally activated internal conversion pathway. In this way, a lower barrier to this internal conversion pathway leads to a greater increase to the PLQE of M_0 at low

temperatures. This may be due to a Marcus intersection of exciton bands, where an increased Stokes shift in M_1 leads to a higher energy at which the bands intersect.

I.8 Coherent oscillations in M_1

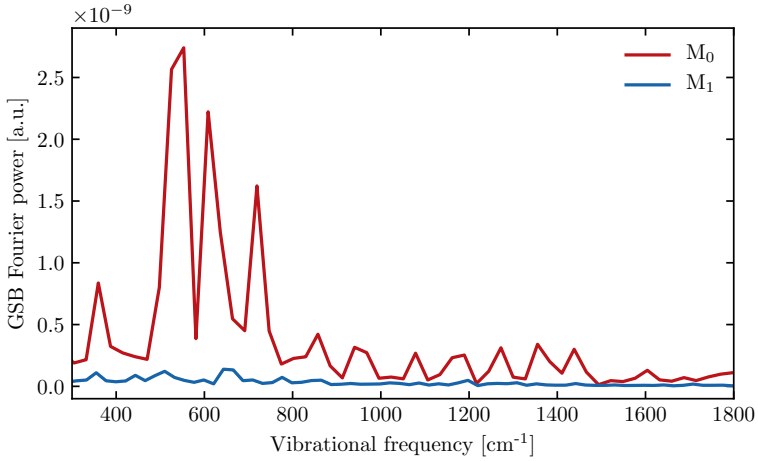

Figure I.10 Fourier power of coherent oscillations in the GSB for M_0 (red) and M_1 (blue).

To explore this assertion further, it follows that coherent oscillations should be suppressed in M_1 compared to M_0. In Figure I.10, we plot the Fourier power of the coherent oscillations for M_0 and M_1 to compare the relative intensity. In M_1, the oscillations are weaker in intensity by $\sim 10\times$, suggesting that the coherently generated exciton wavepacket decoheres in the excited state instead of traversing this internal conversion pathway and oscillating between excited- and ground-states like for M_0. This discrepancy between M_0 and M_1 films is also consistent with a thermally activated Marcus-like intersection of exciton bands.

Appendix II

Supplementary information: High mobility highly luminescent amorphous polymers

II.1 Mobility extraction in this work

Interpreting OFET data with the the behaviour expected in an ideal MOSFET is a powerful tool to probe the charge transport behaviour in semiconducting materials. Comparison with analytical equations gives information about the (i) mobility, (ii) trapping mechanism, and (iii) disorder in the transport DOS by measuring the transconductance as a function varying charge carrier accumulation. At a constant temperature, the mobility can theoretically be extracted in the linear (lin.) and saturation (sat.) regimes using the ideal MOSFET model, as discussed in Section 3.2.3.

However, applying these equations in spite of a deviation from ideal MOSFET behaviour can lead to extraction of erroneous mobility values. The origin of common problems in OFETs arise from (i) contact resistance, (ii) high threshold voltages and (iii) hysteresis due to charge-carrier trapping. These non-idealities can all lead to the overestimation of the mobility. While hysteresis and high threshold voltages are typically easy to diagnose in devices, contact resistance, which can be gate-voltage dependent,[94] and can lead to current crowding effects,[289] is often less obvious.

We observe that using gold electrodes (with a work function of ~ -5.4 eV), a bottom-contacted architecture, and appropriate solution processing can remove these effects in most of our materials. In particular, using solvents with a high boiling point, or a small quantity of non-doping molecular additive as described by Nikolka, Nasrallah, *et al.*,[136] leads to a dramatically improved device performance and stability. While in the MOSFET formulation the mobility is a constant and $\mu_{\text{lin.}} = \mu_{\text{sat.}}$, rearrangement of the MOSFET equations in Equations 2.32 and 2.33 allows for the evaluation of a mobility which, in general, has a dependency on V_{GS}, as shown in Equations 3.1 and 3.2.

By calculating the mobility in this way, we are able to clearly diagnose non-ideal MOSFET-like behaviour in the characteristics. Together with an extraction of V_{Th} using extrapolation of the linear region of the $\sqrt{I_{\text{DS}}} - V_{\text{GS}}$ graph in the limit that $|V_{\text{GS}}| \gg |V_{\text{Th}}|$ to $I_{\text{DS}} = 0$ A, where the device is operated in saturation, we gain a full picture of whether the device is well-described by the MOSFET model.

In Figure II.1, we show the OFET data leading to the mobility extraction used. In all devices, we used semiconductor channels with dimensions of $L = 20$ µm and $W = 1$ mm. A polymer film of $20 - 40$ nm was cast, followed by a Cytop gate dielectric of thickness ~ 500 nm. For each material (in a different colour), we show the transfer characteristics (top) in the linear (dark) and saturation (light) regimes. Below, we show the extraction of the mobility as a function of V_{GS}, using Equation 3.1 for the extraction of $\mu_{\text{lin.}}$, and Equation 3.2 and for $\mu_{\text{sat.}}$ (dashed line). For every material except IDT-H_2BT, we observed a non-ideal dependency of $\mu_{\text{sat.}}$ on V_{GS}. In order to verify our value for $\mu_{\text{sat.}}$, we compared this 'conventional' extraction method for $\mu_{\text{lin.}}$ (dark solid line) and $\mu_{\text{sat.}}$ (light dashed line) with the direct application of Equation 2.33 for $\mu_{\text{sat.}}$ (light solid line) assuming $|V_{\text{Th}}| = 0$ V. All devices here have $|V_{\text{Th}}| > 0$ V, so this methodology provides a lower-bound on the real $\mu_{\text{sat.}}$ at the given V_{GS}. This is because it uses the real device current output, and therefore does not take into account non-ideal behaviour which may, in some cases, lead to a large increase in I_{DS} over a small V_{GS}-range, in spite of a lower overall I_{DS}. Plotting these three extraction methodologies together reveals the inadequacy of the 'conventional' $\mu_{\text{sat.}}$ extraction (using Equation 3.2) in these materials.

Empirically, transfer characteristics in the linear regime behaved in a more ideal way than in the saturation regime. For all materials except TIF-H_2BT and

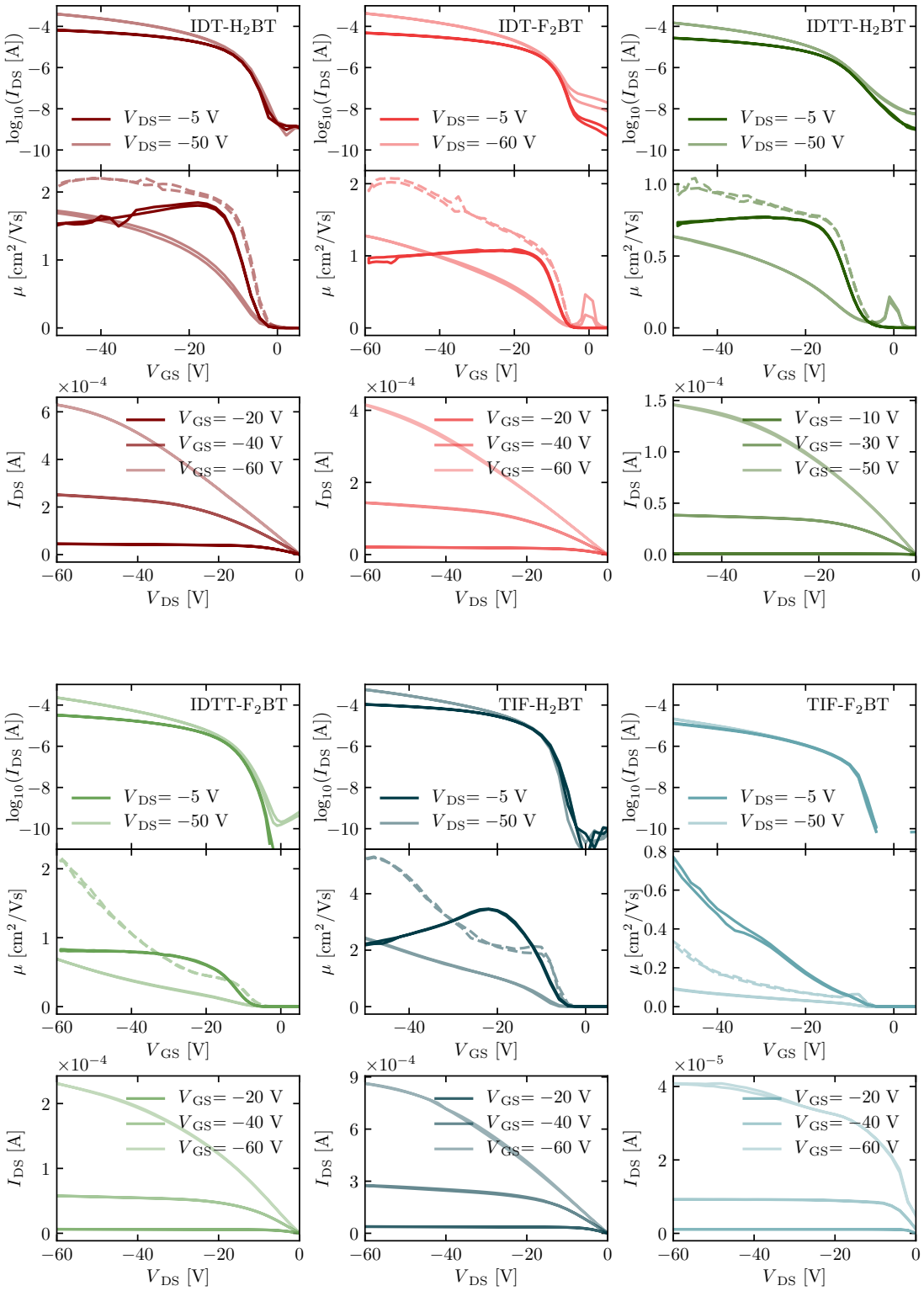

Figure II.1 Mobility extraction and OFET characteristics for polymers in this work.

TIF-F_2BT, the linear characteristics were gate-independent above the threshold. For TIF-H_2BT, contact resistance was higher due to mismatch between the gold work function and a deeper HOMO at -5.7 eV.[180] This leads to an overestimation of the linear mobility, but in the high $|V_{GS}|$ limit, this goes towards the true $\mu_{lin.}$. In this limit, $\mu_{lin.} \sim \mu_{sat.}$ when the latter is estimated using Equation 2.33. Finally, TIF-F_2BT transistors are poorly behaved, and contact resistance from an even deeper HOMO of -5.8 eV leads to low on-currents and non-ideal transfer and output characteristics. It is unlikely that we probe the real mobility in this system, but we observe a mobility here of < 0.4 cm^2/Vs, as estimated in saturation using Equation 3.2. We summarise the extracted μ values and the equation used in Table II.1.

Table II.1 Extracted effective mobility for polymers in this chapter.

Polymer	$\mu_{lin.}$ [cm^2/Vs]	$\mu_{sat.}$ [cm^2/Vs]
IDT-H_2BT	1.4	1.7
IDT-F_2BT	0.86	1.3
IDTT-H_2BT	0.58	0.62
IDTT-F_2BT	0.58	0.69
TIF-H_2BT	2.3	2.4
TIF-F_2BT	0.29	0.093

Another important factor in diagnosing poor device performance can be achieved by using the output transconductance characteristics. It is here that contact resistance often becomes visible, and can lead to a pinching of I_{DS} near $V_{DS} = 0$, and therefore a sigmoid shape in I_{DS} overall. Appropriate choice of electrode materials and solution processing mean that we do not observe this in our devices, except for TIF-F_2BT, which has an exceedingly deep HOMO energy.

Additionally, in the output transconductance plots, after the device 'pinches off' at $V_{DS} > V_{GS}$, I_{DS} should 'saturate' and become constant. With our device top-gated bottom-contacted architecture, we do not observe this behaviour. This is due to a back-channel effect formed at high $|V_{GS}|$ where accumulation near the un-grounded glass substrate leads to a second effective channel, and so I_{DS} continues to increase the applied $|V_{GS}|$. We have observed separately for IDT-H_2BT that fabricating a device on a doped-Si substrate, and grounding the substrate during the measurement decreases

this effect substantially.[136]

II.2 Inter-chain CT excitons

II.2.1 Inter-chain CTs in IDTT-F_2BT

In order to verify the inter-chain nature of the additional luminescence pathway in these materials, we performed additional experiments on IDTT-F_2BT, for whom the second (redshifted) PL pathway is spectrally resolved from the ICT. These experiments are summarised in II.2, and used $E_{\text{pump}} = 3.05$ eV and low fluence < 2 µJ/cm^2.

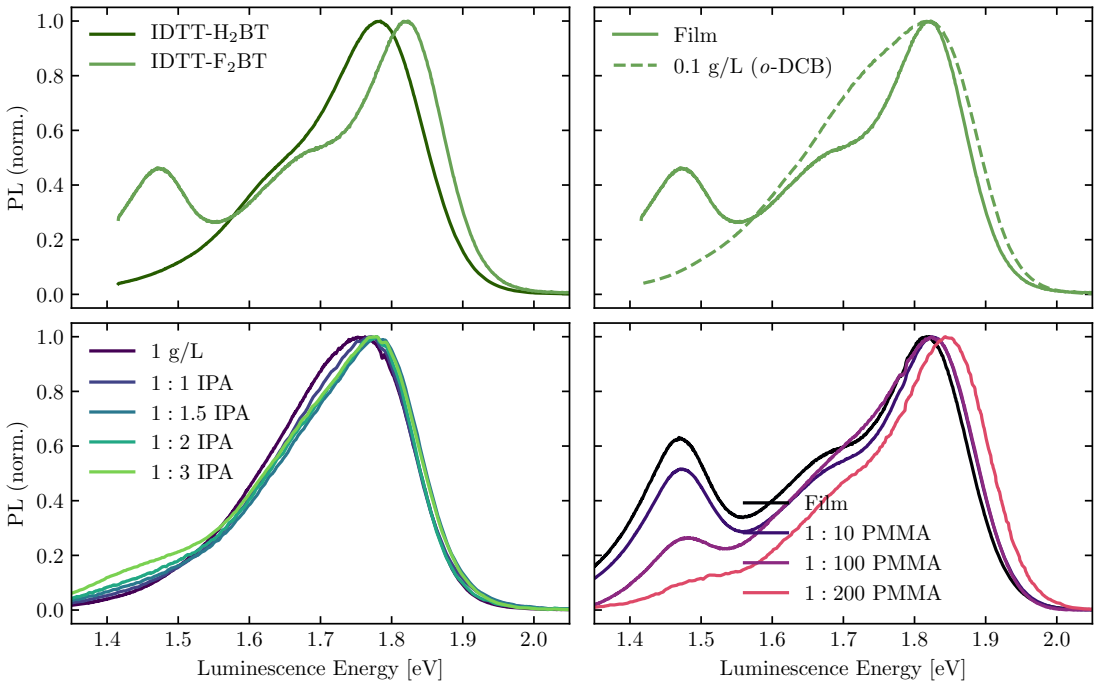

Figure II.2 Luminescent inter-chain CTs in IDTT-F_2BT: PL spectra of IDTT-H_2BT and IDTT-F_2BT (top left), IDTT-F_2BT in thin film and dilute solution (top right), IDTT-F_2BT with increasing volume ratio of non-solvent IPA (bottom left), and IDTT-F_2BT blended with increasing weight fraction of poly(methyl methacrylate) (PMMA) (bottom right).

Firstly, we note in Figure II.2 (top left) that the second PL pathway is present in IDTT-F_2BT, but not in IDTT-H_2BT. More accurately, this implies that a second PL pathway may be weaker, or not spectrally resolved for IDTT-H_2BT.

However, time-resolved PL measurements separately confirm that IDTT-H_2BT has no additional long-lived PL decay kinetic (with $\tau_{PL} > 250$ ps), unlike for IDTT-F_2BT. Secondly, we note that this emissive pathway is not present for IDTT-F_2BT in dilute solution (top right). While the PL lineshape of IDTT-F_2BT in 0.1 g/L 1,2-dichlorobenzene (*o*-DCB) is broader, we do not observe an increase in signal near 1.5 eV. This suggests that the peak below 1.5 eV arises in some way from the aggregation.

To confirm this picture, we added a aliquots of non-solvent propan-2-ol (IPA) to a solution (1 g/L, *o*-DCB) of IDTT-F_2BT to promote aggregation (bottom left). Compared to the neat IDTT-F_2BT solution spectrum (dark purple), we do not see a substantial change in the PL spectrum below 1.5 eV until the solution is comprised of equal parts *o*-DCB and IPA (1 : 1) by volume (light purple). With additional IPA, we observe another peak appearing in the PL below 1.5 eV, and this peak becomes stronger towards the point where there is a three-fold excess of IPA (1 : 3) in the analyte solution (light green). This experiment confirms that the peak below 1.5 eV arises from the aggregation, since its intensity can be controlled by increasing the aggregation in solution.

Finally, in order to show that this pathway specifically involves multiple polymer chains, we blend IDTT-F_2BT with poly(methyl methacrylate) (PMMA; bottom right). In the neat IDTT-F_2BT film (black), the emission pathway below 1.5 eV has a peak intensity of approximately 65 % of the ICT peak intensity. When blended with 10× excess of PMMA (dark purple) by weight, we see a small suppression of the peak intensity of this secondary luminescence. However, this peak is still strong, and is $\sim$ 50 % of the ICT maximum. Upon increasing the PMMA weight excess to 100×, this peak is suppressed further to $<$ 30% of the ICT maximum. Thereafter, the decrease in this peak is rapid, and by an excess of 200×, this peak is $<$ 10 % of the ICT maximum. This experiment confirms the 'multiple polymer chain' origin of this secondary luminescent peak, and suggests that when polymer chains cannot come close together, this emissive pathway is shut down. Owing to its redshifted energy compared to the on-chain ICT, and its substantially increased photoluminescence decay lifetime (discussed in the main text), this decay pathway is likely to involve an inter-chain charge transfer.

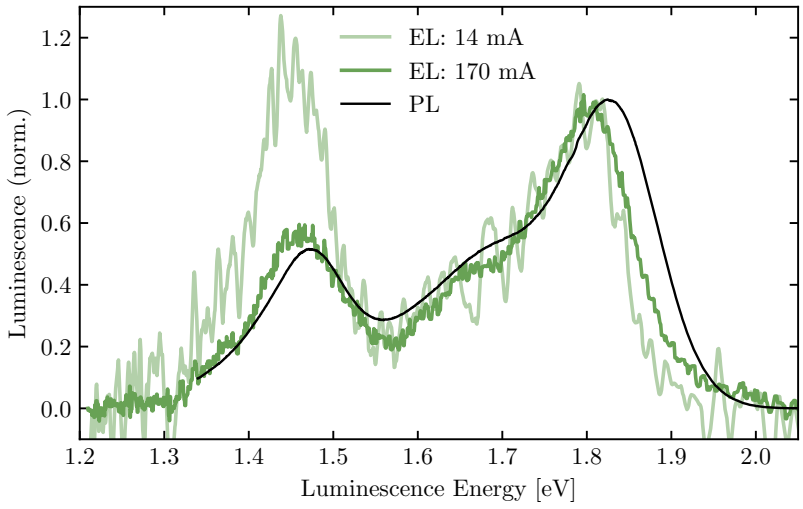

Figure II.3 Electroluminescence (and PL) of IDTT-F_2BT at different currents.

By using an OLED architecture, it is possible to measure the electroluminescence (EL) of the polymer to improve our understanding of this sub-E_g state. The EL is compared to the PL in Figure II.3. At low current densities, most of the EL comes from the inter-chain CT state. This is consistent with Kasha's rule which states that recombination is most likely from the lowest state energy in the joint density of states. This mechanism is likely to involve exciton diffusion to these sites. At higher current densities by $\sim 12\times$, we observe that Kasha's rule is seemingly violated, and the ICT peak at 1.8 eV increases in relative intensity to the inter-chain CT. This behaviour suggests increased relative exciton occupancy of the ICT state as all available inter-chain CTs become occupied. In the steady state, this is facilitated by a substantially longer inter-chain CT decay lifetime. At the same time, the blue edge of the ICT transition increases as all lower energy ICT microstates become filled, and additional excitons fill higher energy microstates to avoid double-occupancy. There is good spectral agreement between the EL and PL.

II.2.2 Inter-chain CTs in IDT-H_2BT

We also observe luminescence from inter-chain CTs in IDT-H_2BT. This is hard to quantify precisely, since precise measurement of the decay lifetime from the PL requires specialised ultrafast techniques and typically high fluence. In Figure II.4, we measure the fluence dependence of the PL spectra. We observe in these polymers that PL can

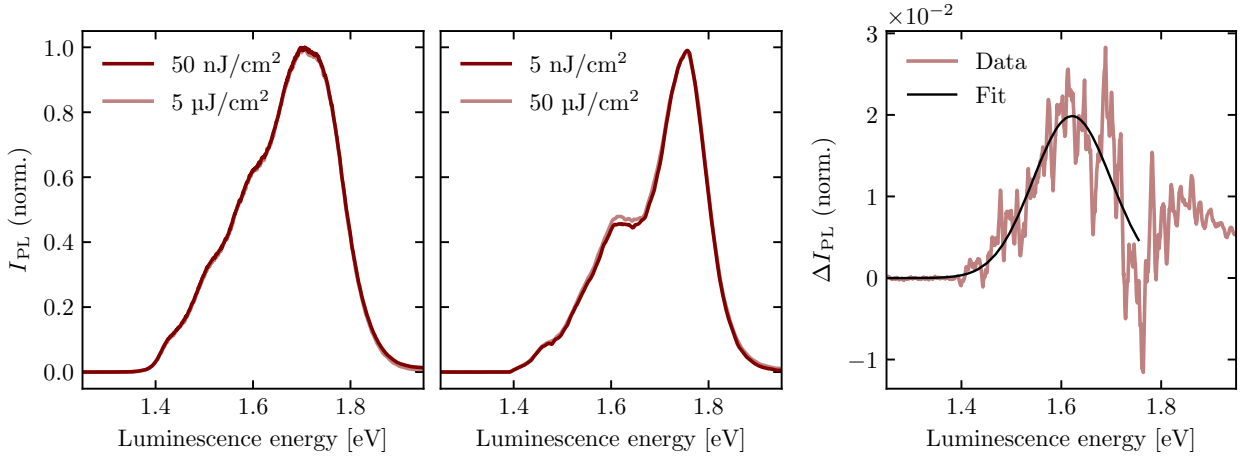

Figure II.4 PL spectra of IDT-H_2BT at different fluence: dilute solution (0.1g/L, *o*-DCB) (left) and thin film (centre) normalised to the maximum. Difference spectrum (right) of thin film PL at different fluence with Gaussian fit.

be quenched efficiently by non-radiative bimolecular exciton recombination, and in IDT-H_2BT, $\Phi \sim 4.5 \times 10^{-3}$ at $f_{\text{pump}} \sim 70$ µJ/cm^2. However, we observe for all of our polymers that the formation quantum efficiency of inter-chain CTs does not depend on the fluence. This is discussed in detail later. Therefore, by increasing the fluence, it should be possible to decrease the PLQE (ϕ_{PL}) of the ICT state, and observe an increase in relative PL from any emissive inter-chain CTs.

The PL measurements in Figure II.4 use $E_{\text{pump}} = 3.10$ eV and fluences as labelled, integrated on-chip in time, and normalised to the maximum. For a dilute solution of IDT-H_2BT (left), we do not resolve a change in the PL spectra with increased fluence. For a thin film (right), we resolve a slight difference around 1.6 eV in the normalised spectra. By subtracting the low-fluence spectrum from the high, we observe an additional contribution to the PL which is otherwise hidden under the strong ICT PL. Furthermore, this peak is redshifted with respect the the ICT, but extremely broad. By fitting a Gaussian lineshape, we recover that this peak is centred near 1.6 eV, and has a full-width at half-maximum (FWHM) of $\sim$ 0.65 eV. Therefore, it is likely that IDT-H_2BT has emissive inter-chain CT states, but this emission is much weaker in intensity than the ICT, and perhaps more similar in decay rate. This makes a more detailed analysis of this state challenging.

II.3 Transient absorption spectroscopy

II.3.1 Spectral features and time evolution

In order to discuss the how the TA spectra gives us information about the population of excited state species, we show the TA spectral evolution for IDT-H_2BT and TIF-H_2BT thin films over the first 1 ns after the pump pulse in Figure II.5. Here, pump photons had $E_{\text{pump}} = 2.33$ eV and the fluence chosen gave an initial excitation density of 5×10^{17} cm^{-3}. We show the transient differential transmission spectrum over three broadband regions: IR (left), NIR (middle), and visible (right).

There is a high degree of similarity between the TA spectra for these materials. For IDT-H_2BT (TIF-H_2BT), we see (i) the GSB above 1.70 eV (2.05 eV) which overlaps spectrally with the steady-state absorption spectrum in the main text. Accordingly, this has a vibronic progression at higher energies, and the 0-1 peak is at 2.00 eV (2.35 eV). Similarly, we see (ii) SE at 1.60 eV (1.9 eV), and by comparison with the steady-state PL spectrum, this peak is most likely the 0-1 vibronic peak of the SE, and therefore, the largest peak at 1.80 eV (2.15 eV) is likely to contain signal from the 0-0 of both GSB and SE. As the SE decays to zero, the 0-1 GSB peak at 2.00 eV (2.35 eV) increases in intensity relative to the 0-0 GSB peak at 1.80 eV (2.15 eV). Finally, below 1.4 eV (1.7 eV), we see a negative signal due to the absorption of the photoexcited states (PIA). In fact, this PIA is very broad, and extends well into the visible band, decreasing the apparent $\Delta T/T$ of the GSB to below zero towards 1 ns for IDT-H_2BT.

In the PIA, we resolve two broad absorption signatures which have their own lifetimes. This is a clear indication that they belong to the absorption of different excited state species. In IDT-H_2BT, the PIA seems to have two humps - one in the NIR ($1.2 - 1.4$ eV, with SE signal of the 0-2 vibronic peak > 1.4 eV), and one in the IR, with the $\Delta T/T$ increasing below 1.05 eV. These humps go to zero on different timescales. The IR PIA goes to zero by 1 ns, and the peak intensity at each timestep correlates strongly with the SE. It is likely that while we do not fully resolve this peak, we observe the blue edge of the PIA of excitons in the ICT state. By contrast, the NIR hump has very similar dynamics - also correlating strongly in intensity with the SE until ~ 1 ns, when the SE has finished, there is still some signal PIA left which does not go to zero. In all likelihood, the PIA due to ICT excitons is below 0.8 eV, but whose tail extends into both IR and NIR bands, giving the similarity in decay to the

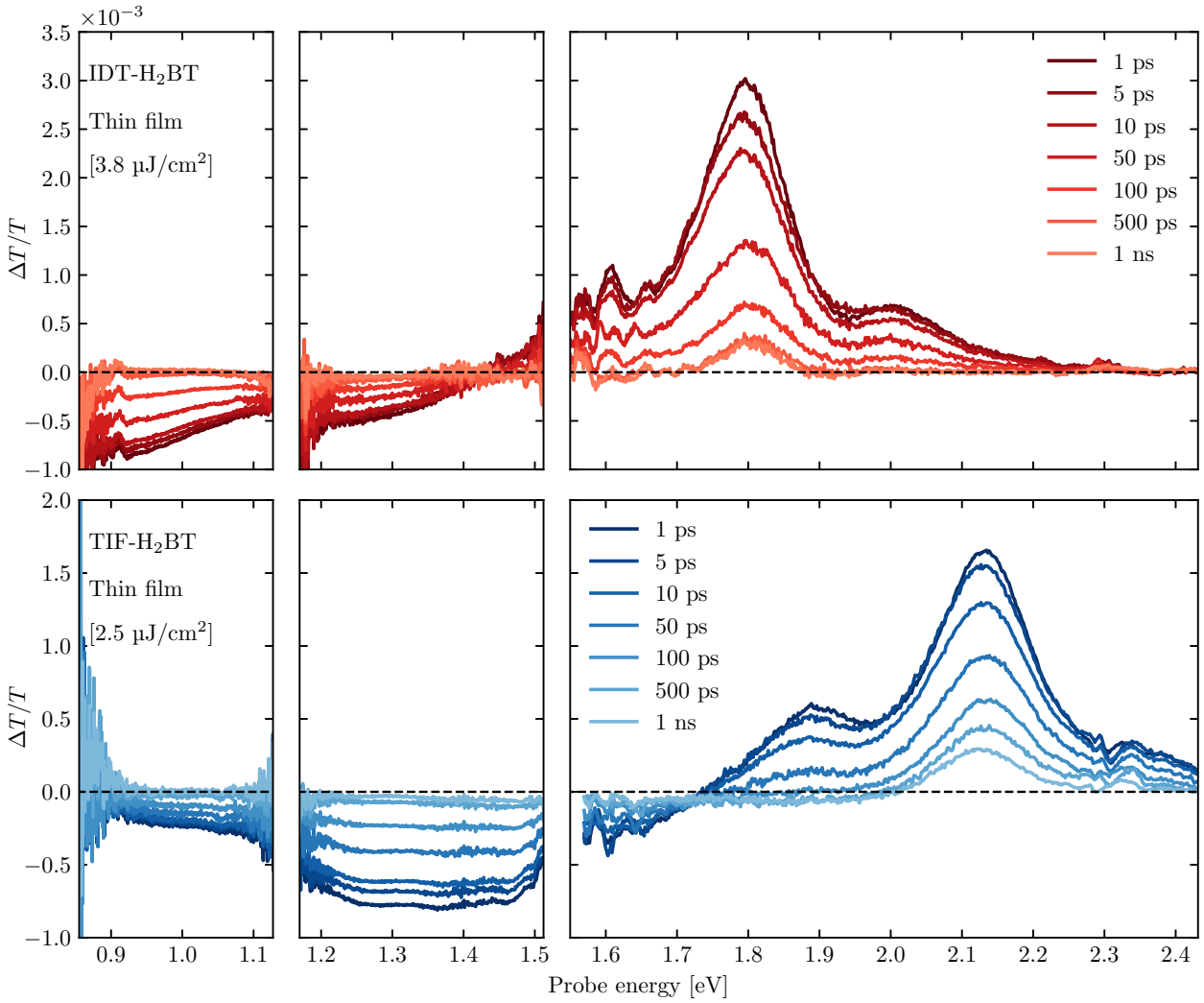

Figure II.5 TA spectral evolution from 1 ps−1 ns for IDT-H_2BT (top) and TIF-H_2BT (bottom).

SE. The remaining PIA signal above 1.2 eV extending into the visible band belongs to another species, and is likely to be inter-chain CT states, judging by its longevity. For TIF-H_2BT, the picture is the same, except the PIA due to ICT excitons is considerably blueshifted to $0.9 - 1.6$ eV, and overlaps with the PIA due to inter-chain CT excitons above 1.2 eV.

The decay kinetics, summarised in Figure II.6, tell the same story. For IDT-H_2BT (left), there is strong agreement between all the (normalised) kinetics of the spectral features. Importantly, while the IR PIA and SE (both arising from ICT excitons)

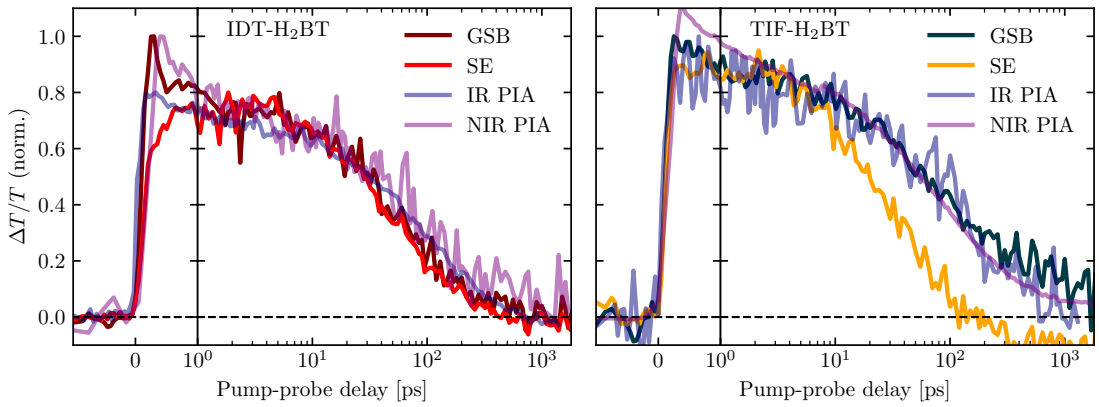

Figure II.6 Evolution kinetics of TA spectral features using $E_{\text{pump}} = 2.33$ eV, and $n_0 = 5 \times 10^{17}$ cm^{-3}.

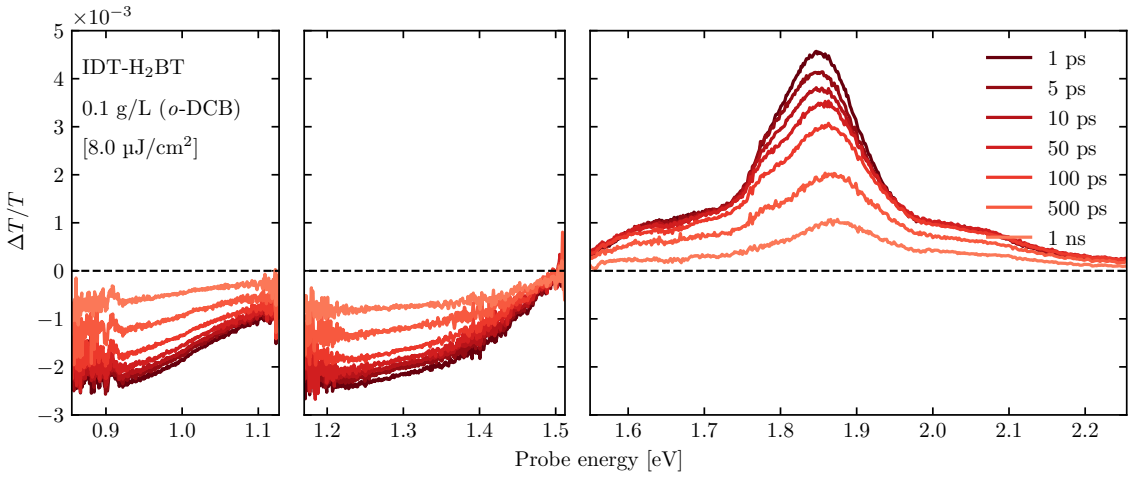

Figure II.7 TA spectral evolution from 1 ps−1 ns for IDT-H$_2$BT (0.1 g/L in o-DCB) using $E_{\text{pump}} = 2.33$ eV.

decay to zero by $\sim$ 1 ns, the NIR PIA and the GSB do not, since they arise from the small population of longer-lived inter-chain CT species. Additionally, it is important to note that all features rise within the instrument response of the setup (of $\sim$ 100 fs), and therefore, both the ICT and inter-chain CTs are populated on ultrafast timescales. The picture for TIF-H$_2$BT (right) is the same. Here, owing to the overlap of NIR PIA and SE, the SE signal (yellow) appears to become negative by 200 ps, but simply decays to zero as before with the IR PIA since it arises from emissive ICT excitons. On the other hand, the inter-chain CT PIA is weaker

but longer lived (as before) and leads to good agreement between the GSB towards 1 ns.

To complete this picture, we show the TA spectra of IDT-H_2BT in dilute solution in Figure II.7. In this case, the exciton dynamics are comparable, except we are unable to resolve a population of inter-chain CTs by 1 ns. This is owing to the longer decay lifetime of the ICT meaning there is still strong SE and strong IR PIA at this time.

To demonstrate the similarity of the exciton dynamics in these materials, we show the TA spectra for all of the materials studied here in Figure II.8 at a low excitation density of 5×10^{17} cm^{-3} between 1 ps−1 ns, and in Figure II.9 at a higher excitation density of 5×10^{18} cm^{-3} between 1 ns−1 µs.

II.3.2 Formation of inter-chain CTs

To determine the quantum yield of inter-chain CTs, we used TA spectroscopy. In each of the polymer materials, we track the transient evolution of the GSB after the pump pulse, and use this as a proxy for the total fraction of excited-state species remaining at a given time. In Figure II.10, we show this for each material at a lower and a higher fluence. At the lower fluence in the 1 ns time window, the transient excitation population has approximately bi-exponential kinetics.

In the TA experiments, we find that the shorter of the two exponential lifetimes is comparable to (but faster than) the ICT PL decay lifetime (τ_{ICT}) in the materials for which we can independently measure the PL decay directly. We therefore assign this first decay rate to the decay of the ICT states in all our materials. In this case, the reason for the shorter τ_{ICT} in the TA experiment is second-order recombination involving exciton-exciton annihilation at higher fluence which shortens the lifetime at earlier times. The longer exponential lifetime is due to inter-chain CT states.

At the higher fluence, we observe that while most of the population is ICT excitons, these recombine much faster via a mixture of first- and second-order recombination. However, the inter-chain CT decay rate is largely unaffected by the higher fluence, and the fraction of the population remaining after the ICTs recombine converges between the two fluences. This is because the branching between ICT and inter-chain CTs occurs on very early timescales, and the effect of shortening the ICT decay does

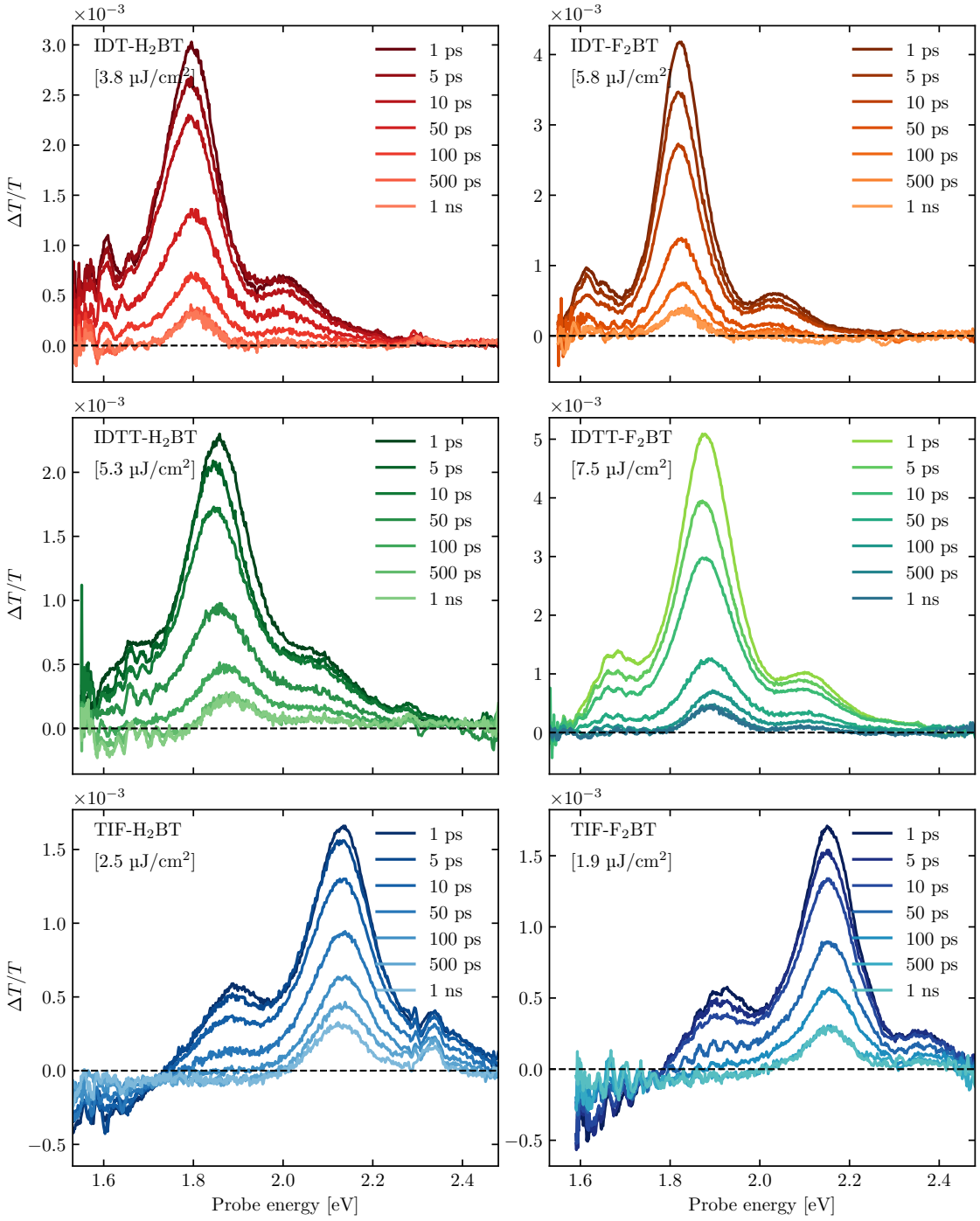

Figure II.8 TA spectral evolution from 1 ps−1 ns. For each sample, $n_0 = 5 \times 10^{17}$ cm^{-3} and $E_{\text{pump}} = 2.33$ eV.

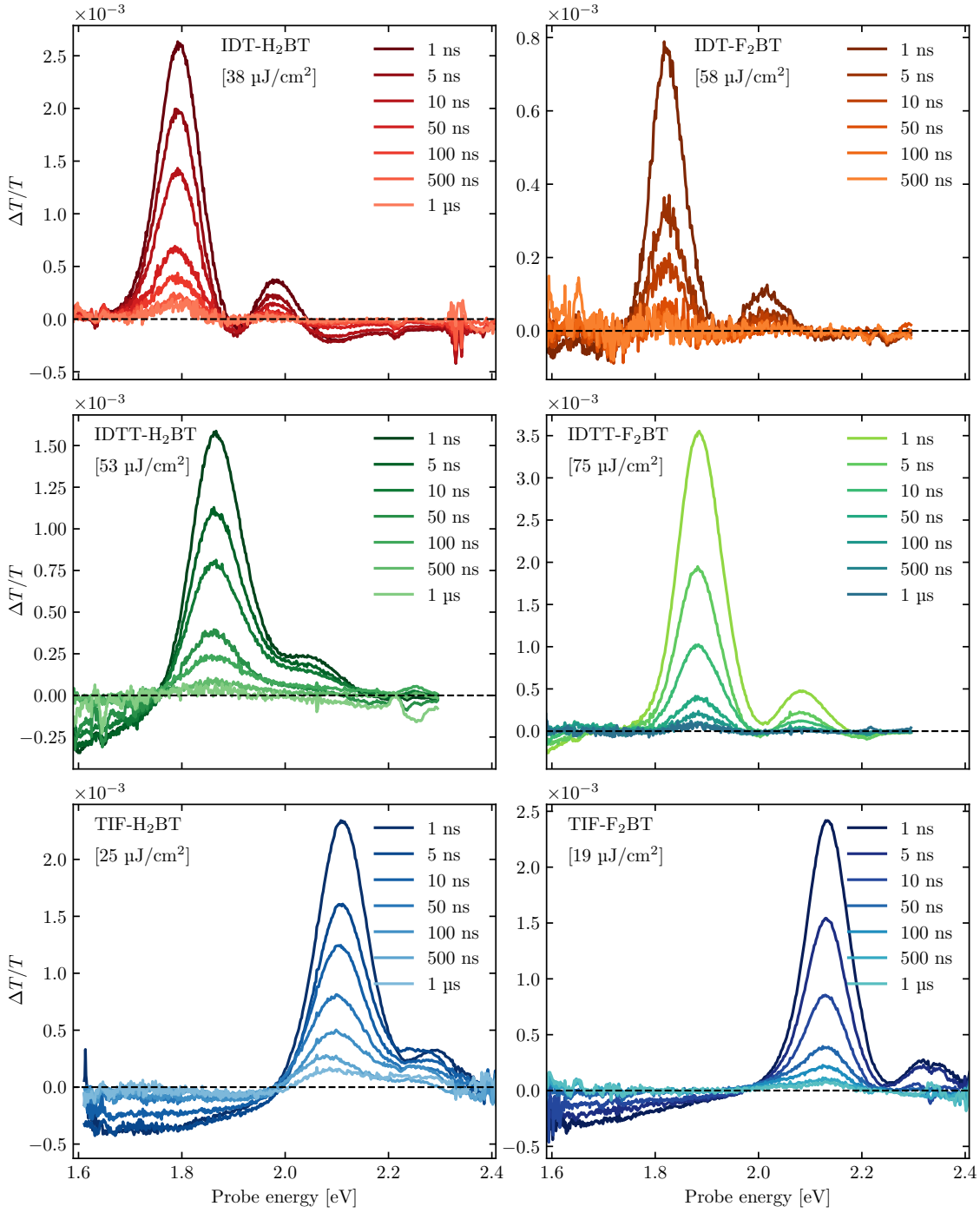

Figure II.9 TA spectral evolution from 1 ns−1 µs. For each sample, $n_0 = 5 \times 10^{18}$ cm^{-3} and $E_{\text{pump}} = 2.33$ eV.

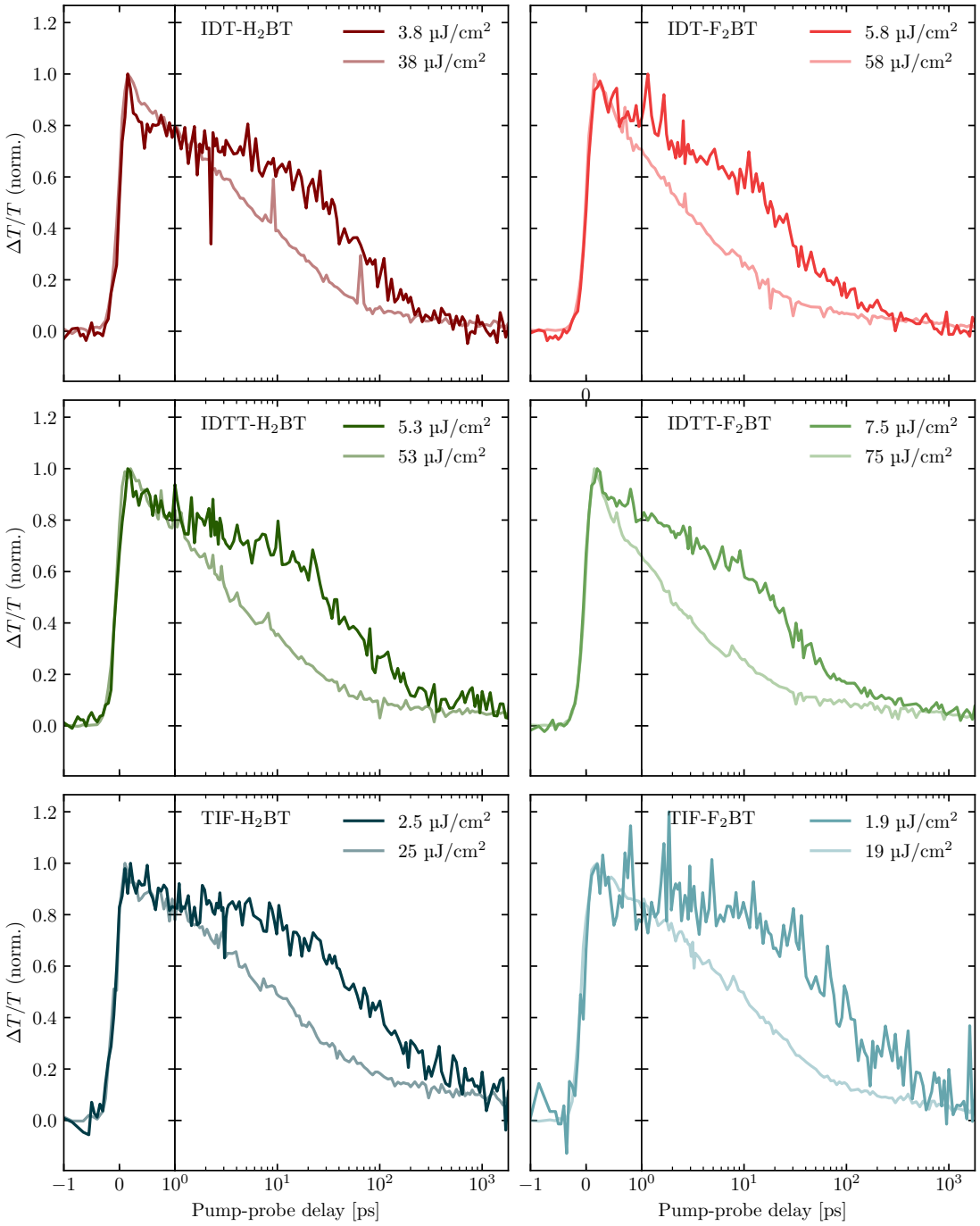

Figure II.10 Kinetic of the GSB (normalised to the maximum) for different fluence. For each polymer, $n_0 = 5 \times 10^{17}$ cm^{-3} (dark) and 5×10^{18} cm^{-3} (light) with $E_{\text{pump}} = 2.33$ eV.

little to decrease the inter-chain CTs remaining after all the ICTs have recombined. Therefore, it follows that at most a very small population of ICTs undergo charge transfer between chains after $\sim$ 400 fs. We speculate that this is owing to the substantially longer lifetime of the inter-chain CTs, and a lower density of states.

To investigate the dependency of the decay kinetics on pump wavelength (or E_{pump}), we measure the decay of the transient GSB with different E_{pump}. This is shown in Figure II.11. Between the samples, we set the fluence to match the $\Delta T/T$ at 10 ps, and retrospectively calculate the initial excitation density (n_0) which was $\sim 10^{18}$ cm^{-3}. The calculated fluences and excitation densities summarised in Table II.2. Using this method, we observe that (i) the un-normalised kinetics are very similar after 10 ps, converging to the same $\Delta T/T$ value by $\sim$ 1 ns, and (ii) we have used appoximately constant n_0 for all E_{pump} between samples. However, before 10 ps, we observe a strong dependency of the kinetics on E_{pump}. Unsurprisingly, pumping higher above E_g leads to a greater excess energy ($E_{\text{ex.}}$) per excitation, with $E_{\text{ex.}} = E_{\text{pump}} - E_g$. Generally, a higher $E_{\text{ex.}}$ leads to a greater degree of GSB cooling on $\sim$ 400 fs timescales, and this is most clear for IDT-H_2BT, whose $n_0 = 2.6 \times 10^{18}$ $\pm$29 % is approximately constant, and whose kinetics converge nonetheless by 10 ps. In any case, the extraction of the ϕ_{CT} (discussed below) uses data on timescales of $\sim$ 1 ns, where the kinetics converge and are independent of E_{pump}.

II.3.3 Excited-state dynamics

II.3.3.1 Determination of ϕ_{CT}

To determine the rate dynamics of the excited states in the polymers, we solved the coupled rate ODEs. Assuming first-order dynamics, the population of state i (n_i) is governed by

$$\dot{n}_j = \sum_i k_{i\to j} n_i - \sum_l k_{j\to l} n_j \tag{II.1}$$

where $k_{i\to j}$ is the rate of energy transfer from i to j. Using the shorthand that $i = 0$ denotes the ground-state, $i = 1$ denotes the 'hot' ICT state (ICT*), $i = 2$ the 'cooled' and emissive ICT state (ICT), $i = 3$ the highest energy inter-chain CT state which may be emissive (CTs light), and $i > 4$ the lower energy inter-chain CT states which are not emissive (CTs dark), and assuming down-conversion only, this leads to the

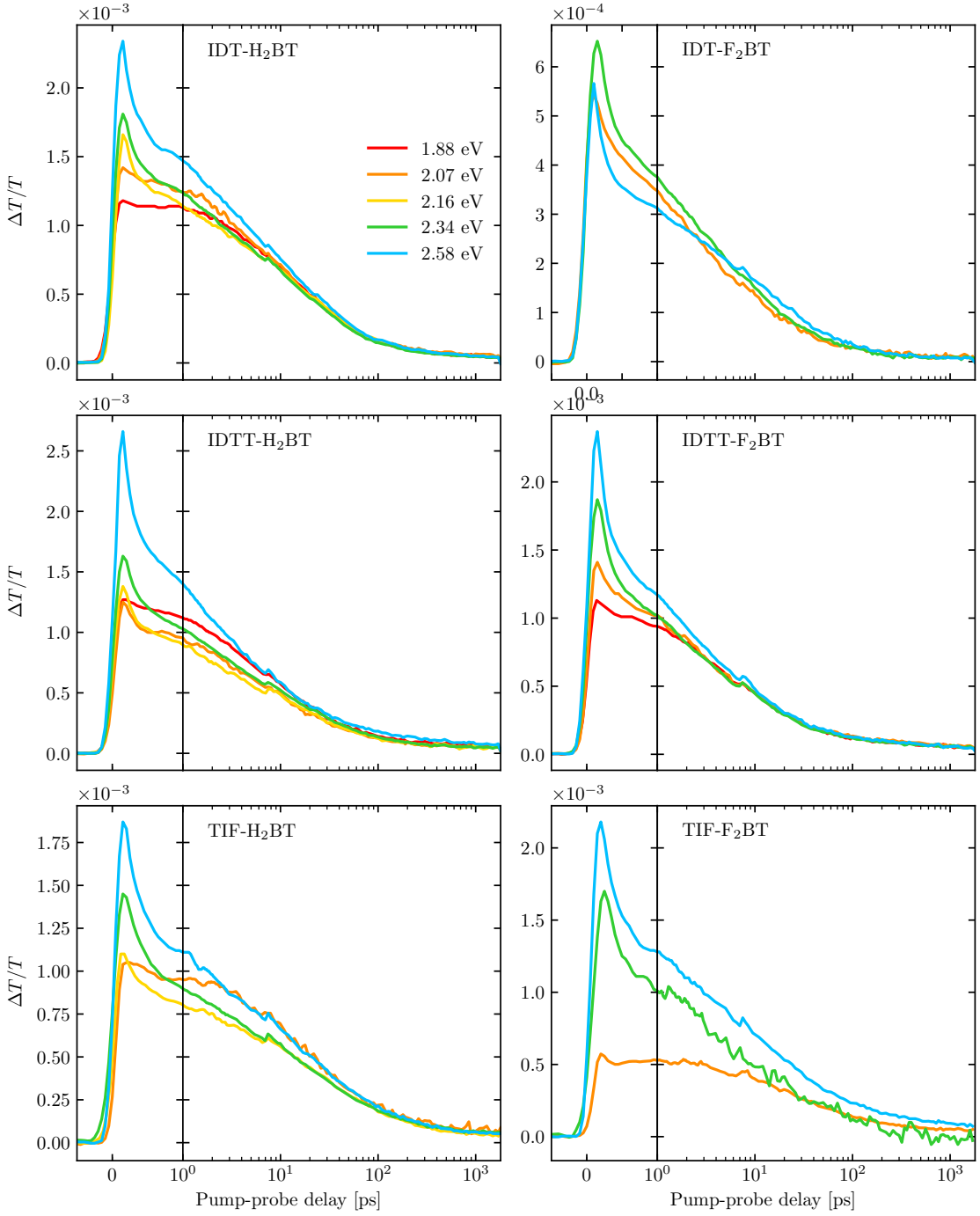

Figure II.11 Kinetic of the GSB for different pump wavelength. For each polymer, $n_0 \sim 10^{18}$ cm^{-3}.

coupled equations

$$\begin{aligned}
\dot{n}_1 &= -k_{1\to 0}n_1 - \sum_{i>1} k_{1\to i}n_1 \\
\dot{n}_2 &= -k_{2\to 0}n_2 - \sum_{i>2} k_{2\to i}n_2 + k_{1\to 2}n_1 \\
\dot{n}_3 &= -k_{3\to 0}n_3 - \sum_{i>3} k_{3\to i}n_3 + k_{1\to 3}n_1 + k_{2\to 3}n_2 \\
\dot{n}_{j>3} &= -k_{j\to 0}n_j - \sum_{l>j} k_{j\to l}n_j + \sum_{i<j} k_{i\to j}n_i
\end{aligned}$$

governing the occupation of the states. There is a convenient simplification in our case. If (i) the ICT and inter-chain CT states are filled on the timescale of the $1/k_1$ (the rise of all PIAs is fast, shown in Figure II.5), and (ii) lower energy states have longer

Table II.2 Fluences and excitation densities for matched $\Delta T/T$ signal.

Material	λ_{pump} [nm]	f_{pump} [J/cm^2]	n_0 [cm^{-3}]	$\bar{n}_0 \pm \sigma$ [cm^{-3}]
IDT-H_2BT	660	1.7×10^{-6}	1.7×10^{18}	2.6×10^{18} ± 29 %
	600	3.7×10^{-6}	3.0×10^{18}	
	575	5.5×10^{-6}	3.7×10^{18}	
	530	4.1×10^{-6}	1.7×10^{18}	
	480	1.1×10^{-5}	2.7×10^{18}	
IDT-F_2BT	600	5.7×10^{-6}	5.8×10^{18}	3.7×10^{18} ± 40 %
	530	6.2×10^{-6}	3.1×10^{18}	
	480	7.8×10^{-6}	2.2×10^{18}	
IDTT-H_2BT	660	4.4×10^{-6}	5.0×10^{18}	4.8×10^{18} ± 22 %
	600	5.6×10^{-6}	5.1×10^{18}	
	575	8.1×10^{-6}	6.1×10^{18}	
	530	5.8×10^{-6}	2.8×10^{18}	
	480	1.7×10^{-5}	4.8×10^{18}	
IDTT-F_2BT	660	4.2×10^{-6}	3.3×10^{18}	4.0×10^{18} ± 17 %
	600	7.3×10^{-6}	5.0×10^{18}	
	530	8.0×10^{-6}	4.5×10^{18}	
	480	1.7×10^{-5}	4.3×10^{18}	
TIF-H_2BT	600	5.5×10^{-6}	2.8×10^{18}	2.6×10^{18} ± 23 %
	575	4.6×10^{-6}	3.2×10^{18}	
	530	2.7×10^{-6}	1.6×10^{18}	
	480	6.5×10^{-6}	2.6×10^{18}	
TIF-F_2BT	600	4.6×10^{-6}	1.6×10^{18}	1.7×10^{18} ± 30 %
	530	2.1×10^{-6}	1.2×10^{18}	
	480	6.5×10^{-6}	2.4×10^{18}	

lifetimes (which we observe to be true empirically), then for $t \gg 1/k_1$, $k_{i\to j} = 0$ for $j > i > 1$, and there is no more exciton transfer at later times. This is the condition that intra-chain/inter-chain branching occurs early.

In this work, we group $k_i = k_{i\to 0} + \sum_{j>i} k_{i\to j}$, and making the simplifications above allows us to write $k_i = k_{i\to 0}$ for $i > 1$ after $1/k_1 \sim 400$ fs. It is convenient to rewrite these equations in terms of k_i which is an observable in the case of the ICT*, ICT and 'CTs light'. Additionally, to account for bimolecular recombination of excitons at higher excitation densities (which we require in order to resolve the GSB towards ~ 1 µs), we add a bimolecular recombination term for the ICT ($i = 2$). Finally, while we expect a continuum of possible inter-chain CTs due to disorder, each having their own decay lifetime, we have assumed three discrete populations for $i \geq 2$ with the rate k_i for simplicity. We solve the coupled equations

$$\begin{aligned}
\dot{n}_1 &= -k_1 n_1 \\
\dot{n}_2 &= -k_2 n_2 - k_2^{(2)} n_2^2 + k_{1\to 2} n_1 \\
\dot{n}_3 &= -k_3 n_3 + k_{1\to 3} n_1 \\
\dot{n}_4 &= -k_4 n_4 + k_{1\to 4} n_1 \\
\dot{n}_5 &= -k_5 n_5 + k_{1\to 5} n_1
\end{aligned}$$

for the picture summarised diagrammatically in Figure II.12.

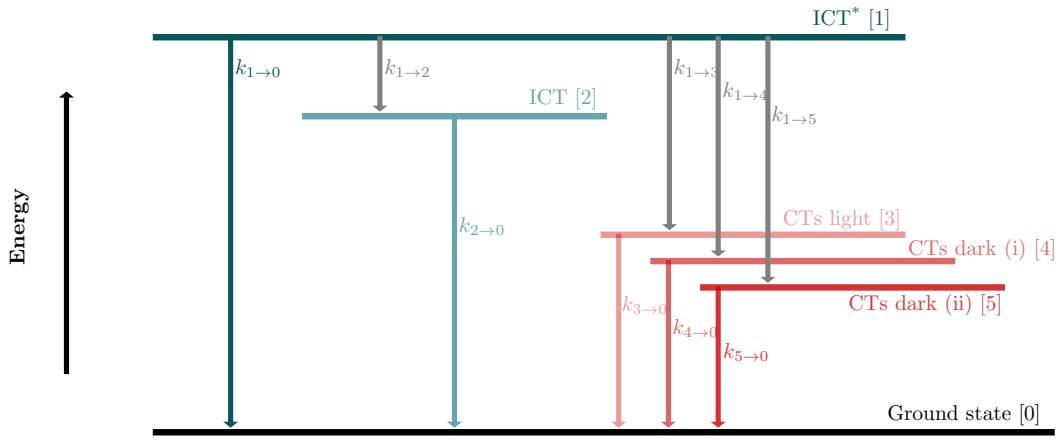

Figure II.12 Energy level diagram separating intra- and inter-chain excitonic species.

By applying the separately observed rates k_1 and k_2 (and k_3 in the case of luminescent CTs), we fit the remaining parameters to the observed GSB between 1 ps−1 µs in **Figure S13**. During the fitting, we note that a strong mutual dependency exists between the pairs of parameters k_i and $k_{1\to i}$, for $i = 3, 4, 5$, and we do not attempt to separate them. Instead, it is more robust to deal with these rates together and we define the quantum efficiency of transfer to a inter-chain CT state from $i = 1$ as

$$\phi_{\mathrm{CT}} = \phi_{1\to 3} + \phi_{1\to 4} + \phi_{1\to 5} = \frac{k_{1\to 3} + k_{1\to 4} + k_{1\to 5}}{k_1} \tag{II.2}$$

in terms of the quantum efficiency of transfer from state i to state j ($\phi_{i\to j}$). The choice of k_i and $k_{1\to i}$ pairs leads to only small variations in the deduced ϕ_{CT}. The measured parameters (in Table II.3) were fixed during the fitting, and the optimised parameters were summarised in Tables II.4 and II.5.

Table II.3 Measured parameters for the GSB of different polymers.

Polymer	k_1 [s^{-1}]	k_2 [s^{-1}]	k_3 [s^{-1}]
IDT-H_2BT	2.5×10^{12}	1.1×10^{10}	-
IDT-F_2BT	2.5×10^{12}	6.4×10^{9}	1.8×10^{9}
IDTT-H_2BT	2.5×10^{12}	1.0×10^{10}	-
IDTT-F_2BT	2.5×10^{12}	1.4×10^{10}	1.3×10^{9}
TIF-H_2BT	2.5×10^{12}	1.8×10^{9}	5.3×10^{8}
TIF-F_2BT	2.5×10^{12}	1.4×10^{9}	3.4×10^{8}

Table II.4 Fit parameters (i) for the GSB of different polymers.

Polymer	$k_2^{(2)}$ [s^{-1}]	k_3 [s^{-1}]	$\phi_{1\to 3}$ [ ]	k_4 [s^{-1}]	$\phi_{1\to 4}$ [ ]
IDT-H_2BT	1.0×10^{11}	2.0×10^{9}	0.05	7.1×10^{7}	0.009
IDT-F_2BT	2.9×10^{11}	-	0.04	1.4×10^{8}	0.007
IDTT-H_2BT	1.8×10^{11}	2.0×10^{9}	0.05	5.5×10^{7}	0.025
IDTT-F_2BT	2.5×10^{11}	-	0.06	7.6×10^{7}	0.011
TIF-H_2BT	1.3×10^{11}	-	0.028	1.0×10^{8}	0.028
TIF-F_2BT	9.1×10^{10}	-	0.027	1.0×10^{8}	0.019

II.3.3.2 Determination of ϕ_{PL}

In the case that only the ICT is emissive, its ϕ_{PL} is simply given by

$$\phi_{\mathrm{PL}} = \frac{\Phi}{1 - \phi_{\mathrm{CT}}} \tag{II.3}$$

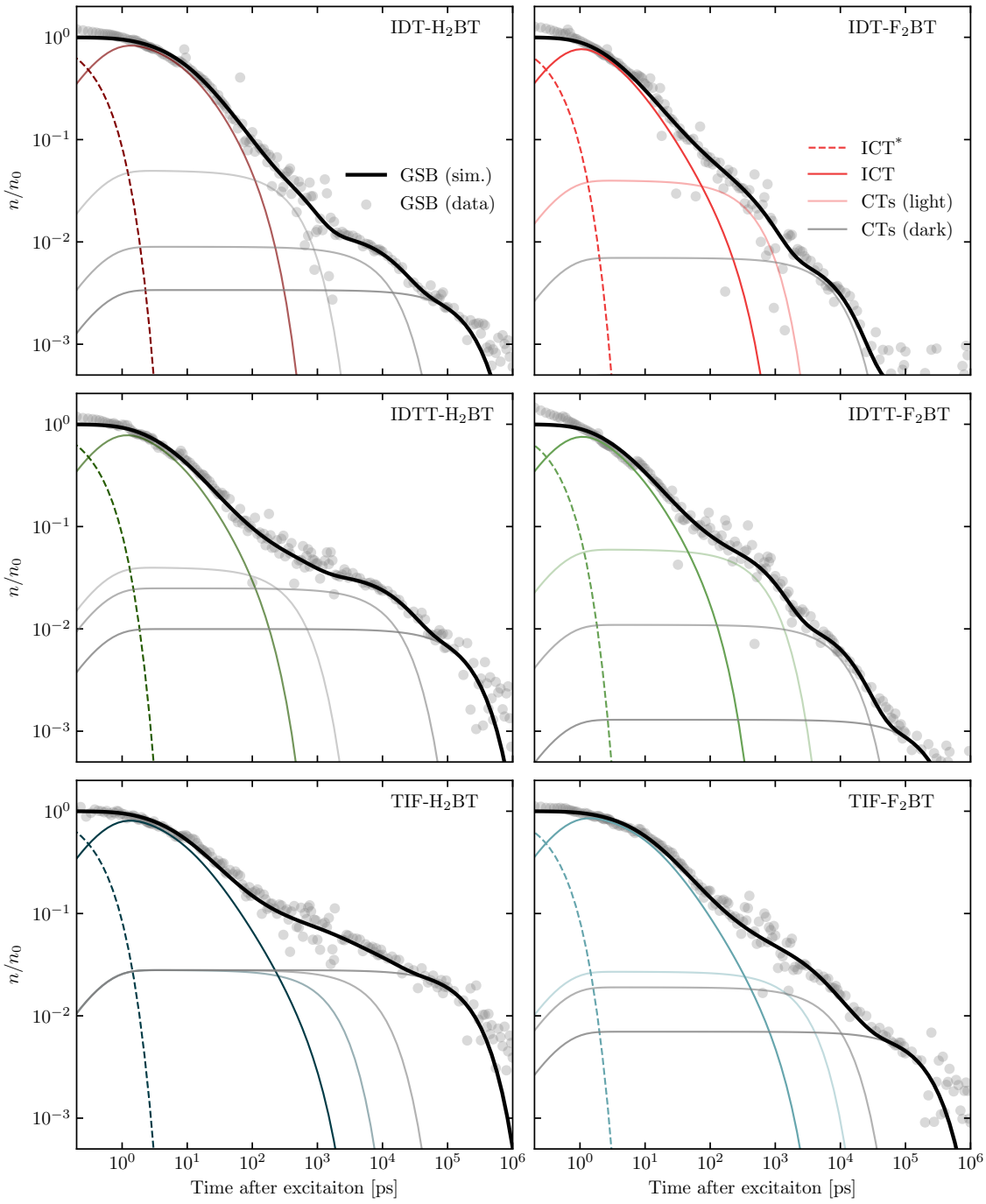

Figure II.13 Excited-state dynamics and GSB fit for different materials. Here, $E_{\text{pump}} = 2.33$ eV and $n_0 = 5 \times 10^{18}$ cm^{-3}.

Table II.5 Fit parameters (ii) for the GSB of different polymers.

Polymer	k_5 [s^{-1}]	$\phi_{1\to5}$ [ ]	ϕ_{CT} [ ]
IDT-H_2BT	4.2×10^6	0.0034	0.0624
IDT-F_2BT	4.0×10^6	0.0005	0.0475
IDTT-H_2BT	4.0×10^6	0.01	0.075
IDTT-F_2BT	4.0×10^6	0.0013	0.0723
TIF-H_2BT	4.0×10^6	0.028	0.084
TIF-F_2BT	4.3×10^6	0.007	0.053

Where both the ICT and interchain species are luminescent, we must consider the radiative and non-radiative rates of decay to determine ϕ_{PL} of the ICT and interchain species respectively. In this section, we use the nomenclature: $k_{R,i\to0}$ as the radiative rate, $k_{NR,i\to0}$ as the non-radiative rate of decay from state i, such that $k_{i\to0} = k_{R,i\to0} + k_{NR,i\to0}$. We also define the PLQE of state i as $\phi_{i\to0} = k_{R,i\to0}/k_1$. For simplicity, we make the additional approximation that decay from ICT* is negligible ($k_1 \to \sum_{i\neq0} k_{i>1}$).

The general equation for the external PLQE (Φ) of such a three emissive-state ($i = 1, 2, 3$) is

$$\Phi = \phi_{1\to0} + \phi_{1\to2} \cdot \phi_{2\to0} + (\phi_{1\to3} + \phi_{1\to2} \cdot \phi_{2\to3}) \cdot \phi_{3\to0} \tag{II.4}$$

and in the limit that $\phi_{1\to0}, \phi_{2\to3} \to 0$, this equation simplifies to

$$\Phi = (1 - \phi_{1\to3}) \cdot \phi_{2\to0} + \phi_{1\to3} \cdot \phi_{3\to0} \tag{II.5}$$

which can be written

$$\frac{\phi_{2\to0}}{\phi_{3\to0}} = \left(\frac{\Phi}{\phi_{3\to0}} - \phi_{1\to3}\right) \cdot (1 - \phi_{1\to3})^{-1} \tag{II.6}$$

The intensity of PL detected $I_i(t)$ from state i at time t is proportional to $\dot{n}_i(t)$ and $k_{R,i\to0}$

$$I_i(t) \sim k_{R,i\to0} \cdot \exp(-k_i t) \tag{II.7}$$

so the time-integrated intensity I_i which we measure is related to

$$I_i \sim \phi_{i\to 0} \cdot n_i(0) \tag{II.8}$$

In the case that there are two emissive species, $i = 2, 3$, then the ratio of their PL intensities is given by

$$\frac{I_2}{I_3} = \frac{\phi_{2\to 0}}{\phi_{3\to 0}} \cdot \frac{n_2(0)}{n_3(0)} \tag{II.9}$$

We can estimate the initial population ratio as the ratio of the formation quantum efficiencies. Although we do not know $\phi_{1\to 3}$, we make the substitution $\phi_{1\to 3} \to \phi_{\mathrm{CT}}$ (which we calculated earlier with a good degree of certainty) in order to underestimate ϕ_{PL} of the luminescent interchain species. Rearranging gives

$$\frac{\phi_{2\to 0}}{\phi_{3\to 0}} = \frac{I_2}{I_3} \cdot \frac{\phi_{\mathrm{CT}}}{1 - \phi_{\mathrm{CT}}} \tag{II.10}$$

and combining **Equation S10** and **Equation S14** gives $\phi_{3\to 0}$

$$\phi_{3\to 0} = \frac{\Phi}{\phi_{\mathrm{CT}}} \cdot \left(\frac{I_2}{I_3} + 1\right)^{-1} \tag{II.11}$$

in terms of measured quantities. The calculated ϕ_{PL} the ICT and interchain states are summarised in the main text.

Appendix III

Supplementary Information: Vibrations in organic emitters

III.1 Raman spectroscopy of host materials

In this study, we screen a broad range of TADF emitters by non-resonant Raman spectroscopy for strong electron-phonon coupling in their low frequency rotational vibrations. In addition to the structures presented in Figure 7.1, we show the structures of the remaining materials in Figure III.1.

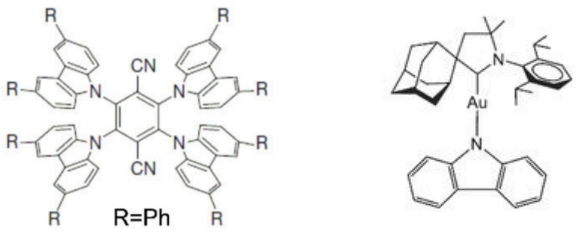

Figure III.1 Additional emitters in Raman study: 4CzTPN-Ph (left) and CMA1 (right), with figures from references [290] and [120].

For Figures III.2 and 7.2, we use non-resonant line at 633 nm, and a backscattering triple-stage measurement described in Section 3.3.4. The samples analysed are powders (both here and in the main text), since it was found separately that preparation of (even very thick) films leads to very small Raman signals.

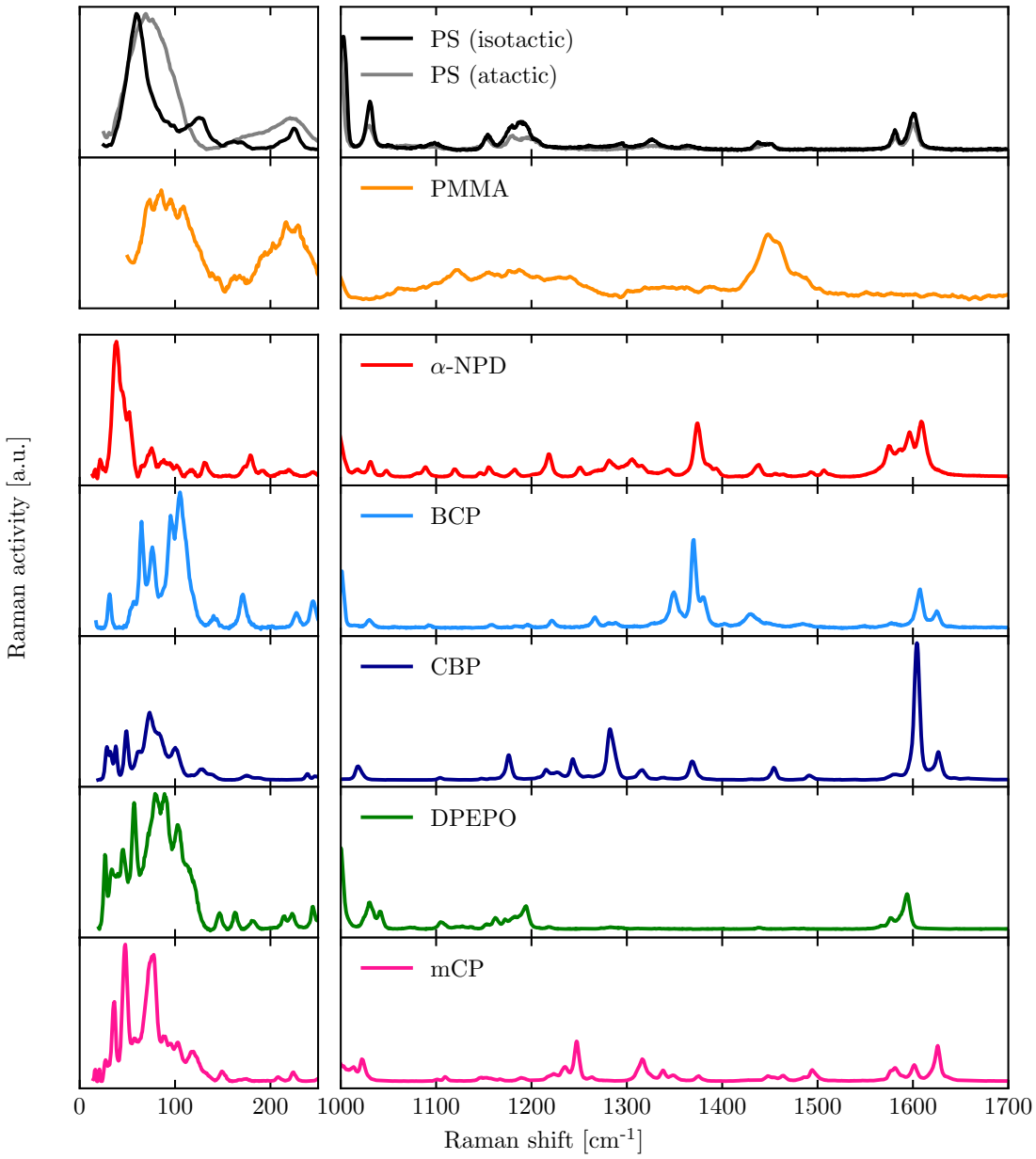

Figure III.2 Non-resonant Raman spectrum of host (non-TADF) materials with rotational freedom.

III.2 Φ_{prompt} and Φ_{ISC}

For completeness, we also include the extracted Φ_{prompt} and Φ_{ISC} values for solution and film PL measurements. These are summarised in Figure III.3.

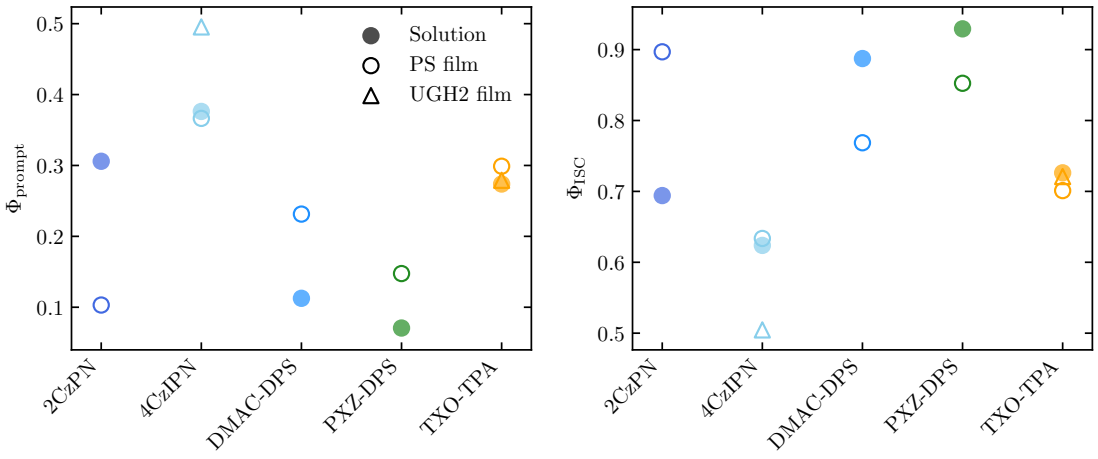

Figure III.3 QE of prompt PL (left) and ISC (right) for TADF emitters in solution (full circles), in PS films (empty circles), and UGH2 films (triangles).

III.3 TA of other TADF materials

In this section, we show the ultrafast-microsecond evolution of two additional TADF materials, 2CzPN (Figure III.4), and TXO-TPA (III.5, which are discussed in the main text). In these figures, solutions (0.1 g/L in toluene) are shown (left) and films (5 %w in atactic PS host) are shown (right). Here, we combine two experiments with time resolution $\sim$ 100 fs (top) and $\sim$ 2 ns (bottom) with a matched $\Delta T/T$ signal between experiments. The fluence used here is summarised in Table III.1.

Table III.1 f_{pump} [J/cm^2] used for TA in NIR.

Material	Solution (short)	Solution (long)	PS film (short)	PS film (long)
4CzIPN	2.08×10^{-5}	5.81×10^{-5}	4.94×10^{-5}	7.64×10^{-5}
2CzPN	2.08×10^{-5}	1.94×10^{-5}	7.80×10^{-5}	8.15×10^{-5}
TXO-TPA	6.76×10^{-6}	3.87×10^{-5}	5.72×10^{-7}	8.15×10^{-6}

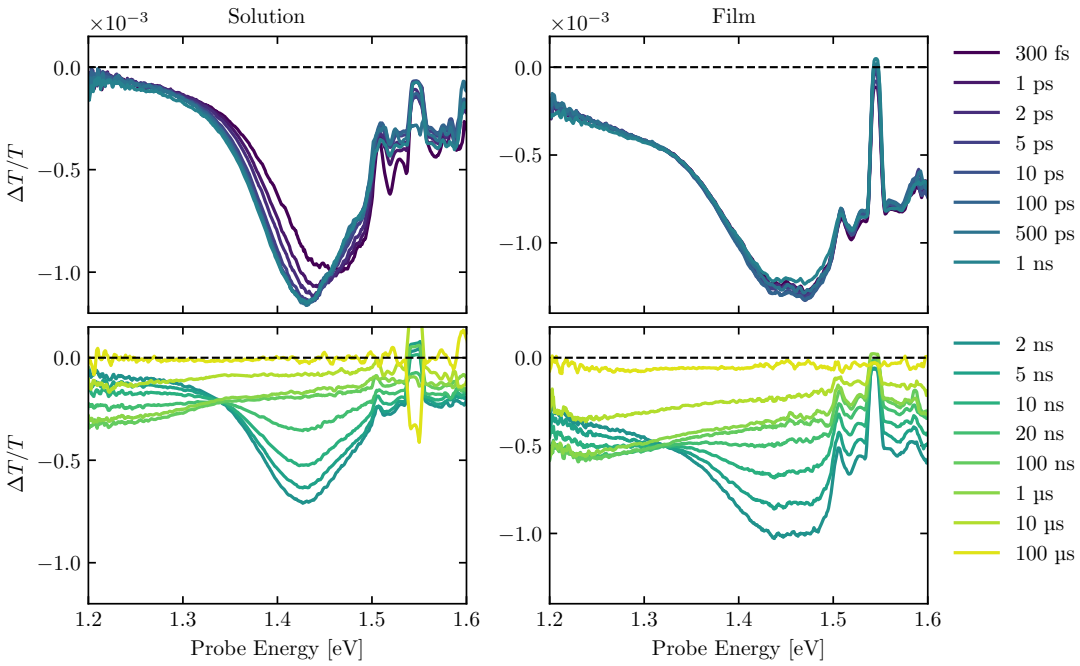

Figure III.4 NIR TA spectra of 2CzPN in solution (left) and film (right).

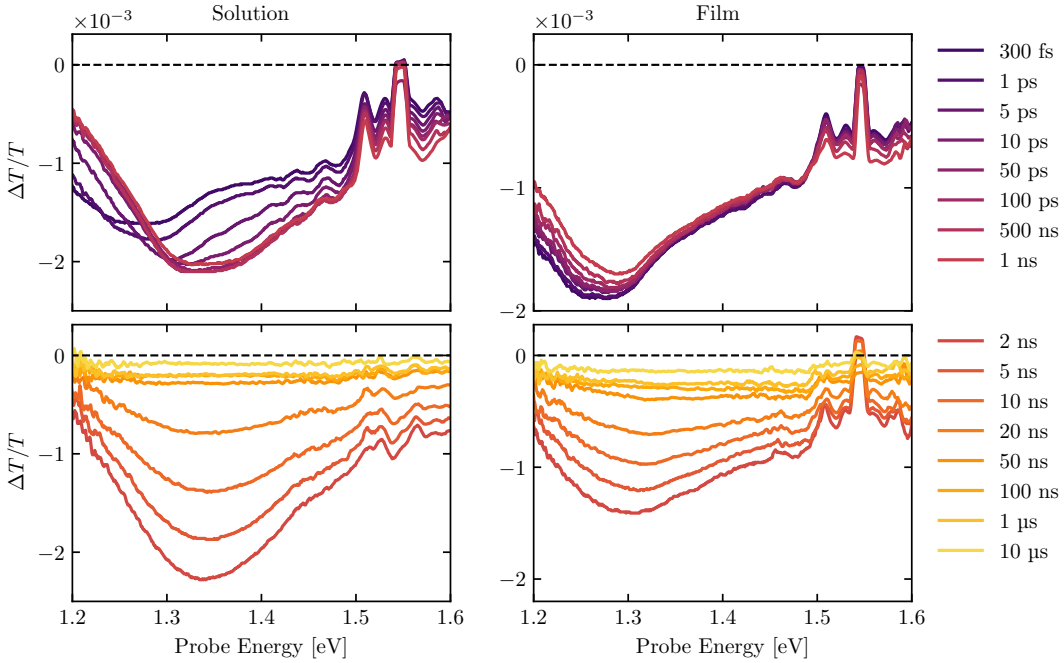

Figure III.5 NIR TA spectra of TXO-TPA in solution (left) and film (right).

Appendix IV

List of publications

[1] Sadhanala, A., Deschler, F., **Thomas, T. H.**, Dutton, S. E., Goedel, K. C., Hanusch, F. C., Lai, M. L., Steiner, U., Bein, T., Docampo, P., Cahen, D. & Friend, R. H. Preparation of single-phase films of $CH_3NH_3Pb(I_{1-x}Br_x)_3$ with sharp optical band edges. *J. Phys. Chem. Lett.* **5**, 2501 – 2505 (2014).

[2] Vikse, K. L., Zavras, A., **Thomas, T. H.**, Ariafard, A., Khairallah, G. N., Canty, A. J., Yates, B. F. & O'Hair, R. A. J. Prying open a reactive site for allylic arylation by phosphine-ligated geminally diaurated aryl complexes. *Organometallics* **34**, 3255 – 3263 (2015).

[3] Senanayak, S. P., Yang, B., **Thomas, T. H.**, Giesbrecht, N., Huang, W., Gann, E., Nair, B., Goedel, K., Guha, S., Moya, X., McNeill, C. R., Docampo, P., Sadhanala, A., Friend, R. H. & Sirringhaus, H. Understanding charge transport in lead iodide perovskite thin-film field-effect transistors. *Sci. Adv.* **3** (2017).

[4] Di, D., Romanov, A. S., Yang, L., Richter, J. M., Rivett, J. P. H., Jones, S., **Thomas, T. H.**, Jalebi, M. A., Friend, R. H., Linnolahti, M., Bochmann, M. & Credgington, D. High-performance light-emitting diodes based on carbene-metal-amides. *Science* **356**, 159 – 163 (2017).

[5] Booker, E. P., **Thomas, T. H.**, Quarti, C., Stanton, M. R., Dashwood, C. D., Gillett, A. J., Richter, J. M., Pearson, A. J., Davis, N. J. L. K., Sirringhaus,

H., Price, M. B., Greenham, N. C., Beljonne, D., Dutton, S. E. & Deschler, F. Formation of long-lived color centers for broadband visible light emission in low-dimensional layered perovskites. *J. Am. Chem. Soc.* **139**, 18632 – 18639 (2017).

[6] Ni, L., Huynh, U., Cheminal, A., **Thomas, T. H.**, Shivanna, R., Hinrichsen, T. F., Ahmad, S., Sadhanala, A. & Rao A. Real-time observation of exciton-phonon coupling dynamics in self-assembled hybrid perovskite quantum wells. *ACS Nano* **11**, 10834 – 10843 (2017).

[7] **Thomas, T. H.**, Rivett, J. P. H., Gu, Q., Harkin, D. J., Richter, J. M., Sadhanala, A., Yong, C. K., Schott, S., Broch, K., Gillett, A. J., Menke, S. M., Rao, A., Credgington, D. & Sirringhaus, H. Chain coupling and luminescence in high-mobility amorphous polymers. (Under review)

[8] **Thomas, T. H.**, Harkin, D. J., Gillett, A. J, Nikolka, M., Sadhanala, A., Richter, J. M., Chen, H., McCulloch, I., Menke, S. M. & Sirringhaus, H. High mobility highly luminescent amorphous polymers. (Submitted)